Air Force Institute of Technology

AFIT Scholar

3-2022

Design and Testing of a Composite Compressor Rotor

Mauro Noel V. De Leon

DESIGN AND TESTING OF A COMPOSITE COMPRESSOR ROTOR

THESIS

Mauro Noel V. de Leon, Captain, USSF

AFIT-ENY-MS-22-M-286

DEPARTMENT OF THE AIR FORCE
AIR UNIVERSITY

AIR FORCE INSTITUTE OF TECHNOLOGY

Wright-Patterson Air Force Base, Ohio

AFIT-ENY-MS-22-M-286

DESIGN AND TESTING OF A COMPOSITE COMPRESSOR ROTOR

THESIS

Presented to the Faculty

Department of Aeronautics and Astronautics

Graduate School of Engineering and Management

Air Force Institute of Technology

Air University

Air Education and Training Command

in Partial Fulfillment of the Requirements for the

Degree of Master of Science

Mauro Noel V. de Leon, B.S.

Captain, USSF

March 2022

AFIT-ENY-MS-22-M-286

DESIGN AND TESTING OF A COMPOSITE COMPRESSOR ROTOR

Mauro Noel V. de Leon, B.S.
Captain, USSF

Committee Membership:

Lt Col Brian Bohan, PhD
Chairman

Frederick Schauer, PhD
Member

Major John Brewer, PhD
Member

AFIT-ENY-MS-22-M-286

Abstract

Additive manufacturing (AM) is known for building representations or replicas of conceptualized engine components, but was never understood as a practical method for manufacturing operating engine components. Modern technological developments have improved to the extent that AM now has the potential to manufacture operating engine components. Polymers survivable at high-temperature conditions and fiber reinforcement materials could be combined to acquire the temperature and strength requirements to be competitive with conventional turbomachinery metals. AM-based and mold-based methods could thus be used to produce compressors made with such reinforced-polymer materials.

The objective of this study was to determine the feasibility of replacing an aluminum P400 compressor with a polymer-reinforced compressor of the same scale using additive manufacturing and casting techniques. This required the use of specimen tensile testing, Finite Element Analysis (FEA), and physical spin testing of a compressor made from the materials of interest: ULTEM 9085, Onyx-carbon fiber, and Epoxy-carbon fiber. This study generated tensile data that shows Onyx-Carbon fiber exhibited the best strength properties at room temperature, but it did not bode well under peak P400 operating temperatures (475 K). ULTEM 9085 also lost stiffness at 475 K, but Epoxy-Carbon fiber exhibited a resistance to tension at this level. The property data achieved experimentally proved to fall below predicted values calculated with the Rule of Mixtures RoM. The tensile data for each material was used with SolidWorks for a Finite Element Analysis to predict failure conditions. Onyx-Carbon fiber predicted failure at 75 kRPM, however, this is not realistic because the SolidWorks model did not account for glassification temperatures. A

modification on SolidWorks could be done to account for such glassification effects, but the complexity of that effort is beyond the scope of this study. ULTEM 9085 and Epoxy-Carbon fiber compressors and predicted to fail at 49 kRPM and 45 kRPM, respectively. The SolidWorks model predicted none of the compressors would reach the full-power 98 kRPM prior to failing. The study concluded that AM compressors and molded compressor hubs were feasible, but they also proved difficult to spin test. Three turbochargers were destroyed after attempting to spin test three ULTEM 9085 compressors. Performance characteristics were ultimately inconclusive. This study ultimate concluded that compressor spin tests required a redesigned test rig. The proposed redesigned test rig features a quill shaft (shaft supported on both ends) as opposed to a cantilever shaft design (shaft supported on one side only) to reduce rotor dynamic concerns. The new rig is powered by an electric motor and features easily replacable angular contact bearings to manage loads.

Acknowledgements

Non nobis, Domine

I would like to thank Lt Col Brian Bohan for his guidance and wisdom in the process of writing this thesis. Never have I understood how frustrating it is to correct a LaTeX error, nor how rejuvenating it is to correct it, until now. It was ultimately with his help I was able to produce a quality product.

I would like to also thank Maj John Brewer and Dr Frederick Schauer for aiding my efforts with their expertise and knowledge. I knew next to nothing about Materials and Turbomachinery and these two fine gentlemen helped me through an unknown body of knowledge. I would like to thank the members of AFRL/RQTC, AFRL/RQTM, AFIT Model Shop, and the AFIT lab whose efforts were critical to the completion of this work.

I would like to thank my fiancée, my parents, my brother, and friends who supported me through the tribulations. Gloria in excelsis Deo!

Mauro Noel V. de Leon

Table of Contents

List of Figures

xv

xvii

xviii

List of Tables

List of Abbreviations

List of Symbols

DESIGN AND TESTING OF A COMPOSITE COMPRESSOR ROTOR

I. Introduction

1.1 Introduction

Additive manufacturing (AM) is often used to visually present a model or an idea for modern technology in a preliminary design phase. 3D printing methods have always been used to exemplify metal-made objects with polymer replicas or manufacturing hobby-purposed objects, such as children's toy vehicles. While 3D printing methods and casting methods still maintain their function as visual replicas, evolving technological developments have made them potential methods for modern turbomachinery manufacturing. More recent work has investigated manufactured polymers for turbomachinery components, but these studies encountered challenges with using AM and molded polymers for turbomachinery application, specifically producing components that can survive the stresses and thermal effects involved for operation. The goal in considering both AM and casting as manufacturing alternatives is to save time in skilled labor, money in raw materials, and potentially mass in the finished product. Ideally, AM and molded polymer-based turbomachinery components will be able to reduce production time, raw material cost, and component mass. There have been some previous AM studies for metal-based turbomachinery.

There is currently only a small subset of materials for studying "engineering-grade" polymers for turbomachinery manufacturing. This is where AM and casting methods can be implemented. The cost-benefit makes polymer AM especially attractive as well as their ease of operations compared to metal printers [2]. These

same cost benefits can be seen with casting as well. While polymer turbomachinery components might have a higher risk of premature failure and short life-span, the reduction in raw material cost can lead to significant cost savings.

Molding methods did not become of considerable interest prior to the introduction of fiber reinforcement. Fiber reinforcement is designed to significantly increase the strength of some base material or matrix material like epoxy resin. Polymers like epoxy resin are known for their temperature resilience, while fiber reinforcements are known for their structural resilience. Therefore, it is predicted that the combination of the two can produce a material competitive with that of conventional turbomachinery metals. Significant studies about micro-gas turbine engines were conducted by Japikse [3], Rodgers [4], and Logan [5] between the '80s and '90s. Their work expanded our understanding of centrifugal compressors by leaps and bounds. However, their conclusions were made prior to the introduction to polymer-based AM and casting methods for turbomachinery. New findings can be drawn by investigating the application of polymer-based manufacturing methods on turbomachinery components.

The present study continues from previous work and aims to fulfill the three primary objectives enumerated below:

1. Characterize the material properties and relevant operating conditions of ULTEM 9085, Epoxy-carbon fiber, ULTEM 1000-carbon fiber, and Onyx-carbon fiber

2. Conduct Finite Element Analysis (FEA) modeling to predict key failure points on a JetCat P400 compressor geometry based on known material characterizations

3. Conduct spin testing to verify accuracy of FEA model failure prediction and

determine actual failure point with a physical compressor.

The first objective is to conduct material tensile testing on the materials of interest to acquire characteristic material property data. The parameters of ultimate tensile strength and elastic modulus indicate how much stress a material can withstand before failure and at the strain behavior as that material approaches its maximum stress value. Material properties are also inputs into a computational modeling program that can provide predictive failure points.

The second objective is to generate a computer-simulated failure prediction with FEA. If FEA proves to predict failure speed accurately, FEA can be further trusted as a method to compare other parameters for optimization, such as geometry and material.

The third objective is to conduct physical spin tests to verify the accuracy of the FEA model and determine the actual failure point of the polymer compressors. The FEA model inherently contains simplifying assumptions to generate a solution while physical spin testing bypasses the assumptions and simplifications to yield the most tangible failure point before placing the compressor in an actual engine.

Figure 1 shows a potential cycle for designing a compressor. Provided an initial compressor design, a survey of working materials is conducted to qualify known materials for their potential in compressor applications. Once quality materials are selected, they are tested (specifically tensile tested) to acquire their properties at varying temperatures. These properties become data entered into the computational model for failure prediction.

The model is then evaluated for its accuracy to predict failure. Inadequate results may require more material testing. If the computer model is successful, a redesign may be called for, depending on the design objective. The compressor might be redesigned to better conform to the material properties quantified from material testing.
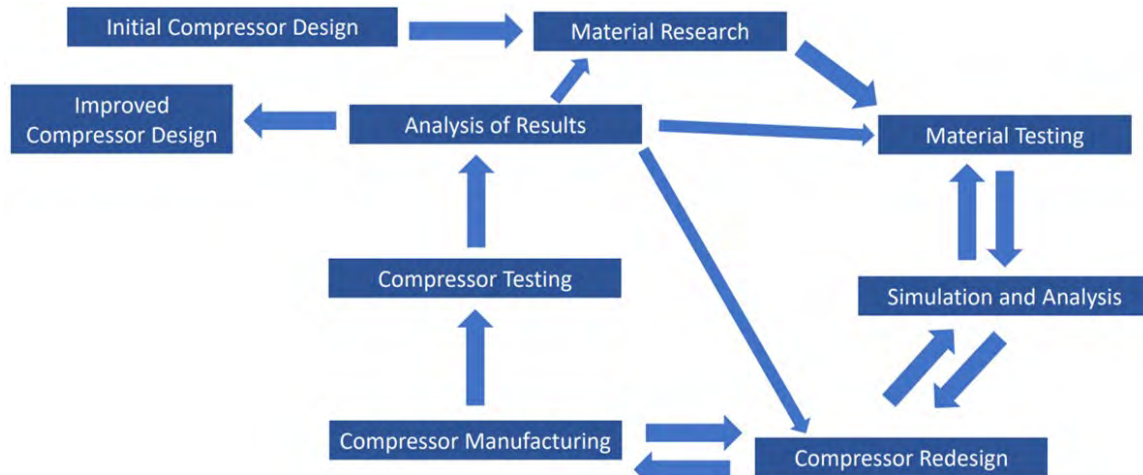
Figure 1. Compressor Design Cycle Process adapted from Bauer [1]

Once the compressor design and material are established, the compressor can then be manufactured. Unknown manufacturing limits, such as thickness or tolerance issues, may necessitate another redesign. Once the compressor is physically manufactured and in hand, the compressor is tested in its desired operating environment and analyzed for sufficiency. If the compressor design is considered insufficient, the design loop is repeated until the desired results are achieved [1, 6].

Another benefit of the use of polymer-based materials is a shorter Research and Design loop by reducing the time and ease of compressor manufacturing due to the short time-lines of AM and molding methods. This study also aims to shorten the Research and Design loop by attempting to validate the SolidWorks Model with physical compressor behavior. Producing a valid SolidWorks Model makes predictive failure assessment more efficient and mitigates the need to manufacture a physical spin test to be certain of failure behavior.

1.2 Contributions

The present study is distinguished from previous work by investigating AM and compression molding as an additional manufacturing method for compressor rotors. The inclusion of compression molding as a manufacturing method introduces the use of discontinuous fiber reinforcement to increase material strength. The advantage of discontinuous fibers is in the fact that the fibers are not limited to only the deposition layers from the printer, and fibers are free to strengthen in every direction. Because of this, Epoxy and ULTEM 1000 with discontinuous carbon fiber are added as materials of interest and have not been previously studied for compressor applications. Another distinction from previous work is the test rig configuration, which will be discussed in more detail in Chapter 3. While it is ideal for testing a compressor for operation with a configuration closely simulating an engine (with a shroud, inlet pipe, and exhaust pipe) for full-on performance analysis, the spin testing was configured to test centrifugally loaded spin only without temperature and pressure considerations. This is because of historical problems of premature failure caused by testing with temperature and pressure. The results of the spin tests further proved the vulnerability of premature failure after the spin tests severely damaged three turbochargers and rendered them inoperable. The ruination of the third turbocharger prompted a design for a new rig to test future compressor specimens with a set up that is designed for variable axial loads with replaceable bearings. This present study solely looked at centrifugal load without the compressor generating elevated temperatures and pressures. If the spin test proves the polymer-molded compressors can survive up to operating rotational speed, further study would be needed to drive the compressor to generate elevated temperatures and pressures.

II. Background

2.1 Introduction

Two types of compressors are most common in gas turbine engines: the centrifugal compressor and the axial compressor. These compressor types are primarily distinguished in two ways. First, centrifugal compressors translate axial flow into radial flow while the axial compressor maintains flow in the axial direction. Second, axial compressors generally produce small compression ratios (1.1:1 to 2:1) per stage and require multiple stages to yield higher compression ratios of up to 50:1. Centrifugal compressors independently produce larger compression ratios (4:1 to greater than 10:1) in one stage, but are typically mass flow limited [7]. In addition, axial compressors have higher efficiency and mass flow while centrifugal compressors have lower efficiencies for larger scale performance, but higher efficiencies for small scale performance. Most engine components, compressors included, are made through casting and machining.

Prior studies have attempted to integrate additive manufacturing (AM) into modern centrifugal compressor technologies [8, 9, 10]. Additive manufacturing is a fabrication method that stacks material layer upon layer to build the object geometry. 3D printing is an example of this and is the most commonly known AM method. The present study follows work by Bauer [1]. Bauer investigated additive manufacturing methods of polymers and composites and verified their repeatability for centrifugal compressor production. Composites are defined as a material comprised of two or more phases [11]. The following literature review outlines previous work that is applicable to researching AM and composite casting for compressor fabrication. The focus of the geometry is on small gas-turbine engines that use centrifugal compressors to get the most compression from a single-stage [7]. In addition to AM, the present

6

study also looked at composite casting as a manufacturing option. Literature that involves known casting methods are also discussed in the following literature review.

2.2 Centrifugal-Flow Compressors

2.2.1 Components and Functions.

Figure 2 shows the geometry of a conventional single-stage centrifugal-flow compressor. These types of compressors consist of two components: an impeller (rotor) (See Figure 3) and a diffuser (stator). The components most crucial to the centrifugal compressor's function are the impeller and diffuser. The compressor receives air at the suction side through the engine inlet. Next, the impeller compresses the air by increasing the flow velocity via rotational motion, forcing air into a smaller channel. The impeller effectively picks up the air and accelerates it outward toward the diffuser. The total pressure is changed at the impeller due to the compressor work done on the air. The diffuser section of the compressor decreases the velocity and increases the static pressure. The total pressure remains constant at the diffuser section because no work is done or extracted. The diffuser reorients the flow from radial to axial flow and channels the air into the combustion chamber. [7, 12]

In aircraft propulsion, there are four engine design types: turbojet, turbofan (or bypass engine), turboprop, and turboshaft. For relevance with the P400 engine, this section will discuss the turbojet engine.

Each turbojet engine is comprised of four vital components, which are the compressor, combustor, turbine, and nozzle, as shown in Figure 4 which contains a cross-sectional view of a conventional turbojet engine. Figure 5 shows a similar lay out except in an actual small-scale turbojet engine. Compressors increase the pressure of air flowing from the intake into the combustion chamber. The combustion chamber

7
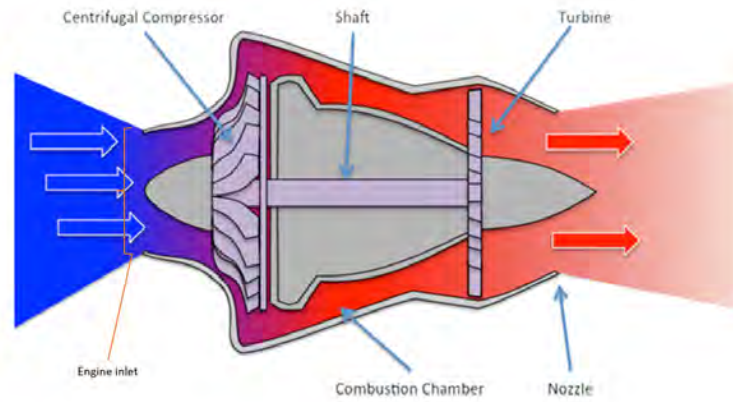
Figure 2. Diagram of Turbojet Engine with Centrifugal Compressor adapted from [13]

Figure 3. Centrifugal Compressor [14]

burns fuel with the air, and the turbine extracts work from the high temperature and high-pressure combustion products. The role of the turbine is not to generate thrust but rather to extract work to drive the compressor. Turbojets are predominantly used for high-velocity propulsion in military aircraft. Thrust is generated by the hot pressurized combustion products expanding through the nozzle. Certain military turbojet engines increase exhaust velocity and, in turn, thrust via afterburning in the exhaust duct. Given the engine size of a P400 engine, it is more practical to consider centrifugal compressors instead of axial compressors typically used for conventional military aircraft.
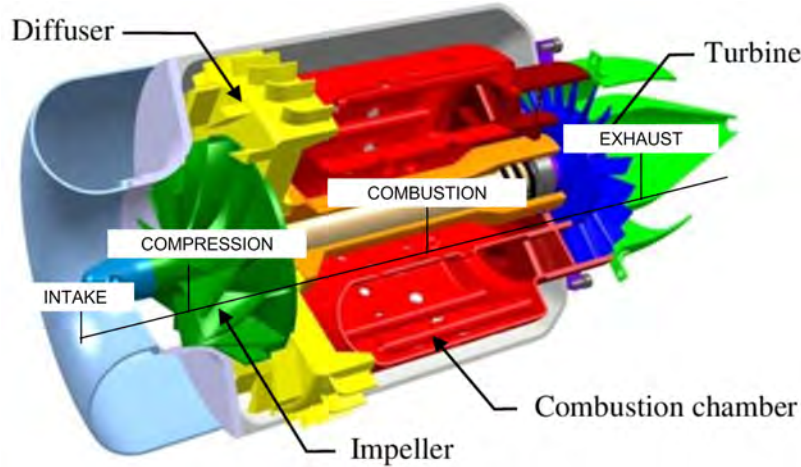
Figure 4. Turbojet adapted from [15]

2.2.2 Engine Stations.

During turbojet analysis, it is necessary to denote engine stations through the engine to aid in the comprehensibility of the analysis. While utilizing compressor station nomenclature can help explain more detailed sections of the compressor, such as the rotor and stator interaction, this study utilizes the commonly used gas turbine engine station nomenclature [1].

As shown in Figure 7, Station 0-2 is the intake of air into the inlet duct. Free stream conditions are represented at Station 0, and the location of air entering the inlet duct is noted at Station 2. Station 2-3 represents the compression of air through the engine compressor stages, in which Station 3 is the entrance into the combustor. Station 3-4 indicates the combustion process in which Station 4 represents the exit of the burner and entrance into the turbine. Station 4-5 represents the extraction of power from the combustion products via the turbine, which drives the compressor, in which Station 5 is the exit of the turbine. Station 5-9 represents the acceleration of high-energy gases to generate thrust, in which Station 9 is the exhaust station [7, 17].

The compressor must be mounted on the shaft with the turbine as a spool for the
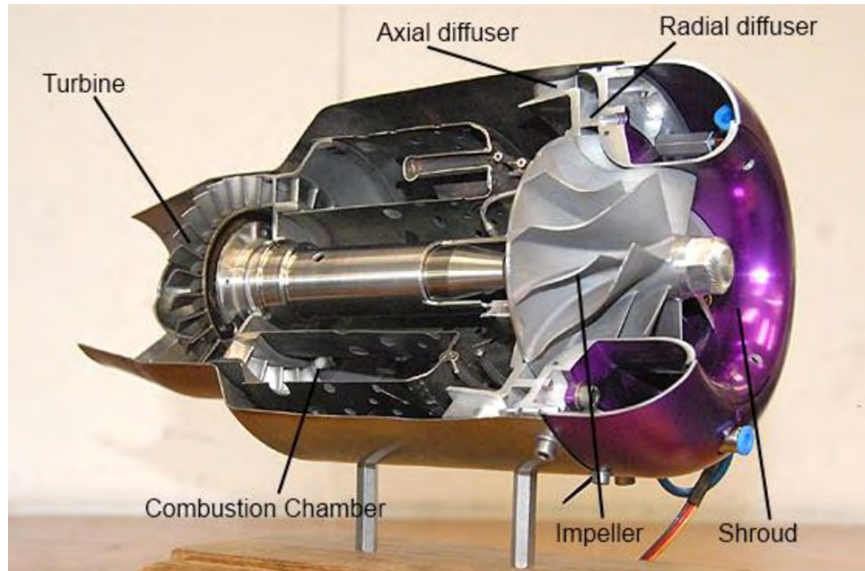
Figure 5. Micro Turbojet Cut Out [16]

engine to operate continuously. The term "spool" refers to the component assembly of the compressor, turbine, and connecting shaft. The turbine drives the entire compressor along their common shaft in single-spool engines, while dual-spool engines are split into two concentric but separate shafts. Its respective turbine in the engine drives each compressor segment. Depending on the application, the turbojet engine can be oriented with a single spool or multi-shaft/dual-shaft engine with distinct low-pressure and high-pressure spools. For this study, a single spool assembly is representative of the P400 engine. [18]

2.2.3   Common Applications.

Two commonly known applications for centrifugal compressors are relevant for this study. The first application is for small gas-turbine engines that generate less than 10 kg/s of mass flow. The JetCat P400 is an example of a small gas turbine engine and has been implemented recreationally for remote-controlled vehicles and
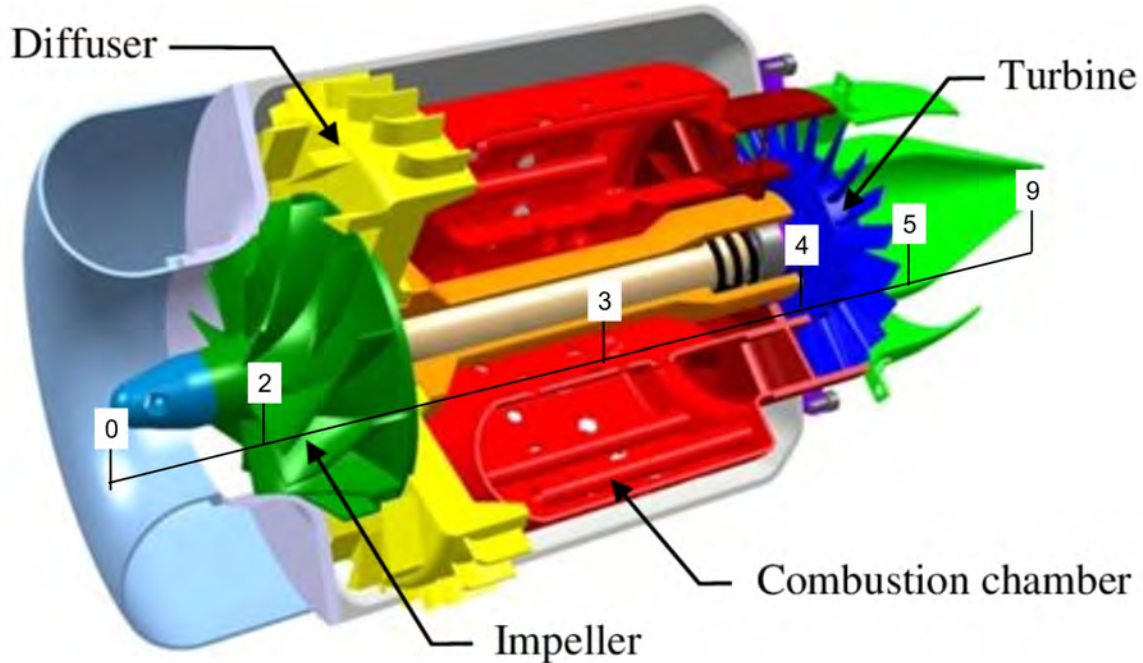
Figure 6. Turbojet with station numbers adapted from [15]

even jet pack-wing suit hybrid vehicles [19]. The goal of this study, similar to that of Bauer's work, is to produce an AM or molded composite compressor for the JetCat P400 engine shown in Figure 8 that can take the place of its conventional aluminum compressor. JetCat P400 specifications are shown in Table 1 from published data. The five key parameters relevant for compressor performance are: pressure ratio, mass flow, idle speed, maximum speed, and weight [1]. To successfully replace the stock machined aluminum compressor, the composite compressor must capably increase the air pressure to the same specified pressure ratio (3.8) and simultaneously move air at a mass flow rate of 0.67 kg/s with minimal losses. From a structural standpoint, the composite compressor should also prove to withstand the specified rotational speed (98 kRPM). It is also desired to produce a composite compressor that is lighter, cheaper, and/or faster to make than the default aluminum compressor with a comparable weight [1].

The other application for centrifugal compressors is frequently seen within a tur-
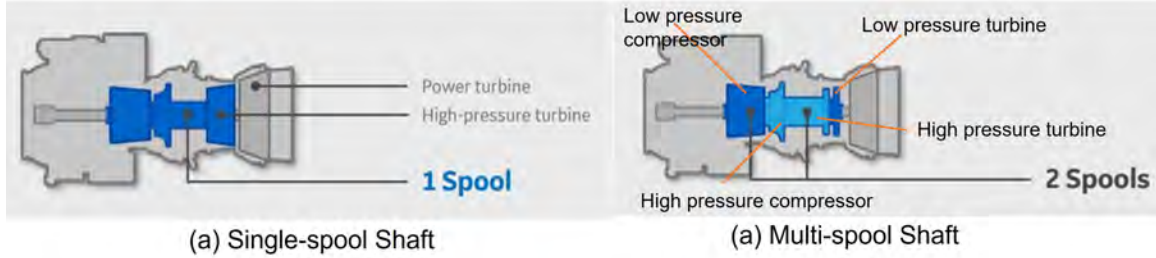
Figure 7. Turbojet Spools [18]

Table 1. JetCat P400 Published Specifications [22]

Pressure Ratio	3.8
Weight	3.65 kg
Mass Air Flow	0.67 kg/s
Idle Speed	30 kRPM
Idle Thrust	14 N
Maximum Speed	98 kRPM
Maximum Thrust	397 N
Exhaust Power	116 kW
Exhaust Velocity	590 m/s
Price	12,000 USD

bocharger. Turbochargers function to force extraneous compressed air into the Internal Combustion (IC) engine's combustion chamber to generate more power [23]. They are often found in vehicles that require that extra power, such as race cars, heavy land vehicles like trucks, and aircraft. For this study, the Garrett GTX5008R turbocharger was used to provide a source of spin for measuring the composite compressor's performance at expected operating speeds [24].

In Bauer's previous work, he compares the P400 and GTX5008R specifications to assure that the GTX5008R turbocharger was a sufficient spin source for compressor performance measurements. Since the GTX5008R has a higher pressure ratio, mass flow rate, and RPM than the P400, Bauer concluded that the GTX5008R could provide the required energy to spin and test the compressor's expected performance to replace the P400's aluminum compressor [1].

(a) JetCat P400 Engine
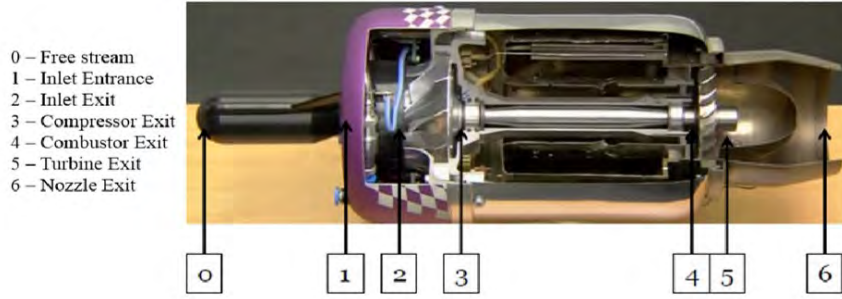
(b) P400 (internal)

Figure 8. Jet Cat P400 and Internal cutout [20, 21]

Table 2. JetCat P400 and GTX5008R Compressor Comparison. * Indicates measured by Bauer [1]

Compressor	π_c	$\dot{m}$, kg/s	RPM_{max}	D_i^*	D_e^*	N_{blades}^*	θ_{blades}
JetCat P400	3.8	up to 0.67	98 kRPM	75 mm	106 mm	14 (7+7)	57.9^o
GTX5008R	4.75	up to 0.95	100 kRPM	80 mm	108 mm	11	46.75^o

2.2.4 Compressor Fundamentals.

2.2.4.1 Velocity diagrams.

Velocity diagrams are the conventional tool for explaining the various velocity vectors involved with centrifugal compressor operation [3, 5, 25]. Figure 10, adapted from Bauer, provides an example of a velocity diagram [25]. It is convenient to analyze compressor velocities with two coordinate systems: a stationary coordinate system (observes the system at motion from outside the rotor) and a moving coordinate system (observes the flow while fixed on the surface of the rotor). In these diagrams, (U) is the compressor blade's rotational velocity, and is defined as the prod-

13
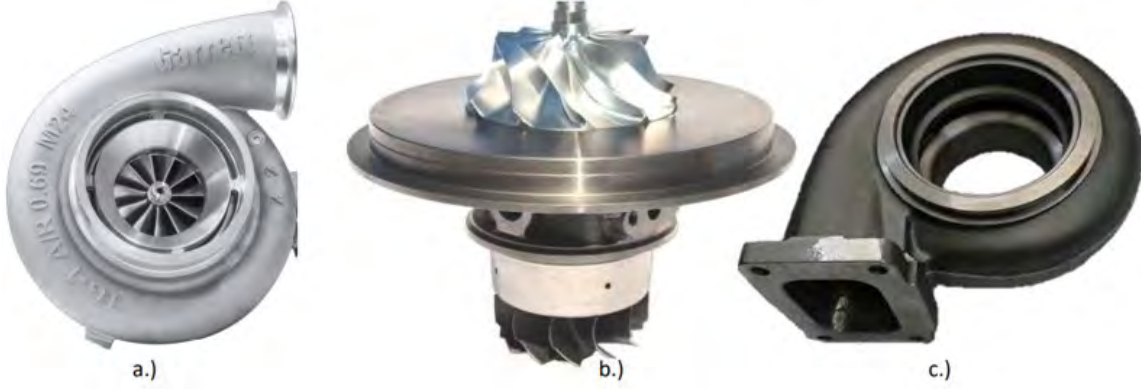
Figure 9. Garret GTX5008R. a) GTX5008R compressor within compressor housing. b) GTX5008R internal assembly or Center Housing Rotating Assembly (CHRA). c) GTX50 Turbine Housing [24]

uct of the angular velocity (ω_j) and the radius distance from the central axis (r_j). (V_1) is the incoming flow velocity and is assumed to be completely axial in direction and therefore is effectively equal to (u_1) the incoming axial flow velocity. Relative incoming velocity is equal to the difference between rotational and axial velocity, as shown in Equations 2. Relative incoming velocity can also be expressed with respect to the angle between the rotational and axial velocities, (β), and is expressed in Equation 3

$$U_j \equiv \omega_j r_j \tag{1}$$

$$\overrightarrow{V_R} = \overrightarrow{u} - \overrightarrow{U} \tag{2}$$

$$V_R = U sin(\beta) = u cos(\beta) \tag{3}$$

The velocity at the compressor exit, (V) is broken into a radial component,(ω), and a tangential component, (v), as shown in Equation 4.

$$\overrightarrow{V_R} = (\overrightarrow{v} - \overrightarrow{U}) + \overrightarrow{w} \tag{4}$$
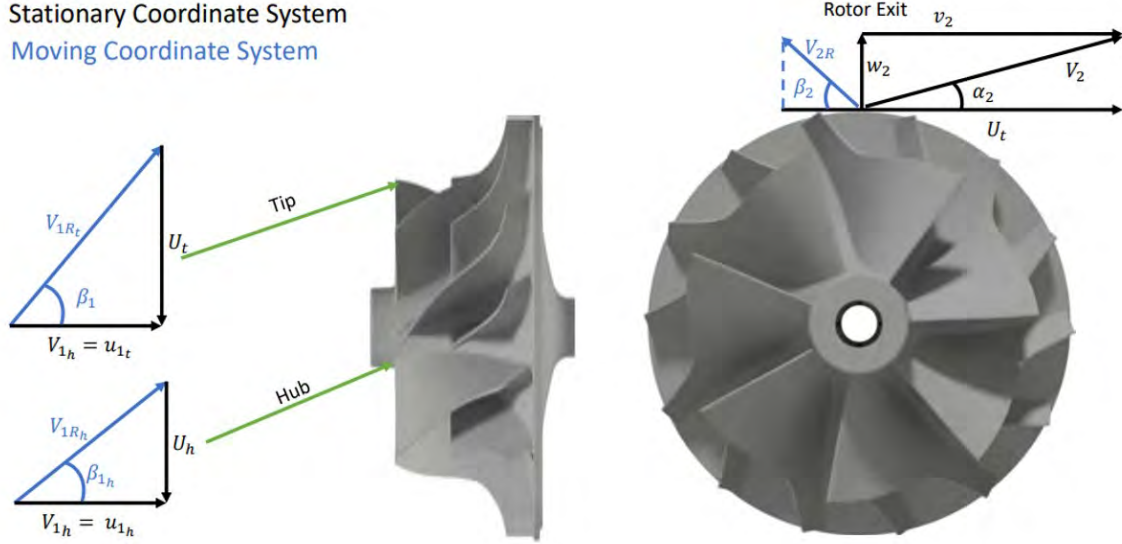
Figure 10. Velocity diagram: Centrifugal Compressor adapted from [1]

2.2.4.2   Mass Flow Rate and Energy Equations.

For analyzing centrifugal compressor operations, it is convenient to view it from the reference frame of the control volume in steady flow, as displayed in Figure 11. Constant mass flow is defined as the density multiplied by the dot product of cross sectional area and average velocity [5].

$$\rho_i(A_i \bullet V_{m,i}) = \dot{m} = \rho_e(A_e \bullet V_{m,e}) \tag{5}$$

Under the assumption of inviscid, steady flow, and constant rotor exit velocity, the compressor torque and power can be calculated in Equation 6 and 7, respectively [5, 25].

$$\tau = \dot{m}(u_i r_i - \omega_e r_e) \tag{6}$$

$$\dot{W}_c = \dot{m}\tau \tag{7}$$

Compressor power can also be expressed based on the change in energy. Mattingly

15
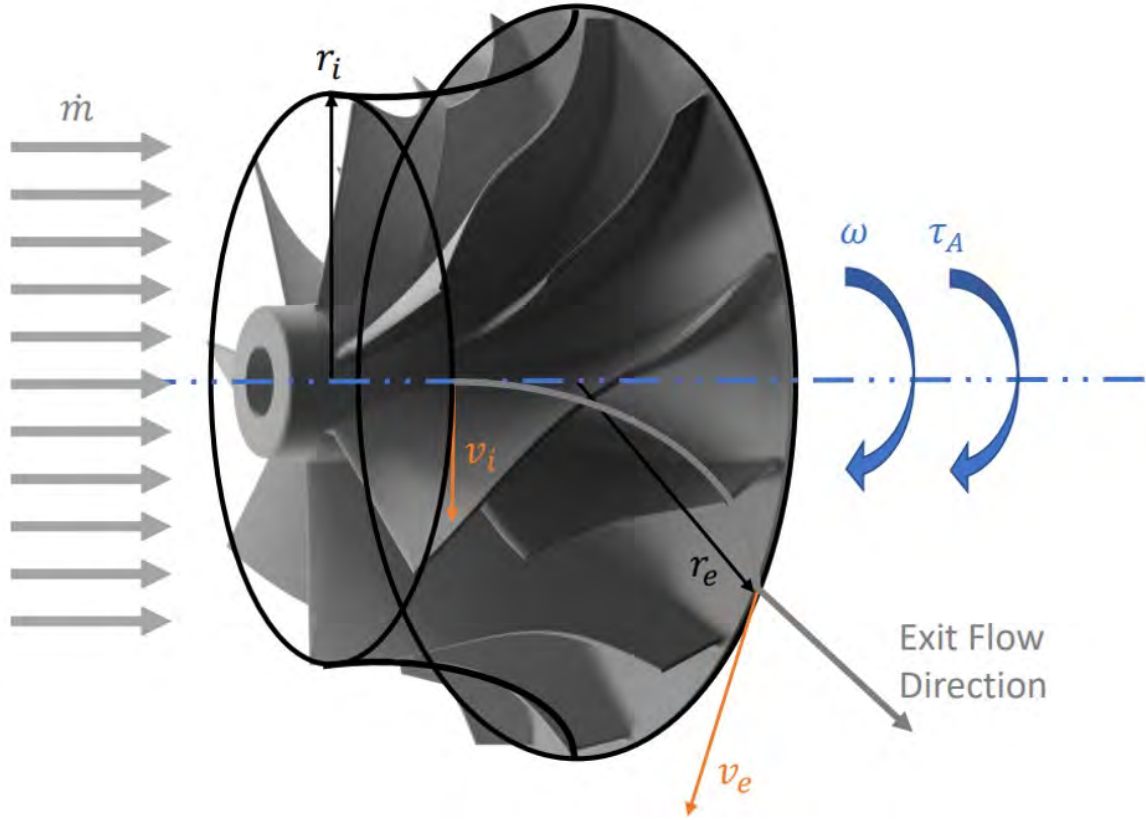
Figure 11. Control Volume of Centrifugal Compressor adapted from [1]

and Logan note that energy transferred to the control volume and the heat exiting the control volume is equal to the work done on the control volume and energy exiting the control volume. This is also more easily understood as compressor power equaling the change in enthalpy before and after the compressor. Under the assumption of steady flow, negligible gravitational effects, and negligible friction, this energy relationship is expressed in the change in enthalpy in Equation 8 [5, 25].

$$\dot{W}_c = \dot{m}(h_{t,e} - h_{t,i}) \tag{8}$$

Combing Equations 7 and 8 yields the Euler Pump equation, which outlines the relationship between the kinetic energy and thermal energy variables. This equation

relates the velocities and radii of the compressor to the enthalpy change in operation [5, 25].

$$\dot{m}(u_i r_i - \omega_e r_e) = \dot{m}(h_{t,e} - h_{t,i}) \tag{9}$$

Under the assumptions of constant specific heats and calorically-perfect gas, Equation 9 above can be simplified further into a relationship of measurable values of temperature, gas properties, and velocities [5, 25].

$$T_{t,e} - T_{t,i} = \frac{v_e U_t}{g c_p} \tag{10}$$

2.2.4.3   Dimensionless Parameters.

Equation 10 is useful for calculating temperature states before and after the compressor. It is not useful for comparing compressors to one another. Unit-based outputs also make general comparisons cumbersome since calculations will require immediate conversion. Nondimensionalizing parameters involved in the analysis make comparison more convenient as immediate conversions are unnecessary. The nondimensionalization of variables is based on Buckingham's Pi Theory and is explained in greater detail in [26]. Three dimensionless parameters are important for measuring compressor performance. These equations are the Flow Coefficient, the Head Coefficient, and the Power Coefficient, each shown in the Equations 11, 12, and 13, respectively [5].

$$\Pi_1 = \Phi = \frac{Q}{UA} = \frac{C_m}{U} = \frac{C_m}{\omega D} \tag{11}$$

$$\Pi_2 = \Psi = \frac{\Delta h_t}{U^2} = \frac{\Delta h_t}{(\omega D)^2} \tag{12}$$

$$\Pi_3 = C_{\dot{W}} = \frac{\dot{W}}{\rho \omega^3 D^5} or \frac{\Delta h_t}{h_{t_1}} \tag{13}$$

These three Π values function to characterize an individual compressor's behav-

ior. Other dimensionless parameters provide dimensionless reference conditions. Only two intrinsic thermodynamic properties, pressure, and temperature are required to describe a thermodynamic system. Therefore, dimensionless versions of pressure and temperature will be implemented to characterize the thermodynamic system for this compressor analysis which are shown in Equations 14 and 15. Other parameters for pressure, temperature, mass flow, and velocities can be corrected using thermodynamic pressure and temperature conditions. The corrected parameters are denoted with a subscript "c" as shown in Equations 16-19 [7]. T_{ref} (T_{ref}) and P_{ref} (P_{ref}) represent reference temperature and pressure in which the most commonly used reference condition is room temperature 25^oC and atmospheric pressure 1 atm. The subscript i represent the property at Station i.

$$\delta = \frac{P_{to}}{P_{ref}} \tag{14}$$

$$\theta = \frac{T_{to}}{T_{ref}} \tag{15}$$

$$P_{ci} = \frac{P_i}{\delta} \tag{16}$$

$$T_{ci} = \frac{T_i}{\theta} \tag{17}$$

$$\dot{m}_c = \frac{\dot{m}\sqrt{\theta}}{\delta} \tag{18}$$

$$\omega_c = \frac{\omega}{\sqrt{\theta}} \tag{19}$$

Additional dimensionless parameters relevant to this study are specific speed (ω_s) and specific diameter (D_s) denoted in Equation 20 and 21, respectively. Specific speed and specific diameter both represent some ratio of flow coefficient (ϕ) and head coefficient (ψ) from Equations 11 and 12. (Q) represents the volumetric flow rate, (g) represents gravitational acceleration, (H) represents the head, and D represents

the physical compressor diameter. The two parameters compare the amount of flow with the magnitude of energy imparted into the flow [3].

$$\omega_s = \frac{\phi^{1/2}}{\psi^{3/4}} = \frac{\omega Q^{1/2}}{(gH)^{3/4}} \tag{20}$$

$$D_s = \frac{\psi^{1/4}}{\phi^{1/2}} = \frac{D(gH)^{1/4}}{Q^{1/2}} \tag{21}$$

The diagram in Figure 12 presents the relationship between specific speed, and specific diameter, at various isentropic efficiencies (η) for a Reynolds number of 10^6. This type of map aids users in discerning a compressor's usefulness in a given application. For example, the compressor in Figure 12, has its highest efficiencies in the regions between specific speed (N_g) of 60-1,500 RPM and D_s of 0.5-2.0. Should the given application's specific speed increase beyond this region, an axial-flow compressor will be a more appropriate and more efficient alternative [27].

Another dimensionless parameter frequently used for centrifugal compressors is the slip factor (ϵ) which is defined as the ratio between exiting swirl velocity and rotor tip speed and is analytically-derived and shown in Equation 22 [5].

$$\epsilon \equiv \frac{v_e}{U_t} \tag{22}$$

Equation 10 can be rewritten in terms of slip factor as shown in Equation 23.

$$T_{t,e} - T_{t,i} = \frac{v \epsilon U_t}{g c_p} \tag{23}$$

The pressure ratio can similarly be expressed in terms of the slip factor.

$$\pi_c = \frac{P_{t,c}}{P_{t,i}} = (1 + \frac{\eta_c \epsilon U_t^2}{g c_p T_{t,i}})^{\frac{\gamma}{\gamma-1}} \tag{24}$$
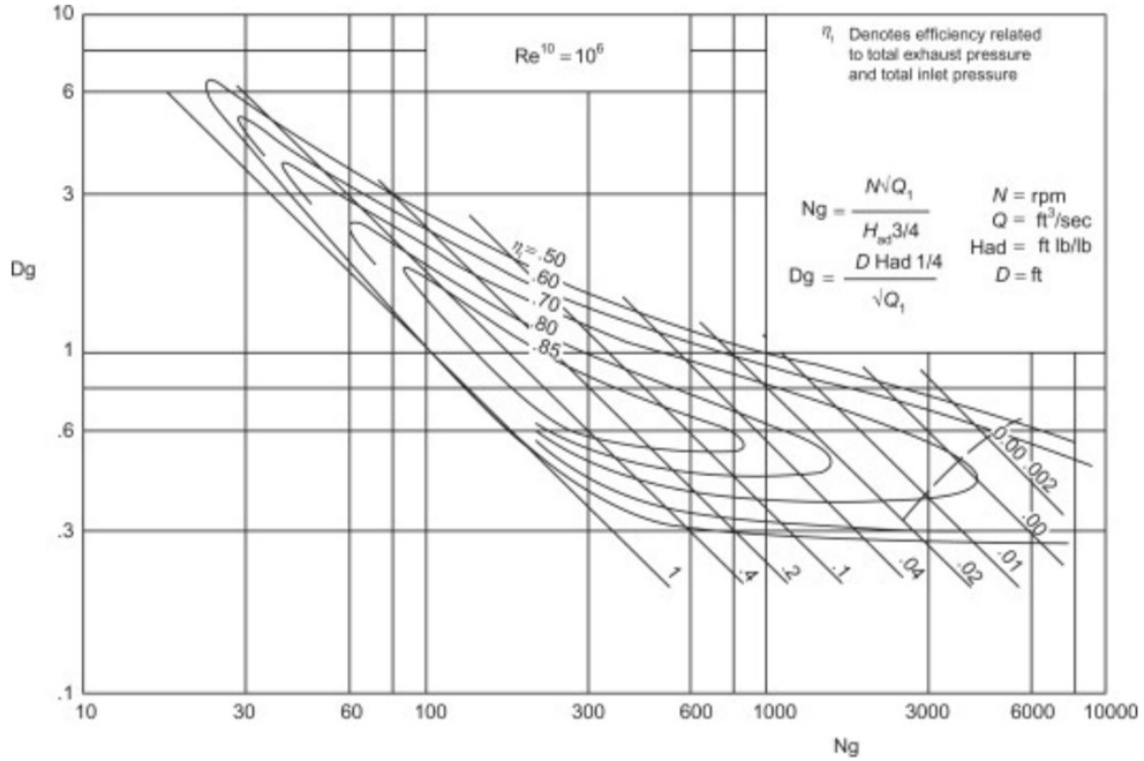
Figure 12. Centrifugal Compressor Specific Speed and Diameter Map [27]

Table 3 lists commonly used slip factors that indicate trends in compressor design. While higher blade counts improve performance, lower blade count minimizes viscous drag, making inviscid compressor analysis problematic for accuracy [25].

The last relevant dimensionless parameter for centrifugal compressor analysis is efficiency. There are two expressions for efficiency. It can either be 1) a ratio between output power and input power or 2) a ratio between ideal input power and actual input power. The second expression is most frequently used for compressors. In an isentropic compression, the temperature ratio relates to the isentropic pressure ratio as described in Equation 25 which represents the ideal amount of work imparted into the flow.

$$\tau_{c,isentropic} = \pi_c^{\frac{\gamma-1}{\gamma}} \tag{25}$$

20

Table 3. Common Equations for Slip Factor, table adapted from [1]

Originator	Slip Factor, $\epsilon =$
Logan[5]	$1 - \pi U_2 sin\beta_2/N_{blades}$
Mattingly [25]	$1\text{-}2/(N_{blades})$
Balje [27]	$1 - 0.75\pi sin\beta_2/N_{blades}$
Busemann [28]	$(1\text{-}2.4)/N_{blades}$
Eck [29]	$[1 + 2sin\beta_2/(N_{blades}[1 - D_{1S}/D_2])]^{-1}$
Pfleiderer [30]	$[1 + 8(k + 0.6sin\beta_2)/(3/N_{blades})]^{-1}$
Stodola [31]	$1 - \pi/N_{blades} * [sin\beta_2/(1 - \phi_2 cot\beta_2)]$
Stanitz [31]	$1 - 0.63\pi/N_{blades} * [1/(1 - \phi_2 cot\beta_2)]$

Conversely, τ_c represents the actual temperature rise due to nonideal work on the flow. Based on the pressure ratio, the nonideal temperature ratio will always be greater than the ideal temperature ratio. The efficiency is denoted in Equation 26.

$$\eta_c = \frac{\pi_c^{\frac{\gamma-1}{\gamma}} - 1}{\tau_c - 1} \tag{26}$$

2.2.5   Structural Limits.

It is difficult to analyze the failure conditions for centrifugal compressors due to their complex geometry. Because of this, finite element analysis (Section 3.3) is the best method for approximating component failure. Passage sizing, blade thickness, and surface roughness are also important considerations as they limit complex geometries [3]. Material comparison for compressor manufacturing will be discussed later in Section 2.4.3.

There are seven areas of potential failure for a centrifugal compressor which are displayed in a study by Japikse in Figure 13 [3]. About 98% of the stresses experienced by the compressor are a result of centrifugal loading, while 0.25% and 1.75% are due to pressure forces and thermal stresses, respectively [32]. Region 4 is the compressor tip and is expected to have the highest temperature. Region 5 is expected to contain the highest buckling load. Japikse also makes four relevant observations

involving compressor stresses: 1) high buckling load is expected at the blade-body interface close to the outer diameter 2) burst failure can occur due to the high bore stresses in the compressor disk 3) thickness distribution of the blades prevent high stresses at the blade roots 4) the shape of the compressor's back face both decrease the maximum stresses and move the location of the maximum stress away from the bore [3].
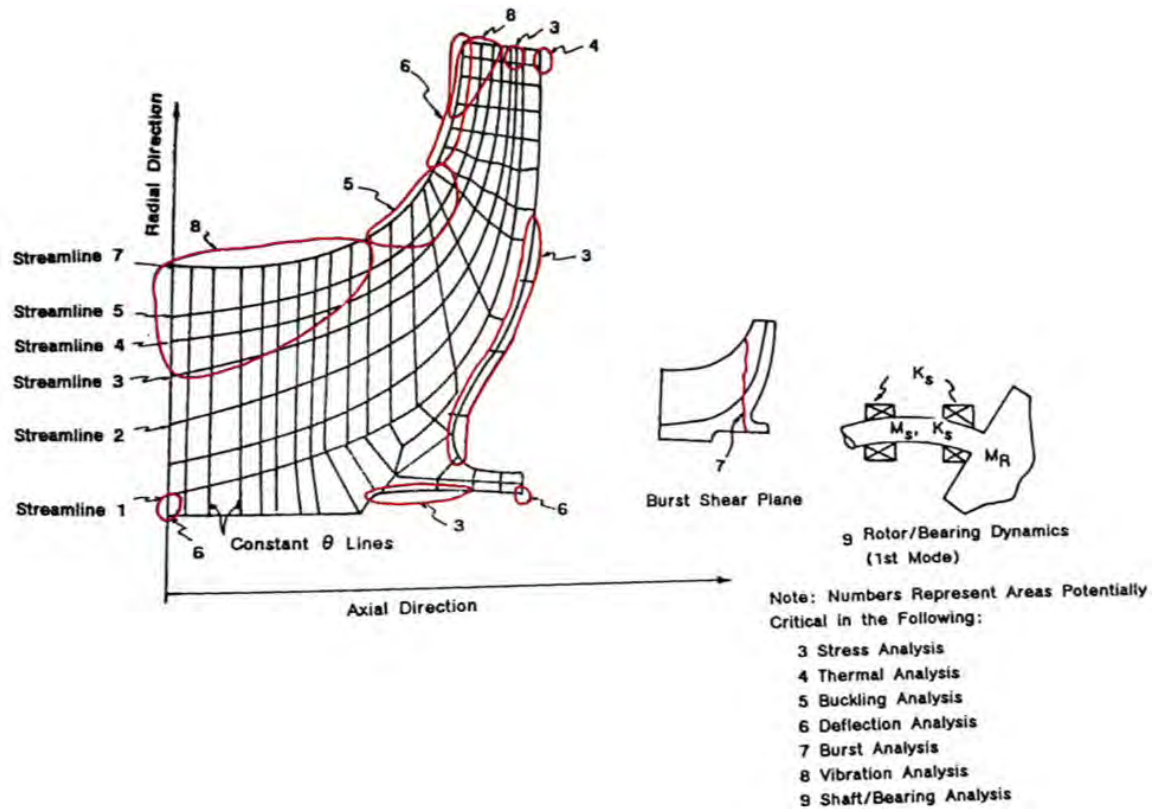
Figure 13. Critical Zones of Stress for a Centrifugal Compressor [27]

The proceeding sections dive into compressor failure. Section 2.2.5.1 derives two simplified structural solutions for compressor behavior when selecting between various materials properties. Section 2.4 outlines previous work that attempted composite compressor experimentation.

2.2.5.1 AN^2 Approach.

To predict axial compressor failure, it is common to use the AN^2 approach where A is the cross-sectional area and N is the rotational speed of the compressor [25]. Unfortunately, this simplified method cannot be implemented for centrifugal compressors as the geometry is to complex. Instead, the analysis of a centrifugal compressor is split into two sections which can be analyzed separately to understand the behavior. Such an approach requires the assumption of isotropic material properties and the assumption of homogeneous compressor models. The first half of this bi-regional analysis is the location connecting the blade and the compressor body at the inducer region, which is effectively at the blade root. Figure 14 displays the point of interest in this analysis: the location of the blade root, which is the most probable location of failure in this model. The blade thickness,(t), and blade length,(L), are measurable and therefore known values [25]. This region can be analyzed with the AN^2 method because it is almost exclusively experiencing tensile stress, as described by Mattingly [25].
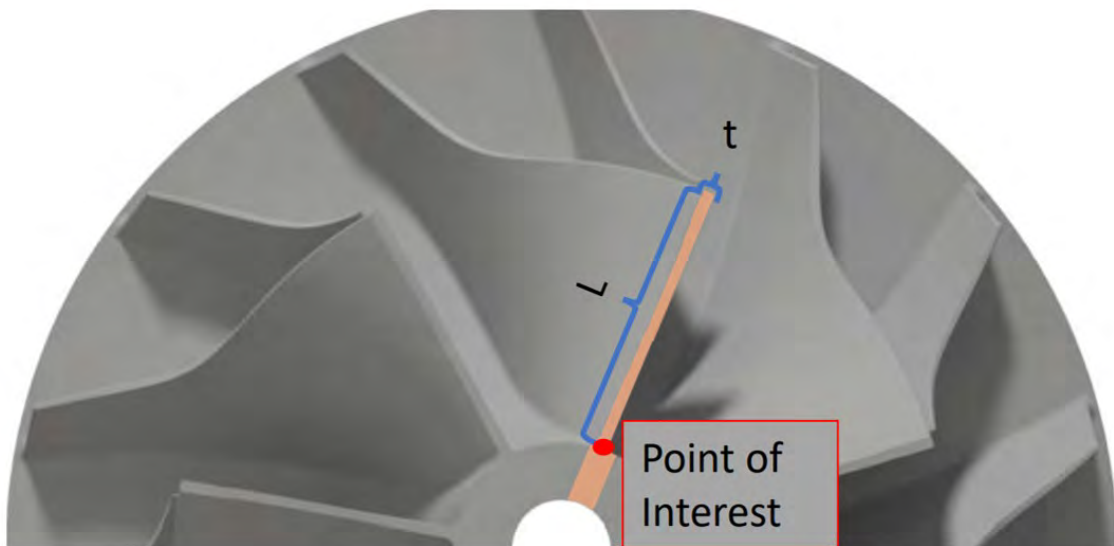
Figure 14. Simplified Compressor Blades adapted from Bauer [1]

When the centrifugal stress (σ_c) is greater than the material's ultimate stress,(σ_u), the blade-disk interface will experience failure. Equation 27 represents the centrifugal force at the location of failure where the blade area, A_b, is the blade thickness multiplied by a small depth, z. If z is a very "small" value, it is factored into the centrifugal stress.

For compressors with constant blade thickness, the stress is determined by Equation 28. Evaluating the integral in Equation 28 yields Equation 29. The compressor experiences failure when the centrifugal stress is equal to the material ultimate stress ($\sigma_c = \sigma_u$), hence Equation 29 replaces σ_c with σ_u. Equation 29 is useful because it distinguishes the compressor material properties of density and ultimate strength (ρ and σ_u) on the left hand side with the designed properties of rotational velocity and radius (σ and r) on the right hand side. If the design of a working compressor is unchanged, the strength-to-weight ratio (σ_u/ρ) must be maintained. The strength-to-weight ratio is also known as specific strength. Reducing the specific strength by one half mandates a reduction in speed by approximately 71% [25].

$$F_c = \int_{r_h}^{r_t} \rho \omega^2 A_b r \, dr \tag{27}$$

$$\sigma_c = \rho \omega^2 \int_{r_h}^{r_t} r \, dr \tag{28}$$

$$\frac{\sigma_u}{\rho} = \frac{\omega^2 (r_t^2 - r_h^2)}{2} \tag{29}$$

The other region of interest in this AN^2 approach is known as the "burst shear plane," which is shown as Region 7 in Figure 13. This plane (shown in Figure 15) is to be treated as a rotating disk that comprises of both a radial and tangential component of stress. The stress in the radial direction (σ_r) is caused by the material

far from the center of rotation pulling the material at the inner regions. The stress in the tangential direction (σ_t) is caused by material resisting outward expansion or hoop stress. The outer radius (r_o), inner radius (r_i), and angular velocity are also annotated on Figure 15 [33].
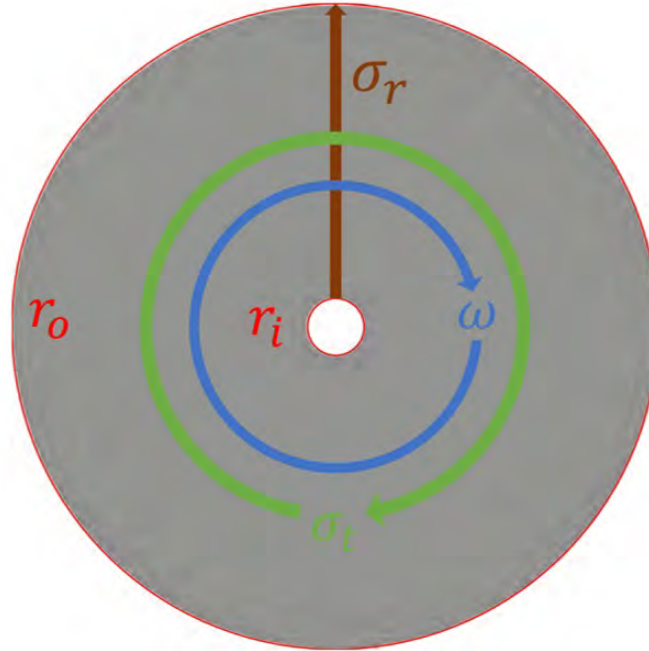
Figure 15. Simplified Compressor Body [1]

Roark outlines equations to determine radial and tangential stresses with the assumption of a constant thickness annular disk [33]. Roark notes the location of both maximum radial stress, ($\sigma_{r,max}$), and maximum tangential stress, ($\sigma_{t,max}$), where the maximum radial stress takes place at the geometric average of the inner and outer radius represented by $(r_i r_o)^{1/2}$, and the maximum tangential stress takes place at the inner radius, r_i [33]. As further described in his work, Roark evaluates both maximum stresses at their specified locations to produce the following equations:

$$\sigma_{r,max} = \frac{2 + \nu}{8} \frac{\rho \omega^2}{2} (r_o - r_i)^2 \tag{30}$$

$$\sigma_{t,max} = \frac{\rho\omega^2}{4}[(3+\nu)r_o^2 + (1-\nu)r_i^2] \tag{31}$$

where Roark evaluates failure as $\sigma_u = \sigma_{r,max} = \sigma_{t,max}$. While specific strength is relevant to avoiding disk burst, Poisson's ratio (ν), prevents rearrangement of Equation 30 and 31 to put material properties on one side (such as yield strength, density and Poisson's ratio) and the design properties on the other side (such as design rotational speed, inner and outer radii). Equations 32 and 33 describe the maximum radial and tangential stress in terms of ultimate strength. Poisson's ratio remains on both sides of Equation 33.

$$\frac{\sigma_u}{\rho(3+\nu)} = \frac{\omega^2}{16}(r_o - r_i)^2 \tag{32}$$

$$\frac{\sigma_u}{\rho(3+\nu)} = \frac{\omega^2}{16}(r_o^2 + \frac{1-\nu}{3+\nu}r_i^2) \tag{33}$$

A broad survey of material properties to substitute for compressors (such as metals and polymers) shows that Poisson's ratio's expected values range from 0.28 to 0.46 [34]. Since $r_o^2 >> r_i^2$, the $f(\nu)r_i^2$ term varies Equation 33 by a trivial 0.18% and can be ignored. This simplifies to Equation 34.

$$\frac{\sigma_u}{\rho(3+\nu)} = (\frac{\omega r_o}{2})^2 \tag{34}$$

Table 4 and 5 uses the three simplified failure equations for blade centrifugal stress, disk radial stress, and disk tangential stress (that is Equations 29, 32 and 34) and compares the standard Al 7075-T6 Material for the P400 compressor to the compressor design properties. These results show that the ultimate strength for Al 7075-T6 will first be exceeded at the inside wall of the shaft because the radial stress term based on design property (which is a function of r_i) is the smallest magnitude.

Table 4. Al 7075-T6 Material Properties, Jet P400 Compressor Design Properties [35]

σ_u	572 MPa		r_h	0.0127 m
ρ	$2,810 kg/m^3$		r_t	0.038 m
ν	0.33		r_i	0.0048 m
ω	10300 rad/s		r_o	0.0686 m

Table 5. Evaluated Simple Failure Equations [35]

Region	Material Property		Designed Property	
	Equation	Evaluated	Equation	Evaluated
Blade	$\frac{\sigma_u}{\rho}$	$2*10^5 m^2/s^2$	$\frac{\omega^2(r_t^2-r_h^2)}{2}$	$0.68*10^5 m^2/s^2$
Radial	$\frac{\sigma_u}{\rho(3+\nu)}$	$6*10^5 m^2/s^2$	$\frac{\omega^2}{16}(r_o-r_i)^2$	$0.31*10^5 m^2/s^2$
Tangential	$\frac{\sigma_u}{\rho(3+\nu)}$	$6*10^5 m^2/s^2$	$\left(\frac{\omega r_o}{2}\right)^2$	$1.24*10^5 m^2/s^2$

Exceeding the ultimate tensile strength is not a guarantee for failure because plastic and elastic behavior will cause stress variations along the complex geometry of the compressor, thus delaying the completion of the failure mechanism. Stress acts in multiple directions during compressor operation. While radial stress may exceed the ultimate strength, hoop stress may not. Failure can be delayed until both the radial stress and hoop stress exceeds ultimate strength, Once both exceed the ultimate strength, the burst shear plane in Region 7 of Figure 13 is created between the two locations of exceeding ultimate stress (i.e. the surface of the tip and surface of the inner radius) and causes overall compressor failure [3].

2.2.6 Compressor Design Considerations.

Currently, three key areas of interest crucially affect compressor design. The first area of interest is tip clearance and its effects on compressor efficiency (Section 2.2.6.1). This is relevant because available AM methods are notably less accurate than Computer Numerical Control (CNC) 5-axis milling methods used over the past few decades. If inaccuracies are significant in the compressor design, it may increase the tip clearance of the standard setup or cause the compressor to be too large for

its respective housing. The second area of interest is surface roughness effects on compressor efficiency (Section 2.2.6.2). Unlike milling methods, AM methods build material in layers which causes surface roughness to be greater in the build direction as opposed to the build plane. The third area of interest is the temperature boundaries along the compressor surfaces (Section 2.2.6.3).

2.2.6.1 Tip Clearance.

To assure smooth impeller rotation, clearance between the compressor blades and the shroud must be built into the compressor design. Too little tip clearance will impinge the blade on the shroud surface as the compressor rotates and the blades deform due to heat and centrifugal forces. The compressor blades might cut the inside of the shroud, or the blades themselves could break on the shroud surface and shut down the compressor rotation. Such a phenomenon happens when the compressor and shroud materials have hardness values of similar magnitudes. Too large of a tip clearance also presents problems. Large clearances can permit compressed airflow downstream of the compressor to travel upstream. This causes high-pressure and low-pressure air to mix and generate significant losses [3]. Like other parameters, tip clearance is usually presented as a dimensionless value, the relative tip clearance ratio, shown in Equation 35. The variable t represents the clearance distance between the blade tip and the shroud surface, while r_t represents the distance between the center of rotation and the blade tip [36].

$$c_t = \frac{t}{t + r_t} \tag{35}$$

The tip clearances for an axial compressor are approximately constant and, therefore can be expressed with straightforward empirical equations. The losses due to tip clearance are expressed as a drag coefficient (c_{D_t}) and are a function of the blade's

tip clearance, height, and coefficient of lift as expressed in Equation 36 [5].

$$c_{D_t} = \frac{0.29t}{r_t + r_h} c_L^{3/2}$$

(36)

Based on the aforementioned losses involved with excess tip clearance, Equation 37 expresses the effect of tip clearance on compressor efficiency. The equation implies that the reduction in compressor efficiency is dependent on the average relative tip clearances between the inlet and outlet of the compressor and a constant value, a. [37].

$$-\frac{\Delta\eta}{\eta_o} = \frac{a}{2}(c_{t,i} + c_{t,e})$$

(37)

The constant a represents the slope of the relationship between efficiency drop with zero clearance and relative tip clearance. The constant a is highly variable and complicates the equation. Between individual compressors, it can range between $a=0.2$ and $a=1.05$. Different parameters have different effects on losses due to tip clearance effects. For example, tip clearance effects tend to be augmented at higher mass flows [38]. The compressor blade height negatively correlates to a, but only with an R^2 (R^2) of 0.33. The number of blades positively correlates with a with an R^2 of 0.2 [37].

Tip clearance effects grow as the compressor scale decreases because current manufacturing methods evaluate the tip clearance as a fraction of the full-scale vane length. This is beneficial because machines can produce tip clearances with fixed accuracy, but it forces the vane length and tip clearance to be a coupled measurement during production. Therefore, the smaller the compressor scale, the greater the tip clearance effect [39].

29
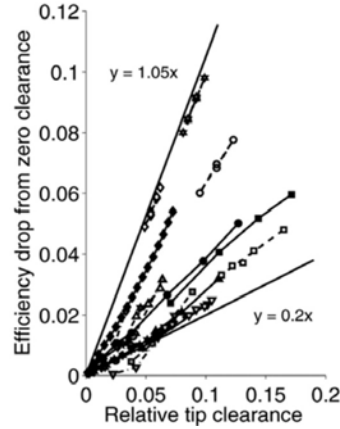
Figure 16. Change in Compressor Tip Losses for Various Compressors [37]

2.2.6.2 Surface Roughness.

The interaction between fluid flow and a solid surface always generates viscous drag. This viscous phenomenon occurs because of the no-slip condition on the solid surface and is a function of the velocity gradient at the surface, and the fluid viscosity. The region of interest is very close to the surface where the velocity profile is linear and is known as the viscous sublayer. [40].

Studies about surface roughness (k_s) often compare with the roughness of a grain of sand. The roughness Reynolds number (Re_k), defined as the ratio of roughness forces to viscous forces, is commonly used to evaluate the primary mechanism of surface drag. Equation 38 expresses roughness Reynolds number where u_t is the friction velocity and ν is the viscosity. Like the well-known aerodynamic Reynolds number, Re, the roughness Reynolds number, Re_k is divided into three regions. Re_k values between 0-5 are known as "perfectly smooth," and roughness effects are considered negligible. Re_k values between 5-70 are considered "transitionally rough," in which roughness effects, as well as viscous effects, are nontrivial. When $Re_k > 70$, the surface is known as "fully rough" and is the region in which the size of the viscous sublayer is smaller than the roughness elements and does not develop. In this region,

the viscous sublayer is considered to virtually disappear, and the primary source of drag is now pressure drag in which the fluid particles transfer momentum to the roughness elements [41].

$$Re_k = \frac{u_\tau k_s}{\nu} = \frac{RoughnessForces}{ViscousForces} \tag{38}$$

Adjustments are made in analysis for roughness when specifically analyzing compressors. The friction velocity is replaced with the relative inlet velocity (V_{1R}) and is expressed in Equation 39. For compressor analysis, the transition region changes from 5-70 to 5-90, which means surfaces with roughness Reynolds numbers greater than 90 are classified as "fully rough". Tang et al. [42] describe a relationship between the change in peak efficiency for a centrifugal compressor as expressed in Equation 40. This change is a function of Ra_w, the weighted average of physical roughness, and b_2, the exit width of the impeller [42]. Adams et al. also describe a relationship between the surface roughness, Ra, and k_s, shown in Equation 41 [43].

$$Re_k = \frac{k_s V_{1R}}{\nu_1} \tag{39}$$

$$\Delta\eta_{peak} = 0.0570963 log_1 0\frac{Ra_w}{b_2} + 0.0322204 \tag{40}$$

$$Ra = \frac{k_s}{11.03} \tag{41}$$

Measurements of surface roughness for complicated geometries can prove cumbersome. For a pen-and-paper analysis, an approximation exists to calculate surface roughness for extruded parts in the following three equations. For these equations, the roughness and thickness must be documented in similar units of length. Equation 42 expresses roughness for angle ranges of $0^0 < \theta < 70^0$ where 0^0 is relative to vertical. Equation 43 expresses roughness for angle ranges of $70^0 < \theta < 90^0$ in which roughness

is evaluated as a linear approximation between the respective roughness at 70^0 and 90^0. Equation 44 expresses surface roughness for a flat surface which is approximated as connected hemispheres. Lastly, Equation 45 expresses the roughness on the back surface and is corrected from the original roughness (multiplication by 1.2). [42, 43]

$$Ra = 0.082\frac{t}{cos\theta} \text{ for } 0^o \leq \theta < 70^o \tag{42}$$

$$Ra = (0.68 - 0.127\theta)t \text{ for } 70^o \leq \theta < 90^o \tag{43}$$

$$Ra = 0.1125t \text{ for } \theta = 90^o \tag{44}$$

$$Ra = 1.2Ra_{0-90^o} \text{ for } \theta > 90^o \tag{45}$$

2.2.6.3 Boundaries in Temperature.

The rise in temperature as a result of air compression is expressed by reformatting the isentropic efficiency from Equation 26. General range for P400 compressor efficiency are historically between 70-90% and can be used to approximate the expected temperature rise across the compressor. The relationship between total temperatures before and after the compressor is shown in Equation 46. Static temperature information is more representative of surface temperatures than total temperatures, so it is also useful to write the exit temperature in terms of static temperature, as described in Equation .

$$T_{t,e} = T_{t,i}(\frac{\pi_c^{\gamma-1/\gamma} - 1}{\eta_c} + 1) \tag{46}$$

$$T_{t,e} = T_{t,i}(\frac{\pi_c^{\gamma-1/\gamma} - 1}{\eta_c} + 1) \tag{47}$$

Figure 17 presents the static exit temperature as a function of exit flow Mach number for various pressure ratios and compressor efficiencies. The compressor pressure ratio and compressor efficiency can be calculated to a confident accuracy, but

the exit flow Mach number (M) is most difficult to calculate and causes a significant offset between the total temperature (T_t) and the static temperature (T_s) with a maximum offset of about 120K. This means that static exit temperatures will lie between 487K for the JetCat P400 compressor. The exit temperature can increase if the pressure ratio (π_c) is increased or the efficiency (η_c) is decreased as mathematical trends of Equation 46 and 47 suggest. Increasing the pressure ratio by 30% or decreasing the efficiency by 10% generates the same effective exit temperature within this temperature range.
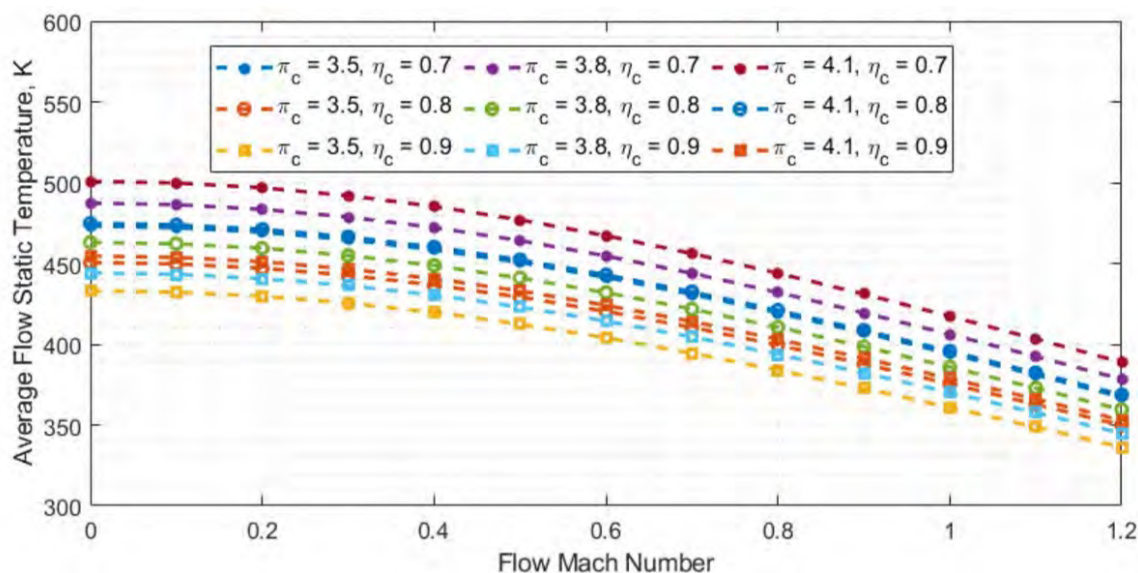
Figure 17. Estimated Static Exit Temperature adapted from Bauer [1]

Since $M = \sqrt{\gamma R T_s}$, another version of Equation 47 exists under the assumption of standard air properties: γ=1.4 and R=287 J/kg-K.

Given the following parameters in Table 6, the expected static temperature is approximately 400K.

Japikse shows the temperature distribution map for a generic centrifugal compressor. Japikse does not provide characteristics for the compressor and denotes that the boundary conditions on the back-face are not reliable. While Japikse's FEA model

Table 6. Compressor parameters [20]

Pressure Ratio	3.8
ϵ	0.6
exit velocity	729 m/s
efficiency	72%
$T_{air,in}$	293K

in Figure 18 does not represent the P400 compressor, it indicates peak temperatures for the model reside in the relevant range of P400 operation at 444K [3]
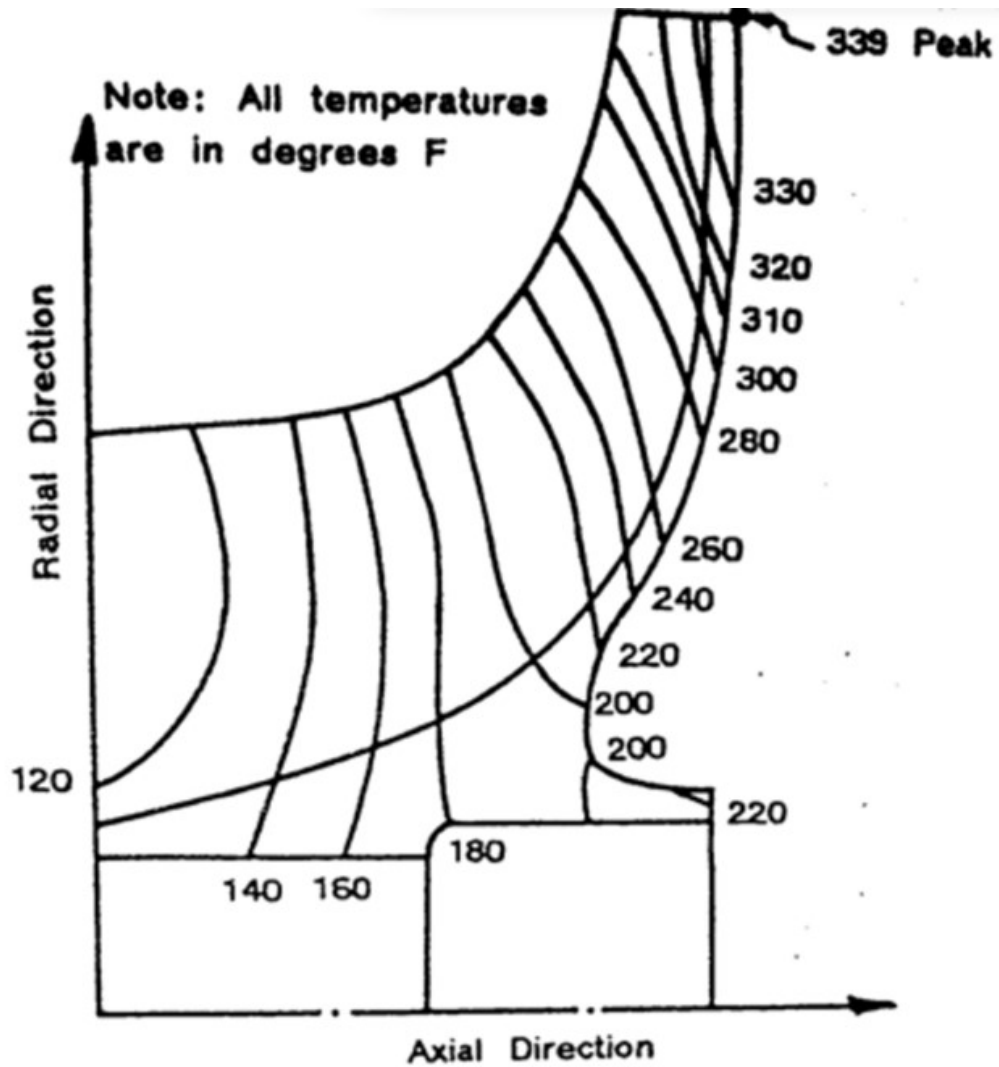
Figure 18. Temperature Distribution for FEA Model [3]

2.2.6.4 Small Centrifugal Compressor Performance Trends.

An excerpt from Van den Braembussche's work [44] presents data of compressor efficiency as a function of absolute flow rate and pressure ratio for various compressors and is shown in Figure 19. The figure data indicates two important efficiency trends: 1) increasing pressure for constant mass flow decreased efficiency, and increasing mass flow for constant pressure ratio increased efficiency. 2) maximum possible efficiency reduces with increasing pressure ratio, no matter the flow rate. The Jetcat P400's performance on this chart is denoted by the star on Figure 19. Another useful data plot is a compressor performance map which describes the relationship between pressure ratio, mass flow, rotational speed, and efficiency for one distinct compressor. Figure 20 shows the compressor map of the GTX500R and indicates the operational region the system [25]. The chart presents speeds between 45k - 100k RPM because 100k RPM is the maximum safe speed below failure while 45k RPM is the lowest speed with significant efficiency; speeds below 45k RPM yield efficiencies too small to be relevant. The left and right bounds of Figure 20 are based on the compressor blade aerodynamics. The maximum mass flow rate is modulated in two ways. The first way is by choking the mass flow along the throat of the inducer, which is independent of the rotational speed. The second way is by choking the throat of the impeller, which increases with U_t^8 [5]. The left limit depends on an occurrence known as the surge that happens if an excessively high-pressure ratio is applied upon too small of a mass flow rate. For centrifugal compressors, a surge occurs because of the Coriolis forces that exist when translating axial flow to radial flow. These Coriolis forces detach the fluid and can lead to blade stall. Similar to high angles of attack leading to wing stall, high angles of the blade relative to the flow can lead to blade stall. In turn, instantaneous loss in pressure generation leads to reverse flow [3]. This phenomenon will continue until the mass flow increases or a catastrophic failure happens. [5]
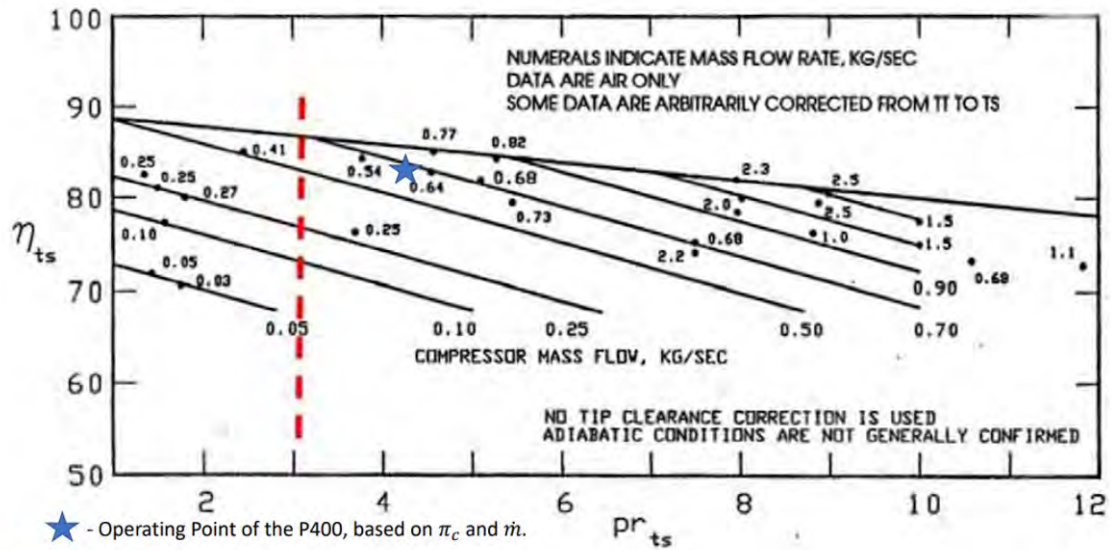
Figure 19. Centrifugal Compressor Pressure Ratio vs. Efficiency at Various Flow Rates. P400 Data Overlaid. Dashed Line Demonstrates Decreasing η_c with decreasing $\dot{m}$. Adapted from Bauer who adapted from [20, 44]

A study by Grannan et al. overlays test results of a micro-gas turbine compressor over a similar turbocharger compressor map, indicating that compressors of similar geometries and operating conditions can achieve similar efficiencies. The JetCat P400 compressor is very similar to common turbocharger compressors used in automobiles which is advantageous as there is a sizeable amount of historical information about performance, safety, and production for these types of compressors. Because P400 compressor is designed for lower pressure ratio and mass flow rate than most other compressors, it will operate in the furthest edge of the compressor map at full thrust performance, as shown by the farthest green star in Figure 21. The green stars represent operating points for the P400. At higher velocities, it reduces from 82% efficiency to 72% efficiency. These outer regions of the map consequentially reduce the efficiency below that of the maximum possible for this size compressor down to 72% compared to the 85% maximum possible as shown in Figure 19. A compressor would be more expedient should the compressor map's shape be long and thin, inciting the
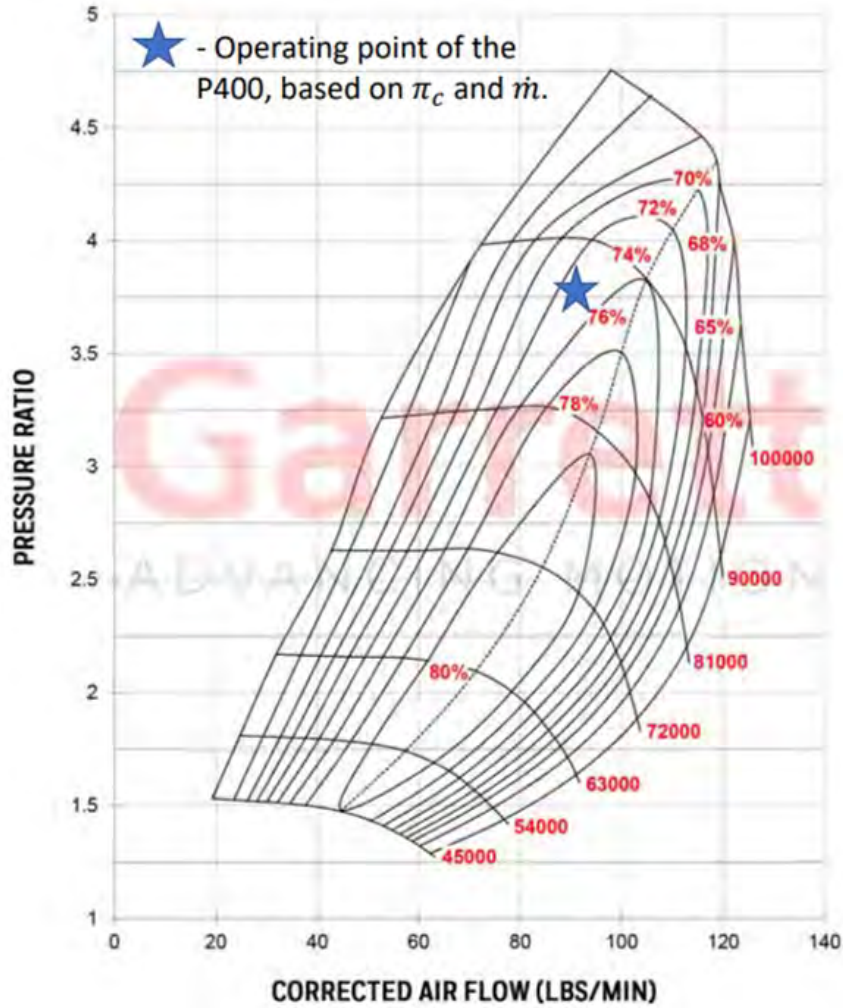
Figure 20. Compressor Map for GTX5008R. P400 Data Overlaid [20, 24]

desired maximum efficiencies toward the expected operating conditions for the P400.
[45]

2.3 Manufacturing Methods

This study primarily focuses on Additive Manufacturing and Composite molding.
A short summary of traditional subtractive manufacturing is provided for complete-
ness. Historically, subtractive manufacturing via CNC machining has been the con-
ventional choice for manufacturing engine components. Other forms of manufacturing
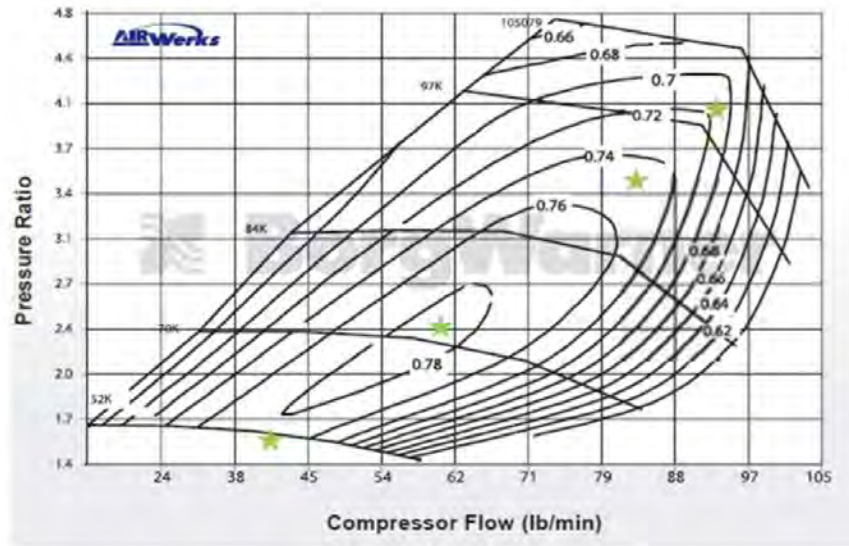
Figure 21. P400 Operating Line Overlaid on S400SX3 Compressor Map adapted from Bauer, adapted from [45]

such as additive manufacturing and molding more often have been used outside of aerospace applications and are still being explored as alternatives for conventional CNC machining. This section will review literature about these three manufacturing methods.

2.3.1 Subtractive Manufacturing.

As the most historically precedented method, subtractive manufacturing is also the most commonly used among the three manufacturing methods discussed for this review. Subtractive manufacturing methods take a billet of a given material and cut away regions from the existing object to leave behind a desired geometric shape. This method has matured enough to yield high-precision and high-accuracy results with automation and computer control. Subtractive manufacturing requires the machine operator to create a tool path to trim layers off the working part in the shape of the desired geometry. While the cost of this tool path does get distributed to multiple compressors, its creation will increase the overall cost of labor. Costs can become

a detriment with high production numbers due to the time for the machine to cut the geometry out of a solid billet. This is because the tooling, in general, is costly for subtractive manufacturing, given that it requires high-strength and high-precision tools to cut high-strength materials into finished parts. [46]

The three most common CNC machining operations are drilling, milling, and turning. Drilling uses multi-point drill bits to produce cylindrical holes in the working part. Usually, the machine operates the drill bit perpendicular to the working part to generate vertically-aligned patterns, but drill bits can be angled to produce more oblique patterns. Drilling is used more for creating holes in a working part, and the accuracy of the cut is limited to the size of the drill bit. Reaming, the widening of the hole on a part, is often done to precisely control hole diameters following a drilling process. Various drilling operations are depicted in Figure 22
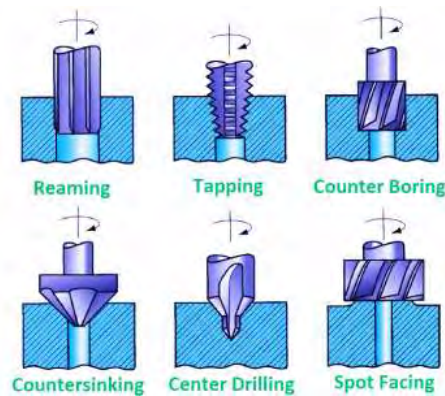
Figure 22. Drilling Operations [47]

Milling uses rotating multi-point cutting tools to remove pieces of material from the working part. The working part is fed in the same direction as the milling tool's rotation to shape the object. Milling produces a broader range of shapes, including complex 3D components compared to drilling. Milling operations can also make holes by interpolating a circle as it cuts, while a drill cannot be used as a mill. Each of the subtractive manufacturing methods can also be combined to make 4 to 5 axis mills

39

that blend lathe and mill operations to produce complex shapes beyond what a lathe or 3-axis mill is capable of alone. Methods of milling are shown in Figure 23
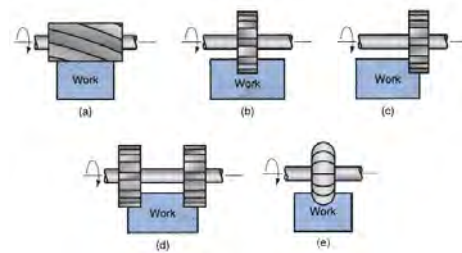
Figure 23. Milling Operations [48]

Turning, or lathing uses single-point cutting tools. The lathe rotates the working part with the cutting tool at the part's surface to remove material and shape the object. This method produces rounded or cylindrical-shaped products. Timing the movement of the cutting tool to the rotation allows the creation of screw threads. [46]. Lathing methods are shown in Figure 24.
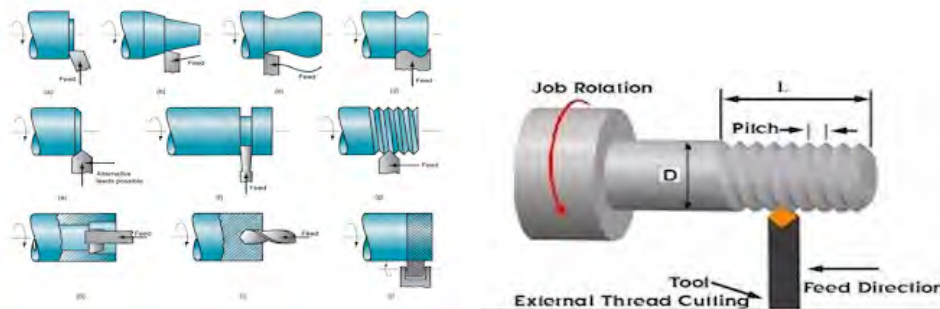
Figure 24. Lathing Operations [49]

compressor parameters

2.3.2   Additive Manufacturing.

Instead of removing pieces of existing material to build the desired object, AM adds material layer upon layer (on the scale of millimeters or μm) in an additive fashion, hence the name. The attraction to AM stems from the fact that high-strength

metal tools are not required and that AM produces less wasted material or scraps via cutting and results in 90% utilization of standard materials. AM also bypasses certain assembly requirements and produces more obscure geometries that subtractive manufacturing cannot due to existing cut-angle limitations inherent in CNC machinings such as internal voids and curved internal passages. [46]

In Gibson's review of AM technologies [2] he addresses six differences between AM and CNC machining, the most common form of subtractive manufacturing. The first difference: existing material inventory is less abundant for AM than CNC machining. Virtually any material can be CNC machined, but AM methods lend themselves toward thermoplastics with particular thermal and viscous properties, metals that can be pulverized or granulated into powders, or polymers that can be hardened or cured. The second difference is that CNC machines usually remove material layers faster than AM methods can build the same amount of layers, but the design-program-build loop is slower for CNC machining than AM. The turnaround time of AM depends predominantly on the available volume of material, while CNC machining depends predominantly on the complexity of the desired geometry. The third difference: AM can generate more complicated geometries than CNC machining methods. This is because subtractive manufacturing requires "cutting through" the working part to edit more complicated regions, such as regions under an overhang. AM does not need to do this since it builds up the geometry, not removes it from the existing volume. Hollow objects or turbine cooling passages that have a twisted design are examples of this advantage in AM. The fourth difference: for AM, the expected accuracy of the outgoing product depends on the chosen AM method. Hobby-tier 3D printers usually print with noticeable build-layer lines because the layers are less refined. In contrast, the higher-end printers print with finer diameter lasers and have less noticeable build

layers. The fifth: AM printers can print a wider range of complex geometries. Large overhangs, hollowed-out sections, and sharp internal corners tend to be difficult to produce with CNC machining but are not problematic for AM methods. The sixth difference: CNC machine programming is very laborious, which takes hours of skilled labor to confirm the machine shapes the geometry accurately, while AM printers only have a handful of settings [2].Due to the anisotropic qualities of AM-built components, the orientation of the build direction will make a difference in material properties. As a result, the build direction must be specified when characterizing an AM product. The three print orientations for AM are pictured based on their test specimen shape in Figure 25. The ZX and XZ directions are the conventional specimen orientations used for publication to exemplify material strength limits.[50]
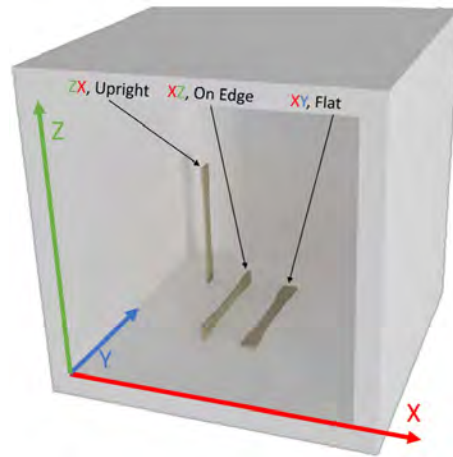
Figure 25. Common Axis Definitions and Build Directions adapted from Bauer [1]

The general premise of AM is to additively build one layer of material upon another until the final geometry is constructed, yet several complicated methods exist to do this. The ASTM F42 Committee on AM Technologies categorizes these methods into seven categories: Sheet Lamination, Binder Jetting, Material Jetting, Directed Energy Deposition, Powder Bed Fusion, Vat Photopolymerization, and Material Extrusion. Every method has its advantages and disadvantages that dispose one to

be more preferable than another for a particular application. Further, the materials accessible for each method and the material properties of the print products differ significantly. This review of AM methods below cover only the relevant AM methods of this study.

2.3.2.1   Sheet Lamination.

Sheet lamination builds 2D regions of material and bonds each layer together, as shown in Figure 26a. There is a sequence of four steps required to accomplish this. First, control the print material's location on top of the build plate. Second, cutting a 2D cross-section of the material layer with a laser or cutting tool, and third, bonding the cross-section to the preceding layer. Fourth, the succeeding layer is placed on top, and the sequence of events is repeated [51]. The above four steps present the form-then-bond process while a different version exists, the bond-then-form process, in which the machine alternates the second and third steps. The method often uses paper such as the vase in Figure 26b, thermoplastics, and a few metals. Adhesives, thermal bonds, clamps, or ultrasonic welds are usually implemented for the bonding step [2]. Sheet lamination has two advantages: 1) each material layer is dependent solely on the circumferential cutting as opposed to the area, which increases the speed of each printed layer. 2) the material for this method is relatively cheap compared to other methods due to its availability. The disadvantages with sheet lamination are the quality of the lower surface finish and the limited accessibility to print material [51]. This is one of the longer-standing AM methods but is still considered in its infancy in development. [1]
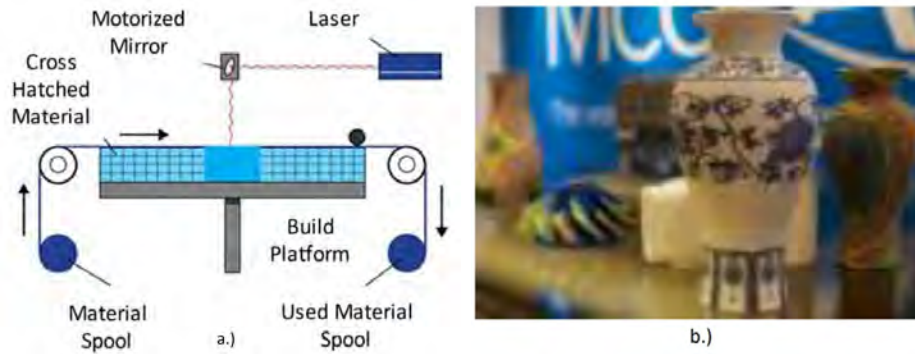
Figure 26. Sheet Lamination, images adapted from [51, 52] a.) Graphical Depiction of Sheet Lamination [51]. b.) Printed Vase example of Sheet Lamination [52].

2.3.2.2 Binder Jetting.

Binder jetting builds a geometry by ejecting a binding agent into a bulk of powder (the process jets a binder. Hence the name "binder jetting"). Ejecting the binding agent over a designated surface area will build a cross-section as shown in Figure 27a. Binder jetting is executed in the following steps: First, a layer of powder is spread across the build platform. Second, the print head ejects the binding agent over the powder bed at in the shape of the desired 2D cross-section. Third, once the cross-section is constructed, the build platform is lowered to jet the next layer with a binding agent, and the process is repeated [51]. Once the entire geometry is constructed, it is usually left alone to allow the binder to cure completely. For binder jetting metals, the printer either sinter (melts) the powder together and then the binder is removed, or the powder is impregnated with another metal that has a lower melting point than the working powder. All materials that can be ground or pulverized, such as metals, ceramics, glasses, wax, and polymer, are usable for this method since they are later held together with a binding agent [2]. The advantageous aspects of binder jetting are the print speed, range of available materials, and print settings. Print speed is an advantage because every layer is bonded with each pass of the print head which makes

the print speed highly dependent on the working geometry's length. The diversity in printable materials permits almost an infinite quantity of combinations for material properties [51].
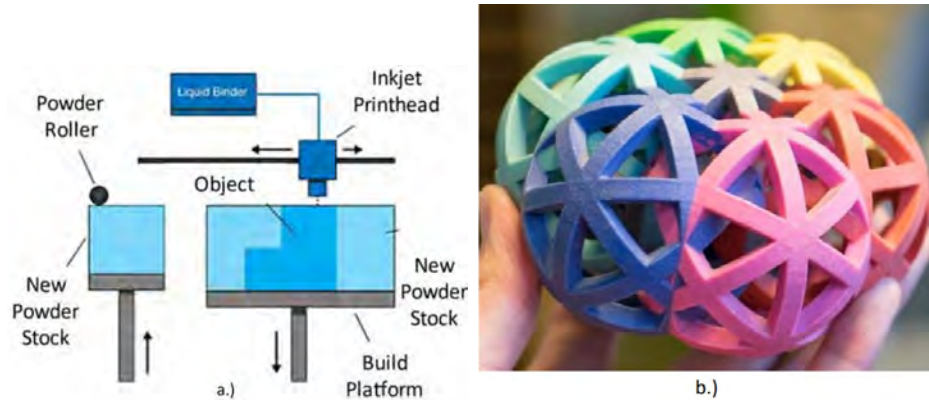
Figure 27. Binder Jetting, images adapted from [51, 53] a.) Graphical Depiction of Binder Jetting [51]. b.) Interlocked Sphere example of Binder Jetting [53].

2.3.2.3 Material Jetting.

This method is effectively the opposite of binder jetting in which the material is jetted into the binder and cured with an ultraviolet (UV) light after each pass. Material jetting also uses the position-deposit-solidify process like binder jetting [51]. There exist four ways to jet the material on the binding agent: deposit-cure, melt-deposit-harden, strain-deposit-harden, and suspend-deposit-evaporate. Deposit-cure ejects material that is curable via UV light. Once ejected, the UV emitter follows the print path to harden the material as shown in Figure 28a. Melt-deposit-harden simply melts the working material, lets it cure, and repeats on top of the next layer. Strain-deposit-harden depends on shear-thinning Bingham plastics (polymers), which can flow smoothly when under high stress. Once the material is ejected on the build surface and the stress removed, the material thickness increases and establishes the geometry. Lastly, the suspend-deposit-evaporate process starts by placing particles

of material (i.e., ceramics or metals) inside a liquid (i.e. methylated spirits). Then, ejects the mixture onto a build platform and lets the liquid evaporate, leaving the desired build material [2]. The main advantages of material jetting are its extreme accuracy relative to other methods, and the variety of colors print as shown in Figure 28b [51]. The disadvantages of this method are the property limits of the common working material as well as the requirement for support material for this method to work [1].
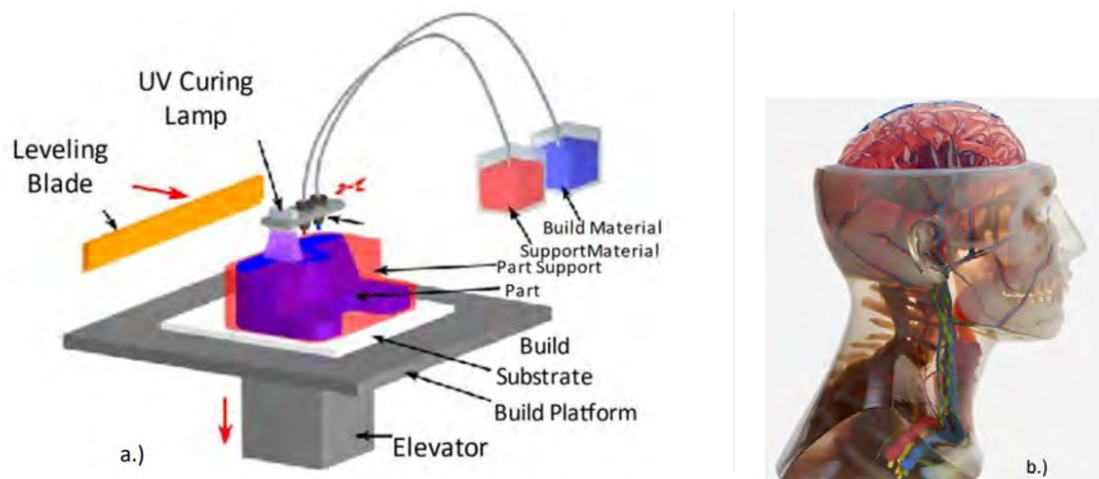
Figure 28. Material Jetting, images adapted from [51, 54] a.) Graphical Depiction of Material Jetting [51]. b.) Full-Color Anatomy Model Example of Material Jetting [54].

2.3.2.4 Direct Energy Deposition.

Direct Energy Deposition (DED) is not frequently used to produce new geometries but more often to repair or modify completed prints. This method ejects material (i.e. metal wire or metal powder) and melts it with an energy source (laser or electron beam). The source of energy heats the ejected material to its melting point and leaves it on top of the build surface to harden, as depicted in Figure 29a [51]. This method is usually implemented with metals, polymers, and ceramics. While similar to CNC welding, DED is applied for more complex geometries beyond that of welding two

components together. Modulating the energy input to the material will modulate the layer adhesion and microstructure for the working material. Another advantage to DED is the manufacturing speed can be downgraded to increase the accuracy and quality of the product microstructure. Disadvantages are a lower quality surface finish, and a smaller inventory of working materials [2].
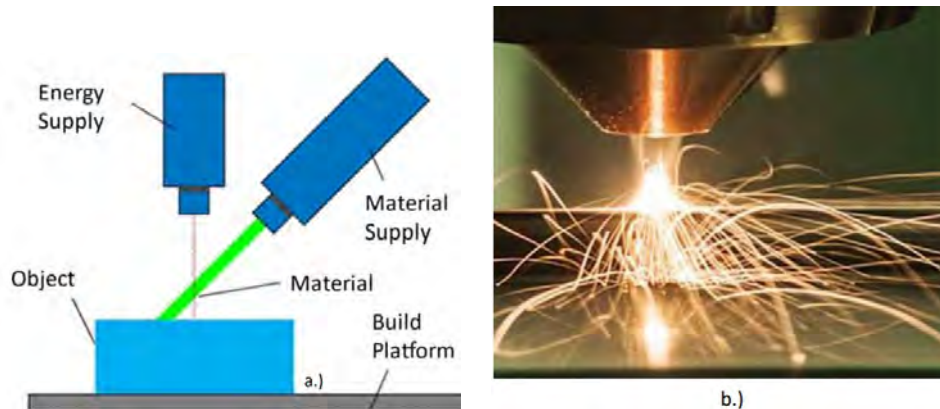
Figure 29. Directed Energy Deposition, images adapted from [51, 55] a.) Graphical Depiction of DED [51]. b.) Metal Deposition with DED [55].

2.3.2.5   Powder Bed Fusion.

Powder Bed Fusion (PBF) is closely related to binder jetting, but it exchanges the ejection of a binder into a powder bed with a laser to melt the powder into desired geometries. Once the powder layer is melted, the melted layer is lowered to cure, and the roller pushes more working powder to build the next layer as pictured in Figure 30a. To reduce thermal warping, a preheat sequence is often used on the build region of the powder. This preheat helps reduce the laser energy required to melt the powder and reduces the cooling effect between build layers, preventing premature hardening. Thermoplastics, ceramics, and weldable materials are the typical materials used in this method. Aluminum tends to be harder to process than other metals because of an oxide layer that forms on the aluminum powder when exposed

47

to air at high temperatures. This can be solved by performing the PBF process in inert gas. Once the building geometry is fused, it is often subsequently post-sintered to reduce the microstructure's porosity. Maintaining the working build geometry just below melting temperature minimizes free energy and generates regions of minimized surface-to-volume ratio [2]. Advantages of PBF are lower costs compared to CNC machine components, the inherent support structure in the process with the surrounding unmelted powder, and the range of usable materials. Disadvantages include a slower print compared to other methods, the reduction in material property magnitudes, limits on the scale of the product build, significant power expense due to the laser and heater, and the existing dangers of working with fine particles [51]. The compressor in Figure 30b was built using powder bed fusion [8].
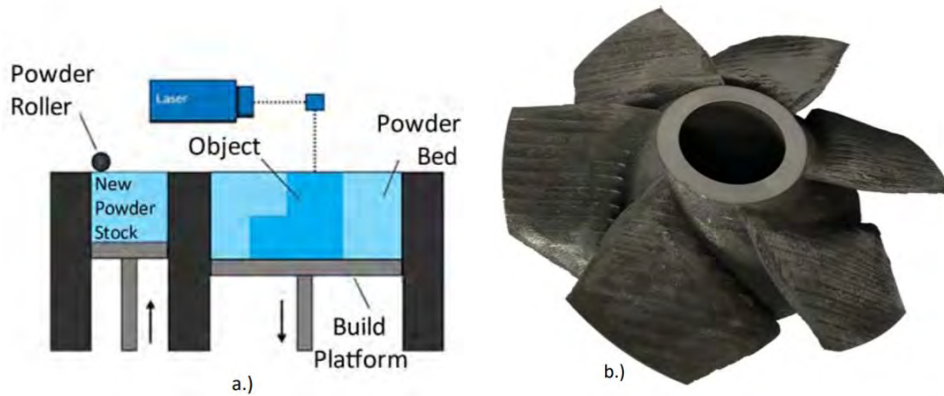
Figure 30. Powder Bed Fusion, images adapted from Bauer, adapted from [51, 8] a.) Graphical Depiction of PBF [51]. b.) PBF Axial Compressor [8].

2.3.2.6   Vat Photopolymerization.

Vat photopolymerization (VP) works with materials that remain in a liquid phase until UV light radiates the material and hardens it. Once the first layer of the liquid is cured to the desired pattern via UV light, the build platform lowers and brings a new layer of liquid photopolymer on top for the next layer to be cured. This method

is iterated until the desired geometry is reached. A diagram of the method is shown in Figure 31a [51]. Once completed, the component is placed in a post-curing box in which a projector radiates UV light over the entire surface area of the building geometry, curing the whole incident area at once. This reinforces build geometry as well as helps to omit anisotropic properties inherent within that incident layer. Only photo-curable polymers can be used to implement this method [2]. The benefits of this method are the speed of the process, smooth surface finish, significant accuracy, and large build volumes. Drawbacks for this method are the costly materials, extensive post-processing, and necessity of support structures [51]. The compressor in Figure 31b was made using VP.
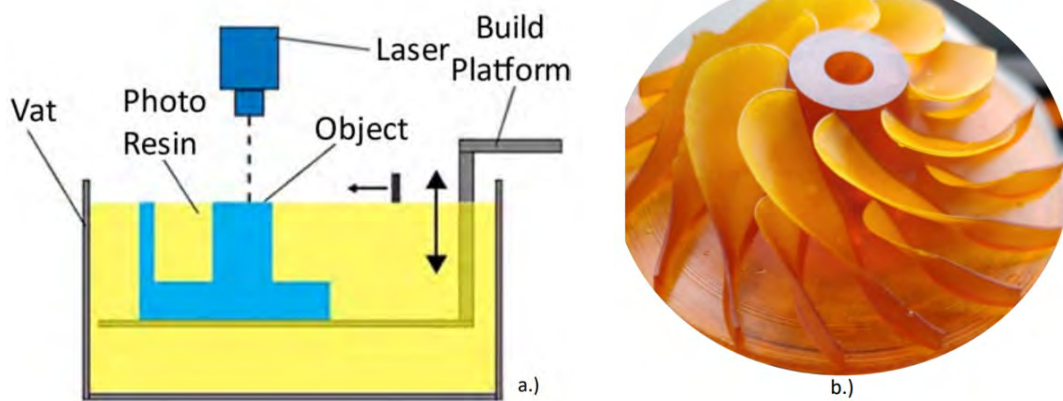
Figure 31. Vat Photopolymerization, images adapted from Bauer, adapted from [51, 1] a.) Graphical Depiction of VP [51]. b.) VP Compressor made of 300-AMB [1].

2.3.2.7   Fused Deposition Modeling.

Fused Deposition Modeling (FDM), also called material extrusion (ME), was a method patented by the founder of Stratasys, Scott Crump [2]. By ASTM definition, FDM is defined as "a material extrusion process used to make thermoplastic parts through heated extrusion and deposition of materials layer by layer" [56]. Hobby-level prints usually contain only one extrusion head. At the same time, industrial-level

printers have multiple extrusion heads, which makes extruding two or more materials simultaneously feasible, such as the model material and support material. Support material can be removed after completion of the print either by the weak adhesion between model and support material or some external method such as removal chemicals or liquid to dissolve the support material.

A visual representation of FDM is illustrated in Figure 32a. The filament material, usually a thermoplastic or polymer, is pushed through the extrusion head via driving wheels. The material is heated beyond its glass transition temperature until it can flow out of the extrusion head and cure on top of previously extruded layers already on the build platform. The extruder applies pressure on the solid filament that pushes the partially liquid material out of the extrusion head and onto the working part. This is done for one layer and repeated for the next layers until complete geometry is formed. Figure 32b depicts a compressor printed via FDM using the hobbyist polymer Acrylonitrile Butadiene Styrene (ABS). This method is known to build geometry in the cheapest, easiest, and quickest fashion compared to other AM methods. The material properties of the final build depend on the manner the print was done and is very anisotropic in nature [57]. FDM results in materials weak in the vertical plane or z-direction but strongest in the horizontal plane parallel with the build platform [50]. Each of the following factors can affect the material properties: gaps of air, raster width, thickness of layers, the quantity of contours, speed of the print, feed rate, direction of build, and temperature of the print [58]. A few of these factors are depicted in Figure 33. Gaps of air exist between the printed lines of material that are not directly adjacent to one another. This indicates that some material overlap is beneficial to the model's strength. However, they can also take away from the accuracy of the model. The quantity of contours characterizes the number of times a layer is outlined before rastering. Rastering is the way that an FDM printer fills in

50

the part based on angles and width sizes such as $+45^o$, 0°, or 90° as shown in Figure 33(a-d). FDM is considered one of the strongest AM methods for polymer-based printing. [2].
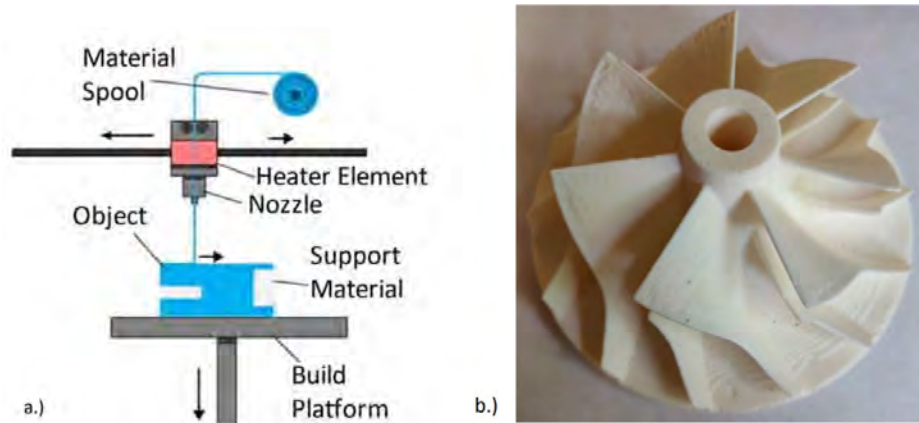
Figure 32. Material Extrusion, images adapted from Bauer, adapted from [51, 1] a.) Graphical Depiction of ME [51]. b.) ME Compressor made of ABS [1].

2.3.3   Composite Molding.

Molding is predominantly implemented for producing polymer-based components. Molding involves the manipulation of molten polymers and leaving it to set as a solid. Thermoset plastics are capable of being melted and reformed as needed, but thermoset plastics cannot be remelted. There are three forms of molding relevant to this study: casting, injection molding, and compression molding.

2.3.3.1   Casting.

Casting is considered the most basic molding process and requires the most straightforward technology.

Polymers are heated to become fluid and are then poured into a mold. Some polymers are already in liquid form before heating (such as epoxy) and can be poured at room temperature. The melted polymer is then left to cool down and solidify,
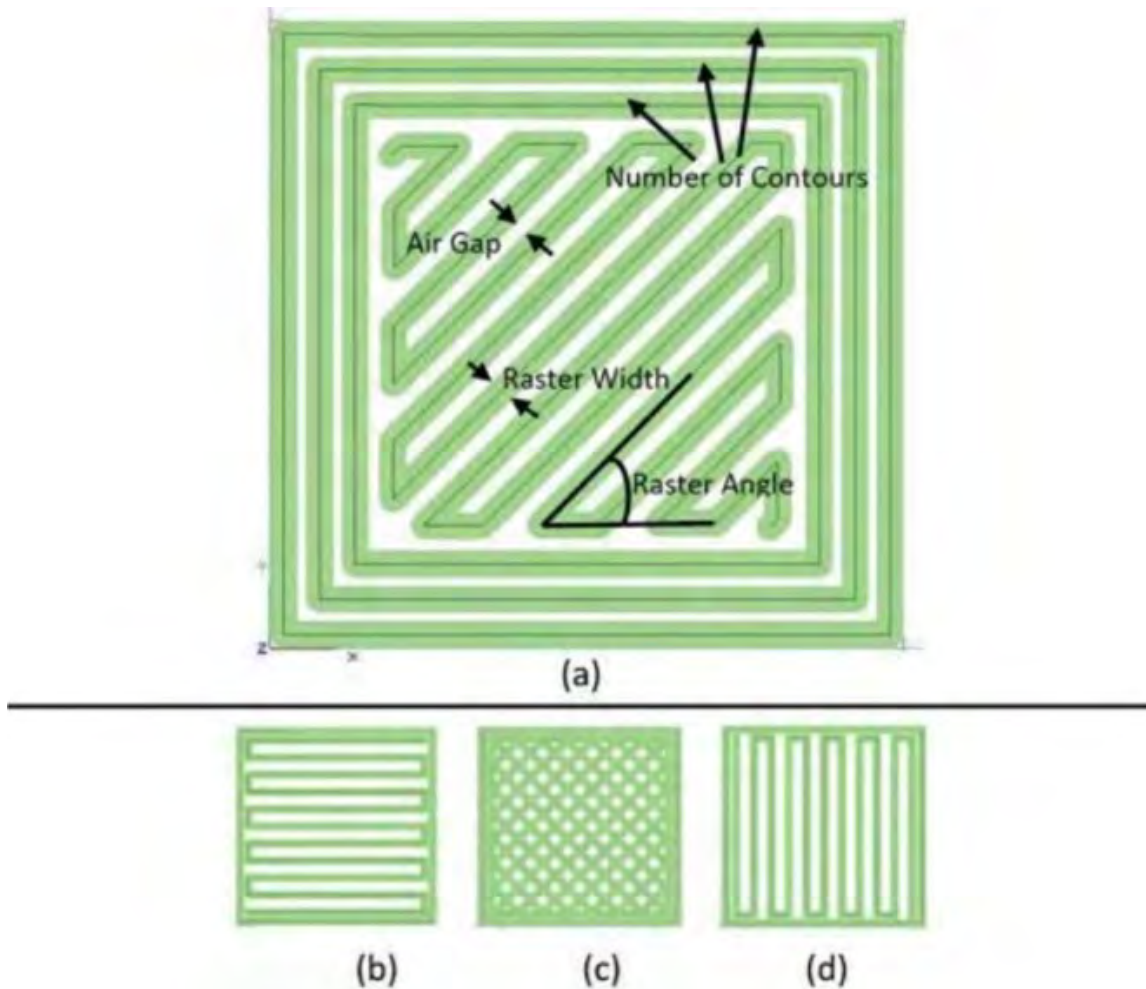
Figure 33. Material Extrusion Parameters. a.) Air Gap, Contours, Raster Width and Angle. b.) Horizontal Fill Pattern. c.) Cross-Hatch Fill Pattern. d.) Vertical Fill Pattern. [58]

or the epoxy is cured through a chemical reaction, before being removed from the mold. This method is implemented for complex geometries and is conducted under low pressure. [59]

Low-pressure casting is distinguished from compression, and injection molding in that casting is conducted at atmospheric pressure to fill the mold of interest instead of using an applied force to press the polymer into the mold cavity. Polymers with high viscosity will not be effective candidates for this method because it is difficult to pour

them at room temperature, as shown in Figure 34. Acetal polymers, polycarbonates, and polypropylene polymers are examples of polymers not fit for this method. Nylon Type 6 and polyurethanes are materials more appropriate for casting. In general, casting is recommended for large-size stock geometries for machining components. [60] [61]

Casting is advantageous because the equipment required for the method is generally low cost and the process itself is not extremely complicated. The polymer material also does not experience a large amount of internal stress since this method does not use an applied force for extraction. Some disadvantages are that the production rate of cast molds is very slow, especially if the cure cycle is long. Dimensional tolerances are not very high because atmospheric liquids can seep into undesired pockets of a mold. Voids due to air bubbles as well as moisture effects are also hard to mitigate because of the atmospheric conditions of casting. [60] This method tends to have high shrinkage rates and is considered the least accurate of the three methods discussed in this study. [62]

Figure 34. Casting [59]

2.3.3.2   Injection Molding.

Injection molding is implemented to generate high-quality 3D objects for commercial production. Polymer is melted in a hopper and then injected in a tightly closed mold. The mold itself is chilled (relative to the polymer temperature) to help the polymer into a cured solid object. The part is subsequently removed from the mold as a solid polymer object [59].

Injection molding is shown in Figure 35. The process begins by closing the mold and injecting a heated polymer into the mold. A motorized screw is generally the mechanism that pushes the melted polymer through the injection barrel and into the mold. Heated bands around the injection barrel are what heats up the polymer to its melting temperature. The injected polymer displaces the air in the mold by pushing it out of the pins designed into the mold for air ventilation. This is important to prevent air bubbles from forming during the process. After filling the mold, the melted polymer undergoes a cure cycle to solidify the material. The cure cycle will depend on the type of resin in the application. Injection molds usually have internal cooling lines where water flows through the mold to constantly transfer heat out as a part of the cure cycle. Once the polymer is cured, the motorized screw is retracted and the cured polymer material is released from the mold. An ejector rod with pins is often the method used to extract the melted polymer. [63]

Injection molding is known to be advantageous with regard to precision and repeatability. The air ventilation mechanism helps prevent voids and the liquid polymer's pressurization helps reach unfilled corners for complex mold geometries. It is a quick process, as cycle times can sometimes be as low as ten seconds, depending on the working polymer. There is little plastic waste due to the high precision and very little seepage. Injection molding comes at a higher initial cost since a specially shaped mold is required to match the fitting of the injection barrel. The size of the

desired part dictates the size of the mold. Injection molding a larger part requires an even larger mold tool and would require an extra expense. Complex shapes with significant overhangs, such as turbine/compressor blades, are complex to make in this process due to the need for multi-piece mold. [64]
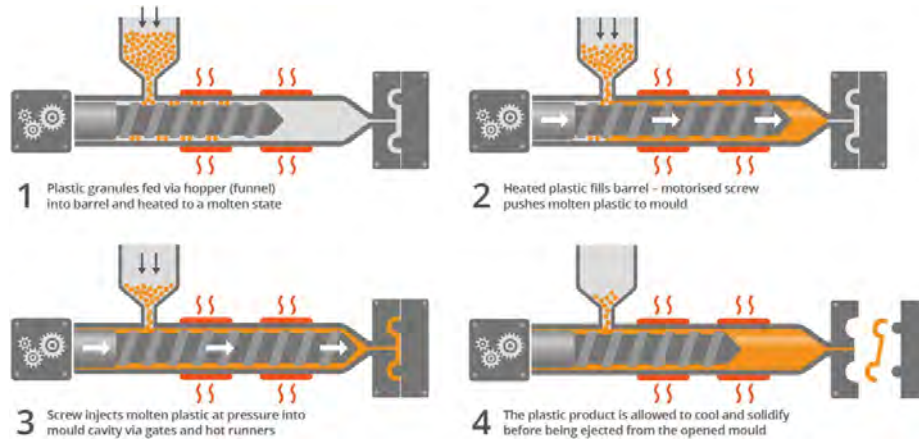
Figure 35. Injection Molding [65]

2.3.3.3 Compression Molding.

Compression molding is a method where a quantity of molding material (usually called the "charge") is compressed between two heated molds to create the desired shape. The process starts by creating the mold tool either by machining, die casting, or 3D printing. The mold is configured as needed with the compression machine with heated plates and overflow grooves to allow for controlled seepage. The charge is prepared at the right volume to prevent seeping that could lead to flashing, excess material between the plates that would need to be removed at the end of the process. The charge is set, and the compression plates apply pressure to the charge to form it into the desired geometry. Heat during the cure cycle softens the charge material to expedite production. Once completed, the finished component is removed, and any flashing is removed manually or via machining. [66].

Compression molding differs from injection molding in that compression molds are closed around the charge, while with injection molding, the charge is supplied to a closed mold cavity. Compression molding is known to be affordable due to low tooling costs and can produce composites that are durable and corrosion-resistant. Compression molding has a few disadvantages when compared to injection molding. Injection molding is better for more complex designs as it can fill finer geometry details more easily than compression molding. Injection molding also requires a shorter cycle time (the span of seconds) than compression molding (the span of minutes) which can drive up the labor cost for compression molding. Compression molding requires lower pressures and cuts down the cost of tooling. [66]

Compression molding is the most laborious of the three molding methods discussed in this study. It is used more often in large-scale production (molding large geometries) instead of mass production (molding a large number of small geometries). Boat hulls and car tires are examples of compression-molded components. [59] Compression molding is shown in Figure 36.
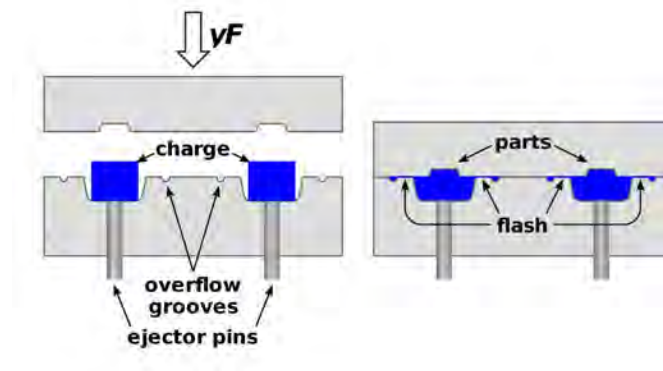
Figure 36. Compression molding [66]

2.4 Materials

In Mattingly's discussion about compressor materials [7], he notes that compressor blades experience billions of high-cycle fatigue via vibrations throughout their own design life. High-cycle fatigue is defined as repeated elastic strain due to low amplitude high-frequency cycles [67, 68]. As a result, the run-out stress, defined as the stress a designated material can withstand forever, is a crucial parameter for material selection. It is important to manufacture compressor rotors out of robust materials, ideally, with high run-out stress, that can withstand the expected operating stresses of a compressor. There are exceptions when a short life part is needed for expendable engines, but longevity is generally desired. This study is working with a short life span engine, which means that the components only need to survive approximately for 6-10 hours. Aluminum and titanium are examples of common compressor materials. Aluminum 2124 alloy has a run-out stress of 82.7 MPa (12,000 psi) at room temperature, which is relatively low compared to titanium 6246 alloy with a run-out stress of about 96.5 MPa (14000 psi) at room temperature. Both aluminum and titanium alloy have poor fatigue characteristics, so they are generally used as materials for low-pressure compressors. Titanium's strength-to-weight ratio is significantly decreased at temperatures beyond 755 K (900°F), so nickel-based alloys are generally implemented for vital components of high-pressure compressors [7]. This study aims to investigate composite materials, specifically carbon-fiber-reinforced composites, that can be used to replace the most costly to manufacture metal materials for a short lifespan engine.

One material study by Feraboli et al. [69] characterized discontinuous carbon fiber epoxy composites. Feraboli et al. conducted unnotched tests and open-hole tension tests to determine key geometric and scaling interactions related to length scale for discontinuous carbon fiber epoxy composites. Notches are holes, usually V-shaped,

that can be potential stress concentrations or weak points on a material surface. Results indicated that the prepreg-based discontinuous fiber composite system is notch-insensitive in the typical isotropic fashion expected for composites. Rather than pure shear, mixed failure mechanisms were common for the tested composite. While the modulus was relatively constant between the various article geometries, the geometry of the test articles nonetheless affected the strength measurements and were shown with considerable variation. Feraboli et al. observed increases in width at 0.5 in intervals yield ± 2 - 10% in strength and a less distinct pattern in thickness [69]. A study by de Villoria et al. [70] evaluated the substructural strength of a carbon-fiber composite reinforced with carbon nanotubes. Experimental results indicate that the overall strength increased with the application of carbon nanotubes with critical bearing stress increasing by 30%, open-hole compression strength increasing by 10%, and bending stress increasing by 40%. Moreover, these overall increases in strength were produced without the cost of increasing the fiber layer thickness, which is possible with nanotube reinforcements. These results, however, are conservative benefits based on the unoptimized quality of the reinforcement layers. [70]

Ekvall and Griffin's work [71] characterized T300/5208 graphite/epoxy with unidirectional tape, unidirectional meaning carbon-fiber pieces were all lined up in the same direction to reinforce the structure. Unidirectional tapes are fibers infused with epoxy resin, while bidirectional fabrics are a weave of continuous carbon fiber that interlaces at either 0, 90, or 45 degrees. Expected benefits from these composite designs are primarily for weight savings which are due to two aspects. First, composites have better specific strength and stiffness compared to metal materials. Second, composites inherently have modifiable material properties that can be adjusted for design requirements. This modifiable nature is distinguished from natural metals as they already have pre-set material properties that are modified relative to their baseline

magnitudes. Ekvall and Griffin applied notches, small holes on the surface of the material, to determine the material's sensitivity to surface damage. Tests ultimately showed that the composite material had a complex relationship between unnotched and notched tensile strength. Ekvall and Griffin concluded that the material was particularly notch-insensitive, meaning the presence of a hole or a notch in the material did not noticeably decrease the strength of the material comprised of unidirectional carbon fiber. [71]

(a) Bidirectional carbon-fiber fabric   (b) Unidirectional Carbon fiber tape
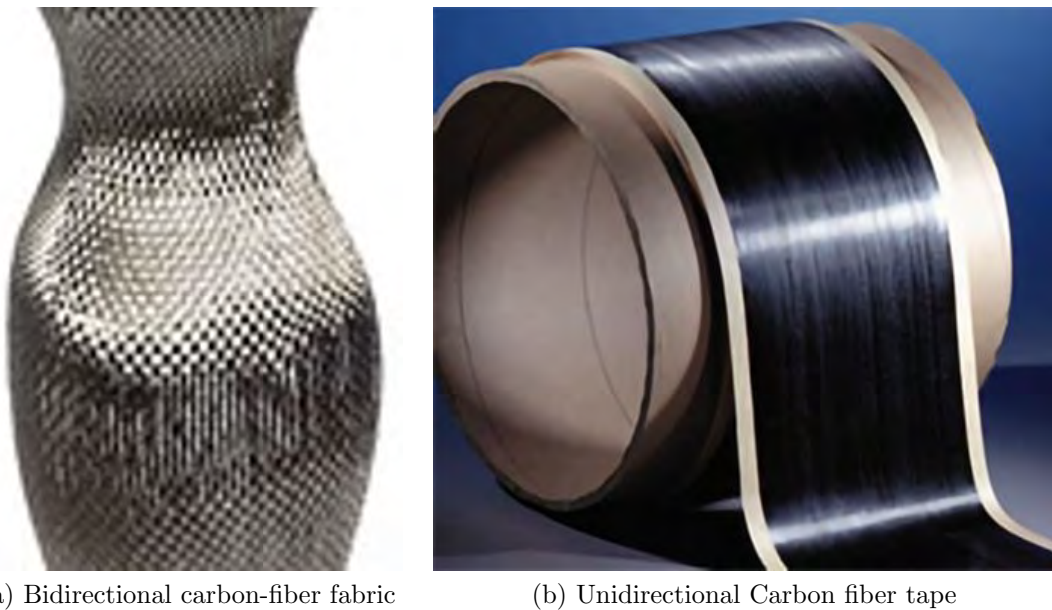
Figure 37. Bidirectional carbon-fiber fabric and Unidirectional Carbon fiber tape [72, 73]

2.4.1 Properties of Composites.

The motivation behind using composites is to produce a material with better mechanical performance and properties than those of the constituent materials alone. A simple composite has two phases: a reinforcement phase (made from a stiffer, stronger, reinforcing material such as carbon fibers) and a matrix phase (considered the weaker phase, the material that is subject to reinforcement such as epoxy or

polymer binders). Some composite fabrication yields an intermediate phase between the matrix and reinforcement called the inter-phase. The composite's properties will be based on the constituent's properties, geometry, and distribution within the composite (i.e. the ratio of reinforcement to matrix material). More uniform material will behave homogeneously while less uniform material will perform heterogeneously. [11]

In contrast to composites, monolithic materials are materials made out of a single substance and are the traditional choice for aerospace applications. Monolithic materials are spread into three categories: metals, ceramics, and polymers. To replace traditional metallic compressor material with an experimental composite, a general comparison between monolithic materials and composites is necessary. [11]

2.4.2 Material mechanics.

At a microscale level, composites benefit from high stiffness and high strength with fiber reinforcement. Composites generally produce fracture toughnesses competitive with monolithic materials. The inclusion of the fiber material with the matrix material expectedly augments the baseline material strength for the matrix material. For example, in adding carbon fiber reinforcement (reinforcement phase) with epoxy (matrix phase), the combination of the two (composite) expectedly augments the material strength relative to the baseline strength of epoxy. Since composites no longer contain uniform or monolithic material properties, multiple-site and multiple-path failure mechanisms exist for composite materials. These failure paths in composites depend on the location of the phase (the phase expected to fail first) with the lower ultimate strain on the relevant body. However, composite materials' inherently high scatter in strength, results in stress concentrations that reduce their transverse tensile strength. Conventional monolithic materials have irregularities that promote brittle

or ductile behavior and their homogeneous nature makes them vulnerable to flaw growth when under long-term cyclical loading. [11]

One of the biggest benefits of composites is that the material properties can be somewhat controlled based on the type and amount of the chosen constituents. Composites are generally analyzed as quasi-homogeneous and anisotropic materials, making the analysis more complex. Conventional monolithic materials are isotropic and homogeneous, making their analysis simpler. [11]

Material properties for composites are predicted by averaging the properties of the constituent materials. For a more robust material property characterization, actual independent experiments in large iteration numbers are conducted. Traditional monolithic materials are less complicated as they simply need two elastic constants and two strength parameters to determine their properties. [11]

Since composite properties are controllable based on constituents, composites can be optimized for weight, stability, and cost based on available data. However, such optimization necessitates reliable material databases, modeling tools, and fabrication methods. Monolithic materials are limited to optimizing one or two geometric parameters as there are several degrees of freedom. [11]

Composites have long fatigue lives and are relatively more maintainable than monolithic materials, but they tend to have problems detecting internal damage. Generally, nondestructive detection methods are required to determine internal damage problems within composites, such as Acoustic Emission Testing or Electromagnetic Testing [74]. Composites are also more resistant to corrosion than monolithic materials. Conventional materials, especially metals, will corrode quicker in hostile environments but are easier to repair when damaged. [11]

Fabrication processes are crucial for composite development, and they generally require simple toolings such as autoclave molding, pultrusion, fiber placement, and resin

transfer molding (RTM). Compared to monolithic fabrication, composite processes are still new, so modern automation and optimization are limited. Most composite fabrications still require extensively skilled labor. Conventional monolithic materials require elaborate tooling and complicated assembly, but most of these fabrication methods are mature and may be automated for a simple application. [11]

The attraction to composites stems from the cost reduction in saving weight, tool costs, assembly complications, and maintenance. These pros, however, are counteracted by the cost of composite raw materials, adversities of working with fibers, and auxiliary materials for fabrication. [11] For the conventional CNC machining of metals, raw materials are cheap and readily available, but the tooling and machining is still expensive despite optimization and development.

This study aims to capitalize on the known advantages of composite materials for propulsion applications in designing a compressor via additive manufacturing and cost-effective molding methods. [11]

2.4.3 Material Property Comparisons.

Documentation of material properties at temperatures above room temperatures is generally not readily available. More often, baseline properties for strength and modulus are published. This section reviews a comparison of material properties such as specific strength, specific stiffness, fracture toughness, peak temperature, thermal conductivity, thermal expansion, cost, and manufacturing time compared between various materials. A study by Bauer compared various candidate materials for compressor manufacturing and their various properties. His first comparison chart compares material specific strength and their respective thermal "resistance" or transition temperature [3]. Figure 38 shows the specific strength as a function of transition temperature for various materials. Bauer first categorized each material

to indicate trends based on their manufacturing method. The first category (black-box) comprises common CNC machine metal alloys used for conventional compressor manufacturing: Al 7075-T6, Ti 6Al-4V, and Inconel 625. Al 7075-T6 is the typical metal used for the JetCat P400 [75], while Ti 6Al-4V and Inconel 625 are both commonly used for turbomachinery applications [3]. In Figure 38 the material properties for these metal alloys were found on MATWEB [76]. These materials tend to have very high specific strength and transition temperatures. The second category (light blue box) is comprised of two powder-bed fusion materials, AlSi10Mg and Inconel Ni 625. Their material properties were found on 3D Systems' Data sheet [77]. These materials tend to have competitive for specific strengths and transition temperatures to conventional metals. The third category (dark blue box) is hobby-level polymers such as ABS and Polylactic Acid (PLA). These materials tend to have very low specific strengths and low transition temperatures for compressor applications that are not competitive with conventional CNC metals. These properties are found in the Stratasys data sheet [50]. The fourth category (purple boxed) is "engineering-grade" extrusion materials such as ULTEM 1010, ULTEM 9085, Antero 800NA, Nylon 12CF, and Onyx. Among these, only Onyx is produced by Markforged [78], while the rest are produced by Stratasys [50]. These materials have moderate transition temperatures ranging between 360-505K, while they have low specific strengths. The fifth category (green box) is the extruded materials with continuous fiber reinforcement. Figure 38 is specifically showing Onyx reinforced with three materials: Onyx-Carbon Fiber, Onyx-Kevlar, and Onyx-Fiberglass. These properties are documented by Markforged [78]. Reinforced Onyx on Figure 38 shows to have the same transition temperature as unreinforced Onyx, has an ultimate strength competitive to those of conventional metals. The sixth and last category (yellow box) is photopolymers exemplified with 300-AMB. While 300-AMB without reinforcement has competitive transition temper-

atures to conventional metals, the specific strength is not as competitive. 3D Systems record properties of 300-AMB. [77].
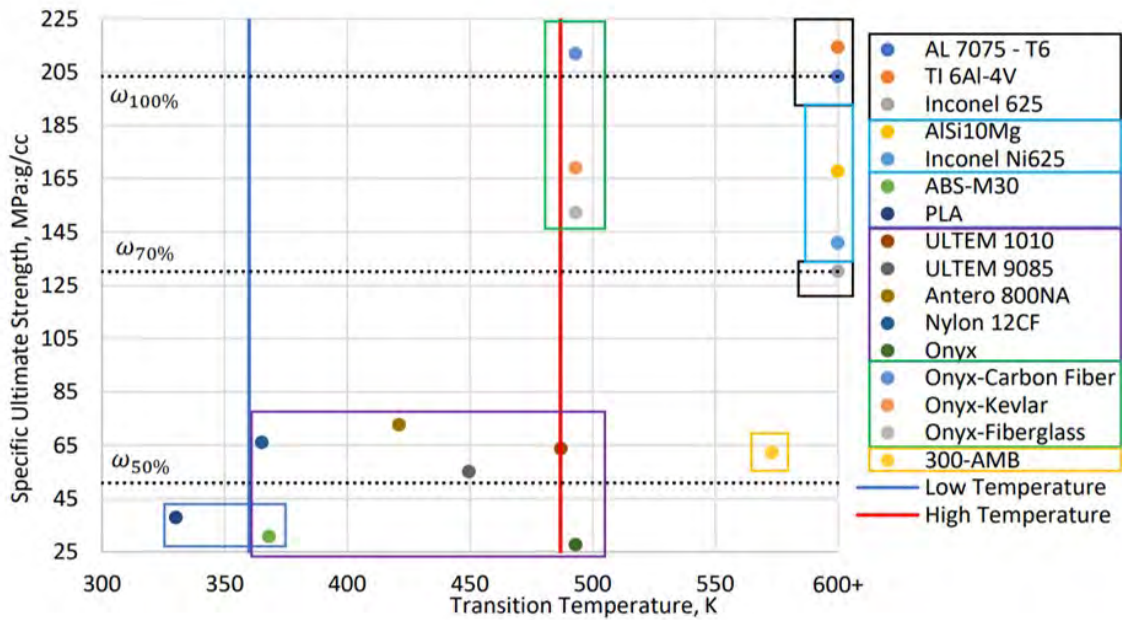
Figure 38. Specific Strength vs Transition Temperature from Bauer [1] who adapted from several sources: [35] MATWEB, [77] 3D Systems, [50] Stratasys, [78] Markforged

Bauer includes a few other details in this particular comparison chart. The dashed horizontal black lines represent different specific speeds $\sigma_u/\rho = C\omega^2$ and are scaled relative to the JetCat P400 operating speed. 100% speed is scaled with the specific strength of the Al 7075-T6, the P400's default material. The speed at 70% and 50% are scaled relative to the 100% speed. Two temperature lines represent the upper and lower bound static exit temperatures for the P400 compressor, where 360K is represented by the lower bound (blue line) representing a conservative temperature at idle speed while 487K is represented by the upper bound (red line) or the highest expected temperature as mentioned in Section 2.2.6.3.

Bauer further discusses the observed patterns of the material properties compared to one another. While the conventional metals had melting temperatures beyond the

maximum static exit temperature, titanium was the only one with greater specific strength than Al 7075-T6. Hobby-level polymers are not competitive in either specific strength or in transition temperature, while engineering-level polymers were slightly more competitive but not enough to match that of metals. All of the engineering-level polymers achieve half of the failure speed of Al 7075-T6 except Onyx. ULTEM and Onyx had transition temperatures that were close to or surpassed the upper band static exit temperature but noncompetitive specific strengths. Onyx-fiber properties showed to have transition temperatures above the maximum static exit temperature and specific strength competitive with conventional turbomachinery metals. Bauer then narrows his focus to ULTEM 9085, 300-AMB, and Onyx with fiber reinforcement based on the properties shown in Figure 38. [1]

While the objective of Bauer's study was to find materials that can withstand the thermal and structural stresses expected in a P400 engine, an AM method would not be a practical alternative if they were more expensive or took twice as long to produce relative to CNC machining. Because of this, Bauer's study also compared the cost as a function of time for the same aforementioned categorized materials. The cost is defined as the cost of manufacturing one compressor, which simplifies the data to one-off builds but also nullifies the advantages of large-scale production. The cost is based off of manufacturer recorded predictions [50, 77, 78] or conversations Bauer had with expert machinists about manufacturing time [1]. Bauer determined the time to manufacture one compressor based on the time between CAD model reception of the technician to compressor completion [1]. Bauer then used this information to produce Figure 39, which represents the cost as a function of time, where the upper point represents the required time period from beginning to end while the lower point represents the time requiring a skilled technician. [1]

Bauer determined that conventional CNC machined metals were the most expen-
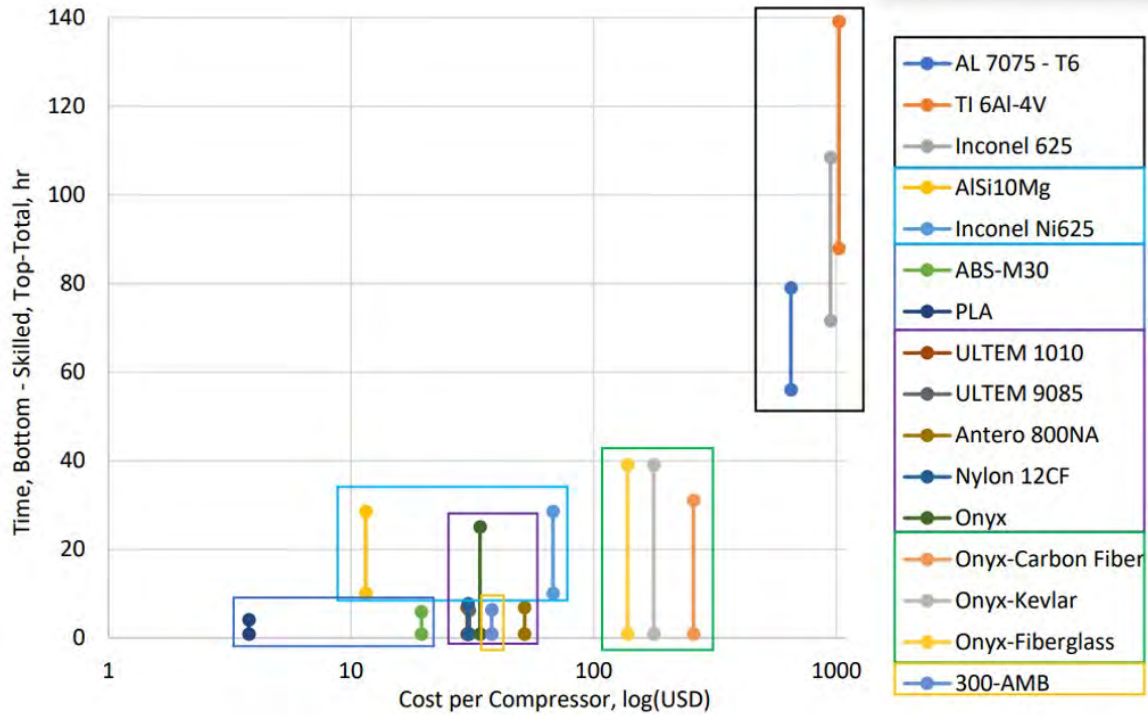
Figure 39. Cost and Time to Produce a One-off Compressor - from Bauer [1] who adapted from several sources: [35] MATWEB, [77] 3D Systems, [50] Stratasys, [78] Markforged

sive to make by one to two orders of magnitude and took the longest to produce. The technician needed more than a week's time to program and implement a CNC machine to produce a single metal compressor. Bauer indicated that the complicated nature of programming CNC machines is why producing a one-off compressor was very costly [1]. Among AM methods, Bauer notes that metals suited for powder-bed fusion required about 10 hours of labor simply to pre-process and post-process the builds. The Stratasys materials and 3D System's 300-AMB took about five hours to complete a compressor. Onyx alone took about a single day to print while Onyx with reinforcement required about 40 hours to complete, both of which used the Markforged printer. Fiber-reinforced polymers were expensive and time-consuming but did not require the same level of skill or labor, therefore reducing the total cost and making them cheaper than conventional metals. In addition, the printer keeps

operating even when the technician leaves the work zone [1].
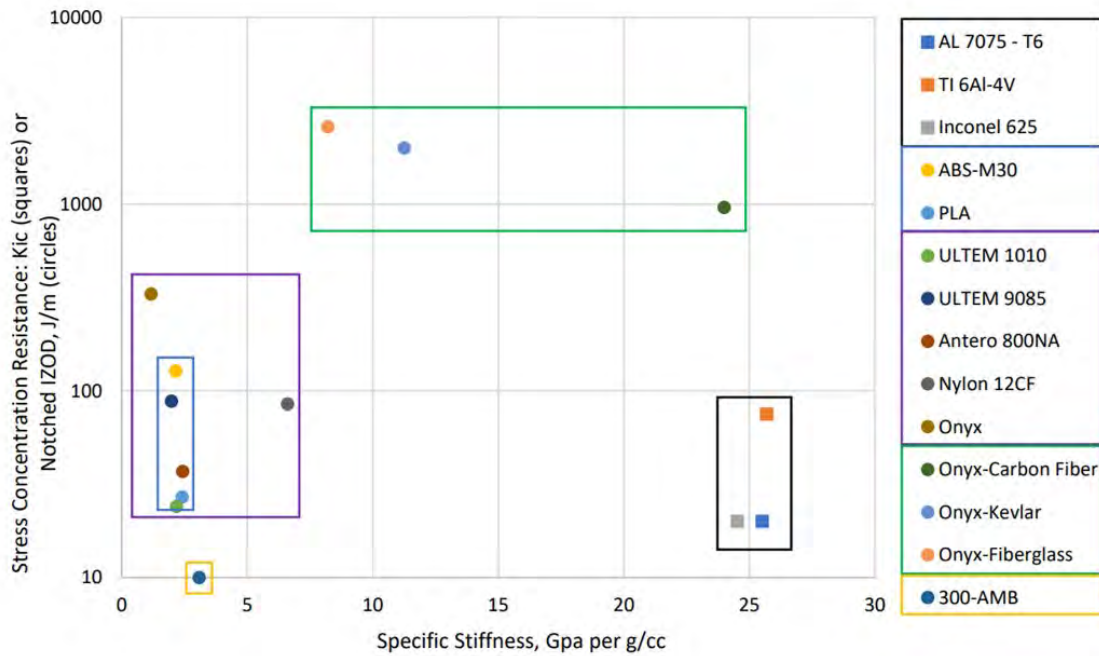
Figure 40. Specific Modulus of Elasticity versus Stress Concentration Resistance - from Bauer [1] who adapted from several sources: [35] MATWEB, [77] 3D Systems, [50] Stratasys, [78] Markforged

Another set of physical properties Bauer compares are the specific stiffness and the resistance to stress concentrations, as shown in Figure 40. Metals and polymers react differently to stress concentrations and therefore require different analysis methods. Stress concentration for metals is defined by K_{IC}. The Izod impact test determines stress concentration for polymers. In Figure 40, reinforced polymers yielded the highest resistance to stress concentration while metals and the majority of unreinforced polymers (except Onyx) produced resistances an order of magnitude lower. For specific strength, polymers without reinforcement had specific strengths that were 10-20% that of metals. Polymers with fiber reinforcement had specific strength between unreinforced and metal values [1].

Another important characteristic behavior Bauer examined is a material's re-

67
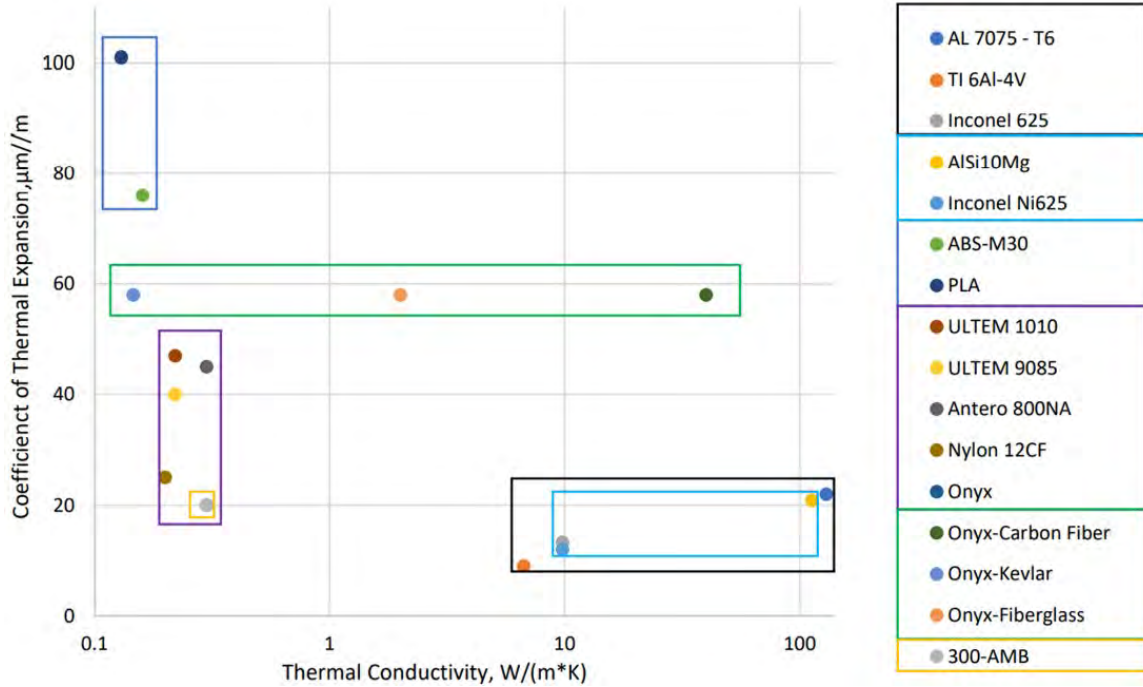
Figure 41. Thermal Conductivity versus Coefficient of Thermal Expansion - from Bauer [1] who adapted from several sources: [35] MATWEB, [77] 3D Systems, [50] Stratasys, [78] Markforged

sponse to changes in temperature as shown in Figure 41, which compares the coefficient of thermal expansion (α) as a function of thermal conductivity. Thermal conductivity indicates how well a material can conduct heat from the blade tips to the areas cooled by air flow. This means that higher conductivity values permit better cooling. Coefficient of thermal expansion indicates how much the material expands, which effectively leads to deformation for a given heat input. The absence of cooling will lead to thermal deformation that results in large thermal stresses and reduce the accuracy of FEA models, which is why expansion and conductivity are compared in Figure 41. In general, high thermal conductivity and a low expansion coefficient are desired. Conventional CNC metals exhibit the highest thermal conductivity and lowest expansion coefficient proving they have the desired thermal qualities. Powder bed fusion materials were the only materials with competitive thermal qualities relative to

CNC metal properties. Hobby-level plastics had the least desired qualities with large expansion coefficients and low conductivity values. Engineering level polymers had lower expansion coefficients but also lower conductivity magnitudes. Reinforced Onyx had moderate expansion coefficients and had advantageous or disadvantageous conductivity depending on its reinforcement material (i.e. kevlar reinforcement would conduct differently than carbon-fiber reinforcement for the same matrix material). Onyx-carbon fiber exhibited the best conductivity among the reinforced polymers. [1]

Bauer further summarizes his list of materials of interest-based on the method of manufacturing, manufacturer, machine, and minimum resolution, as shown in Table 7. Smaller resolutions will reduce the surface roughness as mentioned in Section 2.2.6.2. CNC machining significantly surpasses AM machines in refining surface roughness with modern technology. Therefore, applications that require 2.5μm resolution require CNC machining as the only choice.

2.4.4   Material Testing.

To produce an accurate FEA model, characteristic material property data is inputted into the model. While such data is commonly published for room temperature conditions, material properties for different temperatures are usually not readily available. This was the case for the material properties for Bauer's materials of interest at various temperature conditions [1]. As a result, Bauer needed to conduct tensile testing to acquire data about material property behaviors at higher temperatures, specifically temperatures close to the operating conditions of the P400. Bauer used the ASTM standard test specimen for reinforced and unreinforced polymers which is the ASTM D638 test specimen, and the present study will use the same specimen geometry [79, 1].

Table 7. Material Method, Manufacturer, Machine, and Minimum Resolution, adapted from Bauer [1]

Material	Method	Manufacturer	Machine	Minimum Resolution μm
Al 7075-T6	CNC	N/A	CNC	2.54
Ti 6 Al-4V	CNC	N/A	CNC	2.54
Inconel 635	CNC	N/A	CNC	2.54
AlSi10Mg	PBF	3D-Systems	ProX DMP 320	10
Inconel Ni625	PBF	3D-Systems	ProX DMP 320	10
ABS-M30	ME	Stratasys	Fortus 450mc	254
PLA	ME	Stratasys	Fortus 450mc	254
ULTEM 1010	ME	Stratasys	Fortus 450mc	254
ULTEM 9085	ME	Stratasys	Fortus 450mc	254
Antero 800NA	ME	Stratasys	Fortus 450mc	254
Nylon 12CF	ME	Stratasys	Fortus 450mc	254
Onyx	ME	Markforged	Mark II	100
300-AMB	VP	3D-Systems	Figure 8	50
Onyx-Carbon Fiber	ME-CF	Markforged	Mark II	125
Onyx-Kevlar	ME-CF	Markforged	Mark II	100
Onyx-Fiberglass	ME-CF	Markforged	Mark II	100

Bauer notes that the focus of conducting material tests in this step is to collect data for failure prediction in the FEA model, so the strict compliance to testing itself is not as important as completing the test and acquiring results. The ASTM test standard recommends testing five specimens without obvious physical damage and in all anisotropic directions; however, simplifying the test sequence and relaxing these components of the material test will produce acceptable results for an FEA model. Three materials at five different temperature conditions using ASTM 638 standard would require 225 tests. The displacement rate for the D638 ASTM Type IV specimen is documented for 5 +/- 0.25% mm/min over a test time of 30 seconds to 5 minutes for each specimen [1]. The material test should produce information about the yield strength, ultimate strength, elastic modulus, and Poisson's ratio [79]. While the Poisson's ratio for polymers is commonly understood to increase with rising temperature, the majority of metals, ceramics, and engineering polymers have
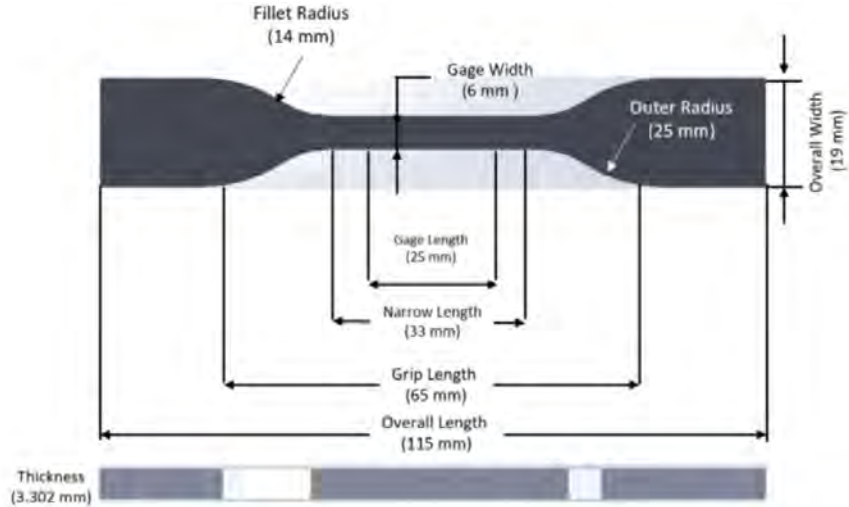
Figure 42. ASTM D638 Tensile Specimen, Standard for Polymers Type IV [80]

Poisson's ratios in the range of 0.25-0.35 [81].

2.5 Finite Element Analysis

The secondary objective of this study is to verify the accuracy of FEA modeling to predict failure speed for additively-manufactured compressors. FEA is ultimately an instrument in the preliminary phase of model authentication because information about how a tool fundamentally works will aid the quality of results. Historically, FEA is often implemented to determine important parameters such as failure speeds, deformation patterns, modal responses, and temperature profiles for centrifugal compressors [82]. However, the complications inherent with AM reduce the accuracy of FEA results. In the engineering design process, it is important to computationally model an engine component before manufacturing to determine how the component will likely perform and what performance limitations exist, based on the current design configuration. This analysis enables designers to re-vector the design without expending the manufacturing efforts to produce a physical test model. One of the modern methods of determining such performance is with FEA, also called finite

71

element methods (FEM).

Conceptually, FEA replaces continuous structures with math models made of elements of finite size (hence the name finite element) with elastic and inertia properties expressible in matrix form. Matrices represent building blocks assembled by a set of rules derived from the theory of elasticity and give static and dynamic properties of the real system. A given set of finite elements is generally known as a mesh because of its mesh-like resemblance. Some software like SolidWorks adaptively generates a mesh over a given geometry. In adaptively-generated meshes, each element's size is designated based on the complexity of the local geometry. An example of this is shown in Figure 43. [75]

FEA ultimately provides computational values for expected stresses and deformations from material properties given thermal and mechanical data. Knowing stresses and deformation of the geometry of interest for various materials can also be used to evaluate different materials for a particular application. [83] Computational Methods such as FEA use conservation variables and transfer-of-state variables represented in a single equation or a system of equations. [84]. The previously mentioned continuity equation, momentum equation, and energy equation in Section 2.2.4.2 are examples of such equations. All three of these equations are in the differential form, which applies to all points in the domain. Balancing linear momentum terms produces Equation 48 which indicates that the divergence of the stresses (σ_i) is equal to the applied body forces (F). With boundary conditions, the problem is simplified and becomes solvable.

$$div\sigma_i + F_i = 0 \tag{48}$$

An infinite number of equations with unknown solutions exist, so assumptions are required to approximate a working solution. While such assumptions reduce accuracy, approximations are better than no solution. Dividing the domain into finite elements

configures the system to determine the numerous unknowns in an approximate solution.
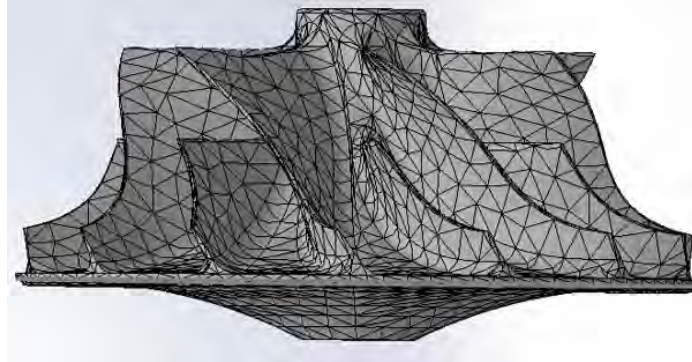
Figure 43. Example Finite Element Analysis Mesh on a Centrifugal Compressor [1]

Constructing too large a mesh will inaccurately represent the physics of the model and induce error. Increasing the number of elements refines the grid and reduces error but can require longer computational time. Calculating the percent error is inherently difficult because it requires foresight of the true solution. Without prior knowledge of the true solution, a grid study is required to approximate the true solution, which is an incremental refinement of the FEA output until it asymptotically approaches what would be considered the true solution [84]. It is commonly understood that refining at small increments will lead to a better approximation. For FEA, this is usually done by calculating "residual" error by subtracting the global results from one refinement from the results of a higher refinement. In the ideal case, if this "residual" error gets smaller with higher refinement, less refinement is required to approach the true solution [85].In theory, one way to eliminate error is to refine the mesh to generate an infinite number of nodes, making it extremely accurate but not practical as it would take an extremely long computational time to calculate. A trade between accuracy and computational time leads to various approaches to the solution [84, 85].

There are few practical examples of FEA historically used for material comparison.

Mohamed et al. [86] used FEA to determine the crash-worthiness of three different materials (steel, aluminum, and a carbon fiber composite) for collision safety. The objective if this study was to determine the material which minimized the deformation of a car door to withstand the highest amount of impact stress [86]. The results of the study found that composites had the highest density but were not strong enough to withstand vehicle impact pressure due to elastic properties and were deemed unsuitable for the collision application. Both steel and aluminum materials could withstand the pressure for the vehicle door. The study concludes that both aluminum and steel alloy are functional but find aluminum more suitable than steel due to its lighter weight. [86]

2.6   Previous work with AM Compressors

There exists a record of previous attempts at additively manufacturing compressor components. In the 1960s, Rolls-Royce investigated the application of composites for the RB162 vertical-takeoff and landing engine. The blades of the first compressor stage remained aluminum, but the following five stages utilized blades that were cast out of an epoxy-fiberglass composite. The study resulted in a 16:1 thrust-to-weight ratio which is twice the thrust to weight of an engine built five years prior, the RB.108 [87].

Polytechnique Montreal studied the implementation of stereolithography to produce functional polymer-based compressors, which proved to be a repeatable process over the span of three years (between '11 and '14). While a few of the working design conditions for the Montreal compressors had lower flow rate, one-third of the pressure ratio, and about 30% lower rotational speed (to prevent premature failure), the study resulted in a successful proof of concept in additive manufacturing compressors [88].

Fernandez et al. [36] studied the application of filament-deposition for producing hydraulic pump impellers out of ABS plastic. Filament-deposition proved to generate a pump impeller with the same or better performance (with post-process smoothing) than the conventional aluminum pump impeller. Fernandez et al. also proved that the extruded impeller was manufactured in 1/16th the time, with 8.9 times less mass and 90 euros less manufacturing cost [36].

Walker et al. [8] attempted to 3D-print a compressor for a JetCat P400. The goal of the study was to prove AM technology could produce a working compressor rotor and to determine limitations that exist for AM engine parts. The compressor was comprised of a combination of plastic and metal components utilizing ABS plastic for the inlet assembly, stainless steel for the mounting plate, and Inconel for the bell mouth and exhaust. Figure 44 contains the hybrid plastic-metal compressor inlet section, both upstream and downstream the inlet. Similar to this study, Walker also uses a Garrett GTX5009R turbocharger to drive the compressor for operation, which is shown in Figure 45b. The performance of the hybrid compressor was limited to 25,000 RPM prior to surface damage or scarring on the suction side of the blade that arose at higher angular velocities. With the concern of continued structural integrity, the risk of mechanical failure became too high to handle the component at operating speed. The maximum operating speed was 98,000 RPM and the analysis expected the compressor to operate at 70,000 RPM. Due to the structural issues, Walker et al. only operated the compressor at 25,000 RPM [8].The work of Walker et al. benchmarks previous work with integrating plastics into compressor technology and highlights potential hazards that can arise with compressor testing, such as surface scarring.

Jia et al. [10] explored the production of compressor impellers with an internal

(a) Upstream inlet for flow control   (b) Back of upstream inlet
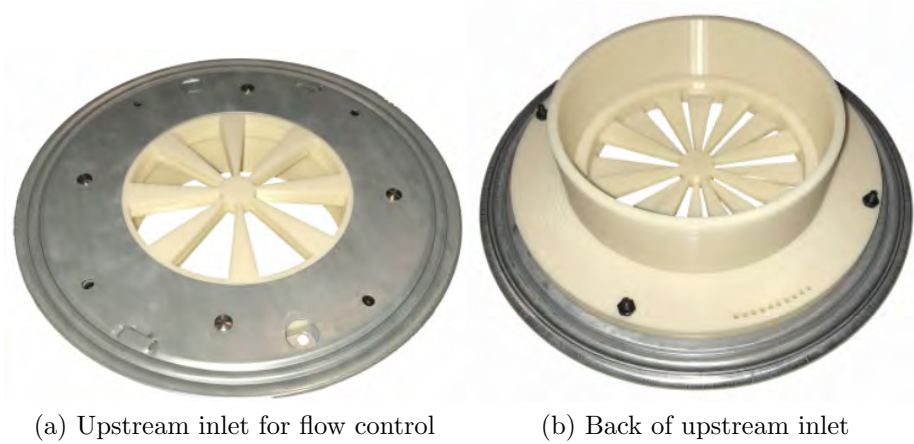
Figure 44. Hybrid ABS steel Upstream Inlet [8]

(a) Compressor rotor   (b) Driving turbocharger
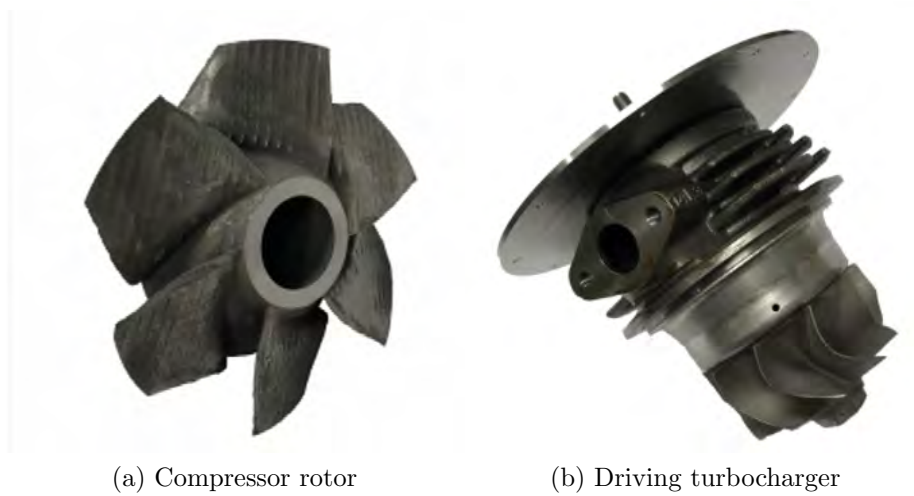
Figure 45. Compressor Rotor and Turbocharger [8]

lattice structure. The lattice structure reduces the mass and moment of inertia of the impellers, which effectively reduces the mass of the overall compressor. This compressor was additively manufactured out of TiAl6V4 titanium alloy. Results from the finite element analysis (FEA) simulation showed similar deformation and stress trends between the lattice impeller and a comparable solid impeller. Jia et al. printed the compressor using an SLM280 metal sintering Laser Printer which allowed the user to control the residual stress and deformation of the part. This option allows the laser power to be proportional to the laser speed, which influences the melting rate

of the powder needed to manufacture the part. Melting rate in turn influences the material properties of the product, and hence residual stress and deformation can be user-controlled with laser power, speed, and width. The lattice impeller reduced both residual deformations by 20.19% and residual stress by 8.72% compared to that of the 3D printed solid impeller. The lattice design also reduced the overall impeller mass by 23.5 %. Jia et al. ultimately produced a titanium compressor that is both lighter and stronger in the lattice configuration compared to a typical solid component. While Jia et al. additively manufactured compressors out of traditional metal instead of plastics or composite, their work is part of the body of knowledge implementing AM in compressor applications. Jia et al. specifically used laser/sintering methods to reduce mass and cost for engine components. [10]

Figure 46. PerFORM and Fractured Accura Bluestone Catridges [9]

Meier et al. investigated the use of AM in printing vaned diffusers by stere-olithography (SL) to make a centrifugal compressor [9]. The diffuser vane was made from a high-temperature plastic, DSM Somos PerFORM, to reduce manufacturing costs attributed to metal. Meier et al. first considered two SL-capable plastic materials: DSM Somos PerFORM and Accura Bluestone. Meier et al. proceeded to

77

conduct a combined temperature-strength test for the two materials to determine the better choice for the application by putting cartridge specimens of both PerFORM and Bluestone into a 420K oven with a 70N load applied over the top of the cartridges. Accura Bluestone fractured under the operating conditions while PerFORM endured and was ultimately chosen for the diffuser material. During material tests, PerFORM has tested for cyclical loads between 12×10^6 and 18×10^6 cycles under temperatures between 296K and 441K. Results indicated PerFORM stiffens under cyclical load instead of showing signs of yielding or fatiguing. Robust survival at such operating temperatures and cyclical loading is expected for degrading polymers. The diffuser vane made with PerFORM did not degrade, and analysis showed no sign of leakage around the outside of the diffuser at O-ring seals. The study concluded that diffusers made from PerFORM meet requirements at the operating conditions expected of a conventional compressor. Results from this study are an example of non-traditional materials for compressor applications. This study presents successful endurance results through cyclical load and temperature, which applies to the present study. Meier et al. tested up to 441K, which is 31K less than the 475K operating expected temperature for the P400 and is this study's temperature upper bound. [9]

In work directly preceding the present study, Bauer [1] examined additive manufacturing materials of a centrifugal compressor rotor, specifically investigating ULTEM 9085, 300-AMB, and Onyx-Carbon fiber as material candidates. Rotors for all three materials were analyzed for comparison to the conventional JetCat P400 made from Al 7075-T6. Between the three composite materials, the 300-AMB compressor FEA yielded the least variation in stiffness and strength for higher temperatures. However, 300-AMB was not printable with the XY plane in the $r-\theta$ plane of the compressor. In addition to the brittle nature of the 300-AMB compressor's thin sections, Bauer's analysis for 300-AMB did not extend further than finite element analysis.

The 300-AMB model is shown in Figure 47. This study aims to verify the repeatabil-
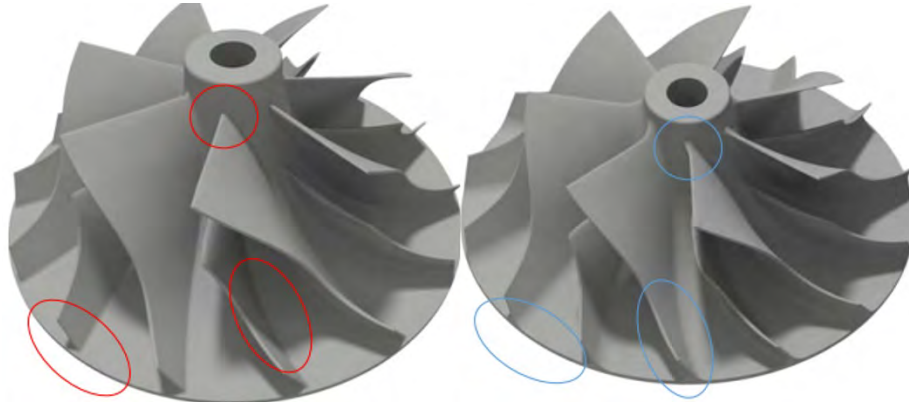
Figure 47. 300-AMB compressor [1]

ity of Bauer's material characterization work in additive manufacturing of compressor rotors with carbon fiber reinforcement. Bauer modeled and built a rotor with ULTEM 9085, and although it failed below the desired operating speed of 98,000 RPM, the failure speed of the actual compressor (72,375 RPM) was consistent with that of the FEA model (72,240 RPM). Bauer's ULTEM 9085 compressor is shown in Figure 48, and the post-failure images for the ULTEM 9085 compressor are shown in Figure 49. Figure 49a-b presents the overall group of fragments produced after failure. Bauer's ULTEM 9085 compressor failure caused an axial load toward the turbine-exit side, which is why the compressor-side shaft is flush with the retainer plate in Figure 49b. Figures 49c-f show a closer look at the failure points of the fragments. The circle in Figures 49c shows the melted plastic coming out of the compressor, while Figure 49 denotes the location of maximum stress indicated in Bauer's FEA model. The circles in Figure 49e-f both indicate a specific crack normal to the plane of failure. The axial load from this test prompted Bauer to install a safety feature in the ,rig which will be discussed further in Section 3.4.1. In Bauer's study, an Onyx-Carbon Fiber compressor (shown in Figure 50) was also modeled with a failure prediction of 160,000 RPM. The compressor was built for testing but failed due to what was understood as
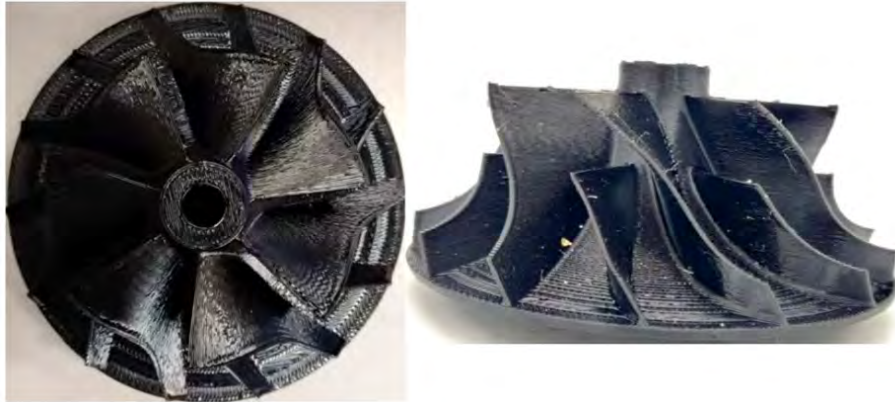
Figure 48. ULTEM 9085 compressor [1]

Figure 49. Post-Failure of P400 compressor, ULTEM 9085. a.) Polymer Fragments. b.) Compressor Shaft Pulled Through. c.) Two Fragments, Melted Plastic. d.) Large Fragment, Top. d.) Small Fragment. f.) Large Fragment, Bottom. Adapted from [1]

"an unrepeatable freak accident." [1] The compressor structure was intact, but the nut securing the compressor on the test shaft melted through the compressor bore as shown in Figure 51 [1]. Bauer prematurely stopped the Onyx spin test with a maximum speed of approximately 34,200 RPM due to observed oscillations at that speed.

Zach Murphy continued Bauer's work with limited success. Murphy successfully
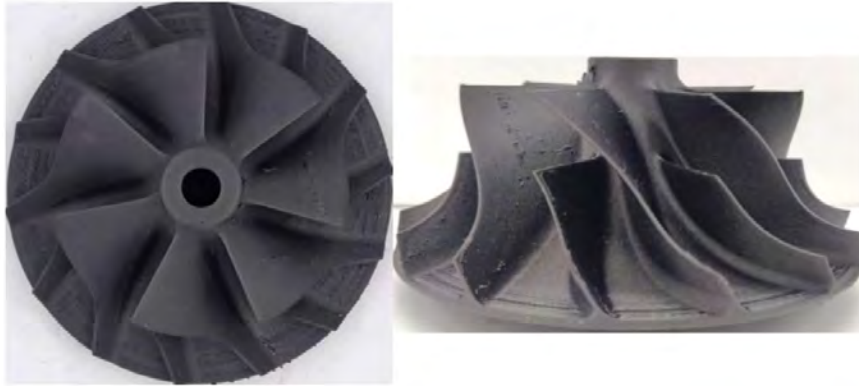
Figure 50. Onyx Carbon Fiber compressor [1]

Figure 51. Carbon fiber onyx compressor failure [1]

produced three Onyx-Carbon fiber compressors, of which two were tested. The first

of Murphy's tested compressors was modified to account for the bore failures from

Bauer's results. Murphy installed an aluminum circular sleeve into the compressor's

bore to reinforce the structural integrity of the failure location at the compressor's

inner radius. Unfortunately, Murph's test run of this compressor did not succeed in

reinforcing the central bore's integrity for long because the aluminum sleeve ended up shearing off of the onyx-carbon fiber compressor, melting through the compressor and kicking back into the turbocharger. Results of this attempt are shown in Figure 52 [89]. Murphy's second attempt improved the aluminum sleeve by changing it from

Figure 52. Murphy 1st onyx CF compressor [89]

a circular sleeve to a hex sleeve, shown in Figure 53. This reinforced the central bore of the compressor to prevent torsional shear failure, but it led to another problem on the back face of the compressor, which is delamination of the Onyx-carbon fiber layers at higher rotational velocities, as shown in Figure 55. [89]
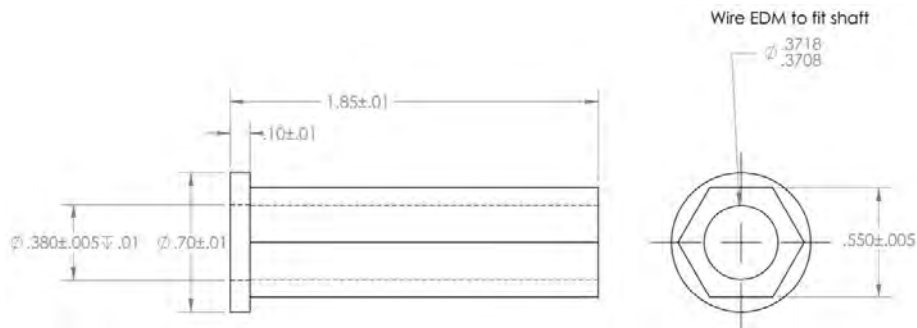
Figure 53. Aluminum Hex-Bore Sleeve (in inches) [89]

Figure 54. Aluminum Hex-Bore Sleeve Manufactured

Figure 55. Murphy 2nd onyx CF compressor [89]

The previous work done by both Bauer and Murphy influenced the experimental set up for the present study. Bauer's failure of the ULTEM 9085 compressor due to excessive axial load required rig modifications to prevent further axial load-related failures. Murphy's aluminum hex-sleeve helped delay bore-section failure that was expected from the FEA model that Bauer produced. The main aspects of these previous studies that are carried over to the present study are the FEA modeling methods as well as some experimental hardware (i.e. rig safety features and hex-sleeve). These details are discussed further in Chapter III.

III. Methodology

As stated in Chapter 1, this study ultimately aimed to fulfill three objectives. The first was to manufacture an AM and cast centrifugal compressor that is less expensive, produced quicker, and potentially weighs less than aluminum. The second objective was to verify if FEA can accurately model failure speed and first-failure location. The third objective was to conduct physical spin tests that validate the FEA model. Section 3.1 discusses the manual molding method required to manufacture the epoxy-carbon fiber specimens. Section 3.2 discusses the material testing method. Section 3.3 describes the FEA model used to predict the failure point for the compressor. Finally, Section 3.4 details the physical spin tests conducted for the compressors.

3.1 Molding

While the Onyx-CF and ULTEM 9085 specimens could be manufactured on their respective printers in a semi-automated fashion, the epoxy-CF molds had to be manufactured manually. While molding methods have been studied and practiced for an extensive period of time, manufacturing polymer-based turbomachinery via molding is relatively new, and no automated method currently exists to produce these types of molded polymer specimens. While the molding process needed to be done manually (increasing the labor time), the benefit of epoxy-carbon fiber casting is that the fibers are able to cross in multiple directions and are not limited to being deposited in layers like 3D printing specimens, thus reinforcing the working geometry in all directions. Different versions of molding methods were vetted based on the quality of the dogbones each method produced. Each of these candidate mold methods was done with epoxy only for the first 2 batches, and epoxy-carbon fiber for the rest.

3.1.1 Test Specimens.

To properly evaluate the strength properties of a material, the materials of interest were made into the shape of designated tensile specimens. The AM-based specimens could be manufactured simply by inputting the desired dogbone geometry into the respective machine and printing the part. Molding epoxy with reinforcement is a relatively new method of manufacturing and, in being done manually, had to be tested in increments of complexity.

As a proof of concept, the epoxy dogbones were first molded without reinforcement using a traditional tensile test dogbone geometry, as shown in Figure 56. The molding process later migrated to different tensile specimen geometry when reinforcement was introduced to assure that a proper amount of reinforcement was included in the test specimen (i.e. traditional dogbones were too slim to fit an appropriate amount of carbon fiber into the gauge section). The ASTM D638 Standard Test Method for
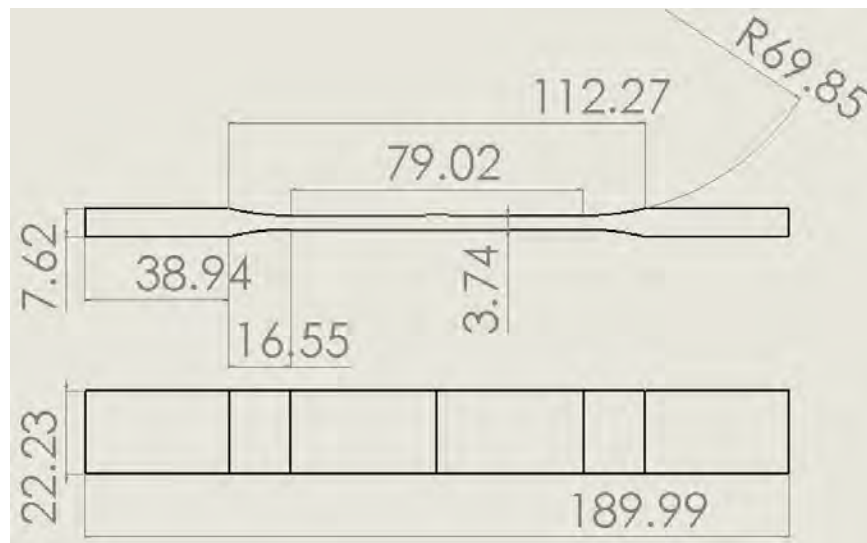
Figure 56. Traditional Dogbone Geometry in mm

Tensile Properties of Polymers was used in this study for material characterization [1] [79]. According to ASTM International, the Type IV specimen is the recommended

specimen type when directly comparing materials of different rigidity (i.e. nonrigid or semi-rigid.) [79]. Since the present study was investigating different materials of varying stiffness and varying reinforcement, implementing the ASTM D638 Type IV was applicable. Figure 57 provides dimensional measurements for the Type IV test specimen [90]. A modified version of this same specimen was also used in this study due to the physical limitations of the available Markforged printer, as discussed later.
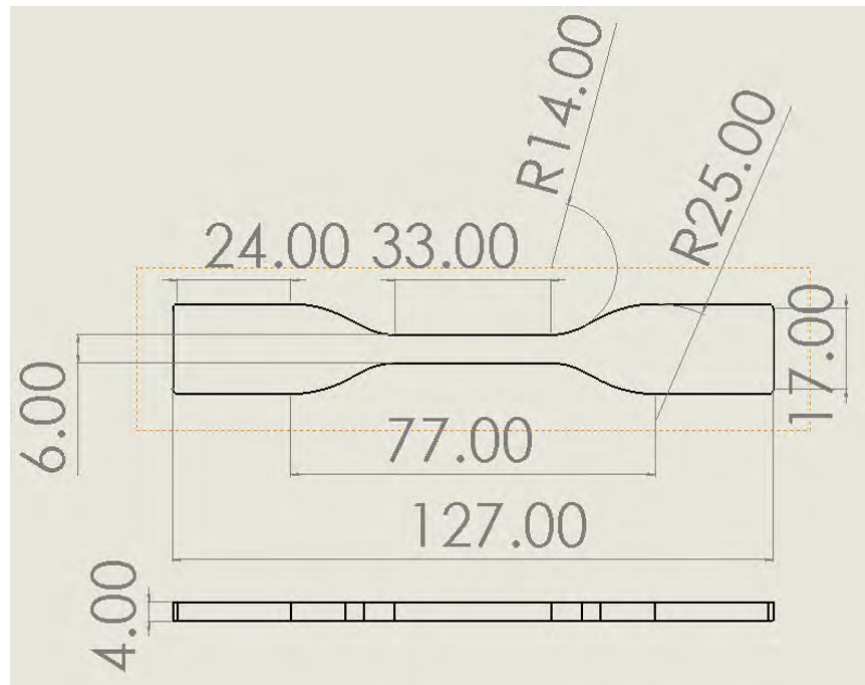
Figure 57. ASTM D638 Type IV Tensile Test Specimen in mm

ULTEM 9085, made by Stratasys, was the first material to be tensile tested and was printed in an XY direction with the widest flat surface against the build plate. Among the 26 specimens produced, two of them were used for calibration, leaving 24 specimens for data collection. Nine of the remaining 24 specimens produced aberrant data, leaving 15 test points remaining.

These specimens augment Bauer's data [1], which was comprised of ULTEM 9085

prints in the XZ and ZX direction. Both directions were printed in Bauer's study in an effort to characterize the anisotropic properties of the material.

Onyx, produced by Markforged, was the second material tensile tested and was printed with continuous filament carbon-fiber reinforcement in the XY direction. The Onyx-carbon fiber parts printed for this study were reinforced at three-volume ratios: 49% Onyx to 51% carbon fiber (49O51C), 54% Onyx to 46% carbon fiber (54O46C), and 35% Onyx to 65% carbon fiber (35O65C). The 49O51C and 54O46C volume ratios were tested using the same ASTM D638 specimen dimensions and XY print orientation as the ULTEM 9085 specimens. However, the 35O65C specimens could not be printed using the exact dimensions of the ASTM D638 model because the printer software would not allow 65% reinforcement into that geometry. The test specimen had to be modified to a larger shape with 4mm of additional width and 1mm of additional thickness, as shown in Figure 58. Since the MTS machine program outputs
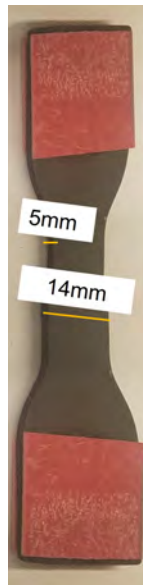
Figure 58. **Modified Tensile Test Specimen with additional 4mm width and 1mm thickness**

load and displacement during tensile tests, the change of dimension was accounted

for by measuring the cross section of each specimen gauge section with calipers. By including the extra step of measuring each specimen cross section, ultimate stress and elastic modulus could be calculated and obtained during post-processing.

Epoxy-carbon fiber was the third material tensile tested, and unlike ULTEM 8095 and Onyx-carbon fiber, was compression-molded as opposed to 3D-printed. The epoxy-carbon fiber was mixed at 85% epoxy and 15% carbon fiber by weight and 90% epoxy and 10% carbon fiber by weight.The details of the equipment used to mold the epoxy-carbon fiber specimens are discussed further in Section 3.1.5.

3.1.2 Epoxy Batch 1: Traditional Dogbone Shape.

Prior to the beginning of this study, two batches of epoxy dogbone molds were attempted (Batch 1 and 2). The first batch contained Supreme121A0 2-part epoxy as the matrix material which required mixing 65g of Part A and 52g of B. This batch was mechanically mixed in a machine and poured into a silicone mold, as shown in Figure 59. All epoxy used in this study followed the same cure cycle as shown in Table 8. A programmable oven, shown in Figure 60, was used to thermally cure the epoxy.

Table 8. Cure Cycle [91]

Cure cycle:
370 K/206 F for 1.5 hrs
394 K/250 F for 3.5 hrs
422 K/300 F for 5 hrs

Figure 59. Specimens in Silicone Mold
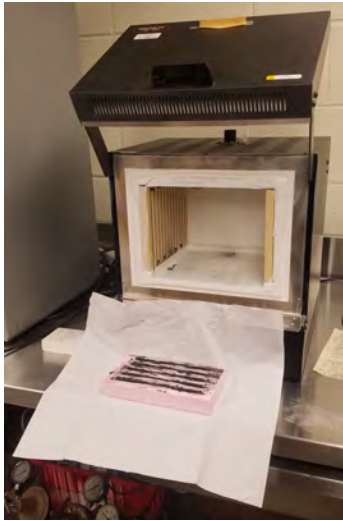
Figure 60. Batch 1-3 Specimen curing Oven

The specimens produced from this first batch had visibly large voids due to the pouring process and lack of degassing. The voids were so significant that only one of the five specimens remained intact after extraction from the mold. It was concluded that if the specimens did not survive extraction from the mold, the specimens were likely not strong enough to survive a full-on tensile test. Because of this, these

specimens were considered untestable. Figure 61 shows the specimens from Batch 1. The edges of each specimen have gaps that indicate the significant voids that existed due to trapped air along with the mold.

Figure 61. Batch 1: Traditional Dogbone Shape

3.1.3   Epoxy Batch 2: Traditional Dogbone Shape.

The second batch attempted to improve from the first batch by degassing the epoxy. The molding process began by mixing the same amount of epoxy from the first batch (Supreme121A0: 65g A, 52g B). This batch was also mixed mechanically in a mixing machine. To degass, the mixture was placed in a centrifuge at 1000 RPM for 1 minute following the recommendation of the epoxy manufacturer, MasterBond. The material was poured into the same silicone mold as the first batch. Initially, the material was supposed to be poured from one end of the mold-negative and flow to the other side to allow an even distribution of liquid material and fill the mold-negative without any gaps. However, the epoxy viscosity was high and could not flow through the narrow gauge section of the mold. The epoxy had to be manually pulled to the other side of the mold negative. The pour process was followed by a 20 minute

degassing in a vacuum chamber. Following the degassing steps, the epoxy was cured in the same fashion as described in Table 8 This batch was also cured in the oven shown in Figure 60. Despite the degassing in the centrifuge and vacuum chamber,

Figure 62. Batch 2: Traditional Dogbone Shape

the dogbone specimens still produced some voids. The voids were reduced from the first batch, which made the specimens strong enough for all five of the specimens to survive removal from the mold. Residual epoxy existed on the top of the mold, connecting all the samples together. This residual needed to be machined off to be tested. However, the first attempt in removing the residual epoxy broke the specimens during the machining process. While the voids were reduced in the second batch, it was concluded that an inability to survive machining residual epoxy likely rendered the specimens unable to survive tensile testing thereafter. As such, tensile tests of Batch 2 specimens were not pursued.

3.1.4   Epoxy-CF Batch 3: Traditional Dogbone Shape.

The third attempt in manufacturing epoxy specimens was the first batch that was conducted by the author during the experimental phase of the present study. This

is also the first batch that included fiber in the mixture. The molding process began by mixing Supreme121A0 with carbon fiber. Supreme121A0 was comprised of 125g of Part A, and 100g of Part B. This epoxy was then mixed with 15g of carbon fiber. The combined epoxy-carbon fiber mixture was mechanically mixed in which 2g of carbon fiber was added at a time until all 15g were included. The epoxy-carbon fiber mixture was degassed in a centrifuge at 1000 RPM for 1 minute. The goal was to "pour" the mixture into the silicone mold, but the consistency was a problem. In incorporating the fiber, the viscosity increased significantly to the point that it could not be poured. The material transformed during the mixture phase and behaved less like a fluid and more like a solid, a stiff steel wool-like substance as shown in Figure 63 which made placing it in the mold a challenge. The stiffness required a manual press into the mold with metal spatulas. The epoxy-carbon fiber was cured in the same fashion as described in Table 8. The specimens were fragile because of the minimal contact between the epoxy and the carbon fibers. This batch of specimens seemed to have more fiber-to-fiber contact (as opposed to fiber-to-epoxy contact), which reduced adhesion during the cure cycle and therefore reduced strength. It was concluded that curing with fiber reinforcement would require pressure to force the material into the mold. All five specimens (Figure 64) remained intact during extraction out of the mold but were considered untestable due to the significantly large voids in the samples.

3.1.5   Epoxy Batch 4: ASTM D638 Dogbone Shape.

The fourth attempt in manufacturing epoxy specimens was the first batch that applied mechanical compression to the mixture in the mold. This compression was added due to the voids that consistently appeared in each of the previous batches and indicated pour molding would not be possible with carbon fiber reinforcement. As

Figure 63. Batch 3 Blend

Figure 64. Batch 3: Traditional Dogbone Shape, Double Thickness

a result, the Wabash 30 Ton Press (Figure 65) was used for this batch and had the ability to press and thermally cure the epoxy under pressure. The molding process began by mixing Supreme121A0 with carbon fiber. Supreme121A0 was comprised of 50g of part A and 40g of part B. This epoxy was combined with 13.5g of carbon fiber (15% of the total weight is carbon fiber). All stages of the mixture were stirred by

hand while incorporating the fiber at arbitrary intervals until fully incorporated. The mixed material was manually placed into the mold-negatives. The one piece mold negative is shown in Figure 66. The Wabash pushed the blend into the one piece mold was approximately 5000 lbf. The epoxy-carbon fiber was cured in the same cure cycle as described in Table 8, with the one addition that this mold was under pressure. When the cure cycle was complete, the excess material that did not get into the mold was sanded off the metal mold plate surface, and the specimens were pressed out using the metal slug cut out of the plate, a result of the mold-making process. All five dogbones were successfully removed and intact.

Figure 65. Wabash 30 Ton Press

Figure 66. Batch 4-5 Mold - 1st compression mold

Figure 67. Batch 4 Specimens

Only small surface defects were observed on samples, as shown in Figure 67, and seemed manageable for specimen testing. Characterizing each specimen required weighing each one on a scale in the AFIT materials lab to quantify variability.

3.1.6   Epoxy Batch 5: ASTM D638 Dogbone Shape.

The fifth attempt to manufacture epoxy specimens used the same procedure as the fourth batch. The reinforcement was reduced to 10% of the total weight. This was done to test if epoxy-carbon fiber adhesion would increase with a slight reduction in fiber content, hoping that the voids observed in the fourth batch would potentially be reduced. Batch 5 also used the one-piece mold shown in Figure 66. On the surface, there was not a drastic difference in appearance between the fourth and fifth batch regarding visible surface defects shown in the Batch 5 specimens in Figure 68. The deeper voids seemed to be less present on the surface with a closer look. Any legitimate reduction in voids would be revealed more quantitatively when comparing Batch 4 and 5 specimens in the tensile test component of this study in Section 3.2. These specimens were also weighed for individual characterization and variability. Both the fourth and fifth batches seemed to contain a common problem with the molding process: the machine applied the majority of the load on the mold plate rather than the specimen material itself due to the geometric design of the plate. The press machine was only applying a uniform load on the entire square-shaped geometry leaving the specimens only to receive a fraction of the actual 5000lbf. At the same time, the rest of the load was distributed across the mold plate surface area.

Figure 68. Batch 5 Specimens

3.1.7 Epoxy Batch 6: ASTM D638 Dogbone Shape.

The sixth attempt to manufacture epoxy specimens used the same procedure as the fourth and fifth batch, but in a different mold. The epoxy blend comprised of 50g of A, 40g of B, 9.0g of carbon fiber (the reinforcement was maintained at 10% of the total weight). The blend was manually mixed as in batch four and five until the fiber was completely incorporated. This batch implemented a new 3-piece mold as shown in Figure 69. The batch specimens outside of the mold are shown in Figure 70. To assure equal distribution of mass and volume for each specimen, the total blend was divided into fifth's by mass. The partitioning of total mass into fifth's was measured with a weighing scale. The targeted mass distribution was 12.60g per mold cavity to assure even distribution. Physical measurements of each partitioned mass weighed in at 12.67 ± 0.02g for each specimen cavity. The extra 0.07g was added to account for losses that may get stuck to the mold. After initial press, the spacing between the top plate and negative plate was 0.028" (0.030" was the design target to ensure

97

Figure 69. Batch 6 with Mold

Figure 70. Batch 6 Specimens

correct thickness parts). The plates were repressed after the measurement was taken.

Upon repress, seepage of liquid epoxy was observed between the bottom plate and the

negative plate, as shown in Figure 71. Enough epoxy was pressed out such that the metal plates were touching at the start of compression. This batch was also pressed at approximately 5000 lb under the same cure cycle temperature sequence. The

Figure 71. Batch 6 with some Seepage

seeped epoxy boned the plates together which made releasing the mold components challenging and time consuming. Based on this result, the bottom plate and negative plate were attached together to prevent/reduce seepage. Adding a stop on to the top plate could help in assuring the mold does not close after reaching the design height which could prevent extraneous epoxy for escaping the mold. Adding such a stop would mean that the specimens would not cure under the same pressure, but the applied pressure from the press plate should remove all of the air pockets that previously posed a problem.

3.1.8 ULTEM 1000 Batch Attempt.

In addition to manufacturing Epoxy-carbon fiber, an attempt at press molding a batch of ULTEM 1000-carbon fiber was also conducted in this study. However, this batch did not successfully produce usable specimens. The carbon fiber existed as chopped tows, where individual separated fibers were desired. An attempt to separate the carbon fibers within the ULTEM 1000 was done by putting the mixture of powdered ULTEM 1000 and carbon fiber (Figure 72a) in a centrifuge machine at

AFIT Building 640, as shown in Figure 72c.
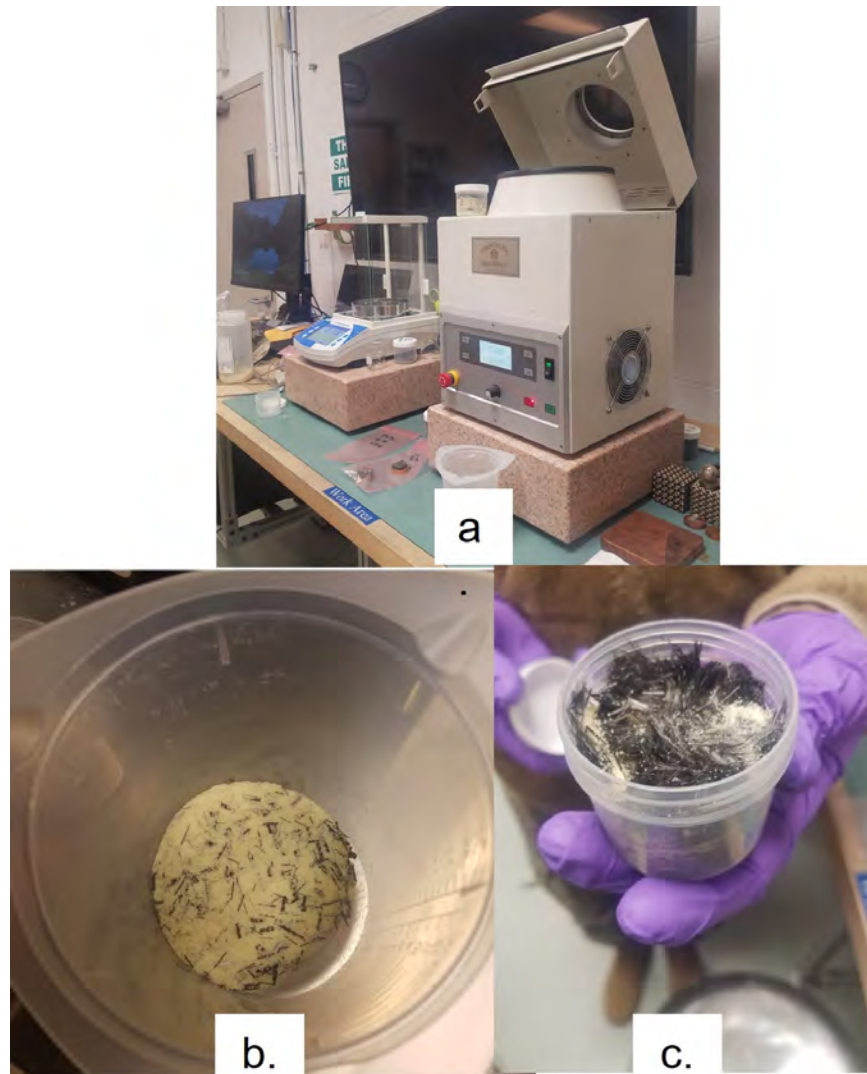
Figure 72. ULTEM 1000 First Blend attempt. a) Centrifuge Machine b) Blend prior to centrifuge c) Blend after centrifuge

Figure 72 displays the first attempted blend. The purpose of putting the ULTEM 1000-carbon fiber blend into the centrifuge was to break up the clumped fibers stuck together (as they are from the factory bag) and allow them to integrate evenly into the ULTEM 1000. If they are not broken up, there could be an uneven amount of reinforcement because certain locations in the volume could contain too much carbon

fiber and others too little. This would cause unwanted stress concentrations in the material and function to oppose the desired increase in strength properties. Instead of separating the fibers, the centrifuge caused the fibers to fluff up as shown in Figure 72c. Based on general observation, it was concluded that integrating fiber into the ULTEM 1000 would be more difficult due to the need to separate the fibers. The expected ULTEM 9084 melt behavior was obtained by the manufacturer and a compression mold of ULTEM 1000-carbon fiber was attempted as shown in Figure 73. A blend was mixed comprising of 41g of ULTEM 1000 with 4.6g of carbon fiber producing a blend of 45.6g of ULTEM 1000-carbon fiber with 10% reinforcement. This blend wa divided equally by mass into the five negatives of the 3-piece compression mold. The material was compression molded with the same 30 ton Wabash Press as the

Figure 73. ULTEM 1000-carbon fiber within 3-piece Compression Mold

Epoxy-carbon fiber specimens. The specimens were pressed at 5000 lbf and heated

to the melt temperature of 400ºC. Mold release was also added to the insides of the 3-piece compression mold to help in post-processing removal.

After the specimens were melted into dogbone samples, the mold was removed to reveal that the specimens in Figure 74 did not survive the compression under temperature. Figure 74a and c show strong adhesion to the mold plate that was

Figure 74. ULTEM 1000-carbon fiber Post Compression Specimens

enough to overcome adhesion between the specimen material during extraction. The residual specimen material in Figure 74b further supports that only 1/3 of the sample

was left in the mold after removing the bottom plates.A closer look at Figure 74c also reveals that some of the ULTEM 1000 powder did not seem to liquefy even at 400°C. The image also indicates that the fibers did not seem to separate at all. This may have contributed to the significant lack of adhesion during the cure cycle as ULTEM 1000 could not get around the existing fibers to melt and adhere the material together. For this study, ULTEM 1000-carbon fiber was not further pursued as a material of interest after the unsuccessful compression mold. Future studies could investigate injection molding of ULTEM 1000 and carbon fiber into dog bone molds. In injection molding, the material is heated and mixed with carbon fiber, and turned in an auger prior to injection into a cool mold. The process of injecting the ULTEM 1000 and carbon fiber mixture through the auger and nozzle may further break up the carbon fibers leading to a better mixture. Additionally, the injection of the hot plastic into a cool mold would cause the plastic to solidify on the mold surface and help prevent sticking to the mold.

3.2   Material Testing

Manufacturers' published material properties [50, 77, 78] are typically at room temperature and are not enough to characterize material behavior at high temperatures. Readily published data is usually presented in "thermal strength" at either the glass-transition temperature (GTT) or heat deflection temperature (HDT). GTT is a characteristic temperature for polymers that indicates the temperature in which a polymer's phase changes from a solid to a liquid [34], while HDT indicates the temperature designated stress, usually 0.455 MPa or 1.82 MPa, that causes a 0.25 mm deflection [92]. These two particular temperatures do not describe the effect temperature has on factors such as ultimate strength or modulus of elasticity and are not as helpful for this study's particular application [1].

103

If readily published material properties were used in an FEA model, the model would ignore thermal effects due to air compression and thermal conduction from the hot side of the compressor. Thus, the model would not be accurate, and the physical compressor would fail at a lower speed than the model's predicted speed. Gathering ultimate strength and elastic modulus data over a range of temperatures and inputting those values into an FEA model of a compressor significantly increases the accuracy of the model [1].

The following sections describe the test methods used to collect material property data over varying conditions. Section 3.2.1 details the tensile test rig, Section 3.2.2 describes the varying temperature parameters of the tensile tests, details the tensile specimens themselves, and outlines the test matrix. Finally, Section 3.2.4 explains how the raw data was translated from force-displacement information to characterize material properties [1].

3.2.1   Tensile Test Rig.

This study used a 3 kip rated MTS machine (max error of 0.49% of the readout [93]) as well as a 22 kip MTS machine (max error of 0.77% of readout [94]). At 36% of the maximum force (which is the range at which the machine is expected to break the specimen) the machine has an error of 0.04% [94]. The sample displacement was calculated via the system's internal measurement system, the Linear Variable Differential Transformer LVDT which is discussed in further detail in Section 3.2.5. Both machines have a full range of 5 inches [93] [94]. The test rig was adapted with heaters to test for strength properties at temperatures above ambient, and are able to raise the specimen temperature up to 1400°C. The tests conducted were well within this range as the maximum temperature of interest for this study was 202°C. Both the 3 kip and the 22 kip MTS Machines are shown in Figure 75.

(a) 3 Kip MTS Machine   (b) 22 Kip MTS Machine
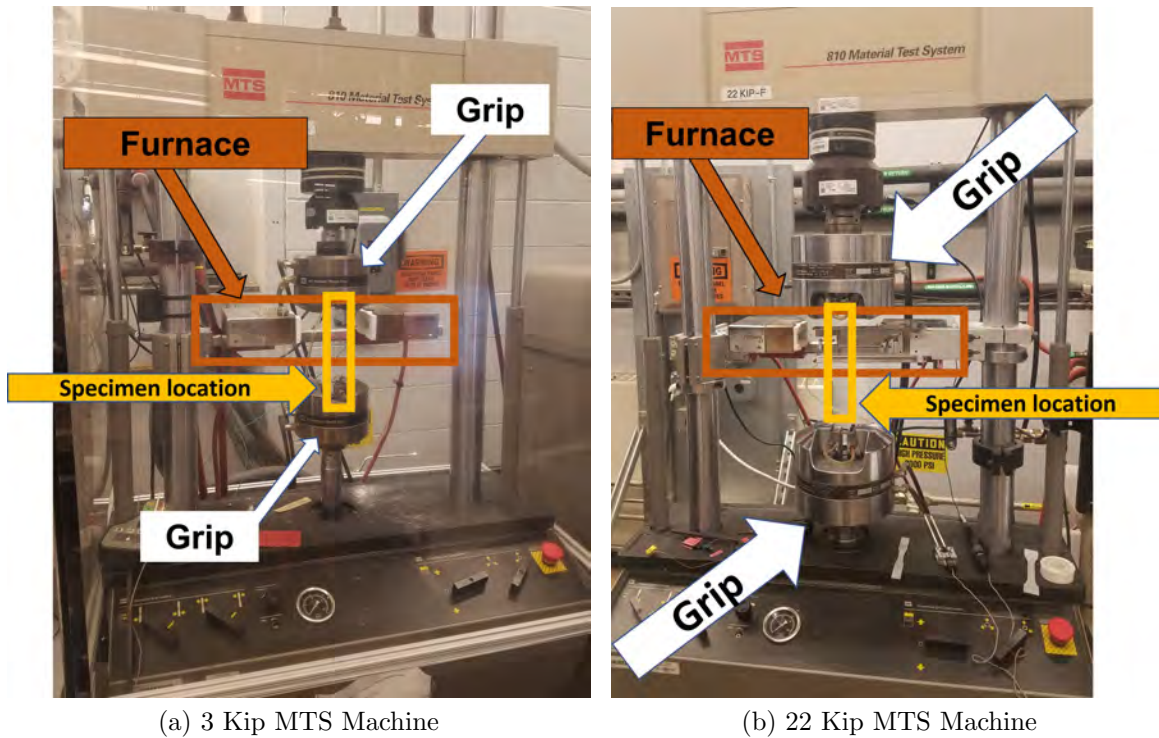
Figure 75. MTS Machines

3.2.2 Test Matrix.

The temperatures tested are within the relevant operating conditions for the P400. The lower bound of the temperature profile is ambient temperature, 293 K. The upper bound is 475 K which is close to the maximum static exit temperature of a P400 compressor (differs from Bauer's 435K [1]). Working in groups of five samples, this study initially tested four distinct temperatures in the desired range with one repeated temperature for random repeatability purposes. However, when a significant error between the furnace and internal temperature of the sample was discovered in the middle of testing, additional temperature values were added. The test matrix for the seven distinct temperatures examined in this study are shown in Table 9.

Table 9. Tensile Test Specimen Matrix and Samples Tested

Material	Temperature (K)							Total Specimen
	293	354	366	414	444	475	523	
ULTEM 9085, XY	6	0	5	2	2	1	1	17
Epoxy Carbon-fiber (15% reinforcement)	2	1	1	1	0	0	0	5
Epoxy Carbon-fiber (13% reinforcement)	1	1	0	1	0	2	0	5
51C49O	2	0	2	2	0	2	0	8
46C54O	1	1	0	1	0	2	0	5
65C35O	0	0	0	0	0	0	0	0

3.2.2.1 Furnace Temperature Correction.

An important nuance in this study is the stark error discovered between the reported furnace temperature and the actual specimen internal temperature. As part of a test to verify the error between the commanded input furnace temperature and the resulting specimen temperature, a broken test specimen with a thermocouple embedded in it was placed in the furnace and heated to a predetermined furnace temperature. There was a noticeable difference in temperature between the commanded input temperature and the actual specimen temperature. This difference grew at higher commanded temperatures. The variation between the commanded input temperature and the actual specimen temperature was plotted in Figure 76. This calibration was conducted for both the 3 kip and 22 kip machine. The setup for verifying furnace temperature variation with surface temperature is shown in Figure 77

While the significant error between the commanded input and actual furnace temperature is unfavorable, the variation is repeatable and thus predictable. This makes a reasonable approximation for specimen temperature possible. The linear equations (shown in Equation 49 for the 3 Kip MTS Machine and Equation 50 for
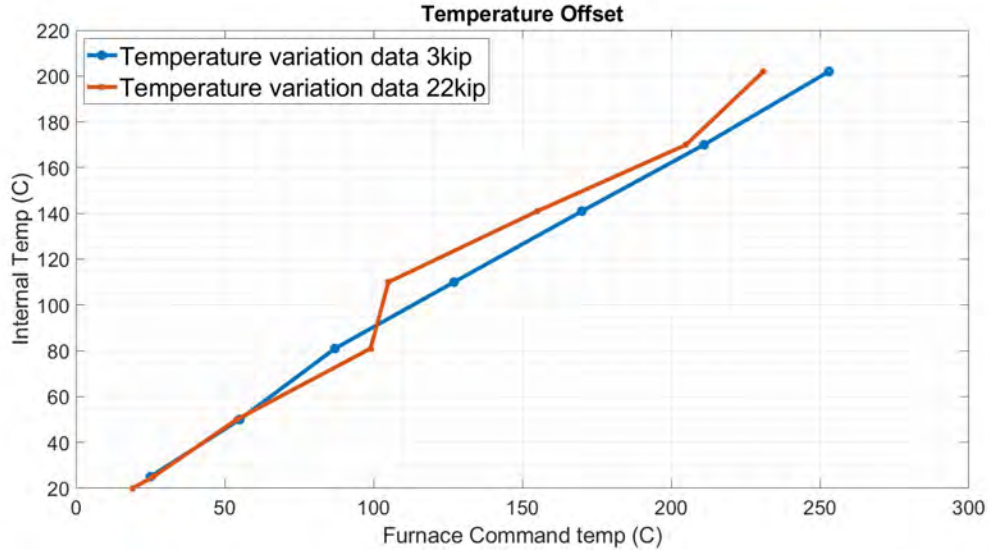
Figure 76. Oven Temperature Variation

the 22 Kip MTS Machine) represent the relationship between the commanded input and the specimen internal temperature. IT represents the Internal Temperature, and CT represents the Commanded Temperature inputted into the oven program.

$$CT = \frac{IT + 12.0}{1.3} \tag{49}$$

$$CT = \frac{IT + 5.0}{1.2} \tag{50}$$

3.2.3   Procedure.

The following procedure for material tensile testing was used for both MTS machines. Prior to clamping any of the specimens on the MTS machine, each specimen grip section had a small tab bonded to all four grip faces on the specimen, as shown in Figure 78. This was required due to the significant clearance between the machine closed-grip distance and then specimen thickness. Without the tabs, the MTS machine could not make contact with the specimen grip section, which is required for

107
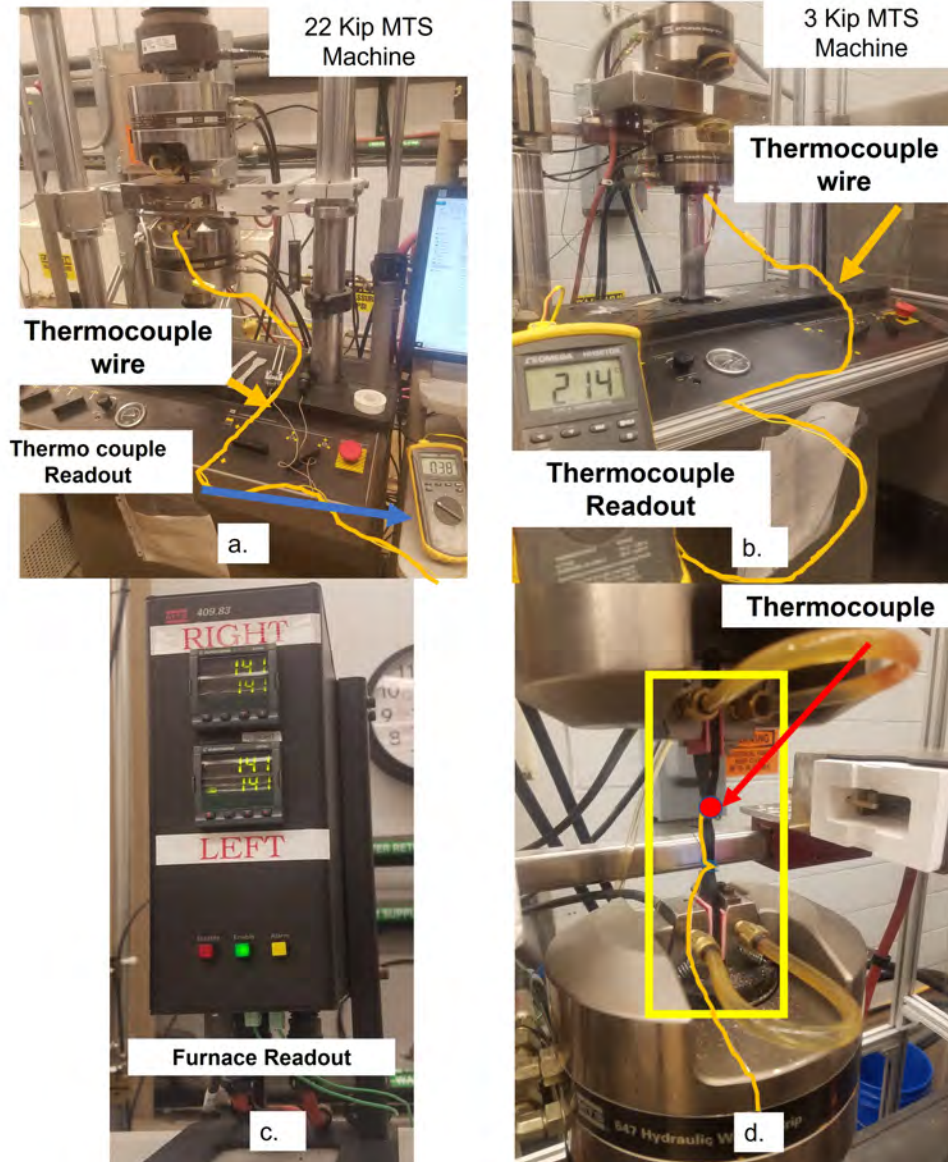
Figure 77. Tensile Specimen Furnace Variation check a) 22 Kip Machine b) 3 Kip Machine c) Furnace Oven Readout

the tensile test to work. Figure 79 shows the two grip points, the furnace, and the command module that were used to conduct tensile tests. To clamp the specimens, each specimen was mounted on the grips (starting top grip to bottom grip). The grip pressure was different depending on which specimen was used. The thinner specimens for ULTEM 9085 and epoxy-carbon fiber required a 2.76 MPa (400psi) grip
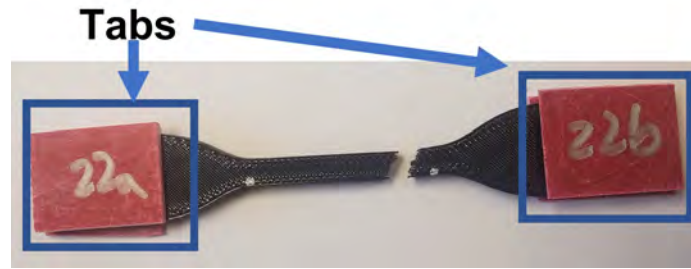
Figure 78. Tensile Specimen tabs

pressure while the thicker Onyx-carbon fiber specimens required a 7.58 MPa (1100psi) or greater grip pressure. There were two MTS modes used for the specimen set up; displacement control mode and force control mode (sometimes called load control mode). The difference is in which of the two is treated as the independent variable and which is the dependent variable by the MTS machine. Displacement control mode sets displacement as a manual input by the user (independent variable) while the machine applies a force relative to its position to match that desired displacement (dependent variable). Conversely, force control mode sets the force magnitude as an input by the user, and the machine matches that amount of force by some responding displacement. The first step to setting up the tensile test was to set the MTS machine into displacement control mode as default and clamp the specimen under the top grip. The second step, before the bottom grip was clamped, was to switch the MTS Machine to force control mode and manually set the force equal to 0 kips. This step is required because the MTS machine will otherwise apply an undesired tension/compression load on the specimen if the bottom grip is clamped in displacement control mode. Setting the force to manually equal 0 kips assures no inadvertent force is applied during the clamping process that would ruin the tensile test results. After the force was set to 0 kips, the bottom grip was clamped on the specimen and the MTS machine was quickly reverted back to displacement control mode to assure no inadvertent displacement occurs with the specimen placed in the grips. From here,
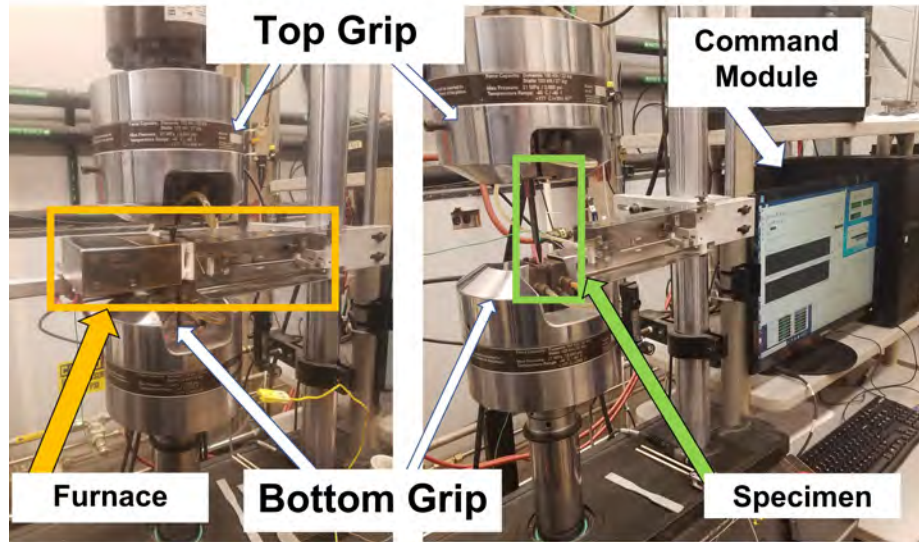
Figure 79. MTS Machine Procedure Set up

the specimen was prepped for testing and the data collection began. If the test point was at room temperature condition, the furnace function was skipped (usually it was kept open) and the test began immediately with the applied load on the specimen. The failure criterion on the machine was met when the MTS machine detected a decrease in force below 75% of the maximum recorded load of that data set.

If the test point required above room temperature conditions, the furnace was closed and raised the internal temperature of the specimen to the desired level prior to applying tensile load. The heating rate of the two heaters 15°C/min. As soon as the heater was at the target temperature, a 15-minute thermal soak commenced to ensure the specimen was at the same temperature as the furnace. Once the thermal soak was complete, the MTS machine proceeded to pull the specimens at a 5 mm/min displacement rate based on the ASTM D638 standard [79]. The ASTM D638 standard required five specimens in each of the anisotropic directions to account for anisotropic effects. However, for this study, the focus was on the XY print direction due to the orientation of the final compressor geometry. Since the focus of this step of the

study was less on complete material characterization and more on the acquisition of strength properties for an FEA model, an abbreviation of the ASTM D638 standard approach was conducted. After the load was applied to break the specimen, the data is collected and post-processed for extraction of material strength properties.

3.2.4   Data Reduction.

The MTS machine records tensile data in force (N) and displacement (mm). Each specimen's stress value was determined via Equation 51. The specimen cross-sectional area was found by averaging five separate measurements of width (w_i) and thickness (t_i) of the gauge section. For room temperature specimens, the strain (ϵ) was calculated by dividing the measured displacement (δ) by the original length (L_o) of the gauge section. Then, that strain was corrected to make sure that the first data point exhibited zero strain (ϵ_0) and, in turn, zero stress. The zero strain calculation is demonstrated in Equation 52. Equation 53 defines the elastic modulus (E), which is found by calculating the slope of the initial 800 points of data from the stress-strain curve. Some specimen tests were quicker than others, such as room temperature specimens which spanned less than 800 points. Room temperature specimens were truncated to only measure the points within the linear elastic region. Lastly, the maximum stress was simply the ultimate strength or the largest recorded stress data point during the test sequence [1].

$$\sigma = \frac{F}{\sum_{i=1}^{5}(w_i/5) * \sum_{i=1}^{5}(t_i/5)} \tag{51}$$

$$\epsilon = \frac{\delta}{L_o} - \epsilon_o \tag{52}$$

$$E = \frac{\sigma_{800} - \sigma_1}{\epsilon_{800} - \epsilon_1} \tag{53}$$

Although the heated region of the specimen was about an inch in length, displacement (during tensile testing) happened along the entire specimen. Assuming the specimen experienced displacement equally along the entire length, then more strain would occur for the same stress, and therefore a smaller value for E. On the other hand, if displacement was assumed to be experienced solely at the heated region, it would neglect the displacement at the unheated regions. This assumption lowers the strain and increases E. The third scenario takes the original E calculated at the unheated regions (E_u) and uses it to predict displacement due to input stress at the unheated regions (δ_u). This unheated zone displacement, δ_u, is then subtracted from the measured displacement to approximate the displacement exclusively at the heated region (δ_h). This process is outlined in Equations 54-56. This third scenario assumes distinct temperature regions and incorrectly ignores conduction. However, it bypasses a more consequential and inaccurate assumption of constant displacement along the entire specimen length [1]. Thus, for this study, the elastic modulus was calculated in post-processing with Equation 54 for the room temperature specimens and Equation 56 for the heated specimens.

$$\delta_u = \frac{\sigma L_u}{E_u} \tag{54}$$

$$\delta_h = \delta - \delta_u \tag{55}$$

$$E_h = \frac{\sigma L_u}{\delta_h} \tag{56}$$

3.2.5 Displacement Measurement.

An important note for the strain measurement of this study is with the method of measuring displacement. There are two common tools to measure displacement for a tensile specimen. The first is the strain gauge which converts strain applied to an

112

electric signal. The strain gauge itself is a resistive elastic unit that varies in resistance based on the strain applied to it. It is considered the most accurate among these two discussed methods. The second is the LVDT which is a type of electrical transformer that converts linear displacement from a zero-point reference into an electric signal representing phase, as direction, and amplitude, as distance. The LVDT is the less accurate of the two since it is not focused on the area of interest, which is the gauge section [95].

As the more accurate of the two tools, the strain gauge is generally recommended. For materials that will have significantly different strain at the grips than in the gauge section the strain gauge is recommended even more so. However, the available strain gauges for this study were not rated to endure up to the temperatures of interest. The MTS machines used in this study also had an LVDT built into them to measure displacement. As a result, the MTS machine's LVDT was used for this study to measure each specimen's displacement, in spite of being known as less accurate to the strain gauge. [95] In the future, it is recommended to measure the strain using both the LVDT and the strain gauge up to the temperature limit of the strain gauge. Then, both sets of strain data can be correlated to produce an approximate linear trend to translate between one method and the other. The half of the trend line that is above the temperature limit of the strain gauge could be extrapolated. In this study, the strain data shown is acquired via the LVDT built into the MTS machines.

3.3   Finite Element Analysis

No closed-form analytical equation exists for centrifugal compressor analysis due to their complex design. A closed-form solution is even more unrealistic when the model includes temperature effects on material properties, which is why FEA models are needed. FEA converts a complicated problem into a large group of solvable

fundamental equations. Complex geometries like a compressor are broken down into numerous nodes. The nodes are connected to one another and track body force interaction, such as centripetal acceleration, as well as forces due to adjacent nodes transferring the effect of their own body forces. Finding the solution to numerous smaller equations representing each node generates an approximate solution very close to that of the actual solution for the entire compressor. Although highly practical, like all models, FEA's approximate solution contains underlying assumptions that do not perfectly reflect reality and contains some inaccuracy. This section outlines the FEA model that was implemented to estimate the speed and location of failure for each compressor material.

To outline the compressor analysis, Section 3.3.1 explains the generation of a compressor CAD model from a physical compressor. Section 3.3.2 explains the mesh generation process for the compressor models. Section 3.3.3 describes the necessity of temperature variation in the FEA model and the relevant temperature bounds. Finally, Section 3.3.4 discusses the structural limits and the failure calculation.

3.3.1   Model Creation.

The compressor model was made by scanning a physical JetCat P400 compressor with the white light method. This scanner detects positions along the surface of the scanned object. In this study, the scanned object is the P400 compressor which has physical dimension as shown in Table 10, relative to the labels on the P400 compressor geometry shown in Figure 80.

Table 10. JetCat P400 Compressor Rotor Dimensions

P400 compressor dimensions	Measurement (mm)
Hub diameter	107
Bore Inner Diameter	9.8
Height	50
Hub Inlet Outer diameter	20

114
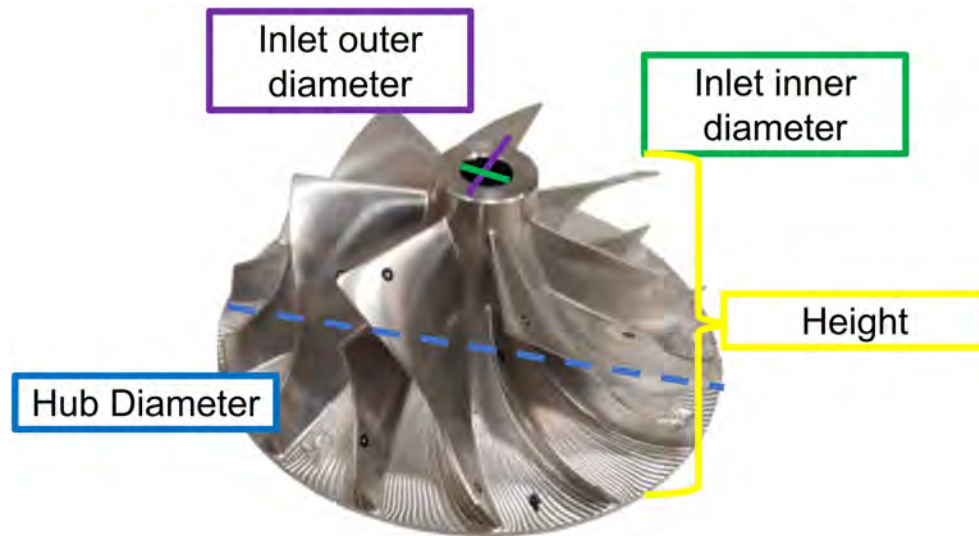
Figure 80. P400 Dimensions

The position data is compiled into a large group of points known as a point cloud that mathematically represents the scanned object. The point cloud forms a series of points to represent the surface of an object and looks very similar to the image of the P400 in Figure 81. However, Figure 81 actually takes it a step further by connecting each of the points with a series of lines that are translated into surfaces. When a point cloud is taken through this extra step, it becomes what is known as a closed model and are often used as inputs for CAD models. These closed models remove illogical planes, adds important dimensions, and assures each compressor blade is identical. Point clouds prove to be slightly inferior to the conventional CAD model in terms of its editability and its printability. The current study recycled Bauer's [1] and Murphy's [89] previous CAD data files.

3.3.2 Mesh Creation.

Once model geometry was obtained, the mesh was the next step in FEA and is a critical factor for accuracy. An increase in the node count will increase the model's degrees of freedom, and an ideal FEA model would have the node numbers increased

115
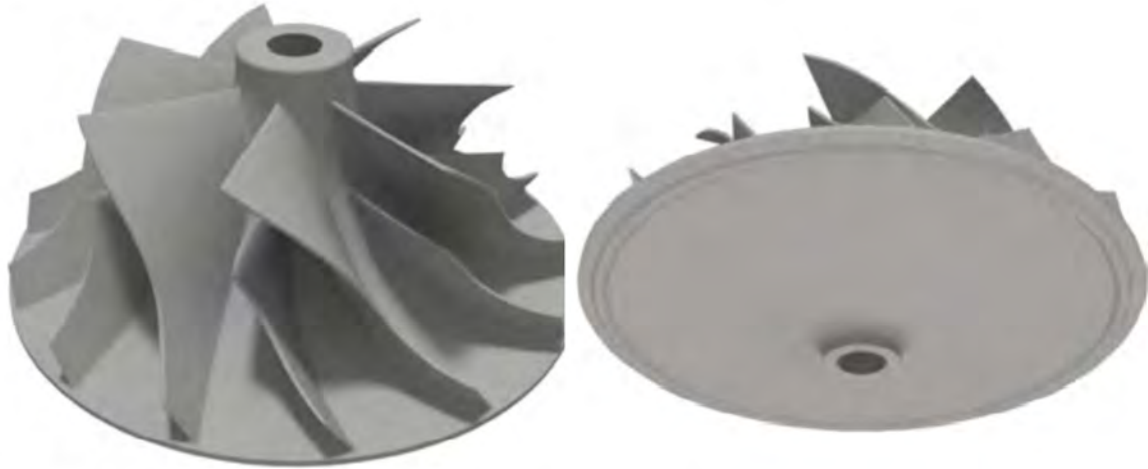
Figure 81. Closed Model of P400 Compressor [1]

until one of the model output value converges to a solution. However, such an approach would make a solution computationally exhaustive to generate. Accuracy and cost are traded off to produce a trustworthy and practical engineering solution. The mesh was constructed using SolidWorks' mesh autogeneration feature. The Solid-Works program divided the model into simple shapes or elements and connected each element at common points or nodes. The auto-meshing feature (which defaults to tetrahedrals) creates the mesh depending on the inputs of "global element size", "tolerance", and "local mesh control specifications" [96]. SolidWorks' mesh control allows users to define element sizes for components, faces, edges, and vertices.[96]. The mesh output from SolidWorks for the P400 compressor is shown in Figure 82.

3.3.3   Temperature Profile.

As mentioned at the beginning of Section 3.2, a constant temperature analysis can give information about failure speeds and locations, but it neglects important factors that drive failure. High temperatures approaching the 475 K upper operating condition put the materials near their limits. Due to the temperature dependence of ultimate strength, any given material undergoing spin testing would likely fail below

116
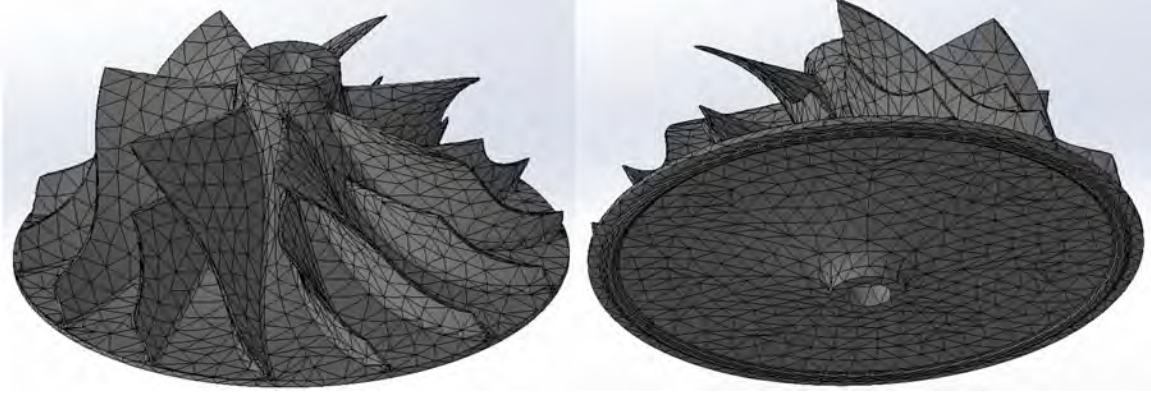
Figure 82. Mesh for Stock JetCat P400

the predicted FEA model speeds if the temperature effects were neglected during the analysis. The SolidWorks Static Thermal module was used to create the thermal profile that matches the boundary conditions discussed in Section 2.2.6.3. The boundary conditions were inputted into the SolidWorks model with the inlet region set to room temperature since the temperature here is prior to compression, while the exit side of the compressor was set to 475 K, which is based on the worst-case (for temperature) operating temperature of the P400 engine. Published information regarding thermal conductivity was included to produce a temperature gradient. Figure 83 shows an example of a thermal profile for an Onyx-Carbon Fiber compressor and Epoxy-Carbon Fiber hub at a lower operating of 438 K.

3.3.4   Structural Profile and Failure Analysis.

The temperature profile gives useful information regarding the compressor's behavior in heat transmission. However, the thermal analysis does not capture the relationship between structural failure and operating speeds. The failure-speed relationship is obtained via structural profile whereby the FEA program calculates the internal stresses based on the input speed and geometry. Then, it calculates deformation based on the elastic modulus data from the temperature-based tensile test
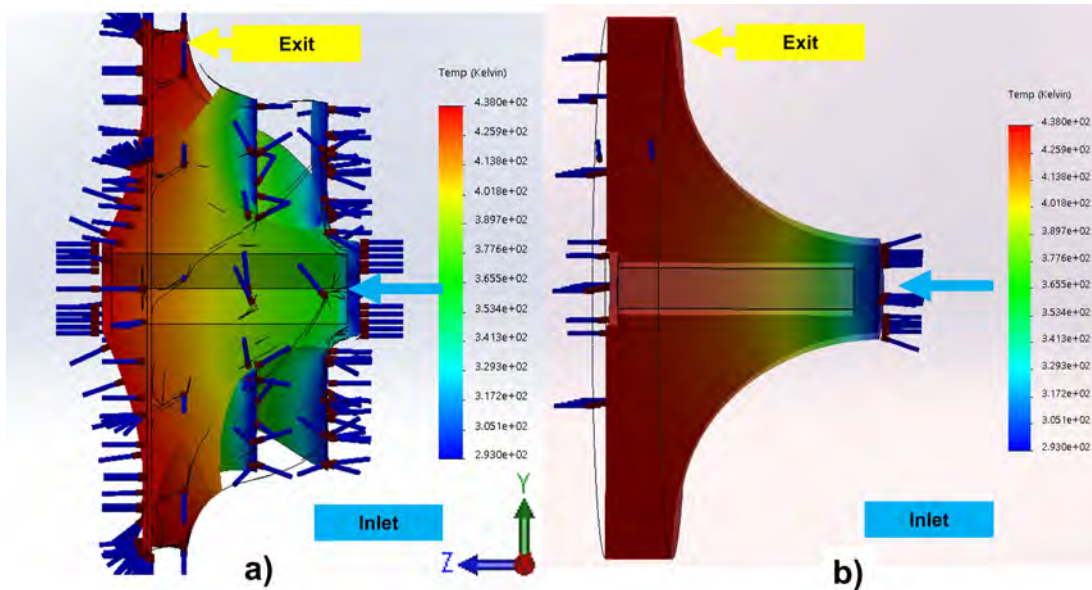
Figure 83. Example of Thermal Profile, Onyx-Carbon Fiber Compressor and Epoxy-Carbon Fiber Hub at 438K

[75].

The SolidWorks Static Structural module was used to generate the structural profile. The module applies a rotational speed on the compressor model about its central axis (the engine shaft) while applying a bearing fixture (artificial constraint) at the front face and back face of the compressor to force rotation only to occur in one plane. In addition, the temperature profile discussed previously was input into the model to allow the temperature varying material properties to take effect and generate a condition-based solution. [75]

Since SolidWorks did not have the built-in capability to input temperature-dependent ultimate strengths in the model data, the temperature variation was accounted for manually. The temperature was assumed linearly proportional to the rotational speed for this model. For every increase in temperature condition, the ultimate strength and elastic modulus were manually increased to the measured values based on the tensile test results in Section 4.1. For example, ULTEM 9085 at 300K will correspond

118

to any speed below 9.8 kRPM, a σ_u of 67 MPa and an E of 1.23 MPa. At 475K, the conditions correspond to a speed of 98 kRPM, a σ_u of 0.237 MPa and an E of 1.78 MPa. The elastic modulus and ultimate stress have individually corresponded to the temperature-speed combination for all three materials. The calculated temperature-speed combinations are shown in Table 11.

Table 11. Temperature-Speed Combination

% of Operating Speed	Temperature, K	Temperature, ^{o}C	kRPM
100% - max power	475	201	98
90%	457	183	88.2
80%	439	165	78.4
70%	420	147	68.6
60%	402	129	58.8
50%	384	110	49
40%	366	92	39.2
30% - idle	348	74.2	29.4
20%	329	56	19.6
10%	311	38	9.8

While FEA helps conclude failure speed and location, some underlying assumptions and simplifications deviate from the real compressor configuration. Three major simplifications were made in the SolidWorks FEA analysis, which contributed to some level of inaccuracy to the FEA model and failure prediction.

1. The surface forces acting on the compressor due to viscous shearing and pressure gradients were neglected because they only contributed to less than 2% of centrifugal forces [3]

2. The assumption the compressor achieved steady-state operation for the thermal and structural analysis

3. The assumption that the working materials all behaved isotropically for both the extruded materials (ULTEM 9085, Onyx-Carbon fiber) and the molded ones (Epoxy-carbon fiber).

The above assumptions boil the SolidWorks model down to two external loads: the thermal and centrifugal loads. While these simplifications decrease the accuracy of the SolidWorks model, they remove complications in constructing the model and allow the program to compute the results more readily. This also focuses the model on the two aspects that most significantly affect failure, which is thermal and rotational effects. Additional details to note for the SolidWorks FEA model are the fact that inertial relief and bearing constraints are required for the model to run. Inertial relief disregards gravity, which is necessary, or the FEA model will assume nothing is holding the compressor and will simulate it falling out into space. Bearing constraints are necessary to simulate the compressor's fixed rotation on one axis, else the FEA model will assume the compressor is spinning out of concentricity with its own shaft. This is not a realistic behavior and will produce displacement results that are unrealistically large.

3.3.5 Compressor Fabrication.

The following sections discuss the fabrication of the compressors of interest. Section 3.3.5.1 discusses the settings used to print the compressors. Section 3.3.5.2 discusses the molding of the compressor hub.In the following section, the process needed to balance the compressors and remove imbalances in the mass distribution of the compressor-turbine assembly that could cause premature failure at the bore is discussed.

3.3.5.1 Compressor Printing.

There were six compressors printed. The first pair of compressors was made out of Onyx-Carbon Fiber by the University of Dayton Research Institute who used the MarkForged Mark II printer. This printer is unique because it can print continuous

fibers separate from its matrix materials. While the printer is designed to print several different reinforcement methods (carbon fiber, high-strength, and high-temperature fiberglass, and kevlar), carbon fiber was specifically used for this pair of compressors. The matrix material was Onyx, which is comprised of nylon [78] reinforced with discontinuous (chopped) carbon fiber [1]. Due to physical print limitations (a limited amount of infill was permitted to print reinforcement in the compressor geometry), these compressors printed with only 35% infill of matrix material which means there are small voids internal to the part [78].

The other four printed compressors were made out of ULTEM 9085 from the Stratasys Fortus 450 mc, located at AFIT Building 640. The Fortus 450mc printed the ULTEM 9085 compressors with 100% infill, but was unreinforced. Each compressor was printed with a flat bottom, and a hex bore to accept the aluminum hex sleeve previously discussed in Section 2.6. The WPAFB Area B model shop machined the back face to the correct specification to test the compressors on the test stand.

3.3.5.2   Compressor Hub Molding.

Following the success of molded dogbone specimens in Epoxy-Carbon fiber, the mold of the more complex compressor hub was attempted. Molding and casting extremely thin geometries, such as blades, tend to be very challenging because such geometries are prone to breaking upon extraction if the mold is not designed to account for removal. Even if such a mold is designed correctly, post-cure adhesion can cause resistance to extraction and add risk for breaking. Compressors with relatively thin blades are an example of this challenge in molding. Because of this obstacle, this study first investigates molding a compressor hub without any blades to verify if it is feasible to mold the simpler shapes of a compressor's geometry. This bladeless hub geometry is used for the FEA analysis alongside the full compressor with the hex

sleeve and custom washer. Previous testing did not show that the compressor failed at the blades first, but rather the hub. Hence, testing for hub structural integrity is valid testing.

The primary failure location of any radial compressor is in the hub. This means that if this test was successful, development for adding blades could be considered further. The hub mold was first modeled in CAD, as shown in Figure 84. The com-
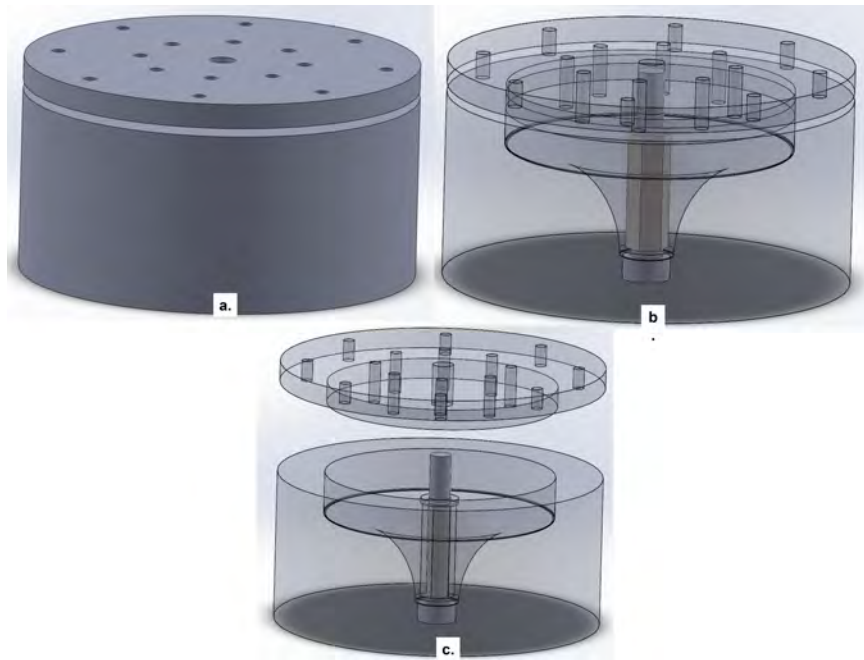
Figure 84. Compressor Hub Mold a) Opaque b) Transparent c) Transparent, Lid Up

pressor hub mold contains jack screws on the lid to aid in post-processed extraction. This model was then made into a physical part comprising of Stainless Steel, as shown in Figure 85a. The aluminum sleeve was installed into the mold as shown in Figure 85a prior to the addition of the epoxy, and thus the insert was molded directly into the hub. Epoxy-carbon fiber blend was mixed and inserted into the mold negative as shown in Figure 85b-c. The blend was comprised of 152g of Epoxy Part A, 121g of Epoxy Part B, and 30g of carbon fiber with a total mass of 304g with 10% carbon fiber reinforcement. The mixture was compressed in the 30 ton Wabash Press. It was
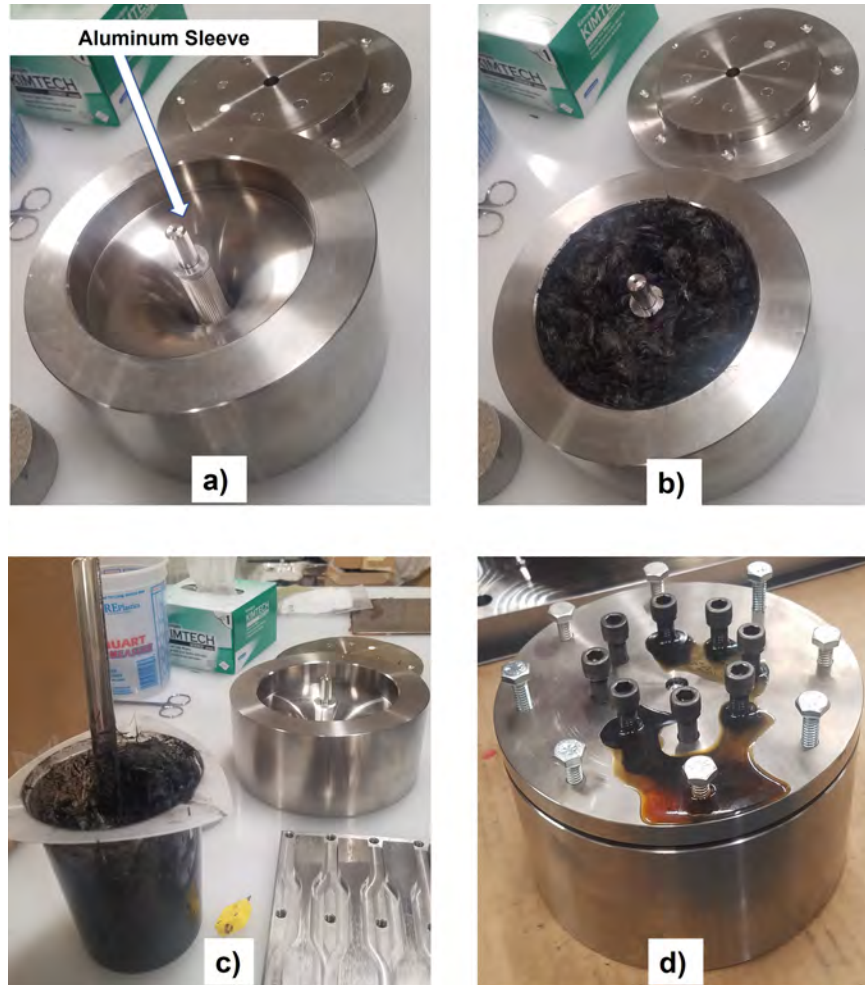
Figure 85. Compressor Hub Mold Processing a) Hub Mold b) Hub Mold with Epoxy c) Preparing Hub Mold for Processing d) Post-Compression Hub Mold

then removed and cured in the oven shown in Figure 60 under the same cure cycle as discussed in Section 3.1.2. The post-cured part inside the mold is shown in Figure 85d. Some leakage can be observed from the inner screw holes in Figure 85d.

The hub mold was released first by removing the lid to expose the compressor hub, as shown in Figure 86a. The axle pin was then removed and the part was pressed out as shown in Figure 86b-c.

Figure 86. Compressor Hub Mold Post-Processing a) Lid up, Hub Exposed b) Hub Removed c) Hub multi-view

Figure 86a indicates some surface voids on the exit side of the hub. The inlet face shown in the multi-view of Figure 86c indicates fewer voids and more of an uneven surface finish. The surface voids in the back face of the hub are not problematic as the back face needed to be machined regardless to adjust the final compressor geometry. The slightly uneven surface finish and successful removal of the hub one piece proved that the molded compressor hub was usable for spin testing.

3.4 Spin Testing

3.4.1 Turbocharger Test Stand.

The Garrett GTX5008R turbocharger was selected to drive the sample compressors due to the similar scale and geometry to the P400 compressor. A turbocharger was chosen because any electric motor would have a hard time driving a 140kW compressor up to 98 kRPM, discrediting it as a practical alternative for full speed, pressurized tests [24]. The turbocharger configuration used in the present study differs from Bauer's rig in previous studies, which included an inlet pipe, exit pipe, and shroud around the compressor. However, these components were removed for this study to verify if the compressor could first operate at ambient temperature with no compression. Inclusion of a compressor shroud constricts the fast moving air to the volume of the inlet/exit pipe line, which causes a build up of pressure and temperature during operation. This is in contrast to operation without the shroud and dispersing the air flow out into the atmosphere. Investigating a compressor's viability at ambient pressure and temperature indicates whether or not the compressor's performance merits further investigating with the shroud attached and pressure and temperature effects included. Removing the shroud isolates the stresses due to centrifugal loads or rotational speed only. Should a compressor survive a high enough speed that useful compression could be obtainable, the configuration with all components was planned to be attempted after to evaluate compressor performance.

The turbocharger test stand was located and operated at 7th Street, Building D (Dbay) on Wright-Patterson Air Force Base. The centrifugal compressor test stand is operated by passing pressurized air through the turbocharger turbine which in turn rotates the P400 compressor made of the materials of interest. There were two sources of air that drove the test stand operation: low-pressure and high-pressure air. Figure 87 shows the entire airflow system of low and high-pressure air leading into the inlet

and exit of the turbocharger.
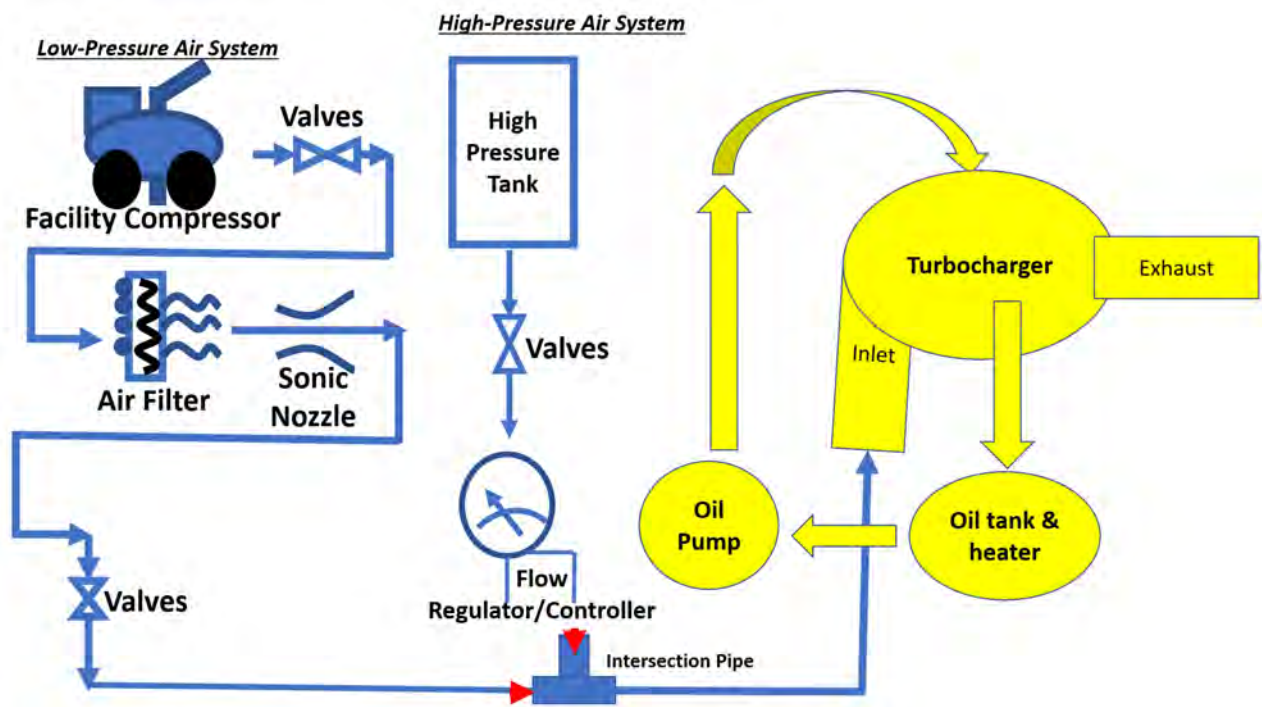
Figure 87. DBay Air Flow System

The low-pressure air system was used the most between the two air supplies and operated at low to medium rotational speeds. The low-pressure air system sources its air from a large facility compressor. The facility compressor passes the air through a series of valves and through an air filter to remove any contamination. Then, the low-pressure air passes through a sonic nozzle and through another series of vales until it reaches the intersection pipe in which it combines with the high-pressure air supply.

The high-pressure air system was used for high rotational speeds. The high-pressure air system pulls air from a facility high-pressure tank that is controlled by a series of values and a flow regulator/controller. Once air passes through both the values and flow regulator, the high-pressure air combines with the low-pressure air at the intersection pipe where they both enter the inlet of the turbocharger turbine.

126

It should be noted that the size of the sonic nozzle installed in the low-pressure air system can dictate whether it is possible for the low-pressure air to provide sufficient air flow to reach higher rotational speeds (without additional flow from the high-pressure air system). Figure 88 depicts the turbocharger test stand setup [1].
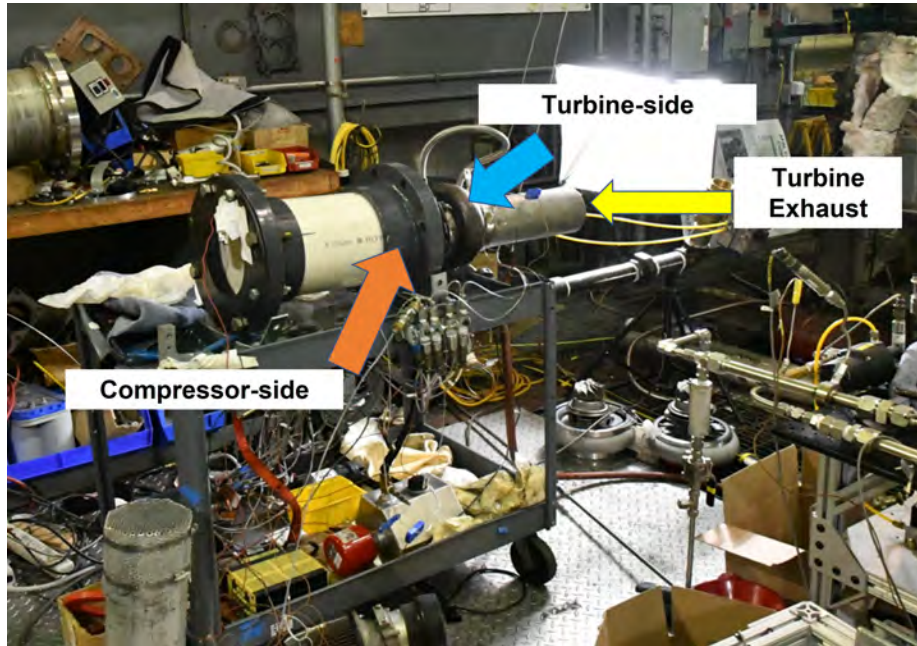
Figure 88. Compressor Test Stand

The high-pressure air transfers energy to the turbine and flows out of the turbine exit. The transferred energy is used to rotate the turbine and the compressor in turn. The air supply can provide above 0.69MPa (100 psig) of pressure, above 2 kg/s of flow rate, and above 450K of flow temperatures. The energy transferred from the turbine drove compressor rotation (which rotated the air around it). While the turbine side has inlet and exit pipes and a volute, the compressor side of the rig only had a large protective Polyvinylchloride PVC pipe. This large PVC pipe was only installed as a safety measure. Should a catastrophic incident happen, the large pipe would protect the surrounding environment from damage. Figure 89 visualizes the inlet and exhaust pipes for the turbine. The turbine intake pipe in Figure 89b was
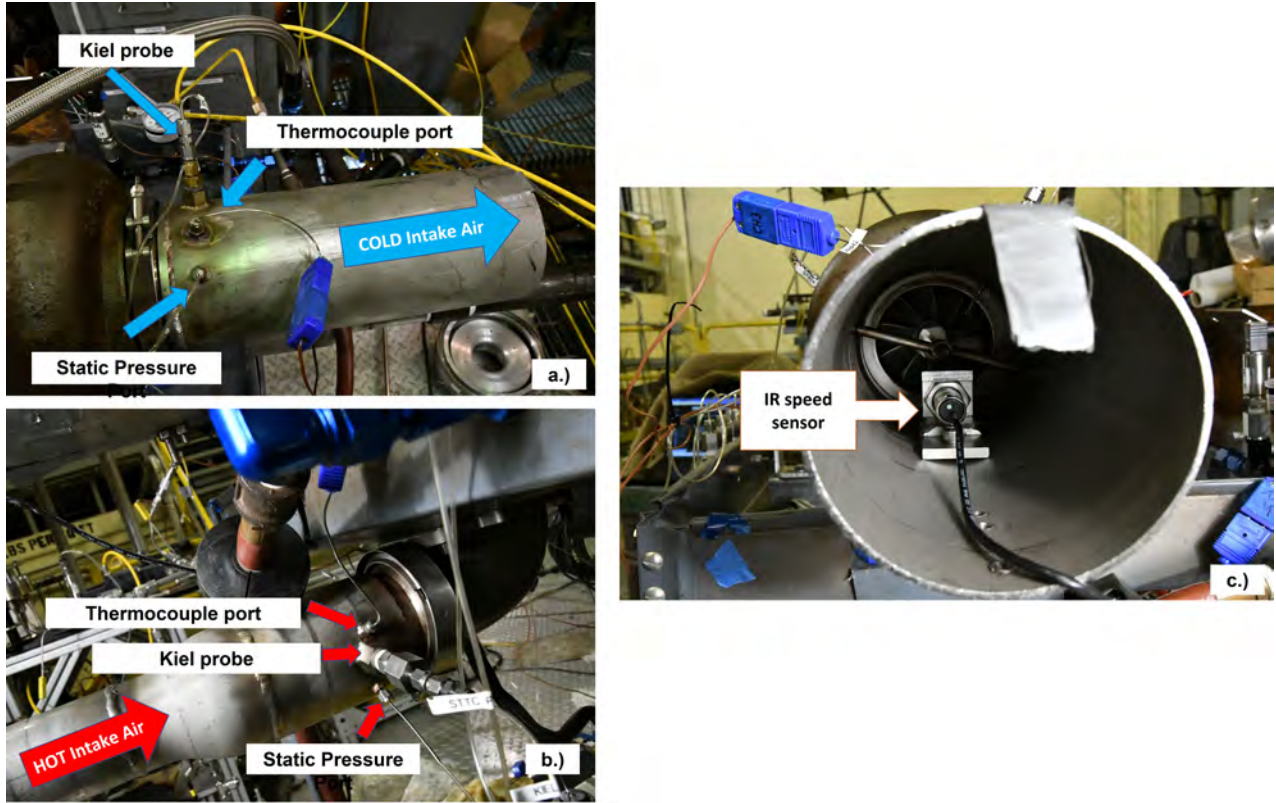
Figure 89. Test Stand Turbine Air Exhaust, Exhaust from Back, and Intake.

connected to the expander section by two pipes welded together, of which one was a 75mm diameter and 150mm long steel pipe and the other was 50 mm in diameter and 150mm in length. Three sensors were mounted to collect data at the intake of the turbine as shown in Figure 89a. The top sensor is a T-type thermocouple. The thermocouple was mounted radially, pointed toward the center of the pipe, and sticks in the flow path. This type of thermocouple is accurate for temperatures between 75-645K making it suitable for this application. It is accurate to $\pm 0.75\%$ of the measured value and has a response time of 0.6 seconds [97]. This thermocouple measured flow temperature radially based on the diameter of the junction, but also the temperature augmented by axially flowing velocity. Therefore, the thermocouple's measured value integrates both static and total temperature [1]. The middle sensor was the Kiel

probe. It measured stagnation pressure and was placed similarly to the thermocouple with the addition that the Kiel probe opening faced toward the incoming flow. The probe measures a pressure range of 0-250 psia with an accuracy of ±0.05%. The bottom sensor was a static pressure sensor. The porthole housing the sensor was made to be small enough to prevent disruption of the flow while also allowing a static pressure sensor reading. The pressure gauge attached to the port measured a pressure range of 0-250 psia with an accuracy of ±0.02% [98]. The Kiel probe and static pressure port were connected to a differential pressure sensor that had a much finer measurement read of 15±0.012 psig in the difference between the two sensor readings. This differential pressure measurement provided the difference between the two sensors so that the total pressure could be determined. Under the assumption of a linear velocity profile in the pipes, the velocity and mass flow rate of the incoming air could be calculated [1].

The turbine exhaust (Figure 89b) was built with a steel pipe of 120 mm in diameter, and 330 mm in length [1]. The same sensors present at the intake side were also attached to the exhaust. The Kiel probe, T-type thermocouple, and static pressure gauge were connected in a similar manner. The only difference was that a different transducer was installed (0-50±0.04 psia) [1] [99].

The infrared IR speed sensor in Figure 89 was a Monarch Instrument ROS rated to measure rotation speeds between 1-250,000 RPM [100]. The IR interruption sensor was installed at the exhaust side of the turbine to measure the rotational speed of the turbocharger shaft. Since the turbine and compressor were mounted on the same shaft, the turbine's rotational speed is understood to be the same as the compressors and is a sufficient reference for measurement. It is common practice to use a magnetic flux sensor to detect rotational speed instead of an IR speed sensor. However, the application of a polymer compressor prevented measuring any magnetic flux. In

addition, the cooler turbine supply gas made it possible to place a sensor at the location of the turbine exit, as is depicted in Figure 89 without fear of overheating. The IR speed sensor was configured so that it was pointing toward reflective tape attached to one of the turbine blades. The protective compressor PVC piping is depicted in Figure 90a. The turbocharger shaft was 9.47 mm in diameter and 57.7 mm in length. This was a crucial measurement because the polymer compressor bore, or aluminum hex sleeve, had to be sized within an appropriate clearance to be securely mounted onto the shaft.
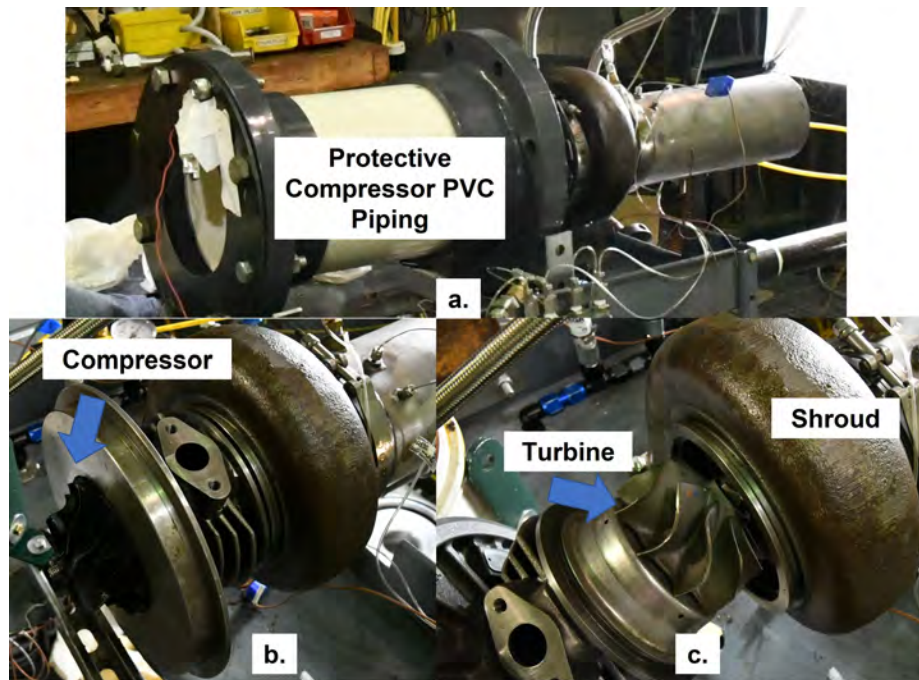
Figure 90. GTX5009R Turbocharger a) Protective Compressor PVC Piping. b) Polymer-based Compressor. c) GTX5009R Turbine and respective housing.
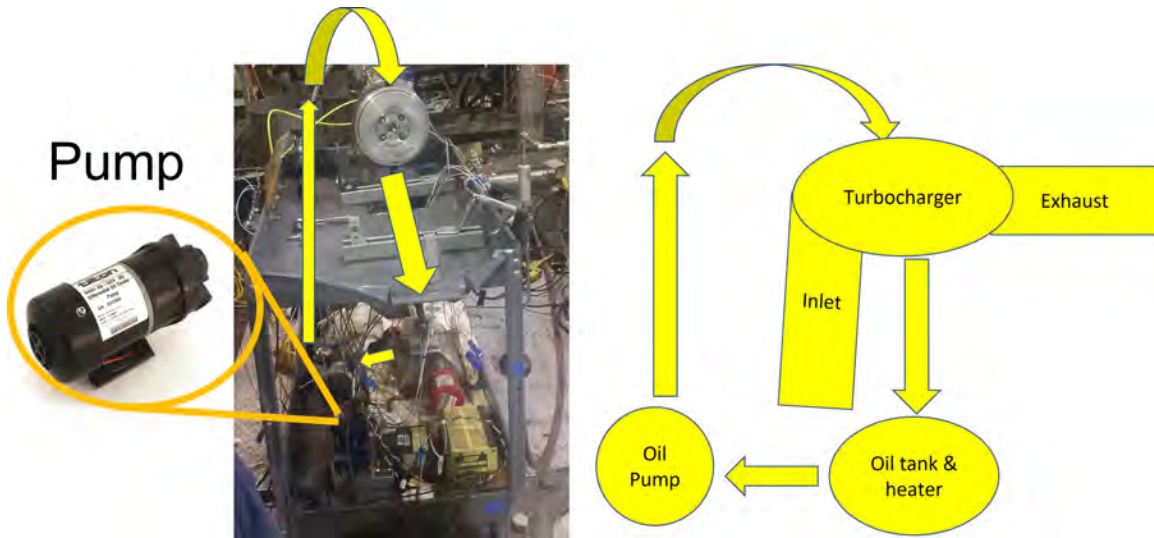
Figure 91. Oil Pump System

The oil lubrication system (Figure 91) was driven by gravity which requires the turbocharger to be mounted above the oil reservoir. The oil sits in a tank that is heated up to approximately 320K. An oil pump pulls the oil out of the tank up to the top of the turbocharger and ejects the oil into the turbocharger. Some of the oil travels into the turbocharger shaft for lubrication and the rest drains down into the oil tank to repeat the process [1].

The last details to discuss on the test stand are two existing safety features designed to help prevent certain failures based on lessons learned from previous work. The first safety feature to the test stand is a "three-way, double-acting pneumatically actuated ball valve" [1] shown in Figure 92. Prior to the addition of this second ball valve, upon compressor failure, there was a one second span between pressure loss to turbine overspin. The second ball valve has a cycle time of 0.12-second [101], which allows high-pressure air to vent and stop the turbine quick enough to avoid another turbine from flying out of the turbocharger. The second safety feature was a bolt welded behind the turbine (Figure 93) to prevent another turbine ejection out of the turbocharger. An inhibitor is inserted into the hole in the center of the bolt. Should

Figure 92. Safety Feature on Test Stand: Pneumatic Three-Way Globe Valve.

Figure 93. Turbine Axial Motion Inhibitor

the turbine begin to move in the axial direction, the bolt would slow down turbine rotation and stop turbine axial motion [1].

3.4.1.1   Compressor Balancing.

A crucial part of the manufacturing sequence, before actual testing, was balancing. If an object with uneven mass distribution rotates, the imbalance will produce a force along the plane of rotation. An uneven mass distribution causes a misalignment between the center of mass (COM) and the axis of rotation. As a result of natural imbalances due to asymmetric printing and molding about the compressor axis of rotation, the compressor installed on the turbocharger assembly required balancing on a balance machine at Air Force Research Lab, Building 490. Balancing assured that the entire turbocharger was balanced to G-6.3 Standards.

An imbalance causes forces to change direction when the mass rotates about an axis which generates oscillating stresses. These oscillating stresses can cause failure by three mechanisms: internal cyclical loads, excitation of the natural frequencies during angular acceleration, and localized stress that exceed maximum allowable stress. In general, engines that use these types of compressors operate by quickly reaching full speed and sustaining that speed for an extended period of time. Such an operation sequence renders the first two mechanisms less problematic to the third. The working materials for this study were expected to operate very close to their ultimate strength, which means that marginal increases in local stress may cause structural failure.

For AM methods, and similarly for molded materials, imbalances could be created due to the asymmetric material deposition around the compressor's axis of rotation. Excess material or voids at any location on the compressor will misalign the center of mass relative to the center of rotation. To realign the two "centers", a particular amount of mass must be removed at a particular location on the compressor. The

exact amount of mass for removal and at which location are not possible to determine without the use of balancing machines. The accessible balancing machines for the study have input data of the mass and diameter of the compressor as well as the turbine-shaft assembly, the nominal speed, and the quantity of turbine blades. Data about the nominal speed and mass aid in balancing relative to the G-6.3 Balancing Standard. The standard originates from ISO 1940/1 which provides standards for aircraft gas turbine rotors and is in the units of mm/s. There is a looser standard known as the G-16 test standard and is sufficient for individual components within an internal combustion engine. The tighter standard is the G-2.5 test standard and is generally for turbo-compressors and gas turbines [102]. The balance stand detects rotational speed using an IR interrupt laser (similar as the turbocharger test stand itself) to measure the rotational position while calculating the location of imbalance. The balance stand used for this study is shown in Figure 94
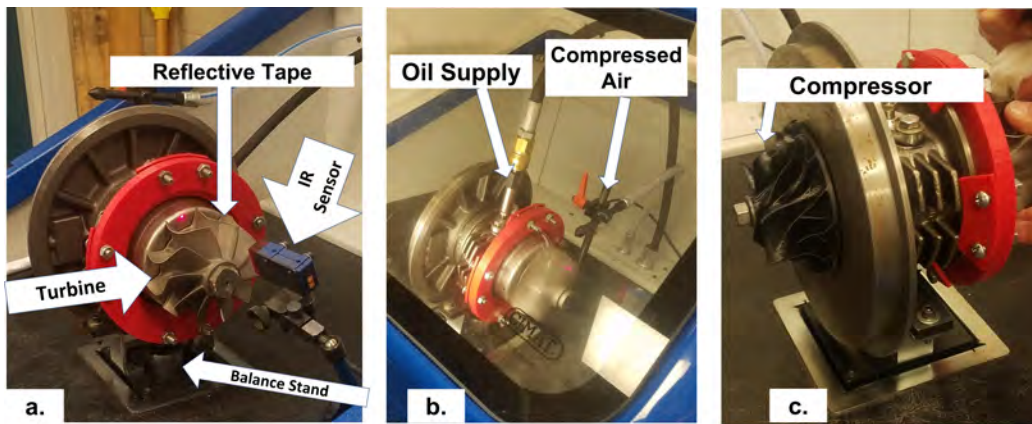
Figure 94. Compressor Balance Stand

Figure 94a contains the laser that must point at the reflective tape on the turbine to properly determine the location of imbalance. The balance stand runs compressed air through the turbine and runs oil through the turbocharger oil line to avoid dry-running, as shown in Figure 94b. The balance stand contains strain gauges and

springs to calculate the magnitude and timing of imbalances, as depicted in Figure
Figure 94c.

With this setup, the turbocharger was spun and the balance stand outputs infor-
mation about imbalancing magnitudes and directions. Figure 95a depicts the data
output of the balance stand. In this particular example from one of the ULTEM 9085
compressors for this study, the balancing machine indicates that removing 0.2054g off
of the turbine at the 0.0 degree position and removing 0.5281g off of the compressor
at the 5.4 degree position will balance the assembly. Figure 95b shows the balanced
result after mass was removed. The green circle in the image denotes the location that
follows G-6.3 Standards for balancing. In this particular example, mass was removed
from the compressor in between the blades to avoid disrupting the compressor's aero-
dynamics. The pre-balanced compressor and post-balance compressor is shown in
Figure 95c and Figure 95d, respectively. Because the compressors were all made out
of reinforced polymers, more mass needed to be taken off of the compressor to account
for the imbalance compared to the metal-based turbine side. This balancing sequence
was required for every compressor manufactured in this study.
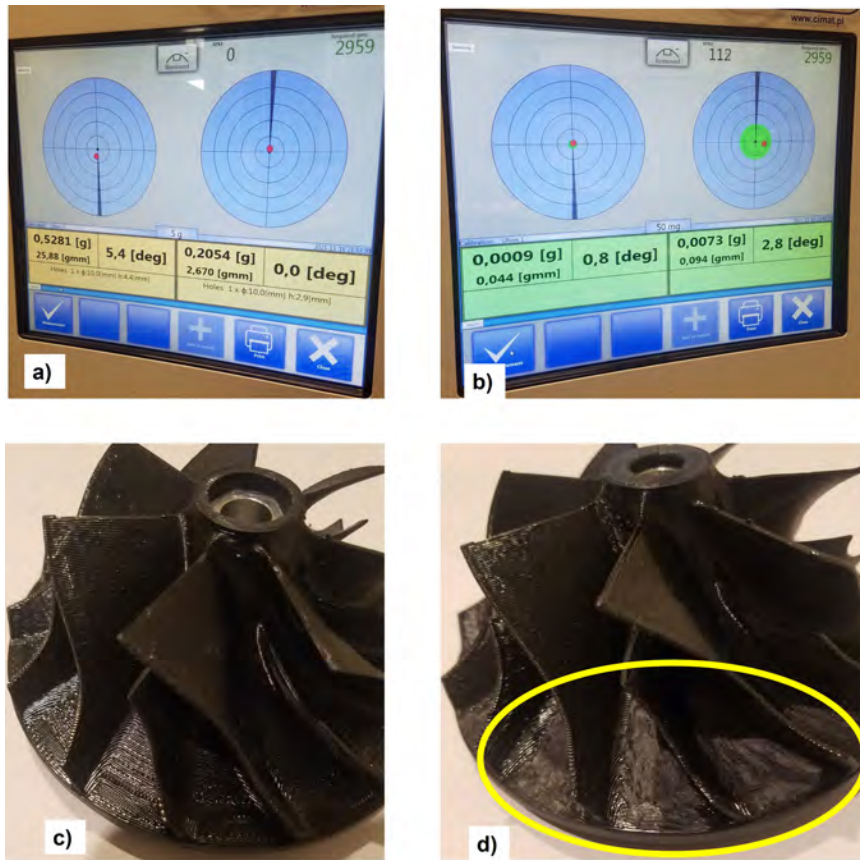
Figure 95. Balance Stand Test Results a) Before Balancing b) Complete Balancing c) Before Mass removal d) After Mass removal

IV. Results and Discussion

4.1 Material Testing

The results from the material testing of ULTEM 9085, Onyx-Carbon Fiber, and Epoxy-Carbon Fiber, are discussed individually in the following sections. Each of these materials have a dedicated section discussing manufacturing accuracy and repeatability, material property results, and failure mechanisms.

4.1.1 ULTEM 9085 Tensile Results.

There were 26 XY printed samples of ULTEM 9085. Among them, all 26 were examined, 9 of which were sacrificed for calibration or demonstrated aberrant test data, and 15 of which were data were successfully collected. All 26 specimen prints are shown below across Figures 96, 97, and 98:

Figure 96. ULTEM 9085 specimens 1 to 10

Figure 97. ULTEM 9085 specimens 11 to 20

Figure 98. ULTEM 9085 specimens 21 to 26

The mean and standard deviations for the specimen cross-section measurements are displayed in Table 12. The XY print thickness had mean measurements of $0.77\% - 1.06\%$ to the design. The width and thickness of each specimen was measured 5 times

138

to account for variability and error in the calipers used to measure the specimens.

Table 12. Measured vs. Designed Specimen Thickness (t) and Width (w), ULTEM 9085

ULTEM 9085	Design t (mm)	Design w (mm)	$\bar{t}$ (mm)	$\sigma(t)$ (mm)	$\bar{w}$ (mm)	$\sigma(w)$ (mm)
XY orientation	4	6	4.25	0.02	6.07	0.03

4.1.1.1 Material Property Results.

Figure 99 shows the stress-strain curve for the 15 XY test specimens with a summary of their mean ultimate stress and elastic modulus values shown in Table 13. The plot shows that the room temperature specimens exhibited the highest ultimate strength at an average of 67 MPa, and the ultimate strength of the material decreased at higher temperatures thereafter. The ultimate stress decreased with rising temperature. The ultimate stress faltered down to a mean of 51.2 MPa at 366 K, a mean of 25.5 MPa at 414 K, a mean of 12.7 MPa at 444 K, and eventually deteriorated to a magnitude of 1 MPa and below for temperature conditions of 475 K and above.

The elastic modulus exhibited similar behavior to the ultimate stress. The elastic modulus maximized at an average of 1226 MPa at room temperature. It also decreased with rising temperature. The elastic modulus falters down to a mean of 1078 MPa at 366 K, a mean of 1006 MPa at 414 K, a mean of 562 MPa at 444 K, and eventually deteriorating to to a magnitude of 4 MPa or below for 475 K and above. Not surprisingly, this indicates a reduction in material stiffness as temperature is increased. At 444 K, the data still exhibited a noticeable resistance in tension, while beyond 475 K the material exhibited no detectable resistance. At the hotter conditions, the material also began to exhibit a "gummy" behavior in which the applied tensile load did not cleanly break the material at a particular point. Rather, the material stretched until the load met the defined failure criterion defined in the

Table 13. Ultimate Stress and Elastic Modulus Data Summary

Temperature (K)	Temperature (^oC)	σ_u(MPa)	E (MPa)
293	20	67	1226
366	93	51.2	1078
414	141	25.5	1006
444	171	12.7	561.5
475	202	0.24	1.78
523	250	0.16	4.14

procedure (a drop-down to <75% of maximum failure, see Section 3.2.3). The room temperature and 444 K specimens exhibited the highest strain of up to 9% of the original length. The 366 K specimens exhibited the lowest strain of 6% of the original length. The highest temperature of specimens reached up to 9% strain due to the "gummy" effect when the material reached beyond its glassification temperature of 186^oC (459 K) [103].
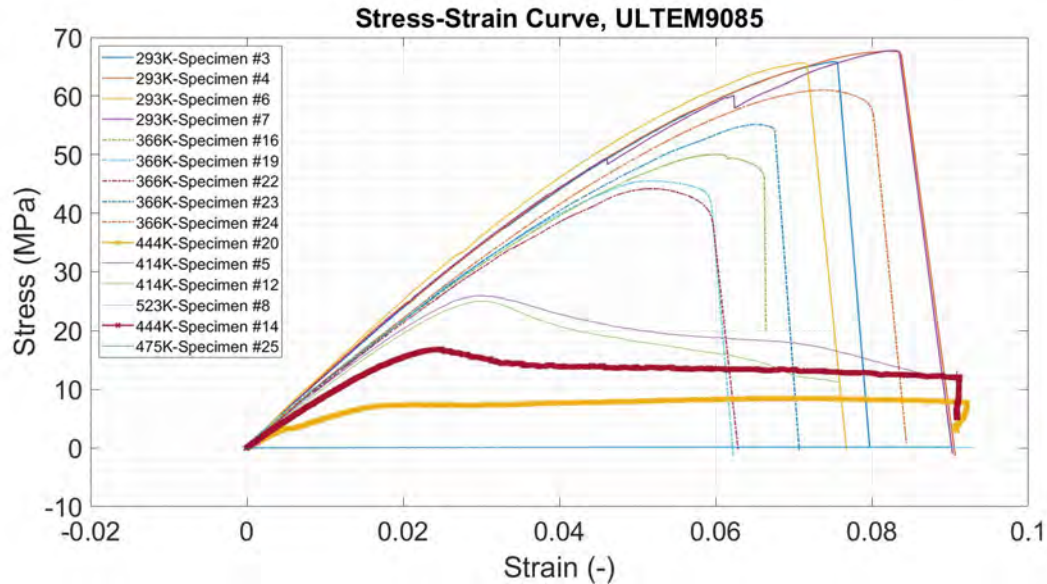
Figure 99. Stress vs. Strain Curves, ULTEM 9085 XY

A summary of the material property results is shown in Figures 100 to 102, which shows the relations between ultimate stress, elastic modulus and temperature. Figures 101 and 102 visually, shows the reduction in ultimate stress and elastic modulus

with temperature, which is consistent with the results of the stress strain curves. Figures 101 and 102 show that the published XY orientation ultimate stress and elastic modulus overestimate the magnitudes by 4.7% and 43.0% difference, respectively. The difference in both the ultimate stress and elastic modulus is nontrivial and would likely require further tests to determine if the difference is due to manufacturing settings or another source. It is possible the difference in output has to do with internal voids within the printed specimens or an inherent difference in the measurement method. The published data for ULTEM 9085 (σ_u= 70 MPa; E= 2.2 GPa) was used for comparison [103].

Figure 100. Ultimate Stress vs. Elastic Modulus, ULTEM 9085 XY

Figure 101. Ultimate Stress vs. Temperature, ULTEM 9085 XY

Figure 102. Elastic Modulus vs. Temperature, ULTEM 9085 XY

142

4.1.1.2 Confidence Interval.

Due to the difference between the published and experimental results, a brief confidence interval calculation was done for the ULTEM 9085 data. A confidence interval, CI, for a given experimental data set provides the range of resulting values that would be expected if the test we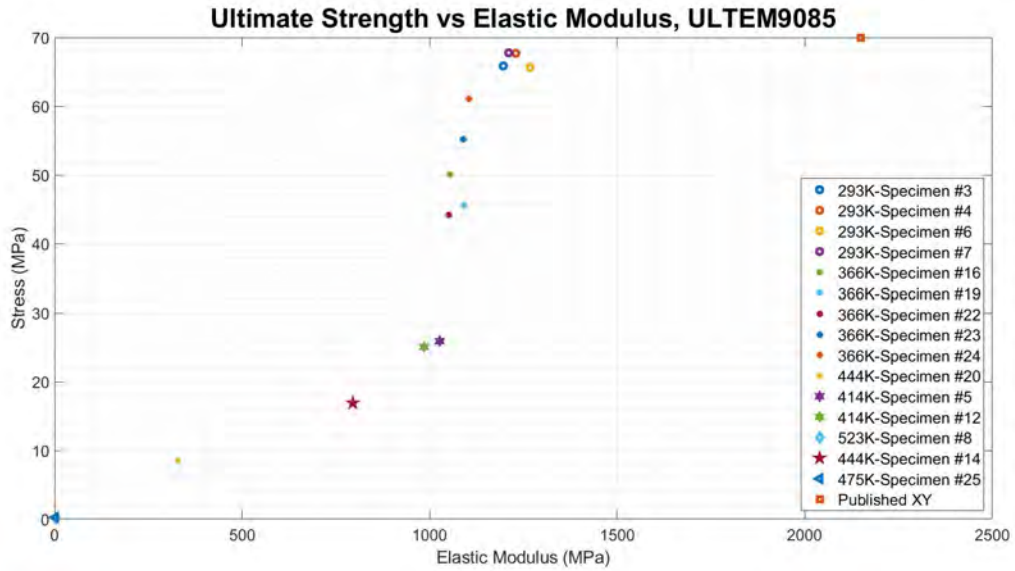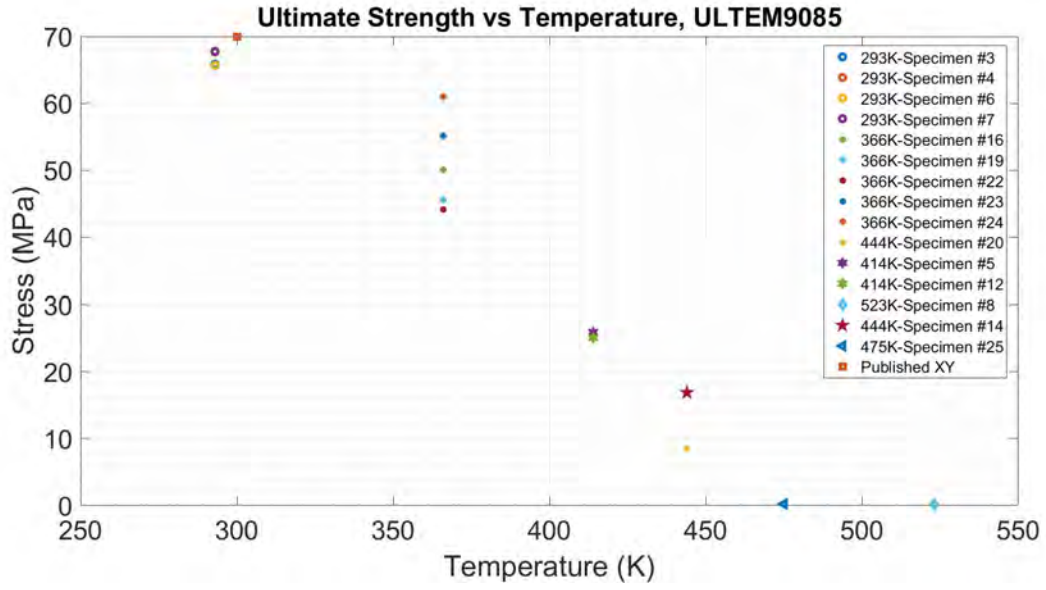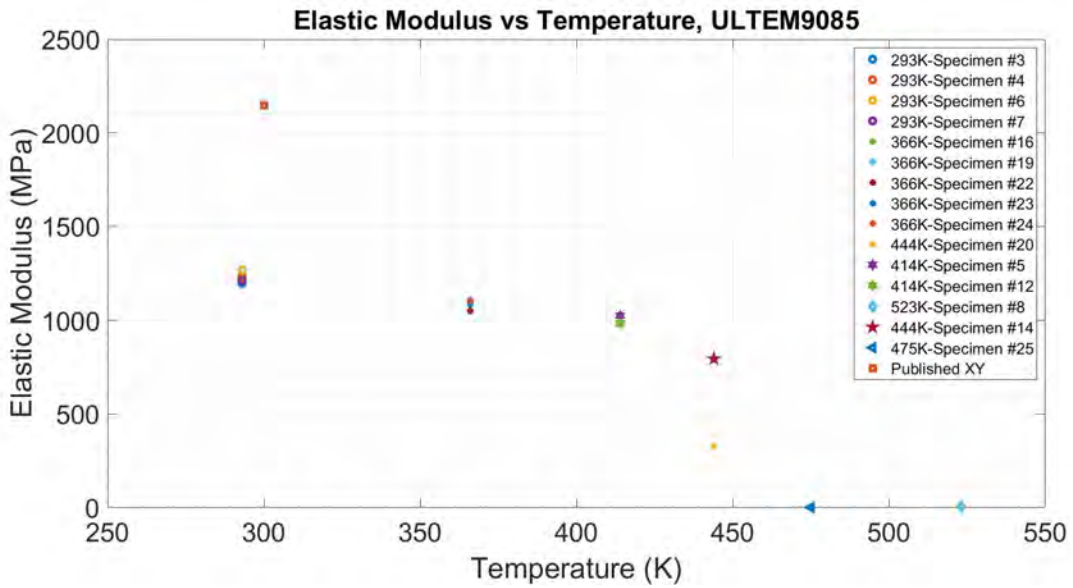re repeated within a designated level of confidence [104]. For this study, the confidence interval calculation provides an interval for the experimental data that would be the expected result if the tensile specimens were pulled again in the same MTS machine. Since the published data does not fall in this interval, it can be concluded some underlying disconnect exists between the experimental data and the published values. Equation 57 is used for the confidence interval calculation,

$$CI = \bar{x} \pm z \frac{s}{n^{\frac{1}{2}}} \tag{57}$$

where $\bar{x}$ represents the mean, z represents the z-score (for 95% confidence is 1.96), s represents the standard deviation, and n represents the number of samples. The equation with the positive indicates the upper bound of the confidence interval and the equation with the negative indicates the lower bound. The 95% confidence interval is often used in practice. With the 95%, one can deduce that there is a 95% chance that the result would be in the calculated range if the experiment was repeated. For the ULTEM 9085 batch (room temperature sample size of 5 specimens), the 95% confidence interval for the ultimate strength is within the bounds of 66.8 and 66.6 MPa. The published value for ULTEM 9085 ultimate strength is 70 MPa which is outside of the confidence interval. This means that there is some disconnect between the experimental and published data. It is likely that the published data assumes bulk properties. This means that the published data expresses properties in the form of a 100% infill monolithic bulk mass which behaves differently than an AM hollow mass or thin fibers. It is likley that the published values do not account for the variability

143

in 3D printing ULTEM 9085. The confidence interval and published ultimate stress is tabulated below for convenience in Table 14.

Table 14. Confidence Interval for ULTEM 9085

	Published Data	CI Lower Bound	CI Upper Bound
ULTEM 9085 σ_u (MPa)	70	66.6	66.8

4.1.1.3   Polymer Failure Results.

Images of the internal component of the gauge section (Figure 103) indicate that the ULTEM 9085 survived the room temperature tests without any issues with thermal deformation. At lower temperatures (293-354 K), the specimens behaved as a stiff polymer, often fracturing specimens into two distinct pieces. At the high temperatures (414-475 K+), specimen deformation was apparent, which indicated ULTEM 9085 is glassifying closer to P400 operating temperature. Closer to 414 K, the deformation was enough to keep the print pattern on the specimen visible. Once reaching temperatures above 414 K, the print pattern thermally deforms to the point that it blends with the specimen altogether like a "gummy" behavior. This indicates glassification at the higher temperature regimes.
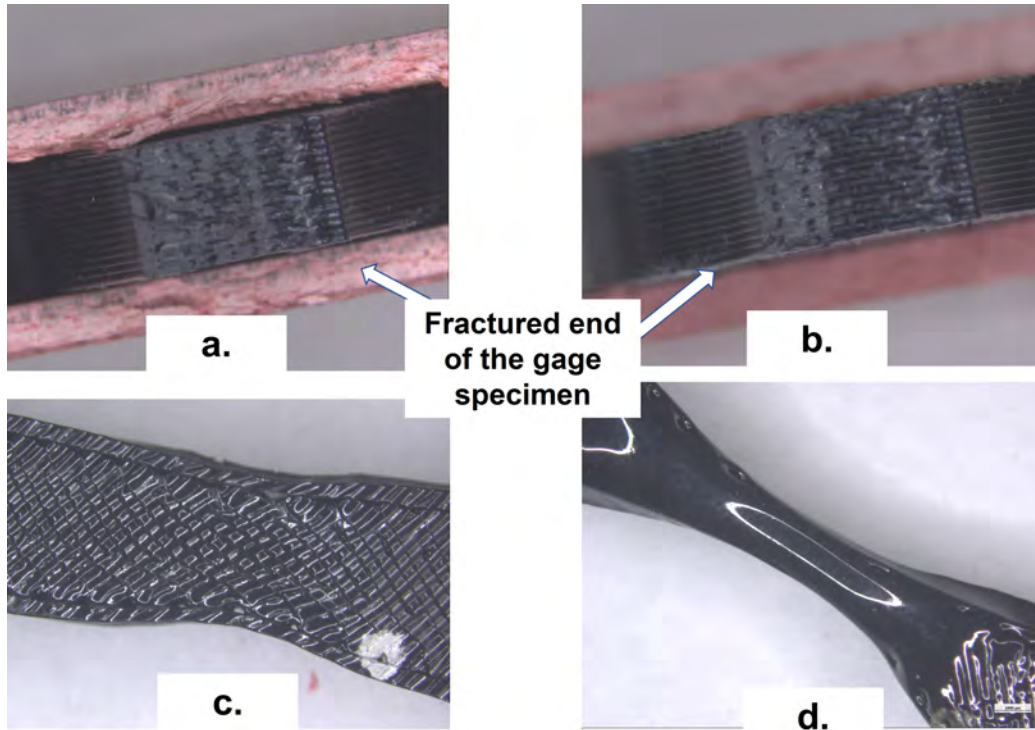
Figure 103. ULTEM 9085 Specimens. a) Specimen 6b, 293 K b) Specimen 23b, 354 K c) Specimen 20b, 414 K d) Specimen 8, 475 K

4.1.1.4 Material Data.

The material properties found for ULTEM 9085 and used for the FEA SolidWorks model are shown in Table 15. The reported elastic modulus and ultimate strength are the average values of the tensile test results for each temperature. The FEA model was simplified by assuming isotropic behavior for the ULTEM 9085. The density (ρ), thermal conductivity (k), Poisson's ratio (ν), and coefficient of thermal expansion (α) were all assumed constant based on published values.

Table 15. ULTEM 9085 Tensile Results

Temperature	293 K	366 K	414	444	457	523
σ_u, MPa	66.7	51.2	25.5	12.7	0.2370	0.1550
E, MPa	1226	1078	1006	561.5	1.78	4.14
α, μm/m-K	65.3 [105]					
ρ, kg/m^3	1,270 [106]					
k, W/(m*K)	0.22 [107]					
ν	0.36 [108]					
GTT (K)	459 [109]					

4.1.2 Onyx-Carbon Fiber Tensile Results.

The second material examined was a blend of chopped-carbon fiber and nylon, proprietarialy known as Onyx by Markforged. Published information about the GTT of Onyx has proven to vary significantly. Markforged does not publish the GTT of Onyx on their website, so most studies have measured it with their own methods. One study documents the GTT of Onyx to be close to room temperature [110]. Another study measured 47°C (320 K) [111] while another source measures 65°C (338 K) [112]. Two other sources that seem to provide the most reasonable answers measure 135°C (408 K) [113] and 172.7°C (445 K) [114]. Even with the highest measure for GTT, Onyx-Carbon fiber was expected to melt prior to hitting the P400 operation temperatures.

This material was known have a weaker ultimate strength at high temperatures than other competing polymers of this study, given that it is known to have a lower glass transition temperature. However, the benefit of using Onyx is the ability to reinforce it with continuous fiber (i.e. carbon fiber in this study), which could significantly increase the composite ultimate strength. The increase in ultimate strength

depends on how much carbon fiber is used relative to the Onyx in each print. As mentioned in Section 3.1.1, three combinations of Onyx-carbon fiber percentages were tested, 49O51C, 54O46C, and 35O65C. These specimens were printed in the sequence also described in Section 3.1.1. There were 20 prints for Onyx-Carbon Fiber. Among them, 10 were 51C49O, 5 were 46C54O, and 5 were for 65C35O. An additional 5 specimens of 46C54O and 65C35O initially existed, but those specimens were destroyed during mechanical calibration, and valuable data was not collected from their tensile pulls. Of the 20 prints tested, 9/10 for 51C49O, 4/5 for 46C54O, and 5/5 for 65C35O were successful. The tested specimens are shown below in Figure 104 with measurement of the samples for mean and standard deviations for the Onyx-Carbon fiber specimen cross-section displayed in Table 16. The 46C54O prints had mean
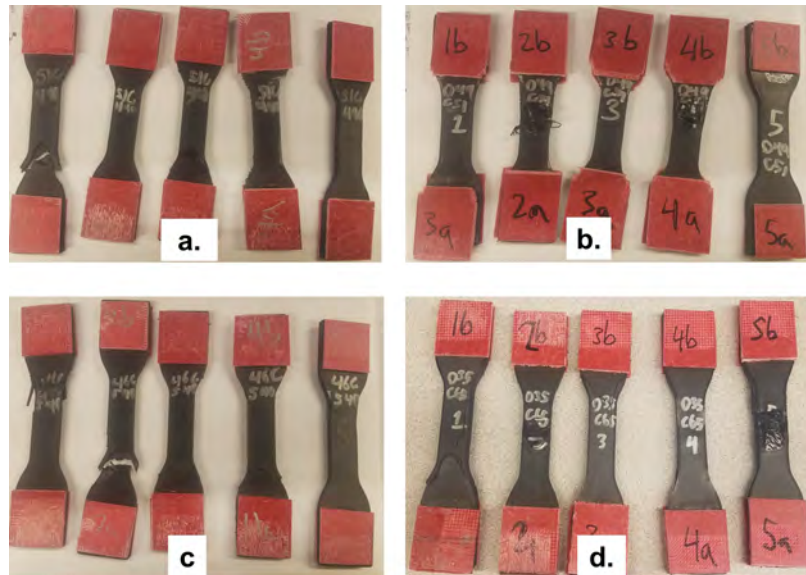

Figure 104. Onyx Specimens a) Onyx 51C49O batch 1 b) Onyx 51C49O batch 2 c) Onyx 46C54O batch 1 d) Onyx 63C35O batch 1

thickness measurements $0.72\% - 1.04\%$ to the design and mean widths that were $0.53\% - 0.58\%$ to the design. The 51C49O prints had mean thickness measurements $1.43\% - 1.20\%$ to the design and mean widths that were $0.55\% - 0.74\%$ to the design.

147

Table 16. Measured vs. Designed Specimen Thickness (t) and Width (w), Onyx-Carbon Fiber

Onyx-Carbon Fiber	Design t (mm)	Design w (mm)	$\bar{t}$ (mm)	$\sigma(t)$ (mm)	$\bar{w}$ (mm)	$\sigma(w)$ (mm)
46C54O	4	14	4.09	0.03	14.4	0.05
51C49O	4	14	4.11	0.03	14.4	0.05
65C35O	5	14	5.10	0.5	14.3	0.2

The 65C35O prints had mean thickness measurements $1.28\% - 1.34\%$ to the design and mean widths that were $0.24\% - 0.27\%$ to the design.

4.1.2.1   Material Property Results.

Among the materials tested in this study, Onyx-Carbon fiber was the strongest with a higher ultimate strength than both ULTEM 9085 and Epoxy-Carbon fiber at room temperature. As a result, it was expected to perform the best at low temperatures. Since it is predominantly made out of nylon, Onyx-Carbon fiber is the least thermally capable material among the three tested and was expected to perform the worst at higher temperatures. Figure 105 shows the Onyx-Carbon fiber tensile test data. Data for 54O46C was not investigated beyond 366 K because it contained the lowest amount of reinforcement and was assessed to be of less interest in terms of performance. 35O65C data represented the highest reinforcement that could geometrically fit into the specimen geometry and was characterized over the full range of temperatures alongside 49O51C. At 293 K, the 35O65C and 49O51C specimens failed with a 13% difference in ultimate strength between each other. Figure 106 compares the tensile data with published results. Since Markforged publishes their Onyx and carbon fiber properties independent of one another, assumptions were made to approximate the properties by applying the Rule of Mixtures (See [115]) demonstrated by Equation 58 where E represents the property of interest (could be σ_u, ρ, etc) and ν is the material volume fraction. This same process has been used for ultimate

strength estimations as well for measuring other forms of reinforcement (i.e. circular glass fiber reinforced polymers [116]). Equation 58 should only be used for materials with unidirectional reinforcement. The published values for Onyx (σ_u= 40 MPa;E= 2.4 GPa) and the continuous carbon fiber produced by Markfoged (σ_u= 800 MPa;E= 60 GPa) are used for the Rule of Mixtures estimation [78].

$$E_{total} = E_{fiber} v_{f,Fiber} + E_{matrix} v_{f,matrix} \qquad (58)$$
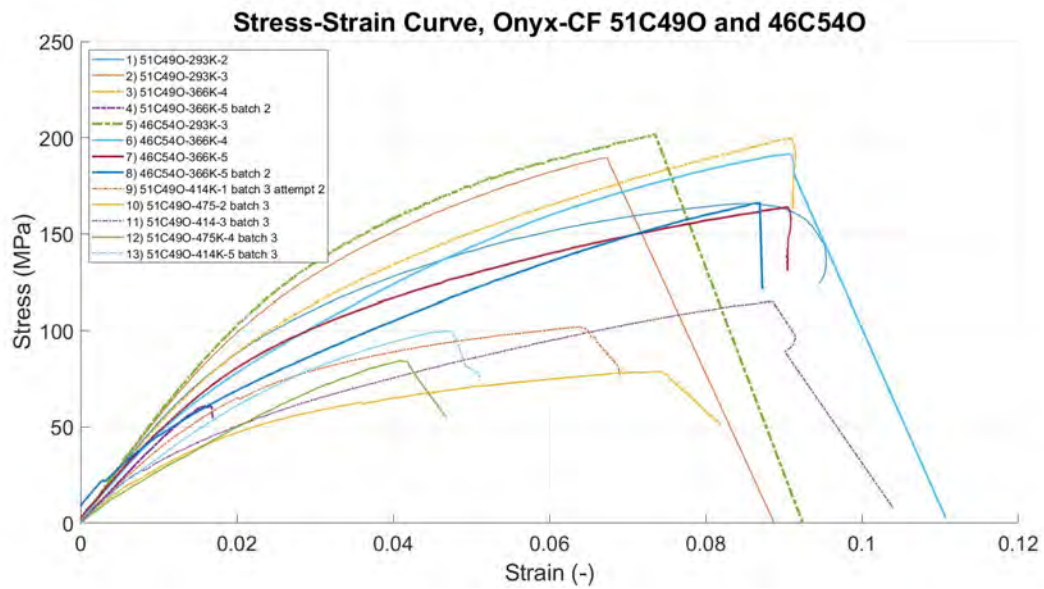
Figure 105. Stress vs. Strain Curves, Onyx-Carbon Fiber

Figure 106. Ultimate Stress vs. Elastic Modulus, Onyx-Carbon Fiber

Figure 107. Ultimate Stress vs. Temperature, Onyx-Carbon Fiber

150

Figure 108. Elastic Modulus vs. Temperature, Onyx-Carbon Fiber

Figure 109. Stress vs. Strain Curves, Onyx-Carbon Fiber 65C35O

151

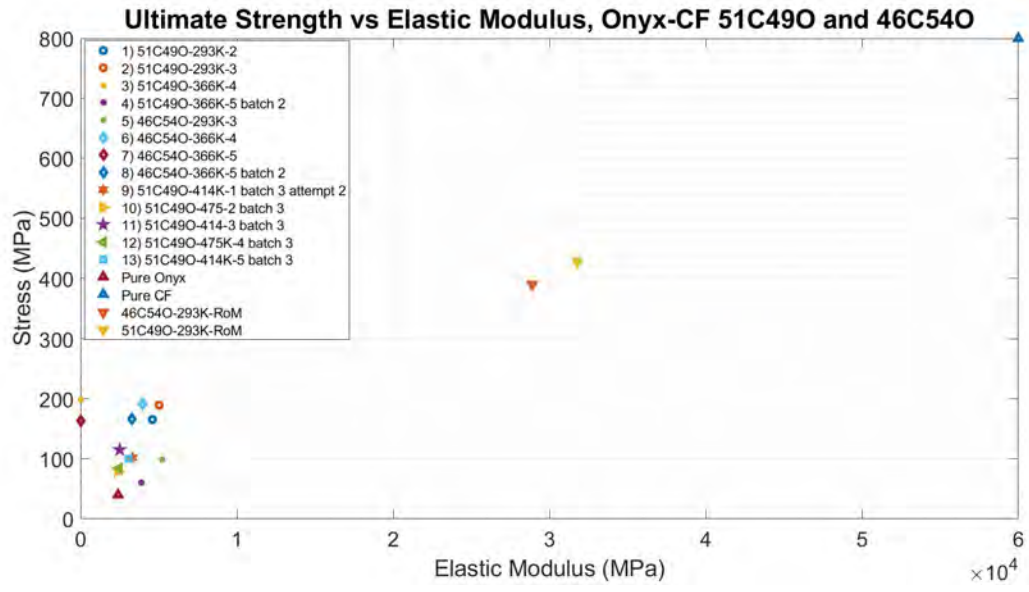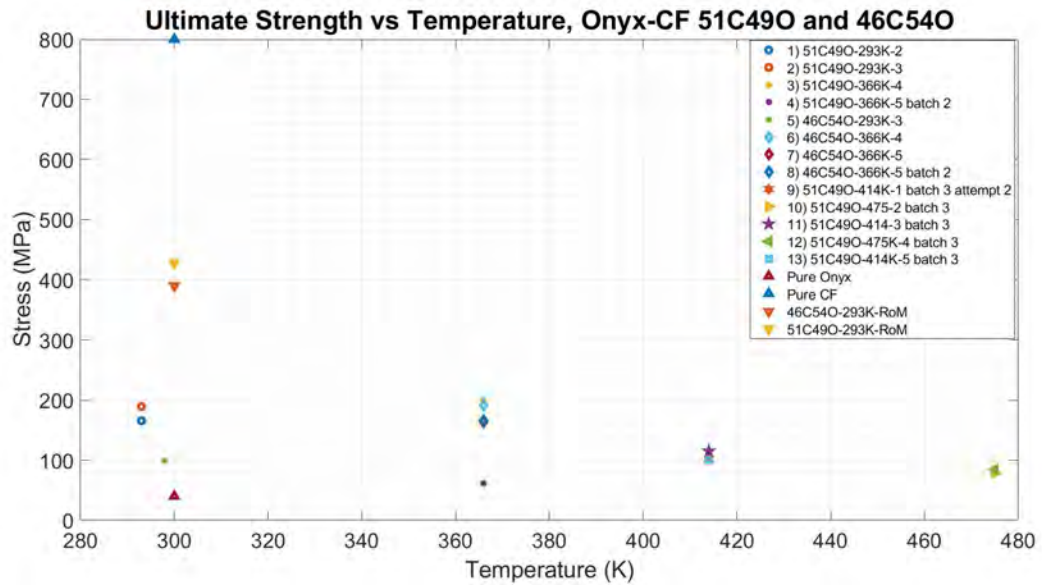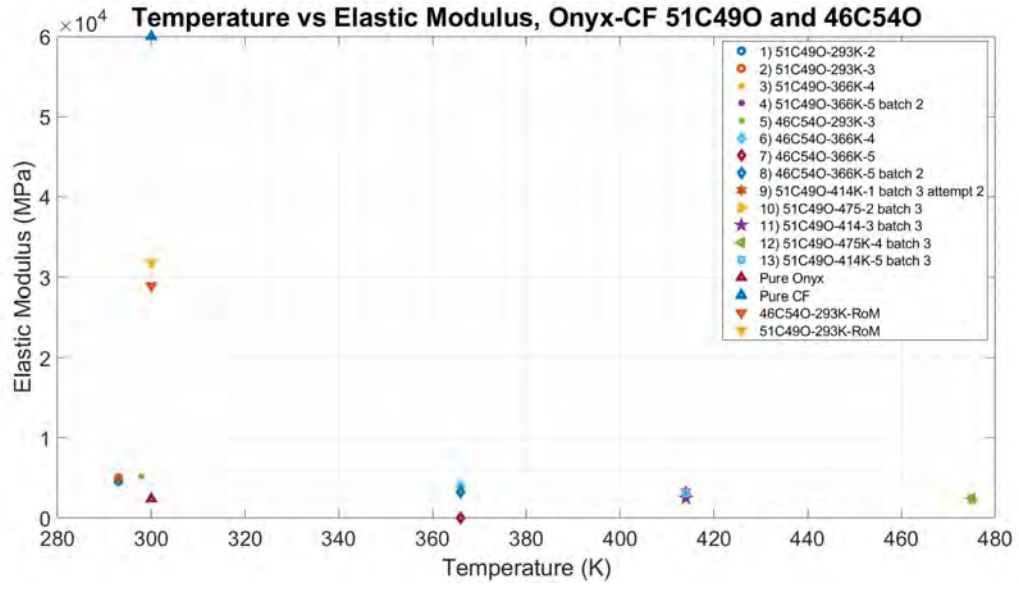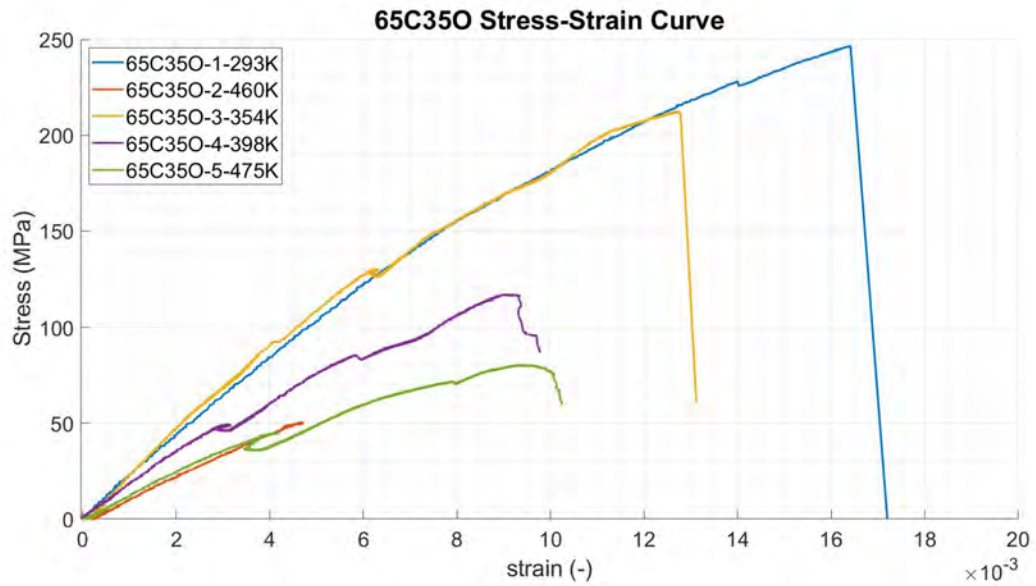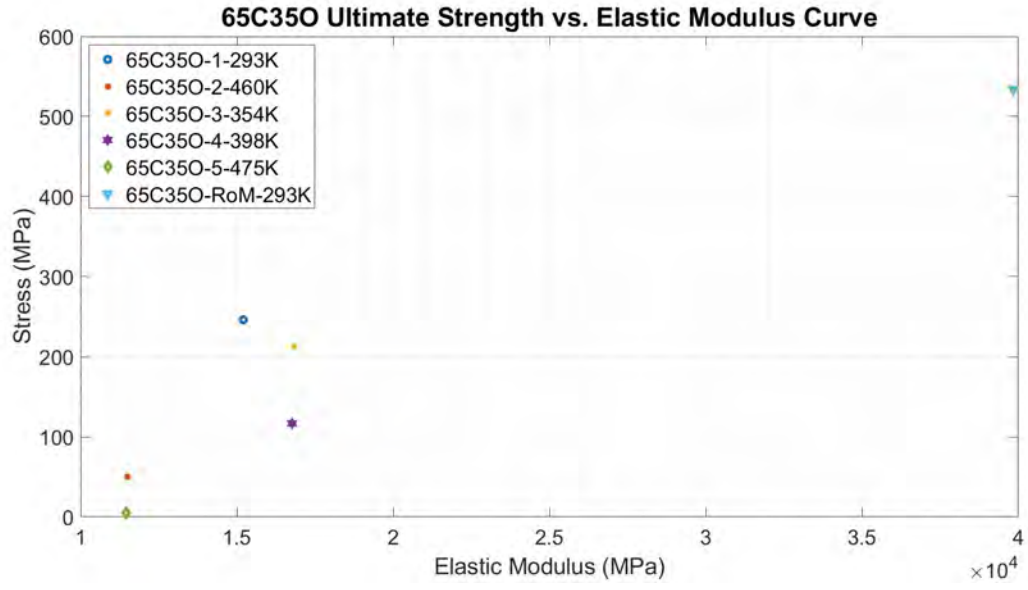**Figure 110. Ultimate Stress vs. Elastic Modulus, Onyx-Carbon Fiber 65C35O**
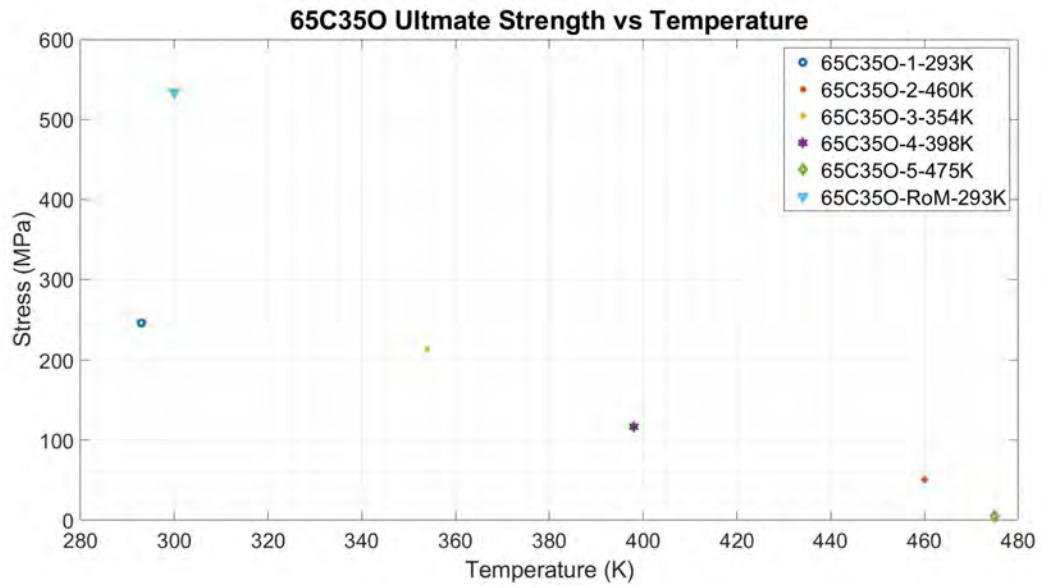
Figure 111. Ultimate Stress vs. Temperature, Onyx-Carbon Fiber 65C35O

152
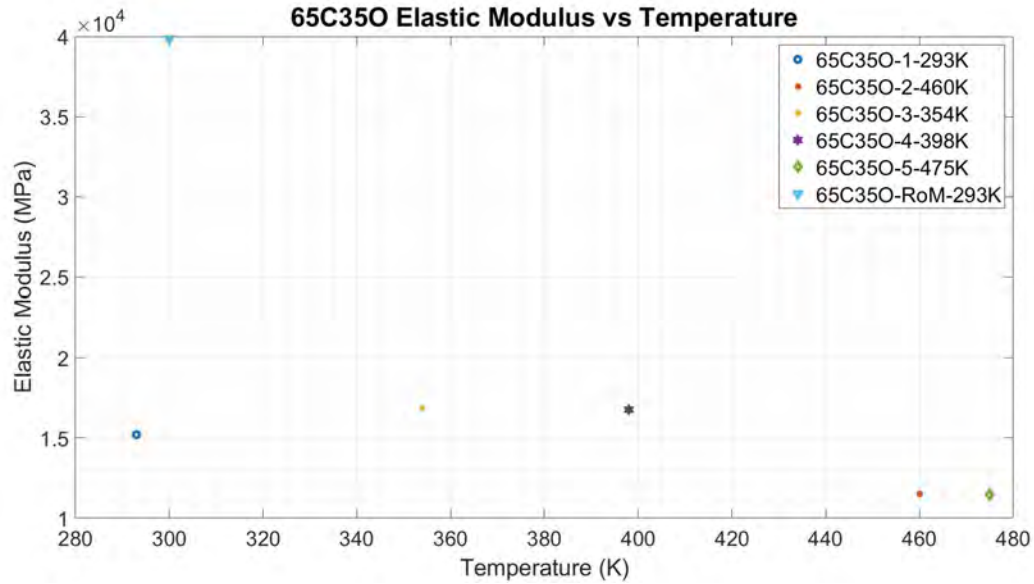
Figure 112. Elastic Modulus vs. Temperature, Onyx-Carbon Fiber 65C35O

For the 49O51C data, room temperature results yielded a significant difference from documented strength properties with a 58% difference in ultimate strength and 85% difference in elastic modulus relative to the Rule of Mixtures (which was based on published values). The 54O46C and 35O65C produced similarly stark differences with the 54O46C data producing a 74% difference in ultimate strength and 82% difference in elastic modulus relative to the Rule of Mixtures, while the 35O65C data produced a 54% difference in ultimate strength and 62% difference in elastic modulus relative to the rule. The fact that all carbon-fiber percentage groups had a consistent order of magnitude in difference could imply underlying manufacturing variability in Onyx printing. These room temperature difference magnitudes are larger than that of the ULTEM 9085 specimen values which implies that Onyx is less reliable in terms of its consistency between published values and actual printed specimens. Further studies with a larger specimen count would be required to investigate that subject further.

Figure 107 for 49O51C and Figure 111 for 65C35O indicates a reduction in

strength at higher temperatures, which is expected. Despite Onyx's reputation for being a weaker ultimate strength at high temperatures, reinforced Onyx still exhibited observable resistance to tension even at higher temperatures. Both the 49O51C and 65C35O remained higher in ultimate strength than the ULTEM 9085 strength values even at P400 operating temperatures. However, this phenomenon is almost certainly due to the reliance on reinforcement in the composite material. This can be concluded based on the fact that Onyx's ultimate strength without reinforcement (40 MPa [78]) is already half that of the σ_u of ULTEM 9085 which makes it impossible for Onyx to exceed ULTEM 9085 without the reliance of carbon fiber reinforcement (800 MPa [78]). Figures 108 and 112 display the quantitative data regarding the elastic modulus as a function of increasing temperature. The stiffness for 49O51C does not seem to display a particular pattern with rising temperature while 65C35O specimens seem to increase in stiffness up to 400 K before dropping down at larger temperatures. More specimen tests would need to be conducted to investigate that phenomenon further.

Between individual specimen groups in 49O51C, the two 366 K specimens failed with a 106% difference in ultimate strength between each other with a standard deviation of 98.1. This difference is extremely high, and the variation in data can be attributed to a manufacturing variability with 3D printing. Further tensile testing would be required to understand how much variability was in effect between the two specimens. The 414 K and 475 K specimens had a lower standard deviation of 8.3 and 6.9, respectively, which likely indicates less manufacturing variability. More 35O63C specimens would be required to further investigate that group of prints for similar variability issues.

4.1.2.2   Confidence Interval.

The 95% confidence interval equation (Equation 57) was once again used for Onyx-Carbon fiber to determine how different the experimental data was relative to the published information. For Onyx, only a sample size of 2 specimens at room temperature for 49O51C can actually be used. The 95% confidence interval resides between 171.8 and 183.5 MPa, where the published value for 49O51C using the Rule of Mixtures is 427.6 MPa, which is more than twice the magnitude of the upper bound of the confidence interval. Like for ULTEM 9085, the published data did not fall in this interval. Only this time, the distance from the interval is much larger. While there are still some differences, it is likely that the published data assumes bulk properties and does not account for the variability in 3D printing Onyx-Carbon fiber. The confidence interval and RoM calculated ultimate stress is tabulated in Table 17 for convenience.

Table 17. Confidence Interval for Onyx-CF

	RoM Calculation	CI Lower Bound	CI Upper Bound
Onyx-CF 49O51C σ_u (MPa)	427.6	171.8	183.5

Voids in the Onyx-Carbon fiber specimens could be causing the stark difference with published data and experimental values. There could also be an issue with adhesion between the carbon fiber and the polymer matrix. While the Rule of Mixtures is an approximation, it does not account for adhesion between polymers and reinforcement fibers. The strength of the adhesive interface between reinforcement and polymer is a factor unaccounted for in the Rule of Mixtures equation. Since the published data in general does not account for combining two materials, plugging in the published ultimate strengths into the Rule of Mixtures could be neglecting adhesion effects and produce an overestimated strength magnitude. Further investigation

would be required to understand this phenomenon.

4.1.2.3   Polymer Failure Results.

Images of the Onyx-Carbon Fiber failure locations are shown in Figures 113 and 114. At low temperatures, specimens failed by the same mechanism in which the outside surface layer failed while many of the internal fibers remained intact, as shown in Figure 113a and c. In some cases, failure on the surface seemed to be instantly followed by delamination of some internal layers due to stress concentrations after failure as seen in Figure 113d.
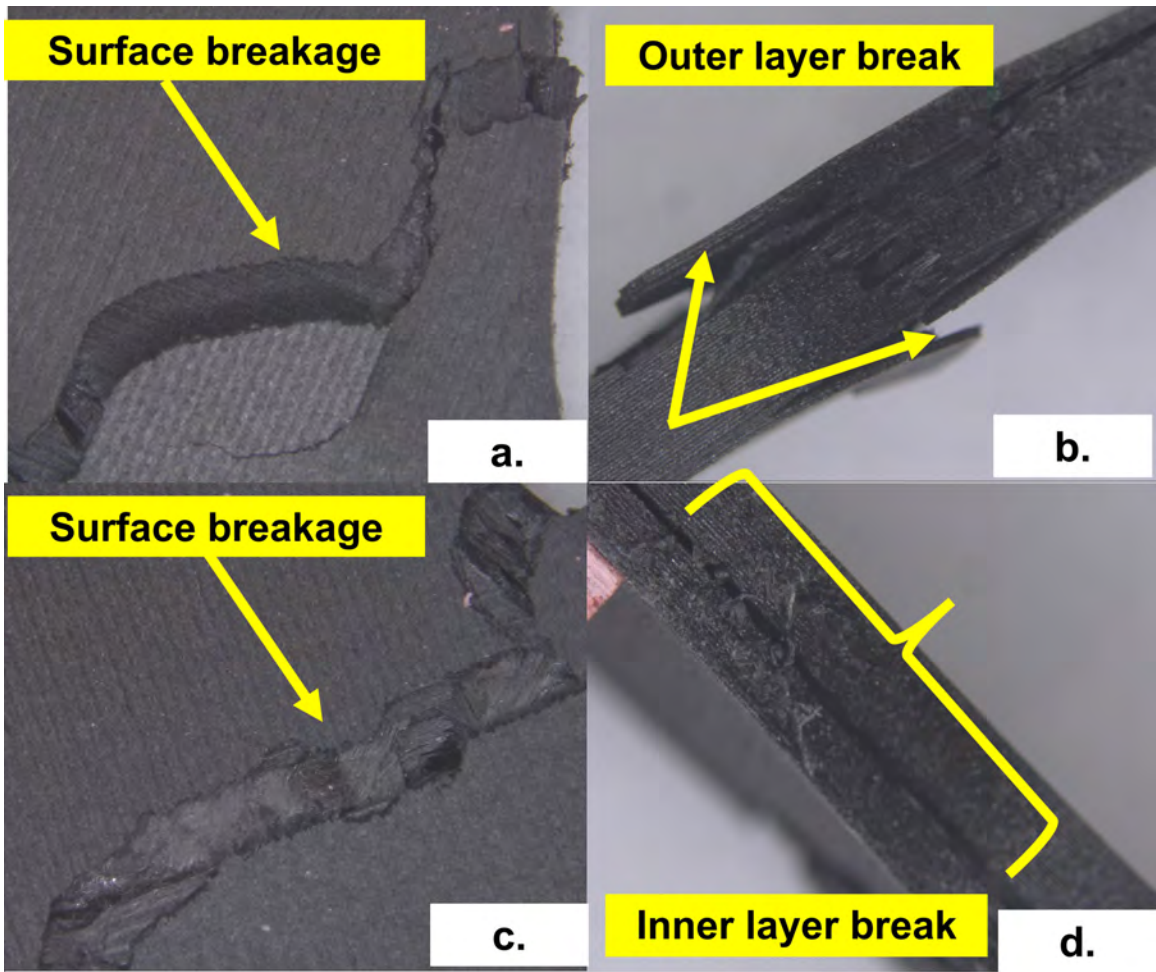
Figure 113. Onyx-Carbon fiber specimens a) 46C54O 3 - 298K b) 46C54O 3 - 298K, second angle c) 46C54O 4 - 354K d) 46C54O 4 - 354K, second angle
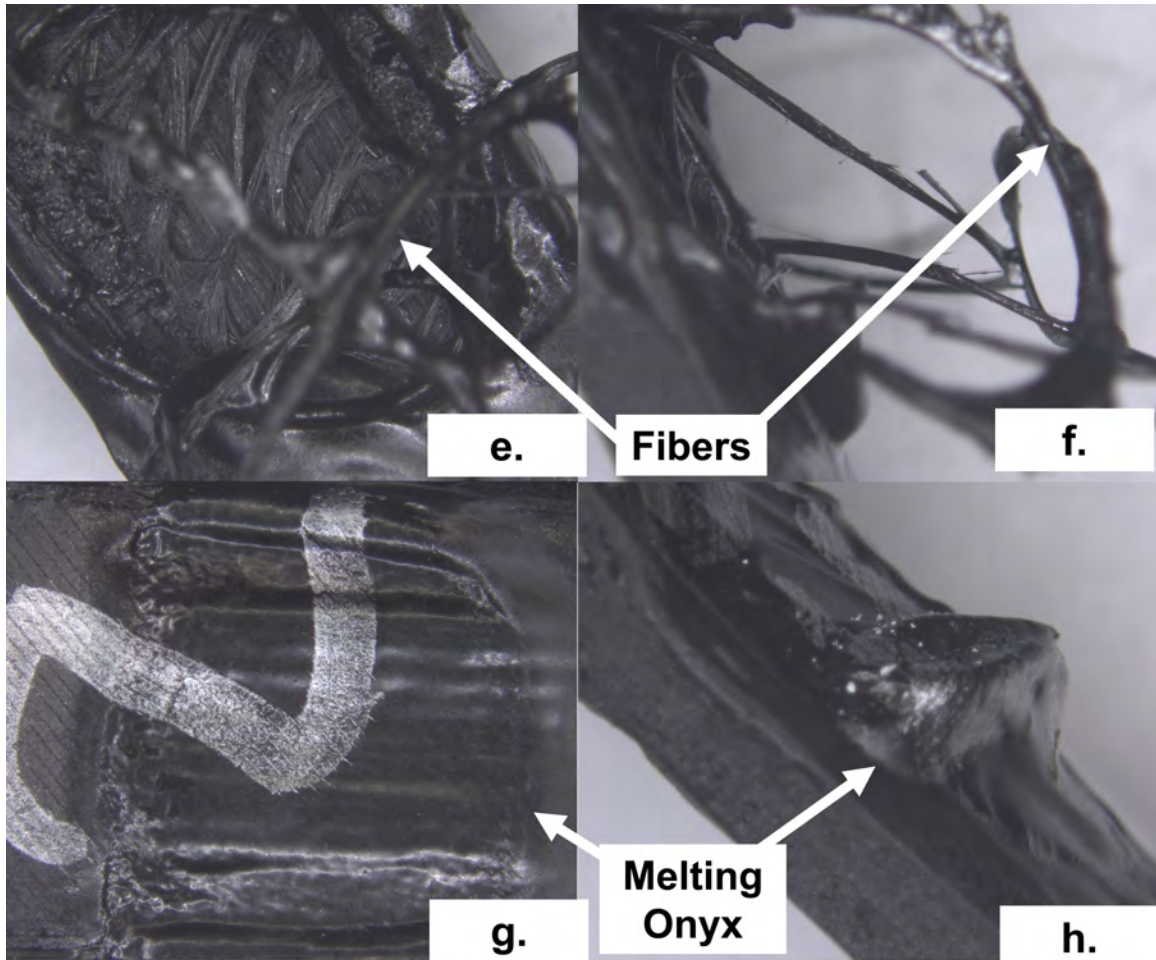
Figure 114. Onyx-Carbon fiber specimens a) 51C49O 2 - 475K b) 51C49O 2 - 475K, second angle c) 51C49O 2 - 475K, third angle d) 51C49O 4 - 414K

At the P400 operating temperature, the thermal disadvantage of Onyx became apparent as the nylon began to melt during the thermal soak phase of testing as shown in the high temperature images in Figure 114. The heat also caused the fibers to expand out of the specimen gauge section as shown in Figure 114e and f, essentially causing the specimen to already fail due to the heat alone. Even though the Nylon was still somewhat intact with the fibers expanding out of the specimen, these high temperature specimens in particular, generated the least load and certainly indicated the inability to survive at P400 temperatures. Onyx is competitive for ultimate

competitive stress (ultimate stress of 800 MPa [78]) but would melt before reaching the operating temperature needed to survive in a P400 engine.

4.1.2.4   Material Data.

Tables 18, 19, 20, and 21 show the material properties input into FEA to represent Onyx-Carbon fiber. The elastic modulus and ultimate stress used were the averages of the tensile results for each temperature regime. The FEA model was assumed isotropic, and the published information describing density (ρ), thermal conductivity (k), Poisson's ratio (ν), and coefficient of thermal expansion (α) were all assumed constant based on published values.

Table 18. Onyx-Carbon Fiber (51C49O) Tensile Results

Temperature,K	293	366	414	475
σ_u, MPa	168	130	106	81
E, GPa	3.11	1.97	2.97	2.41

Table 19. Onyx-Carbon Fiber (46C54O) Tensile Results

Temperature,K	293	366
σ_u, MPa	99.6	174
E, GPa	5.21	2.43

Table 20. Onyx-Carbon Fiber (65C35O) Tensile Results

Temperature,K	293	354	398	460	475
σ_u, MPa	247	212	116	50	4.9
E, GPa	15.2	16.8	16.8	11.5	11.5

Table 21. Onyx-Carbon Fiber Constant Properties

α, μm/m-K	22.3	[117]
ρ, kg/m^3	1,200	[118]
k, W/(m*K)	0.9	[119]
ν	0.43	[120]
GTT (K)	408-445	[112, 113]

4.1.3 Epoxy-Carbon Fiber Tensile Results.

The third material examined was a blend of epoxy and chopped carbon fiber. The epoxy is proprietarily known as Supreme121AO by Masterbond. The motivation the use Supreme121AO is the claim of high temperature on the Masterbond website with a GTT of 473-483K [91]. While the ultimate stress is lower than the competing polymers in this study (ultimate stress of 41-48 MPa [91]), blending it with discontinuous carbon fiber from Fiberglast (ultimate stress of 4551 MPa) [121] was expected to drastically increase the ultimate strength to a competitive magnitude with respect to other engineering-grade polymers and turbomachinery metals. This exceeds the GTT of ULTEM 9085 (GTT of 450K) (77 MPa) [103], [109]. While the GTT of pure Onyx is unpublished on the Markforged website, it can be readily estimated as Onyx is predominantly made out of Nylon which has a low GTT (333-338K) [122] [123] [124].

The advantages in temperature and strength motivate the interest in Epoxy-Carbon fiber. In addition, because epoxy is mixed with discontinuous carbon fibers and poured into a mold, there are no layering effects like those seen from 3D printed parts. This means the epoxy should behave more isotropically with less risk of delaminations. While the carbon fiber was expected to enhance the ultimate strength of the Supreme121AO (similar to the Onyx-carbon fiber blend) the difference in comparison to the Onyx-Carbon fiber lies in the fact that the Epoxy-Carbon fiber implements discontinuous carbon fibers where Onyx was largely reinforced by continuous fiber. The discontinuous carbon fiber was mixed with the epoxy and molded as described in Chapter III. The result of the random nature of the fiber orientation was expected to yield a nonuniform mass distribution among individual specimens and a nonuniform stress profile (i.e. stress concentrations) within a single specimen due to voids or fiber direction. Stress concentrations almost certainly lead to premature failures. While

160

the fiber orientation is not an issue that can be solved without more complicated machinery (i.e. something that straightens the fibers, orienting them parallel to the lengthwise direction), the voids could be reduced by switching from casting to compression molding. This motivated the use of the 30 ton Wabash Press described in Section 3.1.1.

Three batches of five epoxy-carbon fiber specimens (15 total) were tested in this study. The first two batches were manufactured using the 1-piece dogbone press plate as shown in Figure 66, while the third batch used the updated 3-piece dogbone press plate as shown in Figure 69. The first batch of the 1-piece dogbone mold was pressed with 15% reinforcement by weight. The second batch of the 1-piece dogbone mold was pressed with 10% reinforcement by weight because of noticeable viscosity issues at the 15% weight fraction. The switch over to the 3-piece mold plate was due to both deformations that were discovered on the first dog bone plate after the second batch was molded, as well as the determination that the 20 ton Wabash Press machine was only applying a fraction of pressure to the specimens (some pressure distributed along with the mold plate) and not concentrating the stress profile over the specimens, as is desired. The 3-piece press plate geometry helped address these issues in the third batch of epoxy-carbon fiber specimens. The third batch was pressed with 10% reinforcement by weight. Epoxy-Carbon fiber specimens are shown in Figures 115 and 116. The mean and standard deviations for the specimen cross-section are displayed in Table 22. Batches 4 and 5 have predominantly consistent molds with little deviation from the design width and thickness. Batch 6 has slightly more variation than the first two batches in its variation in thickness.

To potentially acquire information on the presence of voids and mass variability in each specimen, the mass of each specimen was measured and reported in Table 23.

161

Figure 115. Epoxy-CF Specimens Batch 4 (15% reinforcement) and Batch 5 (10% reinforcement)

Figure 116. Epoxy-CF Specimens Batch 6 (10% reinforcement)

Table 22. Measured vs. Designed Specimen Thickness (t) and Width (w), Epoxy-Carbon fiber

Epoxy-Carbon fiber	Design t (mm)	Design w (mm)	$\bar{t}$ (mm)	$\sigma(t)$ (mm)	$\bar{w}$ (mm)	$\sigma(w)$ (mm)
15% Batch 4	4	6	4.02	0.01	6.01	0.01
10% Batch 5	4	6	3.99	0.04	6.03	0.03
10% Batch 6		6	3.5	0.07	5.99	.01

Table 23. Specimen Mass Epoxy-Carbon Fiber

Batch 4	#	CF%	Mass (g)
	1	15%	11.62
	2	15%	11.81
	3	15%	11.71
	4	15%	11.25
	5	15%	11.44
Batch 5	6	10%	12.15
	7	10%	12.30
	8	10%	12.88
	9	10%	11.89
	10	10%	12.15
Batch 6	1	10%	10.88
	2	10%	10.88
	3	10%	10.86
	4	10%	10.73
	5	10%	10.83

To compare with the published data, the Rule of Mixtures was applied similarly to Onyx, but with a slight variation. A paper by Pan [125] outlines a modified version of the Rule of Mixtures for the case of randomly oriented fibers as shown in Equation 59. The published values for Supreme121A0 (σ_u=48 MPa;E=5.86 GPa) and Fiberglast discontinuous fiber (σ_u=4551 MPa;E=2.35 GPa) were used for comparison [91, 121].

$$E_{total} = E_{fiber}(v_{f,Fiber})\frac{1}{2\pi} + E_{matrix}(v_{f,matrix})\frac{1}{2\pi} \tag{59}$$

The stress-strain curves for all three batches of tensile specimens are displayed in

163

Figures 117 and 122. The ultimate strength vs. elastic modulus data is shown in Figures 118 and 123 while data displaying ultimate strength and elastic modulus varying with temperature are shown in Figures 119, 120, 124, and 125. Figures 118, 119, and 120. The ultimate strength as a function of mass is shown in Figures 121 and 126.
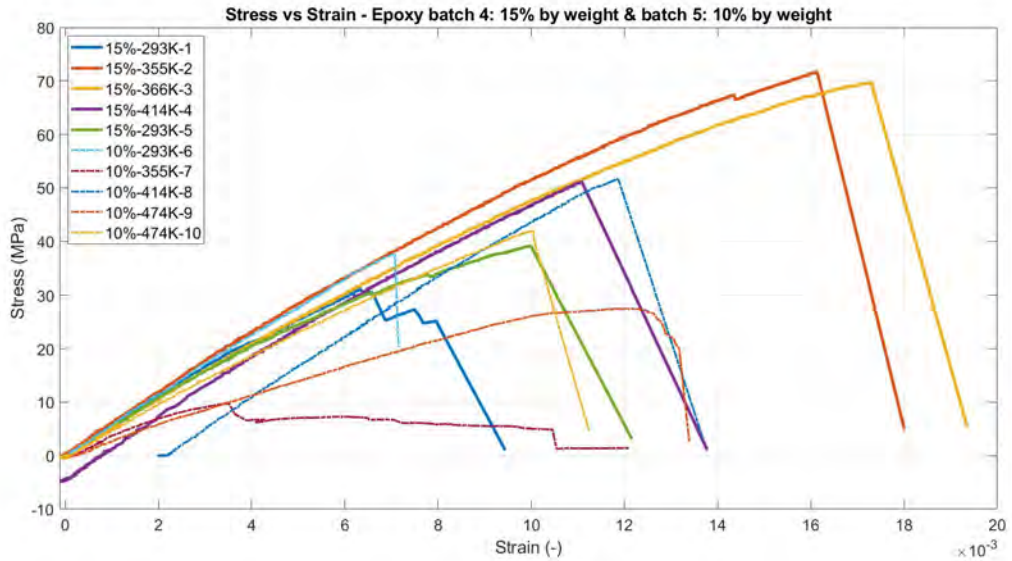

Figure 117. Stress vs. Strain Curves, Epoxy-Carbon Fiber 15 percent by weight Batch 4, 10 percent Batch 5
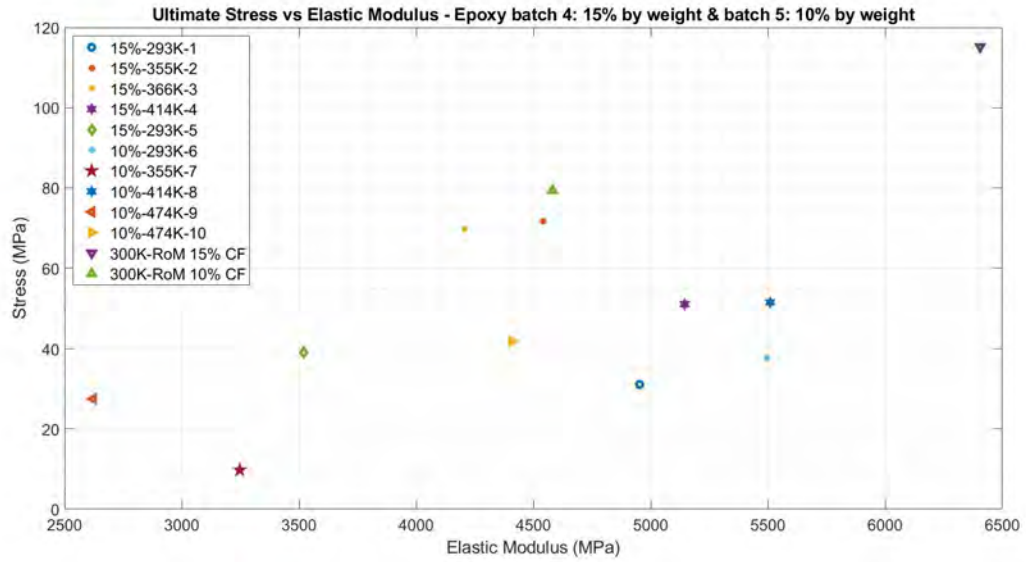
Figure 118. Elastic Modulus vs. Ultimate Strength, Epoxy-Carbon Fiber 15 percent by weight Batch 4, 10 percent Batch 5
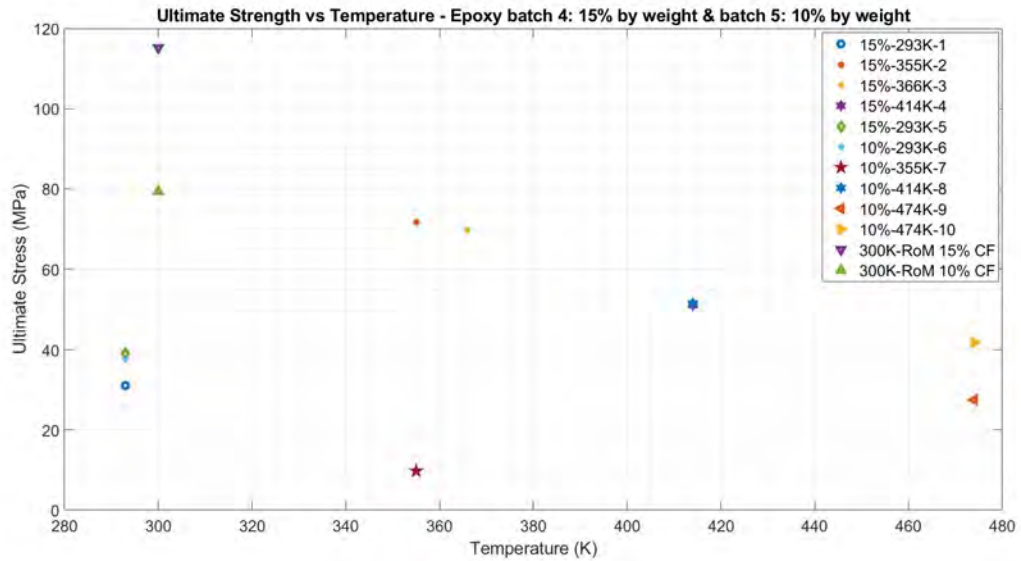

Figure 119. Temperature vs. Ultimate Strength, Epoxy-Carbon Fiber 15 percent by weight Batch 4, 10 percent Batch 5
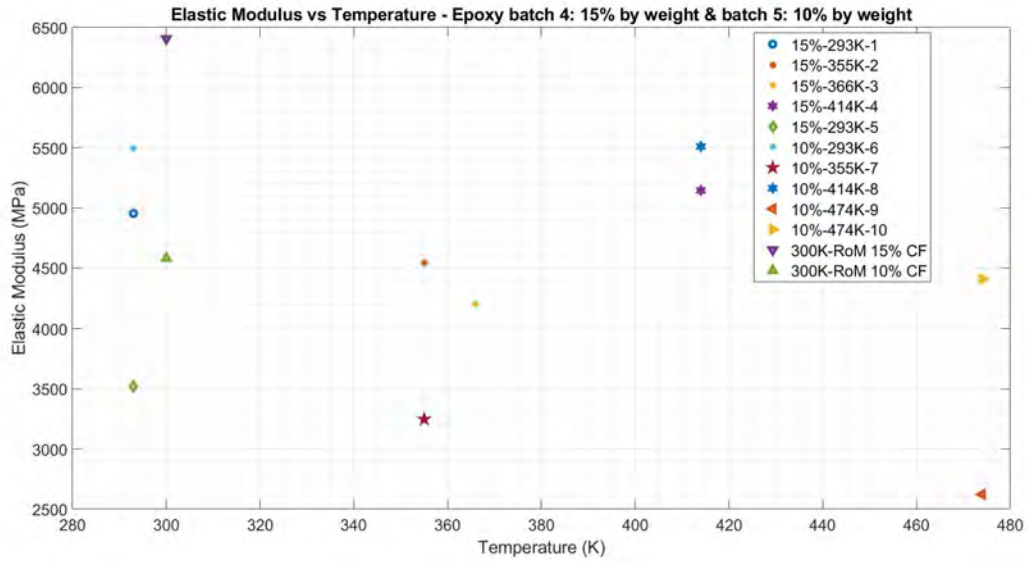
Figure 120. Temperature vs. Elastic Modulus, Epoxy-Carbon Fiber 15 percent by weight Batch 4, 10 percent Batch 5
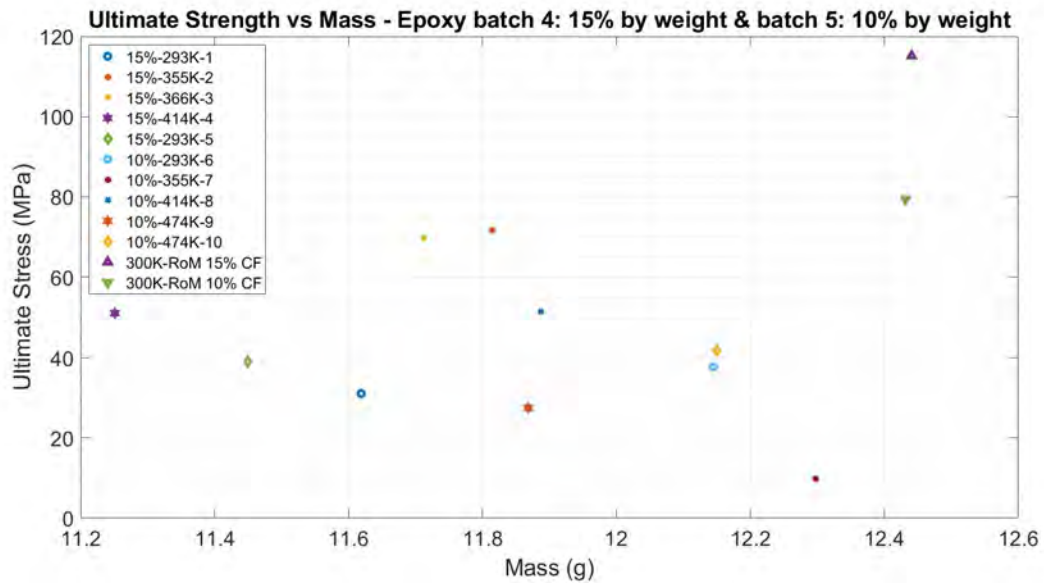

Figure 121. Ultimate Strength vs Mass, Epoxy-Carbon Fiber 15 pct by wght
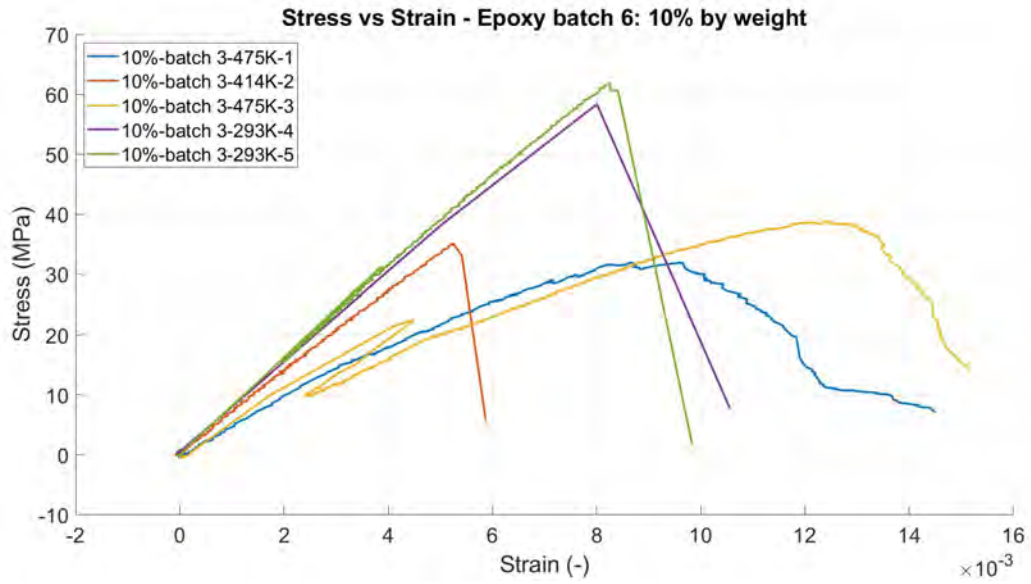
Figure 122. Stress vs. Strain Curves, Epoxy-Carbon Fiber 10 percent by weight Batch 6
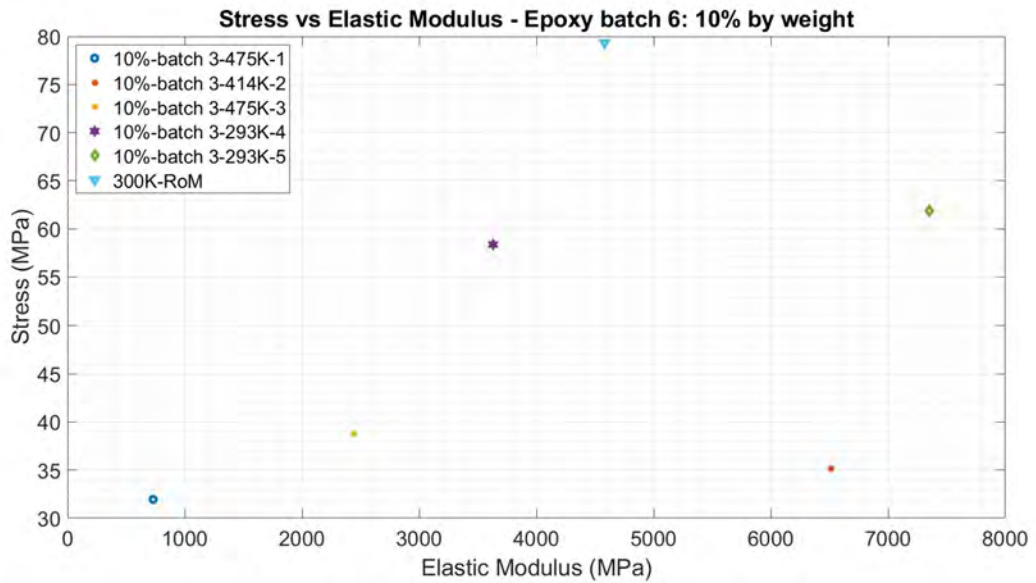

Figure 123. Elastic Modulus vs. Ultimate Strength, Epoxy-Carbon Fiber 10 percent by weight Batch 6
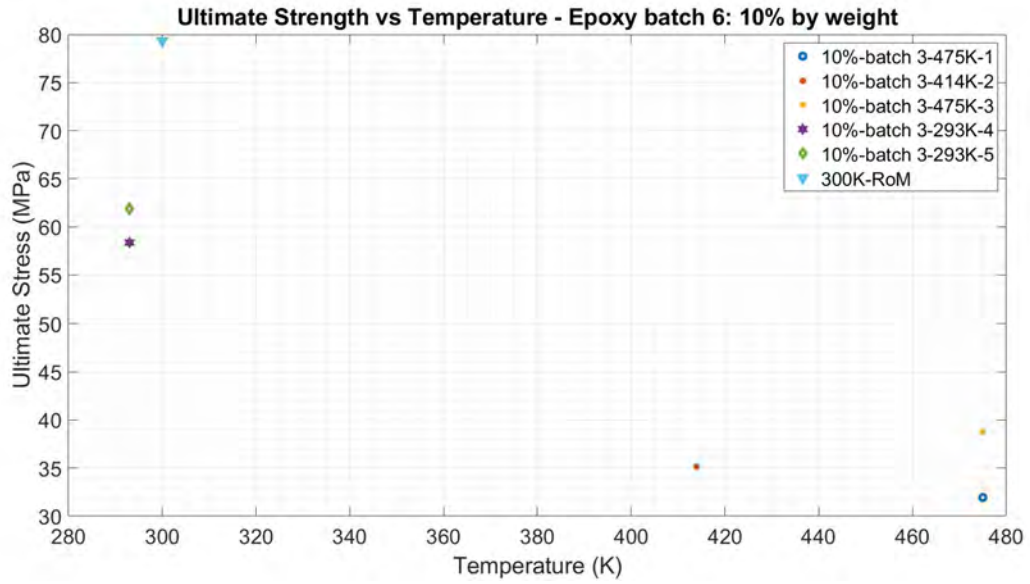
Figure 124. Temperature vs. Ultimate Strength, Epoxy-Carbon Fiber 10 percent by weight Batch 6
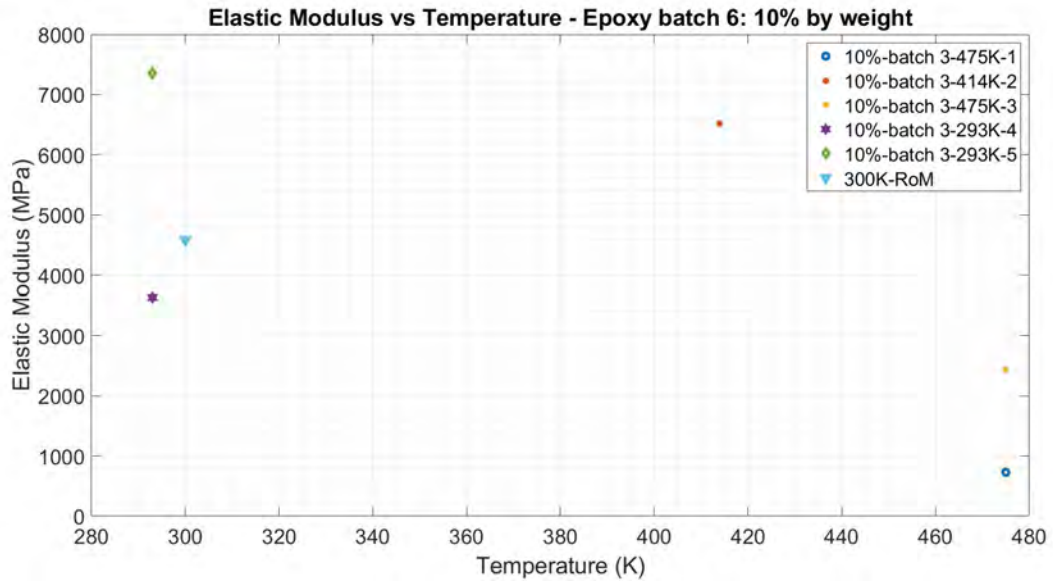

Figure 125. Temperature vs. Elastic Modulus, Epoxy-Carbon Fiber 10 percent by weight Batch 6
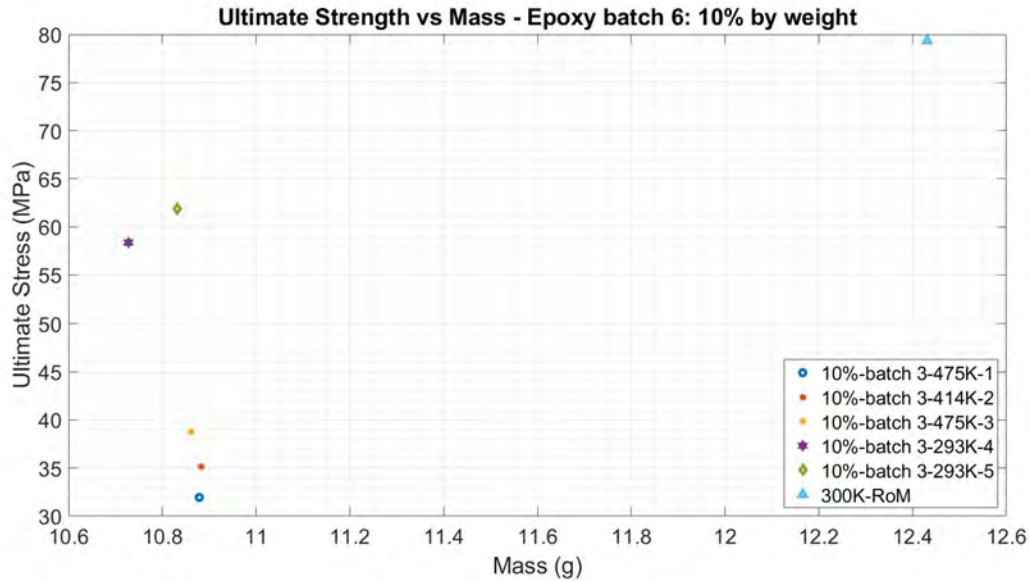
Figure 126. Ultimate Strength vs Mass, Epoxy-Carbon Fiber 10 percent by weight Batch 6

All three molded specimens were measured for the room temperature properties to compare with the published results. Because of the surface defects of the fourth and fifth compression molded batches, the size of the internal voids it was unclear. The significance of the voids would be revealed with the results of the tensile test. The data in Figure 117 displays the data for the fourth and fifth batches and indicates a stress-strain trend different than with the previous two materials. There is not an observable reduction in strength with temperature in the stress strain curve. This becomes apparent when the room temperature curves for both 15% and 10% reinforcement are examined (30 MPa and 38 MPa respectively) in Figure 117. For the fourth and fifth batch, the room temperature specimen did not represent the maximum stress like they did for ULTEM 9085 and Onyx-Carbon fiber. Ultimate strength seems to maximize at around 354 or 366 K and then reduces in magnitude at higher temperatures. It is unclear if the Epoxy-Carbon fiber us some how performing better in tension at that temperature or if the phenomenon has more to do with the inconsistent fill volumes

169

resulting in underlying voids in the other specimens as opposed to the 354 and 366 K specimens. Based on the number of voids produced in the molding work prior to this study, it is likely due to the latter.

The stress-strain relationship for the sixth batch is shown in Figure 122. This batch presents a pattern more consistent with the ULTEM 9085 and Onyx-Carbon fiber results in that the lowest temperature tensile specimens have the highest ultimate strength. That same ultimate strength is reduced as the temperature is increased. Results more consistent with conventional specimen testing could imply an improvement in the mold method in the sixth batch (which implemented the 3-piece mold). The highest temperature specimens have the largest strain at about 0.015 mm/mm.

The fourth batch (15% CF) and fifth batch (10% CF) yielded ultimate stress of 31 MPa and 38 MPa, respectively, with only a 20% difference from one another while the sixth batch (10% CF) yielded two room temperature specimens that both produced a 58 MPa and a 62 MPa ultimate stress (7% difference). Both of these results are still significantly lower than the expected ultimate stress based on the Rule of Mixtures (115 MPa for 15% CF and 79 MPa for 10% CF) which is a significant 70% difference and 52% difference in ultimate stress for the fourth and fifth batch, respectively. As an improvement, the sixth batch also exhibits an 24% difference in ultimate stress with respect to the Rule of Mixtures applied to the published data. While the tremendous difference in the fourth and fifth batch narrated the inherent inconsistency of using molding methods for manufacturing, the improvement of the sixth batch to reduce the difference in ultimate stress to by approximately half of the original difference is a sign of the potential for development and improvement in manufacturing. The increase in ultimate stress with the 3-piece mold indicates such an improvement in the manufacturing method.

The fifth and sixth batches of Epoxy-Carbon fiber were tested for the P400 op-

erating temperature of 475K with both batches testing two specimens each at the operating temperature. The fifth batch produced 28 MPa and 42 MPa ultimate stresses, while the sixth batch produced 32 MPa and 38 MPa ultimate stress. Both sets of operating temperature data average an ultimate stress of 35.3 MPa. This is significant because it indicates that, unlike ULTEM 9085 and Onyx-Carbon fiber, Epoxy-Carbon fiber can generate an observable resistance to tension even at the high operating temperature of the P400 engine. This behavior makes Epoxy-Carbon fiber a potentially better candidate for compressor manufacturing than the other two materials discussed above.

Figures 119 and 124 indicate the ultimate strength and its relationship to temperature. For the fourth and fifth batches, the ultimate strength seems to increase and decrease randomly regardless of temperature, which once again implies manufacturing variability in addition to the temperature varying results. The sixth batch shows a slight trend in reduction in stress with temperature with an average room temperature ultimate strength of 60 MPa and average 475 K ultimate strength of 35.5 MPa. More specimen tests would be required to further understand any temperature correlations with strength. Figures 121 and 126 present the ultimate strength with respect to the mass of each specimen. The data is quite random and does not indicate any pattern or trend of strength relative to the mass of each molded specimen.

4.1.3.1 Confidence Interval.

The confidence interval equation in Section 4.1.1.2 is again used here to determine how different the published values are to the experimental data. Only two specimens in Epoxy Batch 4 and two specimens in Epoxy Batch 6 can be used for this confidence interval evaluation since Epoxy Batch 5 only had one specimen at room temperature evaluated. The limited number of specimens for this calculation could also factor

into the accuracy of the measurement in the confidence interval. The 95% confidence interval for Epoxy Batch 4 (15% CF) was between 33.1 and 37.0 MPa for the published Rule of Mixtures value of 115 MPa. Epoxy Batch 6 (10% CF) had a 95% confidence interval between 59.3 and 61.0 MPa for the published Rule of Mixtures value of 79.3 MPa. For both Epoxy Batch 4 and 6, the published values for the respective carbon fiber percentage did not fall into the range of the confidence interval. Since Epoxy-Carbon fiber used discontinuous fibers instead of continuous fibers, as with Onyx-Carbon fiber, this could be a factor in the difference between published and experimental values. The adhesion is different to that of continuous fibers and could possibly have affected the ultimate strength. An important observation is the fact that progression from using the one-piece mold with Epoxy Batch 4 led to a smaller difference margin between the confidence interval and the published value with Epoxy Batch 6 in that the published value is only 20 MPa higher than the upper bound of the confidence interval. This implies that the 3-piece mold improved the quality of the specimens and brought the specimen's ultimate strengths closer to that of published data. This means that there is some disconnect between the experimental data and the RoM calculation. It is likely that the published data assumes bulk properties and does not account for the variability in molding Epoxy-Carbon fiber. The confidence interval and RoM calculated ultimate stress is tabulated in Table 24 for convenience.

Table 24. Confidence Interval for Epoxy-CF

	RoM Calculation	CI Lower Bound	CI Upper Bound
Epoxy-CF Batch 4 (15% CF) σ_u (MPa)	115	33.1	37
Epoxy-CF Batch 6 (10% CF) σ_u (MPa)	79.3	59.3	61

4.1.3.2 Polymer Failure Results.

The broken Epoxy-Carbon fiber specimens are shown below in Figures 127 - 128. A closer look at the specimen gauge section, shows voids that likely contributed to stress concentrations in Specimens 6, 7, and 8. Specimens 9 and 10 were at the P400 operating temperature and did not separate into two pieces after the tensile test; the two specimens remained as one piece with visible surface failure. Since Supreme121AO's published GTT is 473-483K [91], the epoxy likely began to glassify during the high-temperature thermal soak. This caused the adhesive effect in the specimens to break down and prevented Specimens 9 and 10 from coming apart. The inner sections of Specimens 9 and 10 are still partially intact, likely because the internal fibers remained intact while the surface fibers failed during the tensile test.
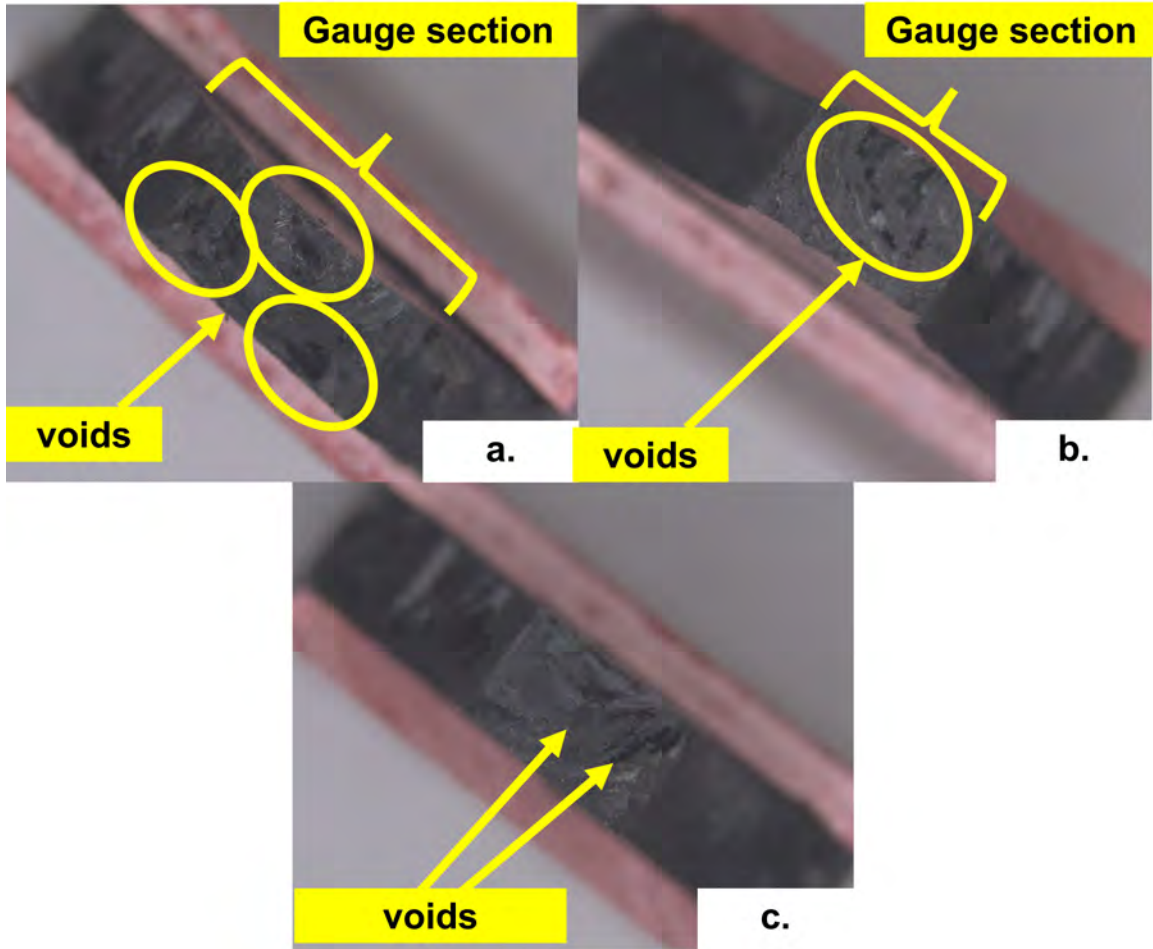
Figure 127. Epoxy Specimens Batch 5 (10% CF): a) Epoxy-CF 6a - 298K b) Epoxy-CF 7a - 354K c) Epoxy-CF 8b - 414K
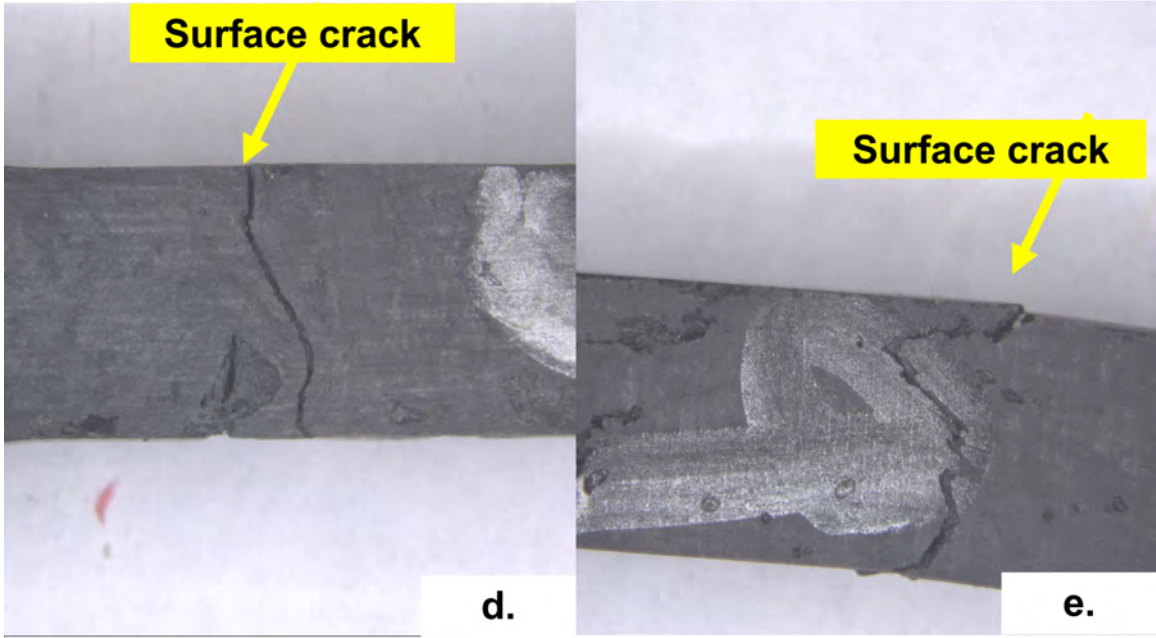
Figure 128. Epoxy Specimens Batch 5 (10% CF): d) Epoxy-CF 9 crack - 474K e) Epoxy-CF 10 crack - 474K

4.1.3.3   Material Data.

The Epoxy-Carbon fiber material properties for the FEA SolidWorks model are shown in Table 25, Table 26, and Table 27. The density (ρ), thermal conductivity (k), Poisson's ratio (ν), and coefficient of thermal expansion (α) were all assumed constant based on published values. The reported elastic modulus and ultimate strength are the average values of the tensile test results for each temperature.

Table 25. Epoxy-Carbon Fiber 1-piece mold (Fourth batch) Property Tables

Temperature, K	293	355	366	414	475
σ_u, MPa	35	72	69.7	51.1	N/A
E, GPa	4.24	4.54	4.21	5.15	N/A

Table 26. Epoxy-Carbon Fiber 1-piece mold (Fifth batch) Property Tables

Temperature, K	293	355	366	414	475
σ_u, MPa	37.7	9.8	N/A	51.6	34.7
E, GPa	5.50	3.25	N/A	5.51	3.52

Table 27. Epoxy-Carbon Fiber 3-piece mold (Sixth batch) Property Tables

Temperature, K	293	414	475
σ_u, MPa	60	35	35.5
E, GPa	5.5	6.5	1.59

4.2 FEA

After material properties were determined for the materials of interest, FEA was conducted with each of these materials applied to the geometry of both the complete compressor and the compressor hub (no blades). ULTEM 9085, Onyx-Carbon fiber, and Epoxy-Carbon fiber properties were applied to the compressor geometry, while only Epoxy-Carbon fiber was applied to the compressor hub. The results of the FEA for each case express a failure estimation with each material. Each material was analyzed with FEA for room temperature as well as rising temperature scenarios. The room temperature cases assume constant material properties at room temperature and is representative of the test rig in its current state without a compressor shroud and without compressive effects. The rising temperature cases match the speed of interest with a linear temperature correlation, as shown in Table 11. The temperature variant cases are more indicative of performance in a compressor shroud. Each of these FEA results are discussed in Sections 4.2.4 (ULTEM 9085), 4.2.5 (Onyx-Carbon

Table 28. Epoxy-Carbon Fiber Constant Properties

α, μm/m-K	65 [126]
ρ, kg/m^3	$1.8*10^3$ [91]
k, W/(m*K)	0.72 [127]
ν	0.29 [128]
GTT (K)	473-483 [91]

fiber), and 4.2.6 (Epoxy-Carbon fiber). Prior to initiating the FEA comparison with different materials, a comparison for the SolidWorks model with and without the hex sleeve is examined in Section 4.2.2. A preliminary model is examined (Section 4.2.3) to determine inconsistencies that may exist between the SolidWorks FEA conducted in this study and the ANSYS FEA conducted in Bauer's work [1] to determine how much variation there is between the two solvers. Section 4.2.1 discusses two features built into each SolidWorks model that match the physical.

4.2.1   Model Features.

Because of lessons learned from previous work, two features were added to the compressor design and are included in the FEA model for more accurate analysis. The first was the introduction of an aluminum hex sleeve into the bore section of the compressor. This hex sleeve functions to take the stress build-up at the bore section. The expectation was that the aluminum core would sustain higher stress and enable the entire polymer compressor assembly to survive to a higher speed. This hex sleeve was accounted for in the FEA model and is the same one shown in Figure 53 in Section 2.6.

The second feature was a custom washer that sits at the inlet side of the compressor. This part functioned to divert compression stress (due to the tightening of the compressor nut) away from the polymer lip of the compressor and apply it on the face of the aluminum hex sleeve. An example of a custom washer is shown in Figure 129. There was a concern that the polymer interface would give way to the metal nut after being tightened and lose the preload on the nut. Loss of this preload could loosen the compressor from the shaft, cause slipping, generate friction heating on the shaft, and melt the compressor. This custom washer was used to assure that the compressor assembly did not lose preload on the nut by applying clamping force through metal

components only. The custom washer is "hat-shaped" to hold the polymer in place while it presses against the aluminum hex sleeve. The "washer-part" of the custom washer was sized to be 0.01 inch off of the polymer lip. While the washer itself is not included in the assembly, the lip region of the compressor in the model is shaped to match the fitting for the custom washer.
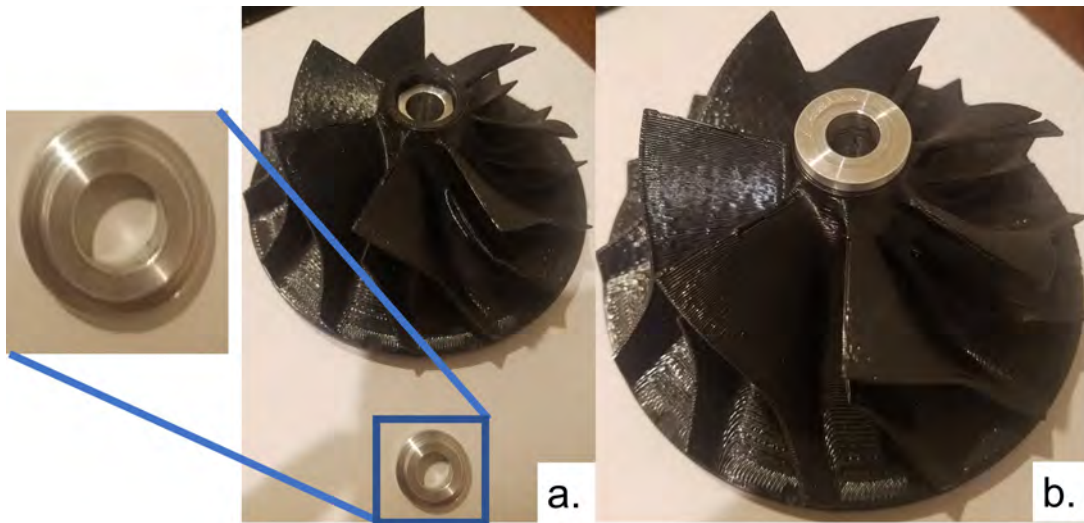

Figure 129. Custom Washer a) Washer Unplaced b) Washer Placed

4.2.2 Compare Hex Out and Hex In.

To initiate the FEA model, the first step was to determine the accuracy of the assembly approach with the inclusion of the hex sleeve and how much variation existed between the cases with and without the sleeve. If the outputs contained a reasonable amount of error that still kept the results in the same order of magnitude, the assembly method could be considered a valid approach for modeling the entire compressor assembly. It should be noted, the hex sleeve, whether included or excluded in the displayed model, was set to be transparent in the SolidWorks for the sake of visibility of stress and deformation profiles of the polymer as shown in Figure 130. Two version of the model was made with ULTEM 9085 as the material and simulated with 384 K
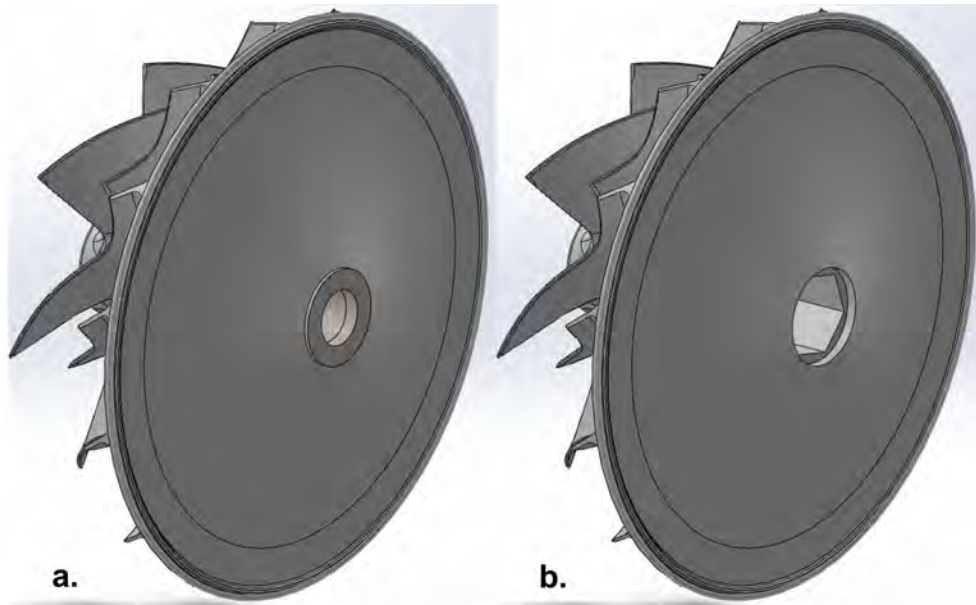
178

Figure 130. Hex Sleeve Transparency a) Hex Opaque b) Hex Transparent

properties. The first was the same compressor with the aluminum hex sleeve removed. The second version included the hex sleeve and was made to verify the accuracy of the SolidWorks analysis method on an assembly file (including both the sleeve and compressor) and to assure the stresses were properly calculated both with and without the hex sleeve in the assembly.

This model is used to measure the predicted stress and deformation at various conditions. It should be noted that the deformations throughout the rest of this study indicate deformation toward the outward radial direction (away from the shaft) and axially toward the inlet side of the compressor. This deformation direction is in all cases without exception and is narrated with an exaggerated scale (13.5x scale) for convenience in Figure 131. For ULTEM 9085 at 384 K with the "Hex Out", Figures 132 (Thermal effects only), 133 (Centrifugal effects only), and 134 (Thermal and Centrifugal combined) display the results for stress profiles and deformation profiles for the varying cases.

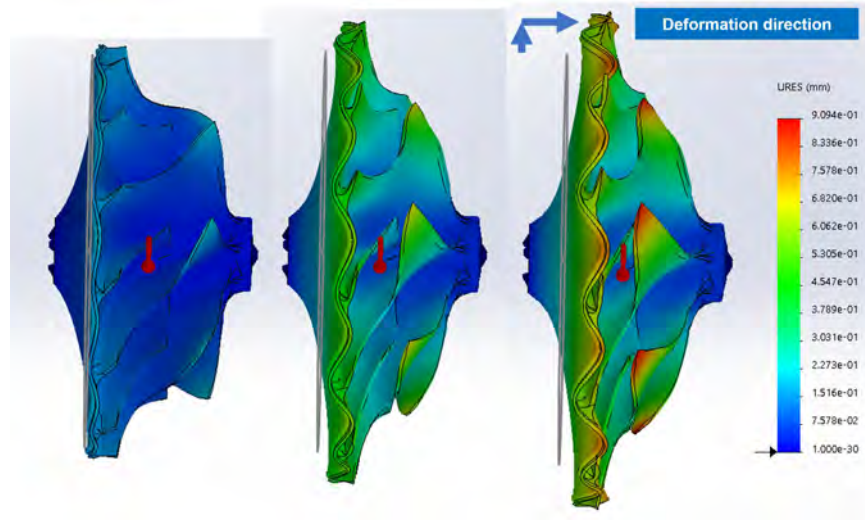For ULTEM 9085 at 384 K with the "Hex In", Figures 135 (Thermal effects only),

179

Figure 131. Deformation Direction

136 (Centrifugal effects only), and 134 (Thermal and Centrifugal combined) display the results for stress profiles and deformation profiles for the varying cases.
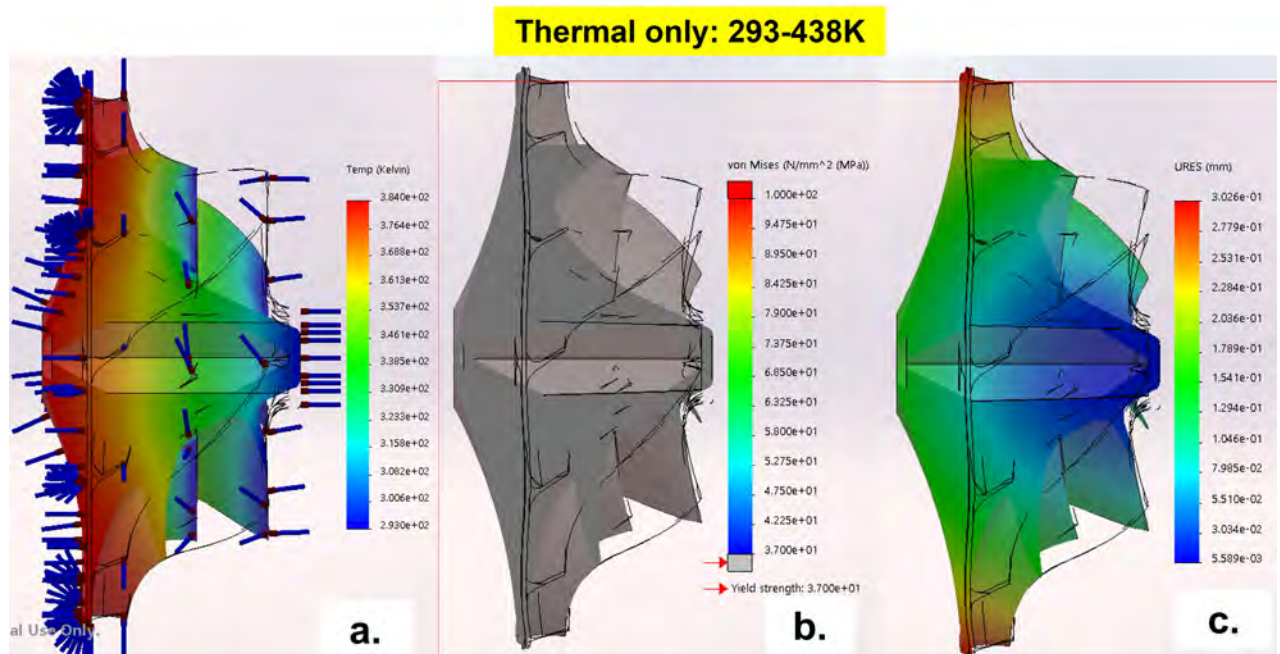

Figure 132. ULTEM 9085 Comparison model 1 - Hex Out Thermal Only a) Temperature Profile b) Stress Profile c) Deformation Profile
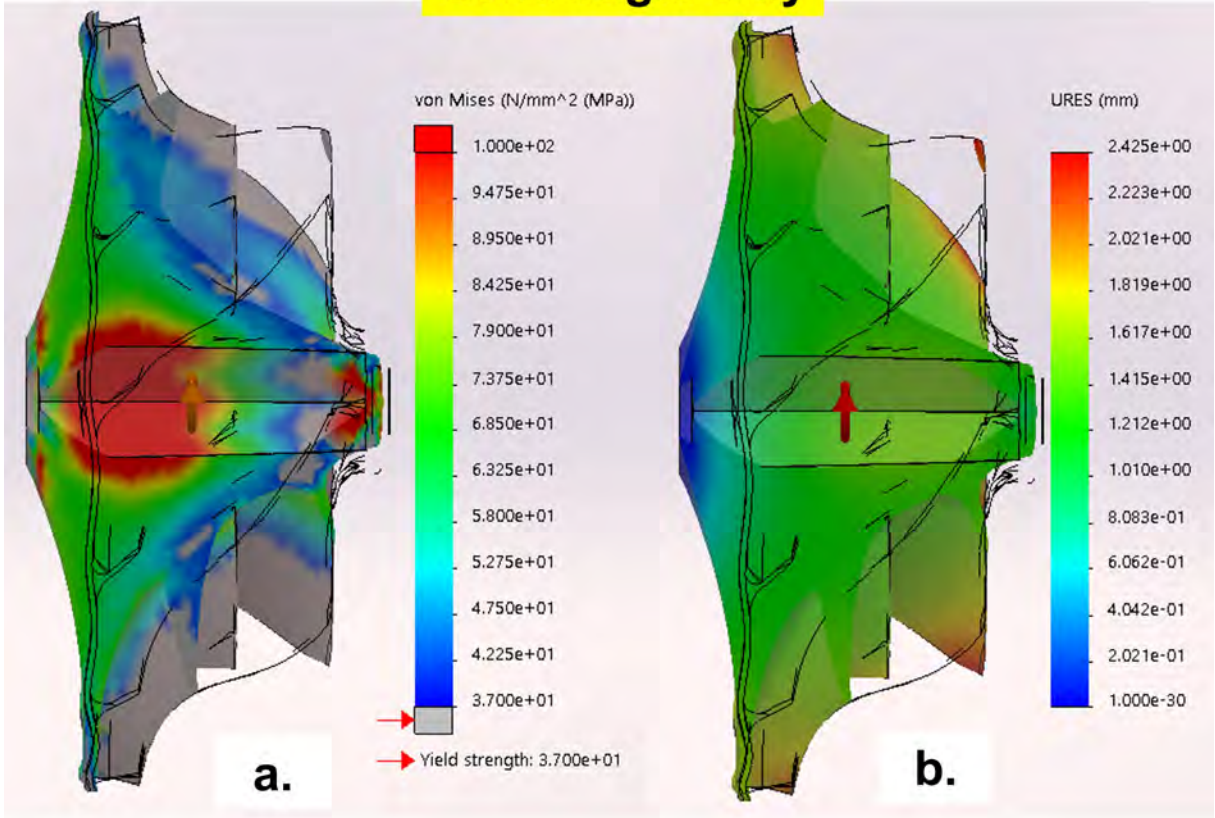
Figure 133. ULTEM 9085 Comparison model 1 - Hex Out Centrifugal Only a) Stress Profile b) Deformation Profile
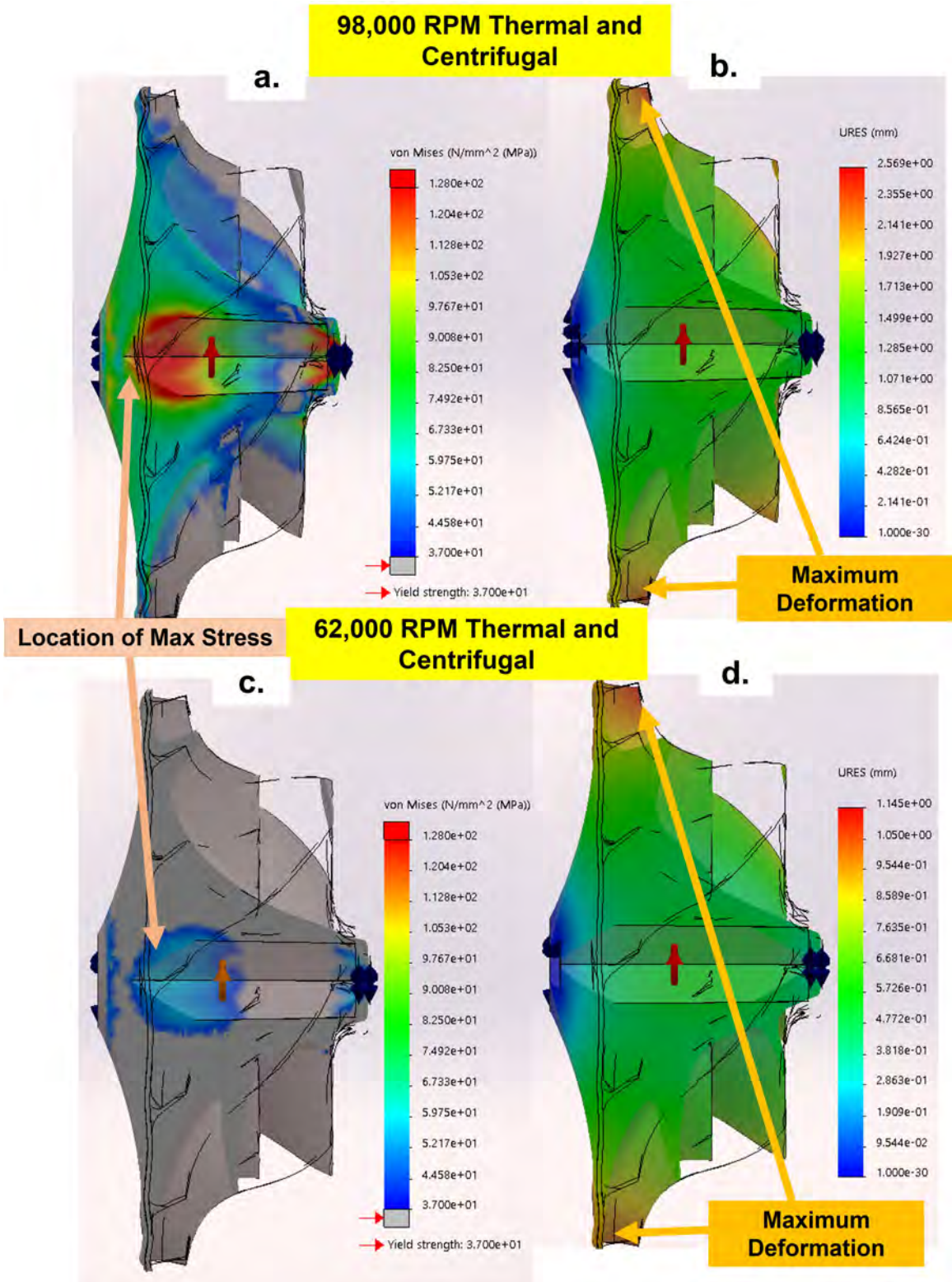
Figure 134. ULTEM 9085 Comparison model 1 Hex Out Thermal Centrifugal Combined a) 98 kRPM Stress Profile b) 98 kRPM Deformation Profile c) 62 kRPM Stress Profile d) 62 kRPM Deformation Profile
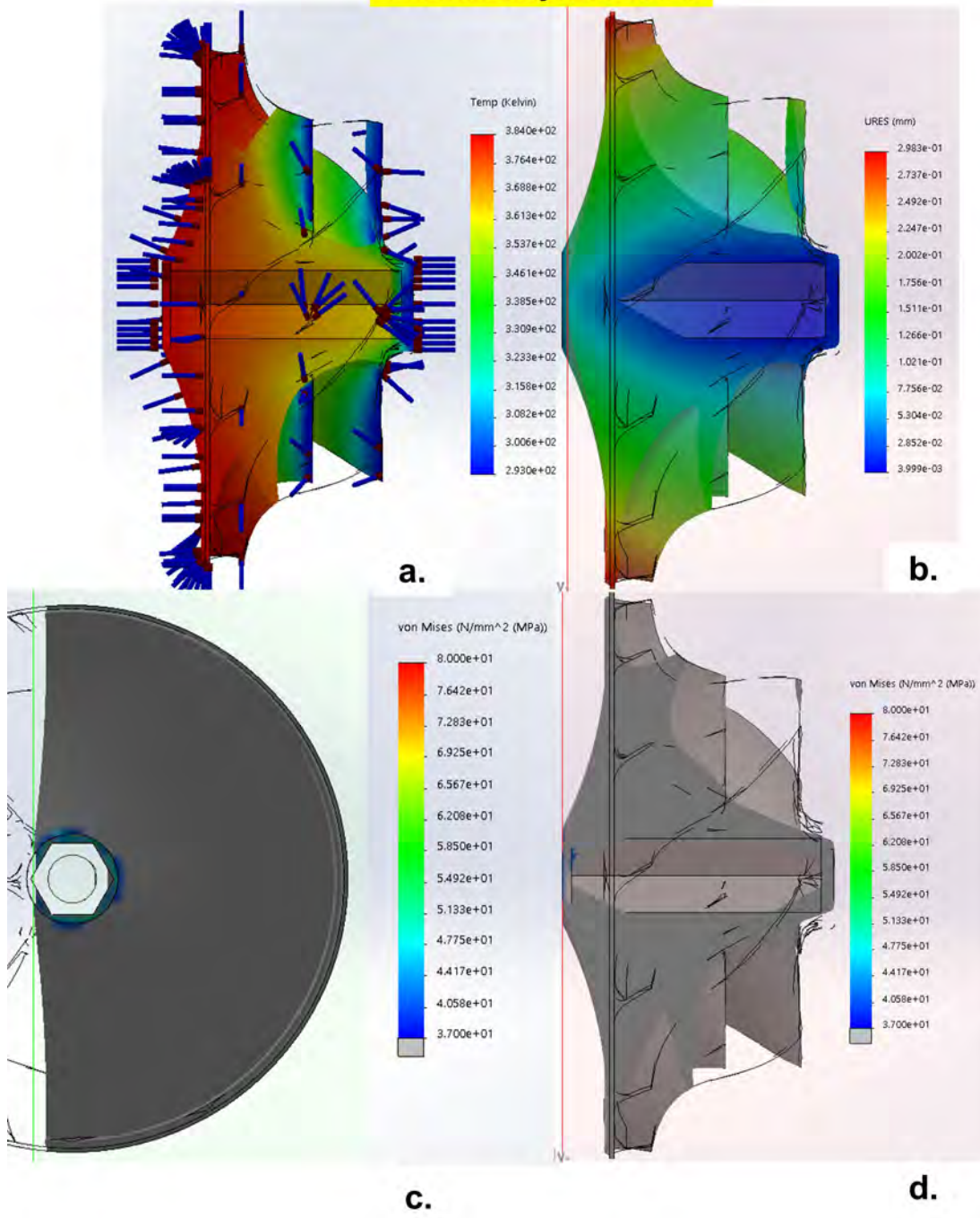
Figure 135. ULTEM 9085 Comparison model 2 - Hex In Thermal Only a) Temperature Profile b) Deformation Profile c) Stress Profile (1) d) Stress Profile (2)
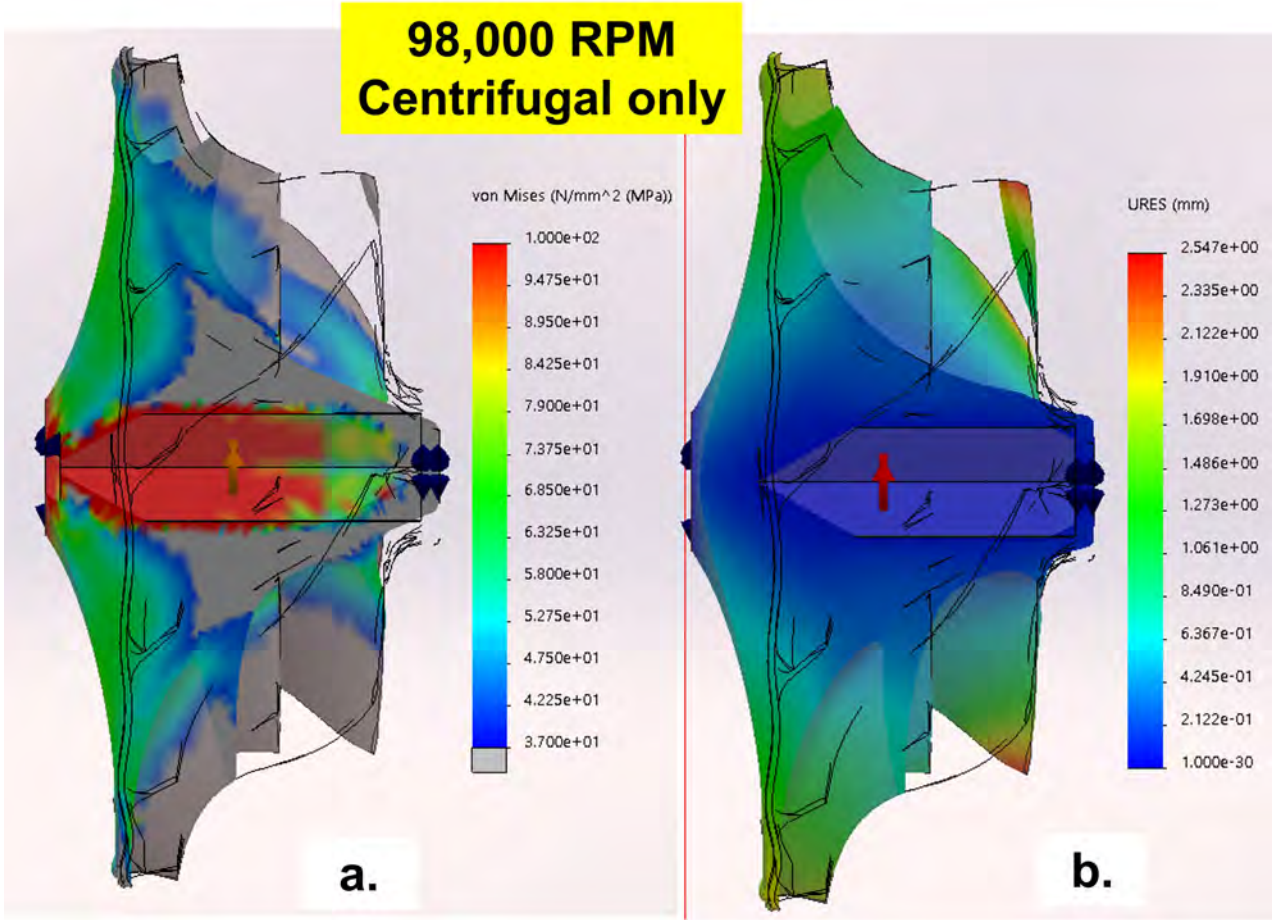
Figure 136. ULTEM 9085 Comparison model 2 - Hex In Centrifugal Only a) Stress Profile b) Deformation Profile
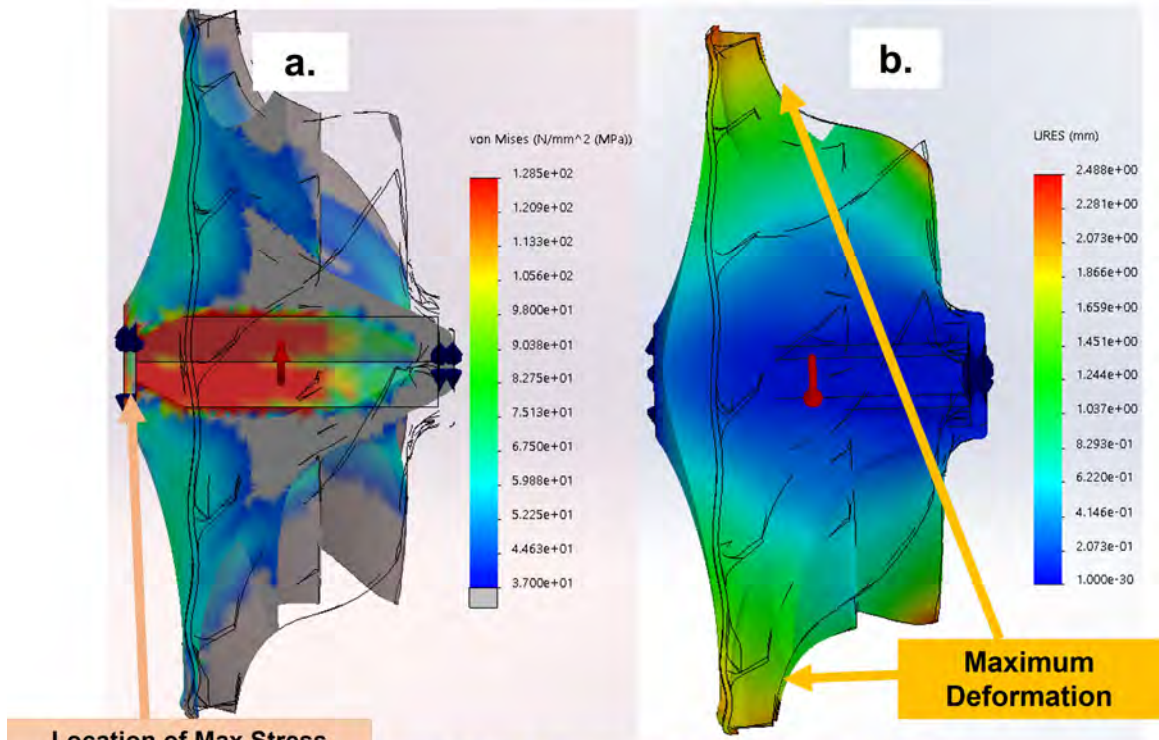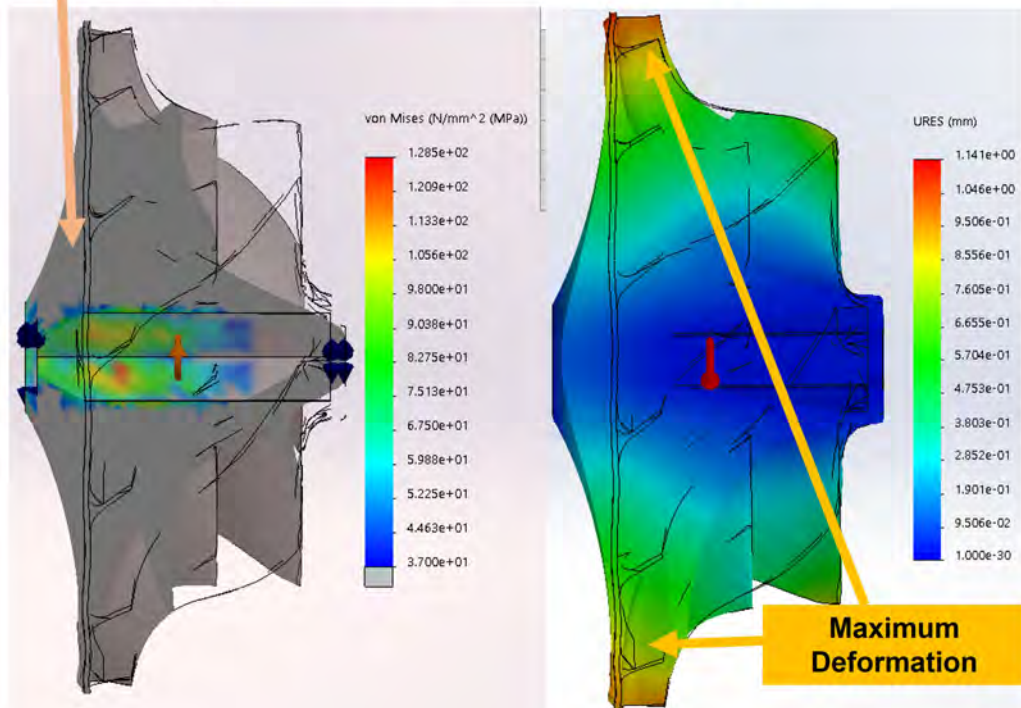
Figure 137. ULTEM 9085 Comparison model 2 Hex In Thermal Centrifugal Combined a) 98 kRPM Stress Profile b) 98 kRPM Deformation Profile c) 62 kRPM Stress Profile d) 62 kRPM Deformation Profile

Comparing the deformation magnitudes was the simplest way to quantify consistency. Table 29 summarizes the percent difference in deformation between the two approaches. Table 29 indicates there is a 5% or less error carry over between the

Table 29. ULTEM 9085 Model Comparison 1 (Hex Void) and 2 (Hex In)

	Maximum deformation (mm)		
	Hex Void	Hex In	% Diff
Thermal Only	0.30	0.30	1.43
Centrifugal Only	2.43	2.55	4.91
Combined 98kRPM	2.57	2.49	3.20
Combined 62kRPM	1.15	1.14	0.35

model with and without the hex sleeve. This result shows that the inclusion of the hex sleeve is accurately accounted for in the FEA model.

4.2.3 SolidWorks and ANSYS Comparison.

The next step was to determine how close the SolidWorks model compared with Bauer's ANSYS results [1]. Since the common material that both this study and Bauer's study investigated was ULTEM 9085, it was chosen as the reference material for the two solvers. Bauer's input data is shown below in Table 30 [1].

Table 30. Bauer's ULTEM 9085 data at 400 K [1]

Temperature, K	400
σ_u, MPa	24.84
E, GPa	1.16
α, μm/m-K	5.76
ρ, kg/m^3	1270
k, W/(m*K)	0.22
ν	0.44

Since Bauer did not use an aluminum hex sleeve, his results were compared to the ULTEM 9085 data in this study without the hex sleeve in the compressor bore. The stress profile of both the SolidWorks and ANSYS model at 98,000 RPM are

shown in comparison in Figure 138a and c, while the deformation profile for the SolidWorks and ANSYS model at 72,375 RPM (Bauer's prediction of ULTEM 9085 compressor failure) are also shown in Figure 138 b and d. The deformation profile for the SolidWorks and ANSYS model at 98,000 RPM are shown in Figure 139a and b.
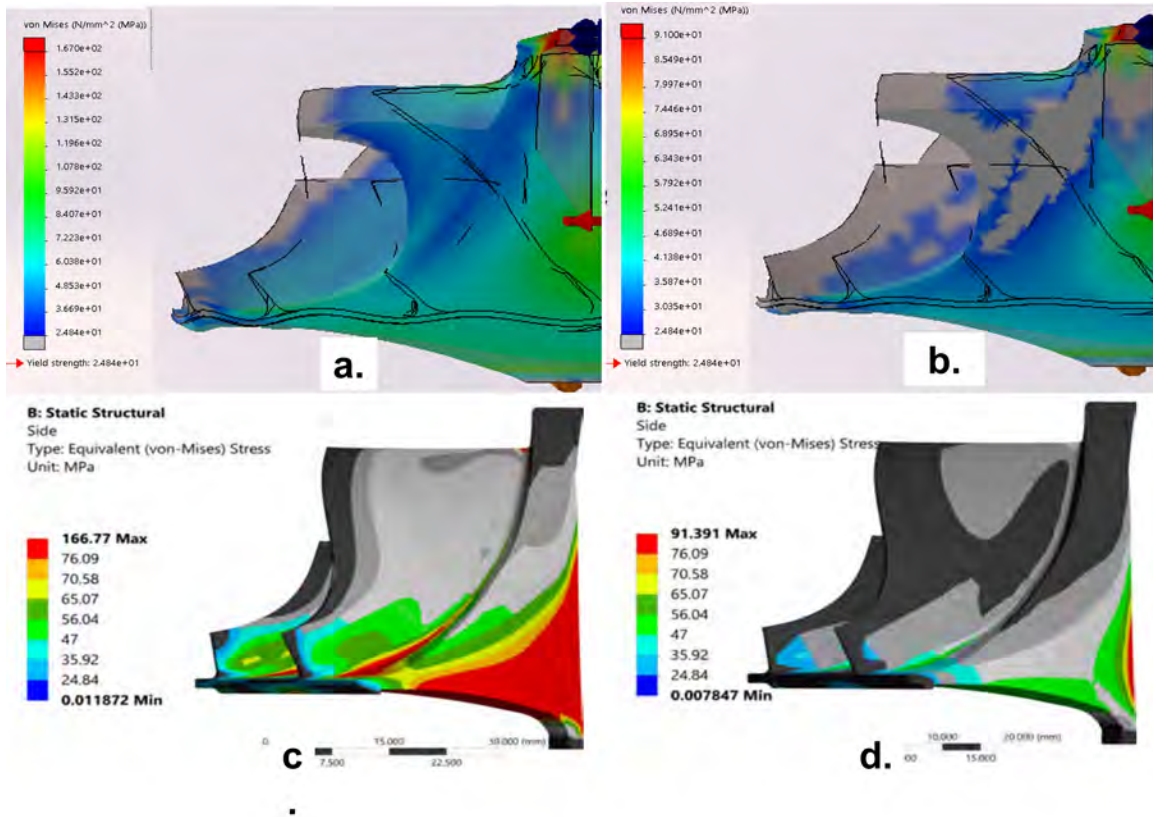

Figure 138. Preliminary Model Thermal and Centrifugal combined outputs a) 98,000 RPM Bauer's data (SolidWorks) b) 72,375 RPM Bauer's data (SolidWorks) c) 98,000 RPM Bauer's data (ANSYS) d) 72,375 RPM Bauer's data (ANSYS) [1]
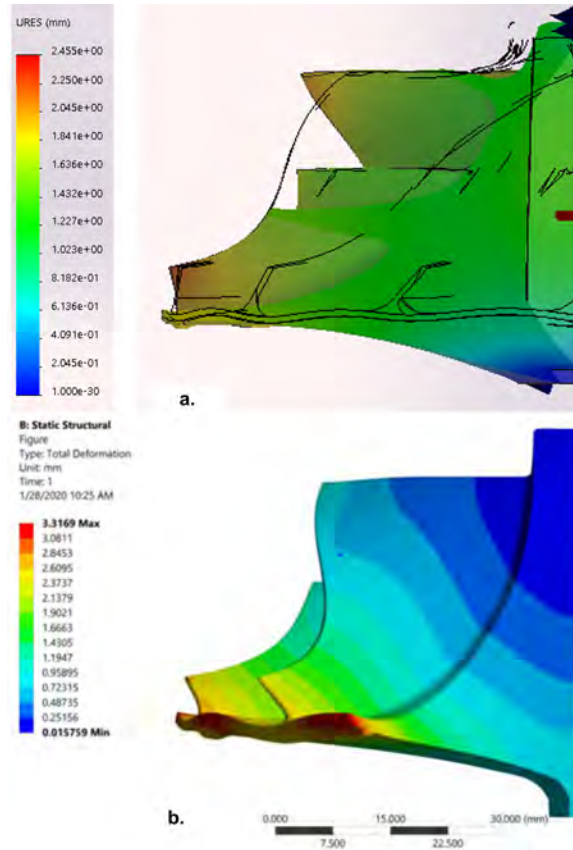
Figure 139. Comparison SolidWorks and Bauer's ANSYS data a) Deformation Solid-Works 98 kRPM b) Deformation ANSYS 98 kRPM

The combined displacement output results shown in Figure 139 have a maximum displacement of 2.3 mm for the SolidWorks model, which is within ±1 mm of Bauer's ULTEM 9085 compressor deformation result (3.3mm [1]). However, Bauer's stress plot indicates that the majority of the compressor is already experiencing yield prior to reaching 72,375 RPM as indicated in Figure 138b in which the regions that are gray are under the ultimate stress while the regions that have color indicate surpassing ultimate stress. Because of the large region of failure in the compressor, Figure 138b implies that the onset of failure likely would occur at a lower speed than 72,375 RPM. In both Figure 138a and b, there exists a concentration of stress along the bore, which is similar to Bauer's ANSYS model. However, unlike Bauer's model, the

188

maximum stress of 167 MPa on the SolidWorks model was located at the inlet lip of the compressor bore. What Figure 138 ultimately shows is that the SolidWorks FEA model simulates a yield over a larger region on the model than Bauer's ANSYS model. This difference between the two models could be due to some underlying differences in the solvers. The concentration of stress at the lip section in the SolidWorks model could be due to a difference in constraints-since the SolidWorks model used two bearing constraints (front and back of the compressor bore) to assure the compressor did not change axial location during the static analysis as discussed in Section 3.3. Bauer does not comment on the constraints of the ANSYS model in his studies.

While the results show that the FEA model produced a different profile in stress between SolidWorks and ANSYS, the rough values in stress and deformation are within the same orders of magnitude as Bauer's data. Because of this, the model was used to further investigate other compressor material cases.

The last point regarding Bauer's relevant work is the criteria for impingement. Bauer uses the maximum deformation for the stock AL-7075-T6 at 400 K and 98,000 RPM as the deformation limit for impingement since it was understood that the P400 compressor was designed with enough clearance for the stock compressor to deform at full operating conditions. This study defined the impingement limit using the same Al-7075-T6 material analyzed in the SolidWorks model for maximum deformation. The only difference is that this study used 475 K and generic Al-7075-T6 material property data available in the SolidWorks inventory as a reference value. The SolidWorks outputs for the Al-7075-T6 data is summarized with only deformation information for brevity shown in Figure 140. This figure notes that the maximum total deformation magnitude for the Al-7075-T6 compressor at peak operating conditions is 0.31 mm. In the SolidWorks direction convention, total deformation refers to the vector-summed deformation in the radial, tangential, and axial directions. Radial

189

and axial are the most relevant in this study since deformation in either of those two directions could lead to impingement on the shroud. As such, the total displacement of the stock compressor was further broken down into its radial component (0.28 mm) and axial component (0.016 mm) as representative impingement limits. Radial and axial deformation for the stock compressor are also shown in Figure 140b and c, respectively. Thus, this amount of deformation must exceed these values to be considered for impingement.
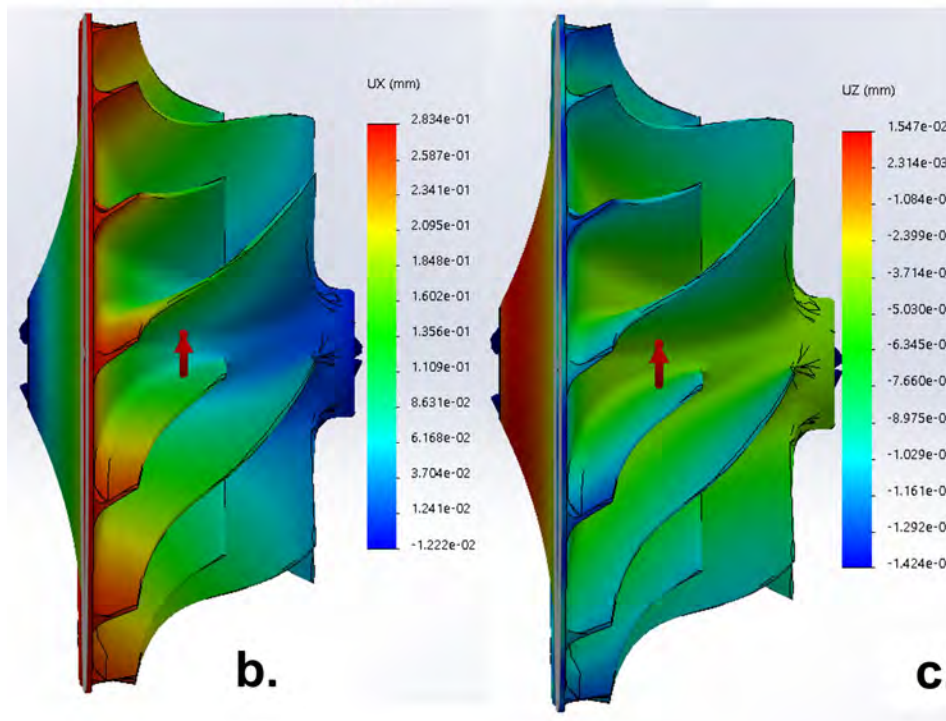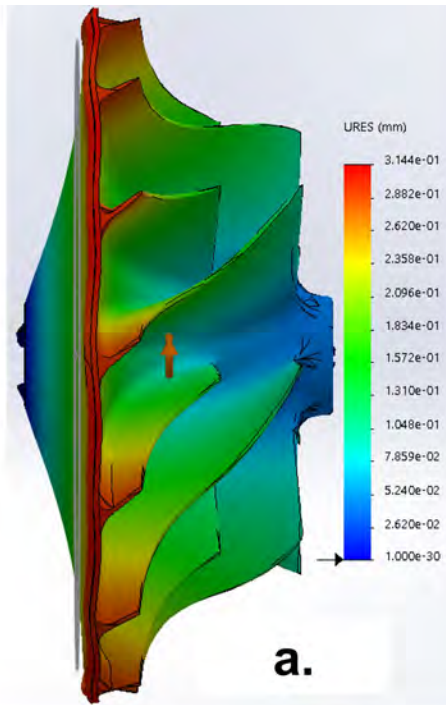
Figure 140. Al-7075-T6 Compressor 475 K 98 kRPM Deformation a) Total Deformation b) Radial Deformation c) Axial Deformation

4.2.4 1st Compressor: Modified JetCat P400, ULTEM 9085.

4.2.4.1 ULTEM 9085 FEA-Temperature Variant Model.

The compressor was modeled for both P400 temperature conditions and for room temperature conditions. Each version of the FEA model for the ULTEM 9085 compressor was incremented from room temperature and 0 RPM to thermal and rotational conditions expected for full-power P400 operation (98 kRPM and 475K).

Figure 167 (In Appendix A, Section A.1) displays the temperature profile, the deformation due to temperature effects, and the stress due to temperature effects. The stress profile due to temperature shows that the model does not exhibit yield due to the temperature effects. Temperature effects cause the compressor to experience a total deformation of 0.29 mm. Figure 168 (In Appendix A, Section A.1) shows the stress and temperature profile solely due to centrifugal effects. Maximum stress due to centrifugal loads is located at the bore section, and stress exceeding the ultimate strength is visibly observed at the bore section. The compressor experiences a total deformation of 2.55 mm due to centrifugal effects. Figure 141 presents the stress and deformation due to both temperature and centrifugal effects at speeds of 98,000 RPM and 62,000 RPM. The stresses exceed the ultimate strength of ULTEM 9085 at the bore section of the compressor. The maximum total deformation is 2.49 mm at 98,000 RPM and 1.41 mm 49,000 RPM which implies impingement as it exceeds the 0.31 mm criterion for impingement on the shroud. The radial and axial deformation results in Figure 169 (In Appendix A, Section A.1) show 0.7 mm radial deformation at the outer edges of the blade tips and 0.3 mm axial deformation at the inner blade tips closer to the inlet side, which exceeds that of the stock compressor at operating conditions. It was determined from the model during this incrementing of thermal and rotational conditions that the compressor would fail at 49,000 RPM and 384K.
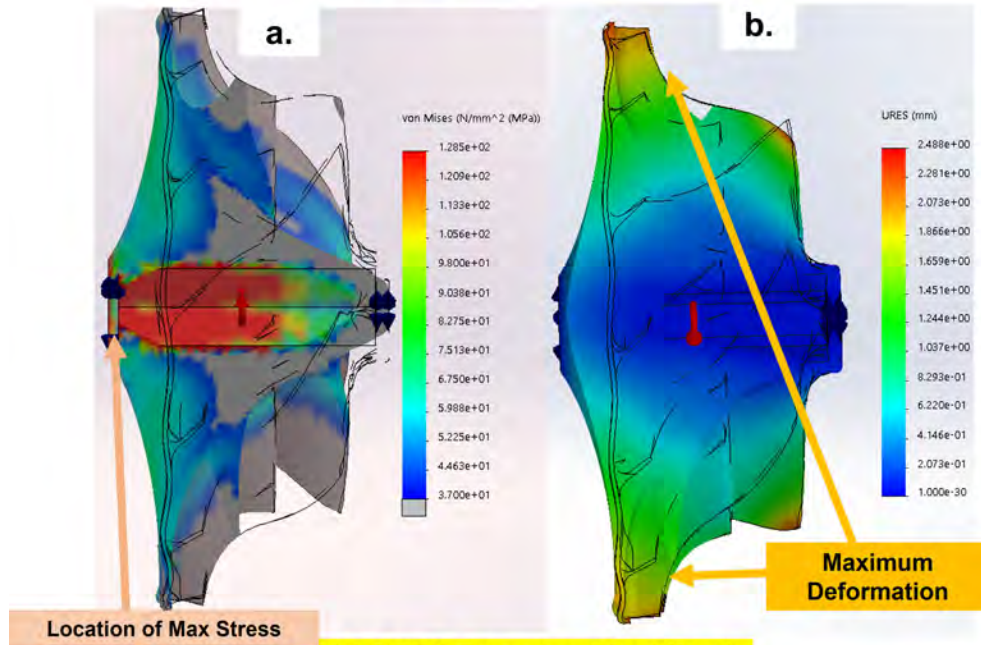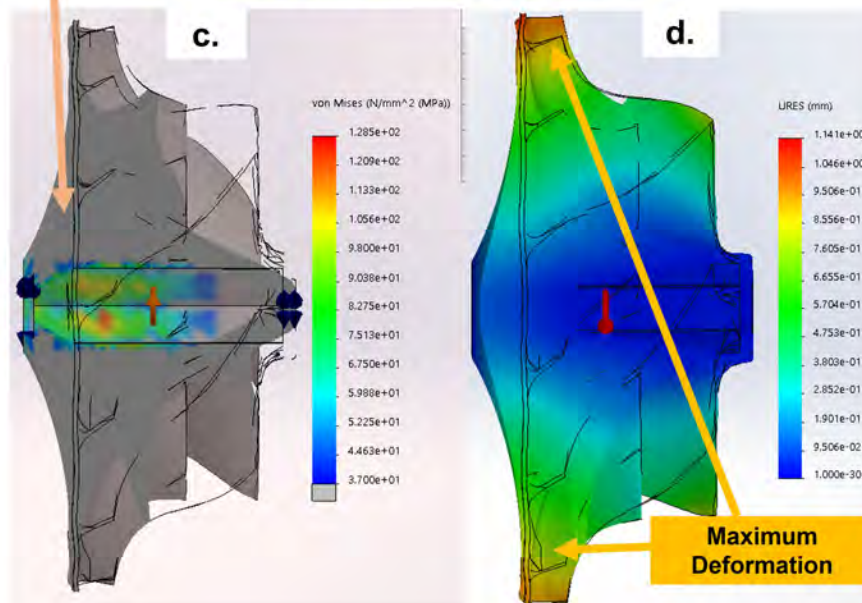
Figure 141. ULTEM 9085 Compressor Temp Centrif Comb a) Stress 98 kRPM b) Deform 98 kRPM c) Stress 49 kRPM d) Deform 49 kRPM

4.2.4.2 ULTEM 9085 FEA-Room Temperature Model.

Figure 170 (In Appendix A, Section A.2) displays the temperature profile, the deformation due to temperature effects, and the stress due to temperature effects. Figure 171 (In Appendix A, Section A.2) shows the stress and temperature profile solely due to centrifugal effects. Maximum stress due to centrifugal loads is located at the bore section. The total deformation is the vector sum of both axial and radial deformation. The compressor exhibits 2.29 mm of total deformation at the blade tips due to centrifugal effects. Stress exceeding the ultimate strength of ULTEM 9085 is observed at the bore section. Figure 142 presents the stress and deformation due to both temperature and centrifugal effects at speeds of 98,000 RPM and 62,000 RPM. The stresses exceed the ultimate strength of ULTEM 9085 at the inner bore region of the compressor. The total deformation at the blade tips is 2.28 mm for 98,000 RPM and 0.905 mm for 62,000 RPM which implies impingement as it exceeds the established impingement limit. The radial and axial deformation results in Figure 172 (In Appendix A Section A.2) show 0.61 mm radial deformation at the outer edges of the blade tips and 0.79 mm axial deformation at the inner blade tips closer to the inlet side, which exceeds that of the stock compressor at operating conditions. It was determined from the model during this incrementing of thermal and rotational conditions that the compressor would fail at 62,000 RPM at room temperature.
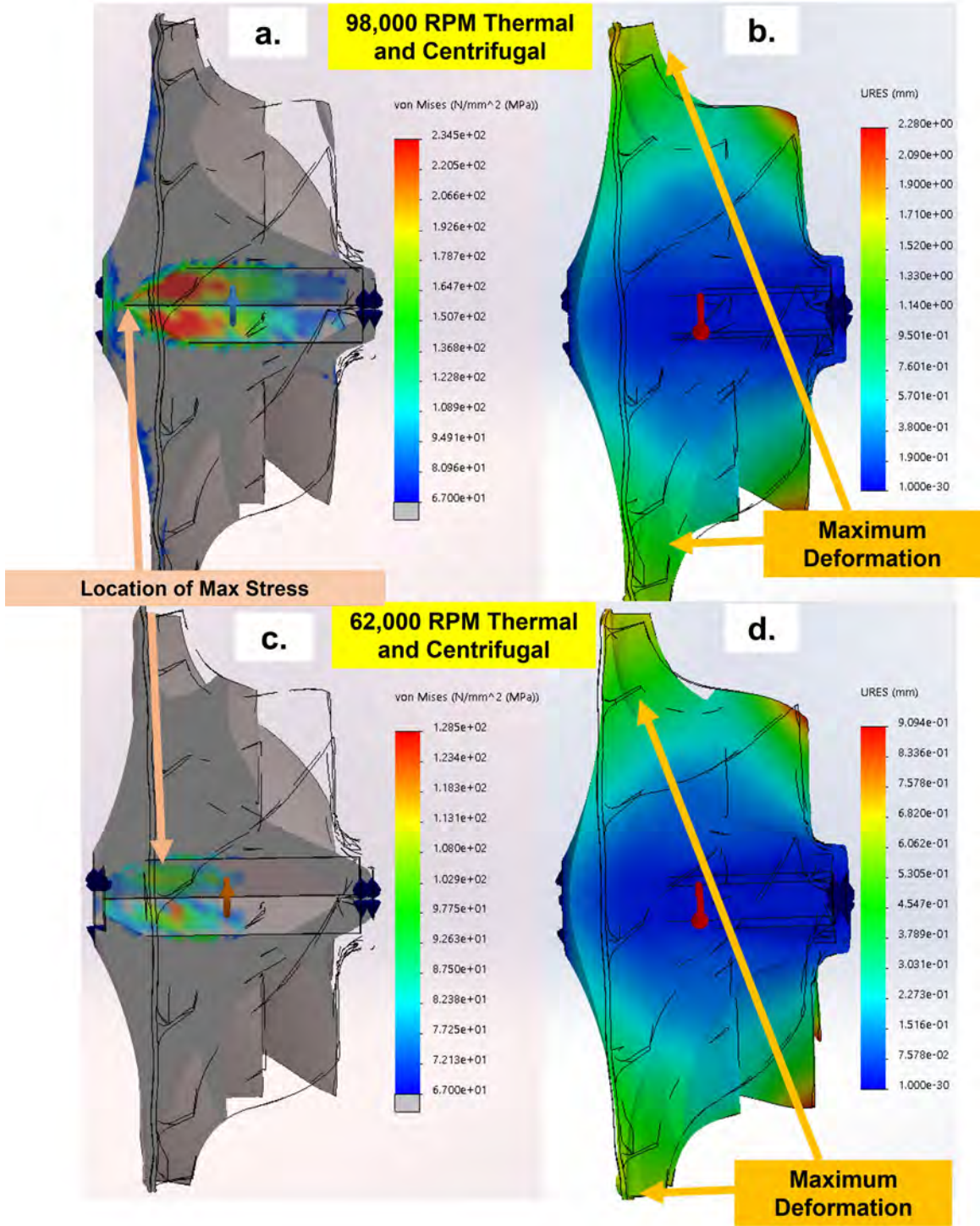
Figure 142. ULTEM 9085 Compressor RMT Temp Centrif Comb a) Stress 98 kRPM b) Deform 98 kRPM c) Stress 62 kRPM d) Deform 62 kRPM

4.2.5　2nd Compressor: Modified JetCat P400, Onyx-Carbon Fiber.

Two Onyx-Carbon fiber compressors were printed at 35% infill with reinforcement. While reinforcement and maximum infill (relative to matrix) were desired, Onyx's temperature limit deemed it less desirable for this application. Further reinforcement-infill combinations with Onyx were not pursued thereafter. Since Onyx has the highest ultimate strength at room temperature, it was used as a reference for maximum possible operation at room temperature. The Onyx-Carbon fiber compressor was expected to perform the best among the three compressors at room temperature and perform the worst among the three at high temperatures. However, the SolidWorks FEA model does not have an input for glassification temperature and would therefore be an inherent inaccuracy in the model if it were run at the highest temperature feasible for Onyx-Carbon Fiber. The compressors available in this study would themselves not be representative of the full capability of Onyx-carbon fiber given the 35% infill. Like the ULTEM 9085 compressor model, the Onyx-carbon fiber model was incremented from room temperature and 0 RPM to thermal and rotational conditions expected for full-power P400 operation (98kRPM and 475K).

4.2.5.1　Onyx-Carbon fiber FEA-Temperature Variant Model.

Figure 173 (In Appendix A, Section A.3) displays the temperature profile, the deformation due to temperature effects, and the stress due to temperature effects. The stress profile shows that the model does not exhibit yield due to the temperature effects alone, and the compressor deforms 0.17 mm. Figure 174 (In Appendix A, Section A.3) shows the stress and temperature profile solely due to centrifugal effects. Maximum stress due to centrifugal loads is located at the bore section and stress exceeding the ultimate strength of the Onyx-Carbon fiber is observed. The compressor has a total deformation 0.96 mm at the tips of the compressor blades. This

196

deformation expands the direction of axial and radial deformation toward the inlet side of the shroud and would lead to rubbing on the shroud. Figure 143 presents the stress and deformation due to both temperature and centrifugal effects at the speeds of 98,000 RPM and 75,000 RPM. The stresses exceed Onyx-Carbon fiber ultimate strength at the bore region of the compressor. The maximum total deformation is 1mm in the axial and radial direction for 98,000 RPM and 0.66 mm (which is 1.89 mm less than the deformation of ULTEM 9085 at 384 K) for 75,000 RPM which implies impingement since it exceeds the 0.31 mm impingement criteria for the shroud. The radial and axial deformation results in Figure 175 (In Appendix A, Section A.3) show 0.53 mm radial deformation at the outer edges of the blade tips and 0.36 mm axial deformation at the inner blade tips closer to the inlet side which exceeds that of the stock compressor at operating conditions. It was determined from the model during this incrementing of thermal and rotational conditions that the compressor would fail at or around 75,000 RPM and 438 K. While seemingly optimistic, this model for Onyx-carbon fiber is not comprehensive because it does not account for glassification temperatures. More likely, Onyx-carbon fiber would melt or at best lose its ability to resist tension at temperature based on tensile test samples, when trying to operate as high as 438 K.
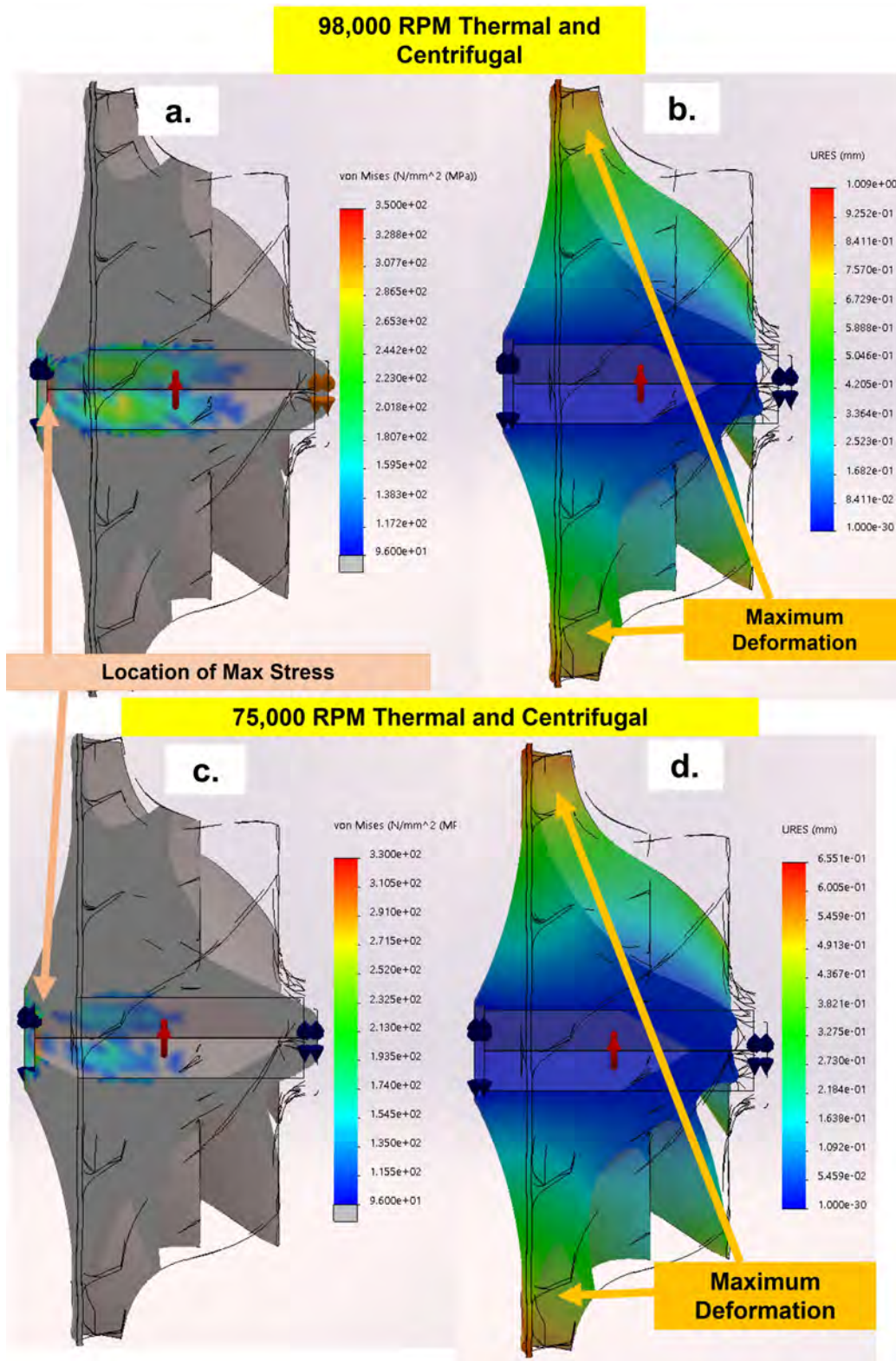
Figure 143. Onyx-CF Compressor Temperature Centrifugal Combined a) Stress 98 kRPM b) Deform 78 kRPM c) Stress 75 kRPM d) Deform 75 kRPM

4.2.5.2   Onyx-Carbon fiber FEA-Room Temperature.

Figure 176 (In Appendix A, Section A.4) displays the temperature profile, the deformation due to temperature effects, and the stress due to temperature effects. Figure 177 (In Appendix A, Section A.4) shows the stress and temperature profile solely due to centrifugal effects. Maximum stress due to centrifugal loads is located at the bore section, and the onset of failure is observed. Compressor experiences a total deformation of 0.55 mm in toward the inlet direction due to centrifugal effects which exceed the impingement limit which is 1.75 mm less than the centrifugal deformation of ULTEM 9085 at room temperature. Figure 144 presents the stress and deformation due to both temperature and centrifugal effects at the speeds of 98,000 RPM and 85,000 RPM. The stresses exceed ultimate strength of Onyx-Carbon fiber at the bore section of the compressor and the maximum total deformation is 0.55 mm in the axial and radial direction for 98,000 RPM and 0.42 mm in the axial and radial direction for 85,000 RPM which implies impingement. The radial and axial deformation results in Figure 178 (In Appendix A Section A.4) shows 0.28 mm radial deformation at the outer edges of the blade tips and 0.36 mm axial deformation at the inner blade tips closer to the inlet side which exceeds that of the stock compressor at operating conditions. It was determined from the model during this incrementing of rotational conditions that the compressor would fail at 85,000 RPM at room temperature. Onyx should deformation less and reach higher operating speeds than ULTEM 9085 at room temperature.
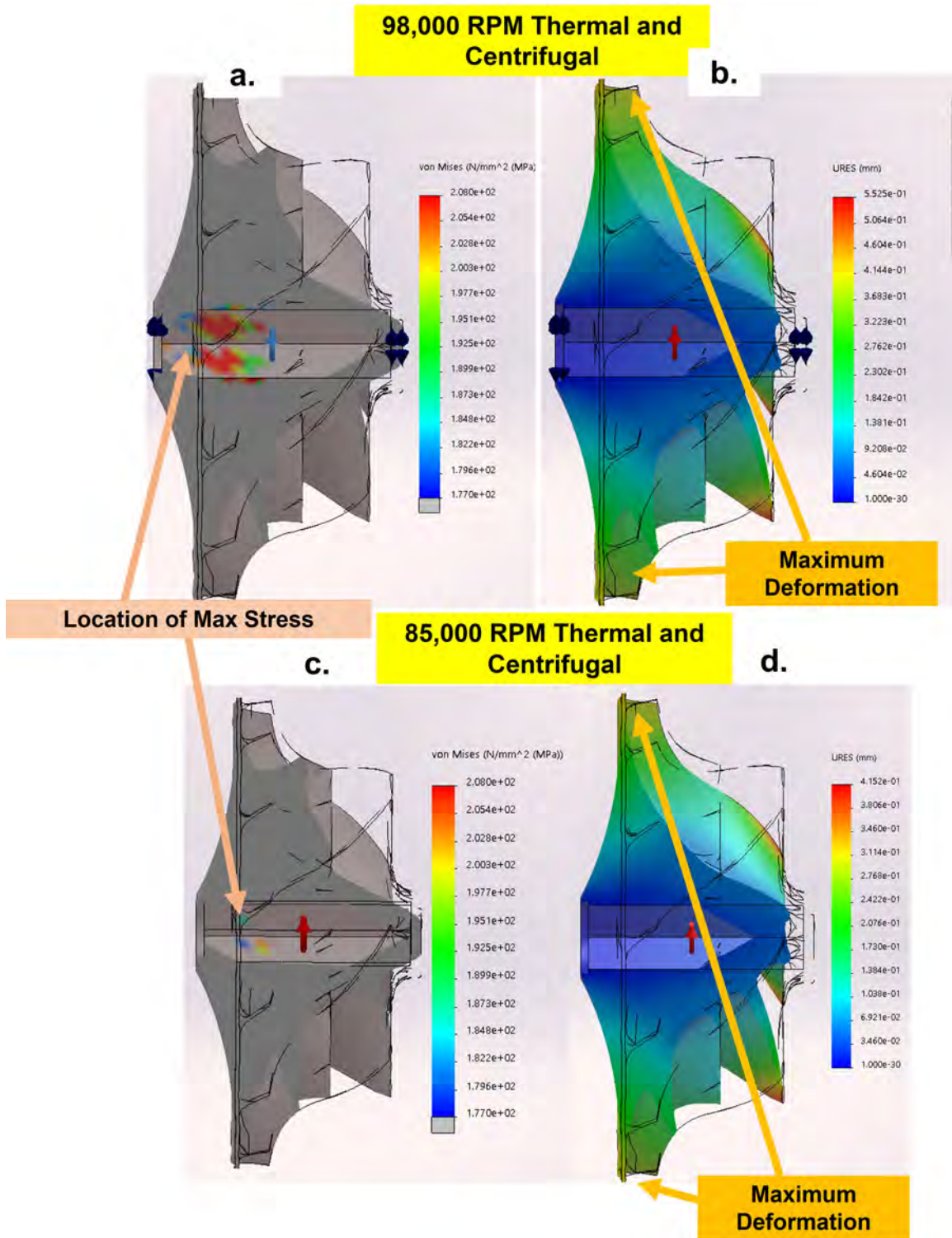
Figure 144. Onyx-CF Compressor Temp Centrif Comb RMT a) Stress 98kRPM b) Deform 98kRPM c) Stress 85kRPM d) Deform 85kRPM

4.2.6 3rd Compressor: Modified JetCat P400, Epoxy-Carbon Fiber.

The Epoxy-Carbon fiber compressor was the last compressor analyzed. Because it exhibited the best stiffness behavior during tensile specimen testing, in that it held significant tension at P400 operating temperature, it was expected to perform the best at elevated temperatures. It was similarly anticipated that the random orientation of the fibers cause a nonuniform stress profile on the compressor hub mold and hence the reinforcement strengthened every direction since the fibers were not aligned in just one direction. Because of the complex geometry of the compressor blades, only the hub was planned to be molded. As such, the FEA model geometry had blades removed to match the physical hub. The full-bladed compressor made out of Epoxy-Carbon fiber was also modeled thereafter to understand to predict failure for an Epoxy-Carbon fiber compressor.

There were two versions of this compressor FEA model that were used. The first version uses the compressor hub without the aluminum hex sleeve in the model. The second model is the compressor in Epoxy-Carbon fiber with the aluminum hex sleeve molded in. These models were conducted at two temperatures, the first at the highest temperature prior to indicated failure and the second at room temperature. The failure location for both temperatures is most commonly seen at the interface between the hex sleeve and the epoxy component.

4.2.6.1 Epoxy-Carbon fiber FEA-Temperature Variant Model - Hub, No Hex Sleeve.

The first epoxy case modeled was the compressor hub without the hex sleeve with temperature variance. Figure 179 (In Appendix A Section A.5) displays the temperature profile, the deformation due to temperature effects, and the stress due to temperature effects for the Epoxy-Carbon fiber hub. The stress profile due to

temperature shows that the model does not exhibit yield due to the temperature effects alone. Temperature effects at 376 K caused a vector-summed deformation in the axial and radial direction toward the inlet side of 0.28 mm. Figure 180 (In Appendix A Section A.5) shows the stress and temperature profile solely due to centrifugal effects. Maximum stress due to centrifugal loads is located at the bore section, and stress exceeding the ultimate strength of the Epoxy-Carbon fiber is visibly observed. The stress profile seems to be slightly different for the Epoxy-Carbon fiber hub than the ULTEM 9085 and Onyx compressors. Since there are no fins in this geometry, the stresses exceeding the ultimate strength appeared in the bore section and at the lip of the compressor hub. The compressor had a total deformation toward the inlet side of 1.43 mm due to centrifugal effects at the edges of the hub. Figure 145 presents the stress and deformation due to both temperature and centrifugal effects at 98,000 RPM and 55,000 RPM. The stresses exceed ultimate strength at the bore of the compressor hub for 98,000 RPM, and the onset of failure began at the bore section for 55,000 RPM. The maximum total deformation toward the inlet side of the compressor was 1.60 mm at 98,000 RPM and 0.65 mm toward the inlet side at 55,000 RPM which implies impingement for the 98,000 RPM case, and for the 55,000 RPM case right before failure onset. Since the hub configuration was never expected to operate in a shrouded environment, the radial and axial deformation component break down was saved for the later case with the full compressor configuration (Section 4.2.6.3). It was determined from the model during this incrementing of thermal and rotational conditions that the compressor would fail at 55,000 RPM and 376K.
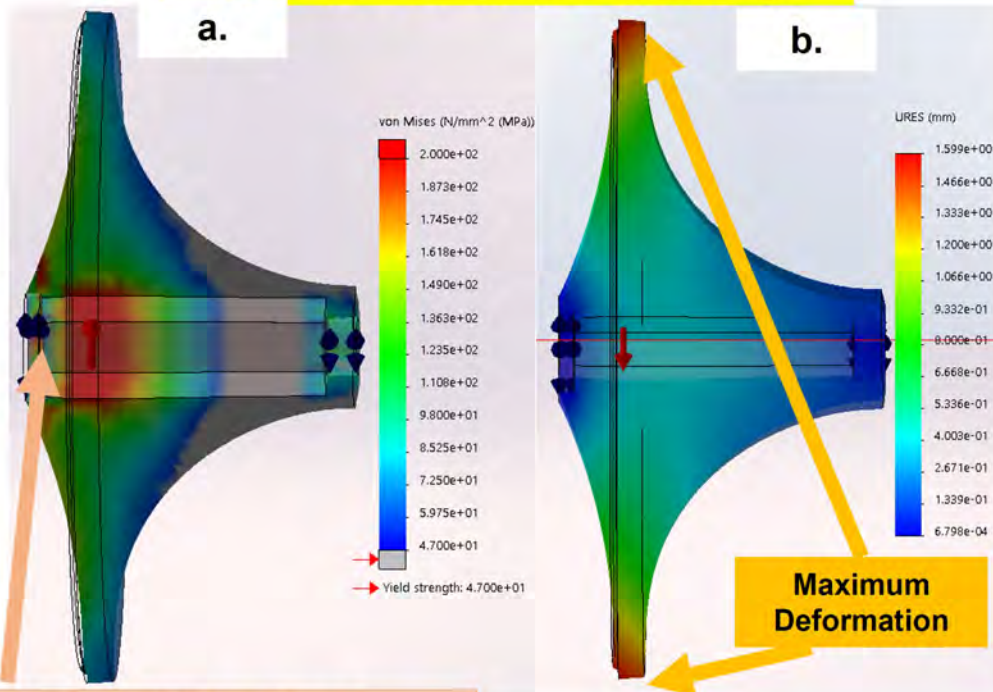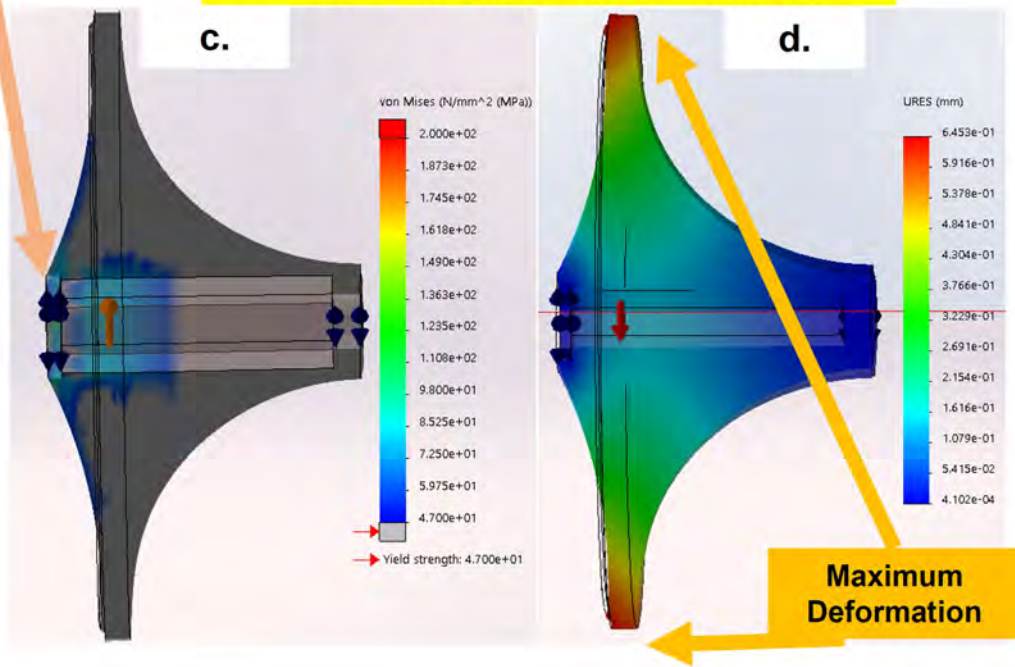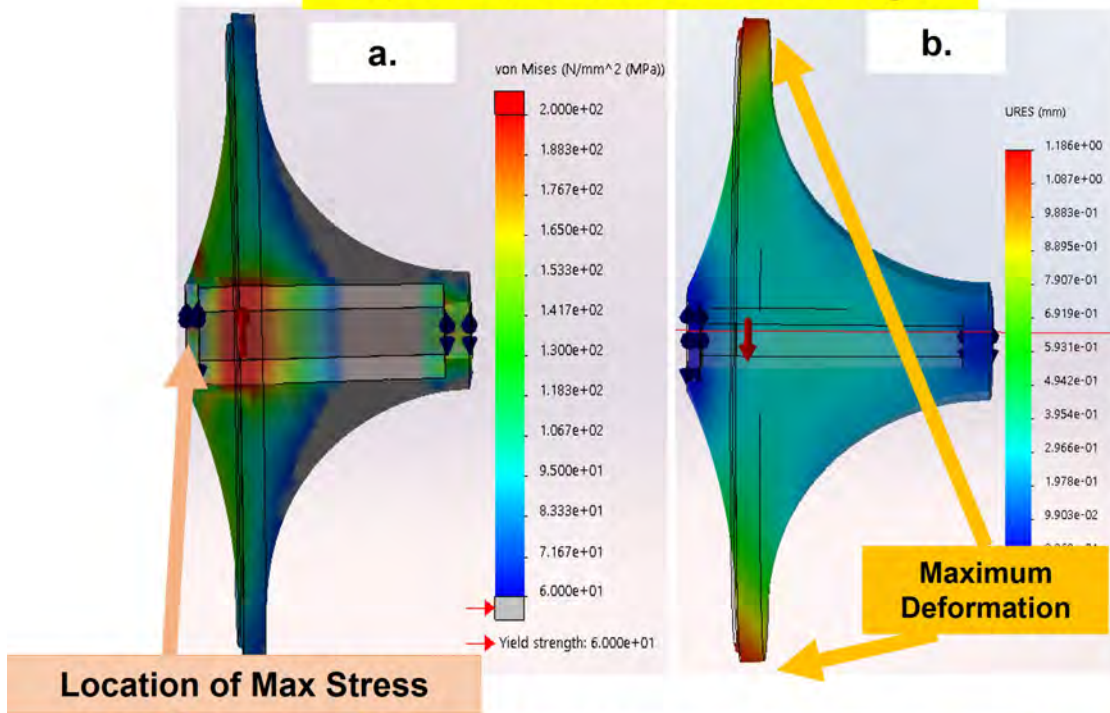
Figure 145. Epoxy-CF Hub Temp Centrif Comb a) Stress 98kRPM b) Deform 98kRPM c) Stress 28kRPM d) Deform 28kRPM

4.2.6.2 Epoxy-Carbon fiber FEA-Room Temperature - Hub, No Hex Sleeve.

The second Epoxy-Carbon fiber case modeled was the compressor hub without the hex sleeve at room temperature. Figure 181 (In Appendix A Section A.5) displays the temperature profile and the deformation due to temperature effects. Figure 182 (In Appendix A, Section A.5) shows the stress and temperature profile solely due to centrifugal effects. Maximum stress due to centrifugal loads is located at the bore section, and similar stress is observed at the lip of the hub. Stress exceeding the ultimate strength is observed since the gray areas indicate stresses below ultimate strength. The compressor deforms 1.18 mm toward the inlet side due to centrifugal effects which indicates impingement effects from the rotation alone. Figure 146 presents the stress and deformation due to both temperature and centrifugal effects at the speeds of 98,000 RPM and 60,000 RPM. The stresses exceed ultimate strength at the bore and lip region at 98,000 RPM and only at the bore for 60,000 RPM. The maximum total deformation is 1.19 mm at 98,000 RPM and 0.45 mm at 60,000 RPM which implies impingement at full speed and at 60,000 RPM. Since the hub configuration was never expected to operate in a shrouded environment, the radial and axial deformation component break down was saved for the later case with the full compressor configuration (Section 4.2.6.4). It was determined from the model during this incrementing of thermal and rotational conditions that the compressor would fail at 60,000 RPM at room temperature.
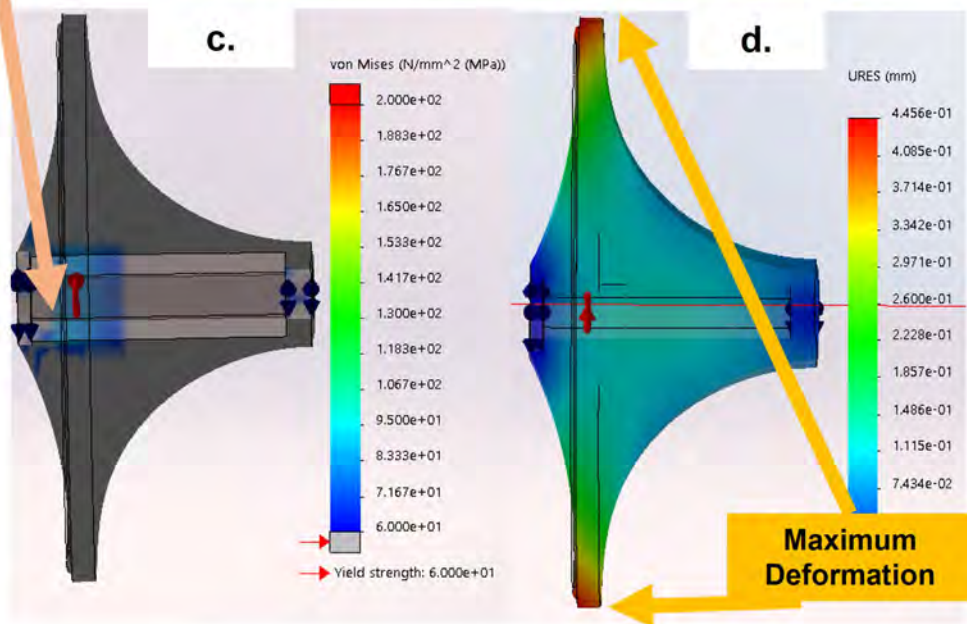
Figure 146. Epoxy-CF Hub Temp Centrif Comb Room Temp a) Stress 98kRPM b) Deform 98kRPM c) Stress 40kRPM d) Deform 40kRPM

4.2.6.3 Epoxy-Carbon fiber FEA-Temperature Variant Model - Compressor, with Hex Sleeve.

Figure 183 (In Appendix A, Section A.5) displays the temperature profile, the deformation due to thermal effects, and the resulting stresses due to thermal effects. The stress profile shows that the model does exceed the ultimate stress due to the thermal effects at the location of the bore, which reaches about 70 MPa. Temperature effects deform the compressor by 0.26 mm, which indicates that thermal effects alone will not lead to shroud impingement. Figure 186 (In Appendix A, Section A.5) shows the stress and temperature profile solely due to centrifugal effects. Maximum stress due to centrifugal loads is located at the bore section, and stress exceeding the ultimate strength of Epoxy-Carbon fiber is observed with a maximum stress of about 477 MPa. The compressor experiences a total deformation of 0.92 mm, which indicates impingement due to centrifugal loads. Figure 186 presents the stress and deformation due to both temperature and centrifugal effects at 98,000 RPM and 45,000 RPM. The stresses exceed ultimate strength of Epoxy-Carbon fiber at the bore region of the compressor at 45,000 RPM. The maximum total deformation is 2.19 mm which implies impingement as it exceeds 0.3 mm. The radial and axial deformation results in Figure 185 (In Appendix A, Section A.5) shows 0.39 mm radial deformation at the outer edges of the blade tips and 0.20 mm axial deformation at the inner blade tips closer to the inlet side which exceeds that of the stock compressor at operating conditions. It was determined from the model during this incrementing of thermal and rotational conditions that the compressor would fail at 45,000 RPM and 387 K.
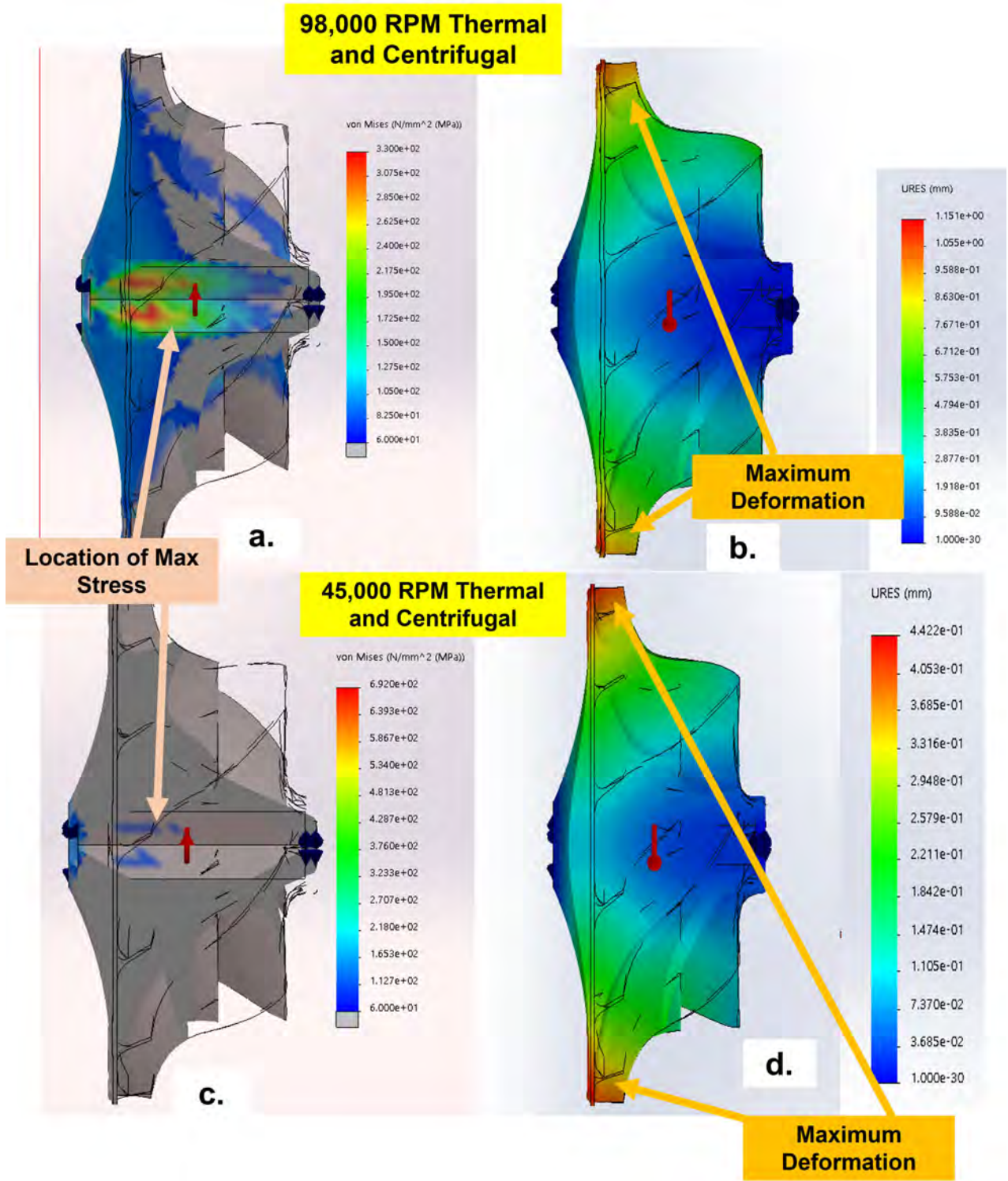
Figure 147. Epoxy-CF Compressor Temp Centrif Comb a) Stress 98kRPM b) Deform 98kRPM c) Stress 45kRPM d) Deform 45kRPM

4.2.6.4   Epoxy-Carbon fiber FEA-Room Temperature Model - Compressor, with Hex Sleeve.

The third case modeled was the full-bladed compressor with the hex sleeve with temperature variance. Figure 186 (In Appendix A, Section A.5) displays the temperature profile, the deformation due to temperature effects, and the stress due to temperature effects. Figure 187 (In Appendix A, Section A.5) shows the stress and temperature profile solely due to centrifugal effects. Maximum stress due to centrifugal loads is located at the bore section, and stress exceeding the ultimate strength of Epoxy-Carbon fiber is observed. The compressor experiences a total deformation of 0.74 mm due to centrifugal effects, which overshoots the criteria for assuring no impingement. Figure 148 presents the stress and deformation due to both temperature and centrifugal effects at the speeds of 98,000 RPM and 50,000 RPM. The stresses exceed ultimate strength of Epoxy-Carbon fiber at the bore section of the compression. The maximum total deformation is 0.76 mm for 98,000 RPM and 0.20 mm for 50,000 RPM which implies impingement is exected for 98,000 but not as for 0.2 mm. The radial and axial deformation results in Figure 188 (In Appendix A, Section A.5) shows 0.14 mm radial deformation at the outer edges of the blade tips and 0.14 mm axial deformation at the inner blade tips closer to the inlet side which is within limits deformation relative to the stock compressor at operating conditions. It was determined from the model during this incrementing of thermal and rotational conditions that the compressor would fail at 50,000 RPM at room temperature.
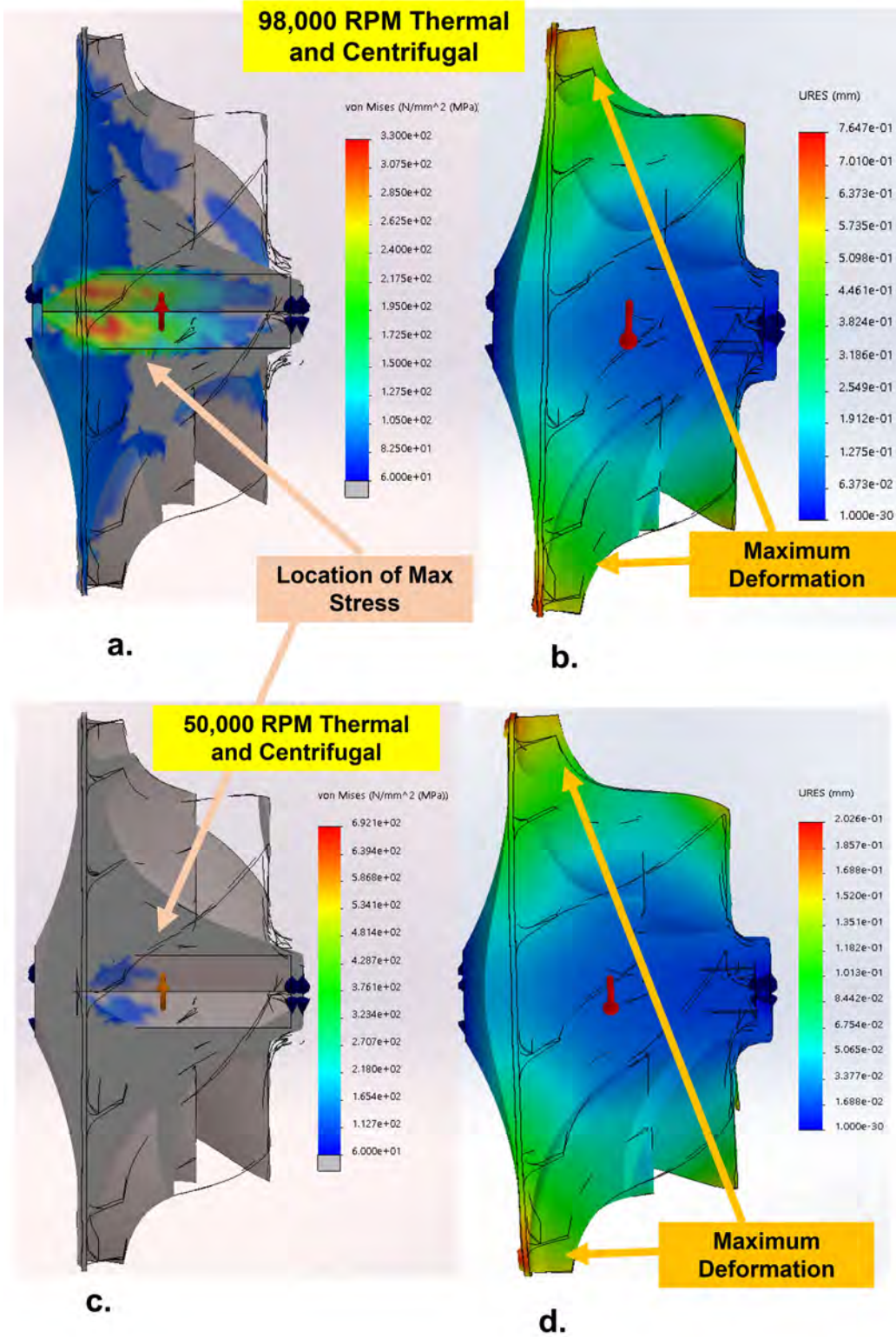
Figure 148. Epoxy-CF Compressor Temp Centrif Comb Room Temp a) Stress 98kRPM b) Deform 98kRPM c) Stress 50kRPM d) Deform 50kRPM

Among these models, Onyx-Carbon fiber achieved the highest expected speed (75 kRPM) and temperature (438K) compared to the other materials of interest. However, this doesn't consider its glassification temperature. At room temperature, Onyx-Carbon fiber reached 85 kRPM which is the highest speed exhibited. ULTEM 9085 and Epoxy-carbon fiber reach a maximum speed of 49 kRPM and 45 kRPM for the high temperature conditions respectivelly and may fair better in high temperature conditions as they still produce resistance to tension. Epoxy-carbon fiber produced the least deformation of 0.26 mm, which is a deformation magnitude within the deformation limit defined by the Al-7075-T6 model.

4.3 Print and Mold Results

4.3.1   3D Printed Compressors Results.

One of the challenges of 3D printing complex geometries is the significant overhang, as discussed in Section 2.3.2. There are two ways to solve this; the first method is to place supports during the 3D printing process to hold overhangs and avoid dripping of AM material. The second method is to print a modified version of the desired geometry with a flattened face and machine off the flattened face after the print is completed. To print the ULTEM 9085 and Onyx-Carbon fiber compressors the latter method was used. To print the compressor on a flat plate, the following geometry was used as shown in Figure 149. Figure 149a and b show the geometry for print and Figure 149c shows the geometry after machining.
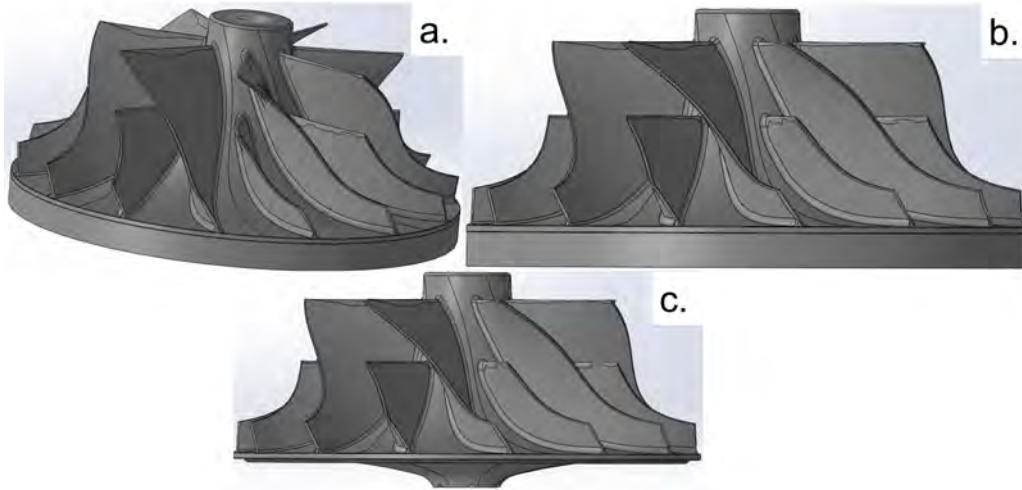
Figure 149. Printed Specimens a) Prior Back Face Surface Finish b) Prior Back Face Surface Finish (2) c) After Back Face Surface Finish

The ULTEM 9085 compressors printed at AFIT were smooth finished out of the print and had an even smoother back face after the flattened back was machined off. This is shown in Figure 150
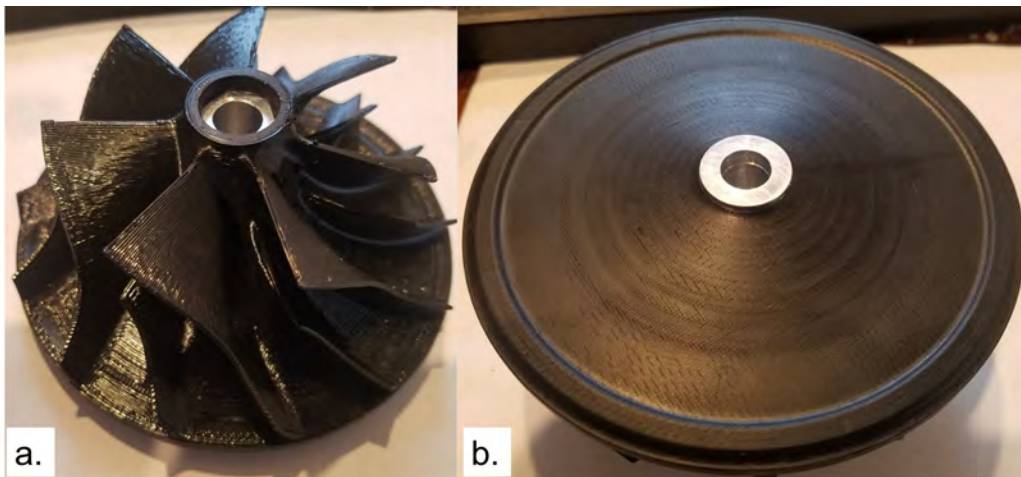

Figure 150. ULTEM 9085 Compressor a) Inlet side b) Exhaust side Post-machined

Onyx printed by UDRI had a slightly rougher surface finish out of the printer. The flattened back face was also machined. The surface finishing of the back face

211

revealed the voids built into the model (given that it is 35% infill). This is shown in Figure 151
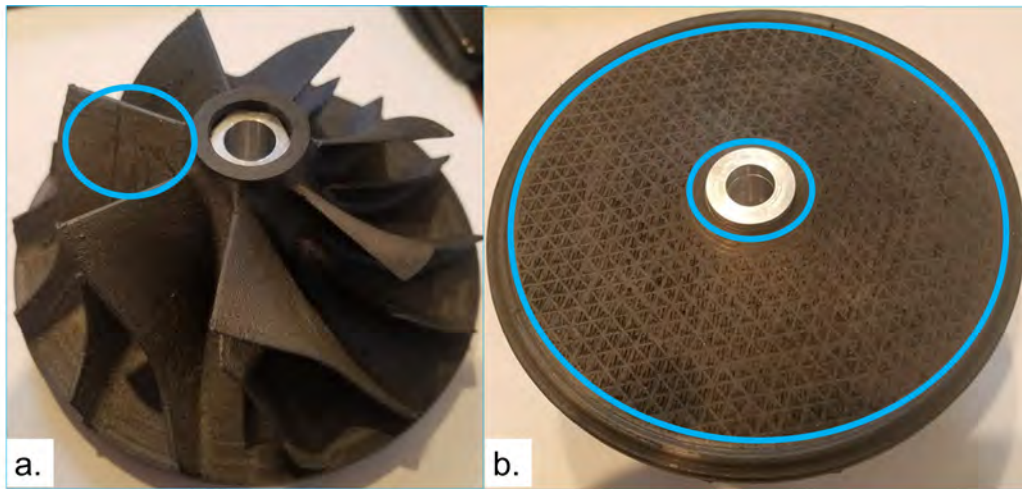

Figure 151. Onyx-Carbon Fiber Compressor a) Inlet side (circled drips) b) Exhaust side Post-machined (circled voids)

4.3.2   Molded Hub.

The steps required to mold the Epoxy-Carbon fiber compressor are shown in Figure 152. Figure 152a shows the compression mold prior to being filled with the Epoxy-Carbon fiber blend while Figure 152b shows the mold filled with the blend. Figure 152c displays the mold filled with the Epoxy-Carbon fiber blend and the top plate sitting on top of the blend. The bulky consistency of the blend caused a large clearance (larger than the designed clearance of 0.03") when the top plate was placed on the blend. This required the mold (with blend inside) to be pressed close to design clearance in Figure 152d. The mold was pressed down to 0.028" which was close enough to design clearance to proceed with the cure cycle. Since the screws in the top plate were required to stay in position to prevent leakage, a press block in Figure 152d was placed on the top plate to assure the 30 Ton Wabash Press would not damage the screws when applying pressure.
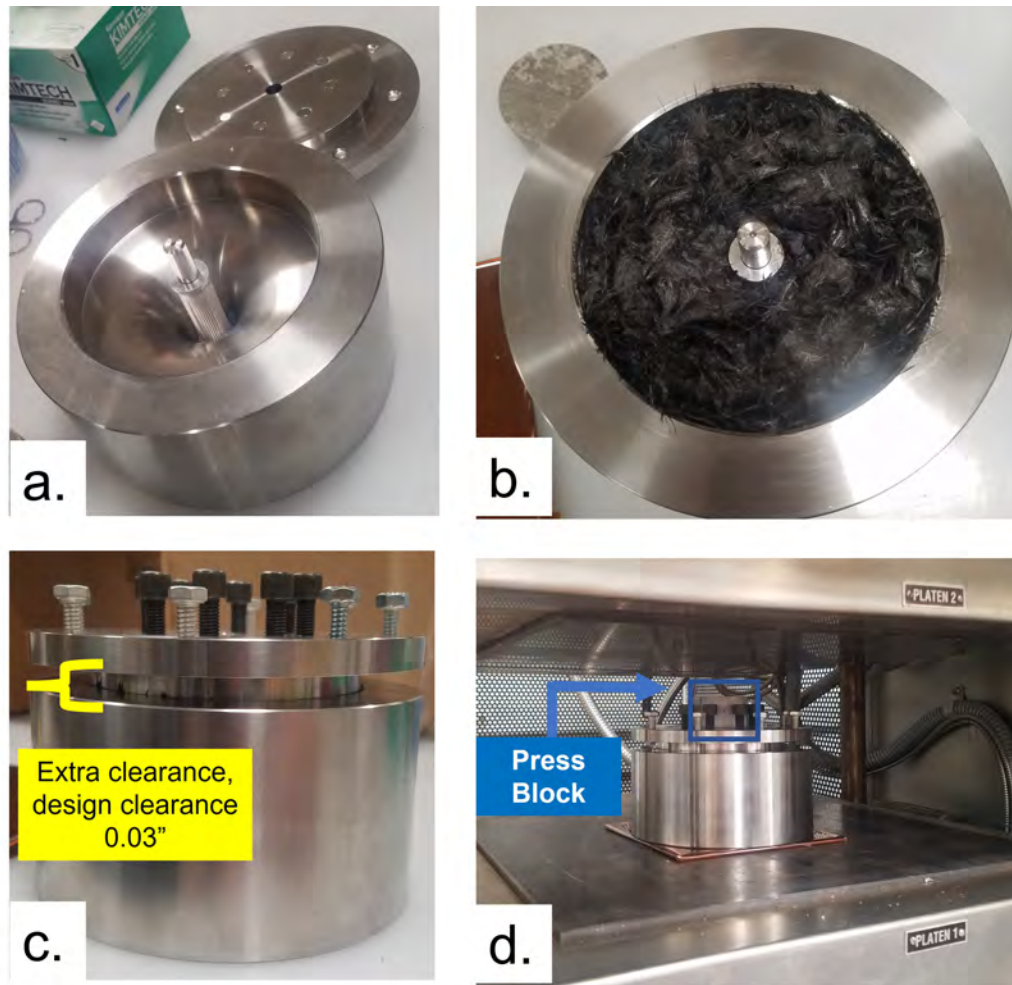
Figure 152. Hub Compression Molding Steps

The results of the inlet and exhaust side of the Epoxy-Carbon fiber hub is shown in Figure 153. The back face for the hub mold was also designed to be flattened and would require post-processed machining of the back face prior to spin testing. The molded hub was also accomplished and contained some noticeable surface imperfections. There appear to be surface voids on the back face, however, these are not problematic since the back face will be machined for spin testing. The inlet lip was molded with some jagged imperfections that would require some additional machining as well.

Figure 153. Epoxy-Carbon Fiber Surface Finish

4.4 Physical Spin Test

4.4.1 Failure Analysis.

Determining the mechanism and location of the physical compressor failure is difficult without visual evidence, so two cameras were used in this study, a low-speed and high-speed camera, to catch any visual data that could be detected from observation. However, all of the failures experienced in this study did not result in external component failures and failure behavior was not captured on camera. Figure 154 provides a visual of the camera views with the low-speed panic record camera and the high-speed Phantom Camera. In this study, each of the cameras were in the same position for all runs. Figure 155 displays the camera position relative to the test stand.
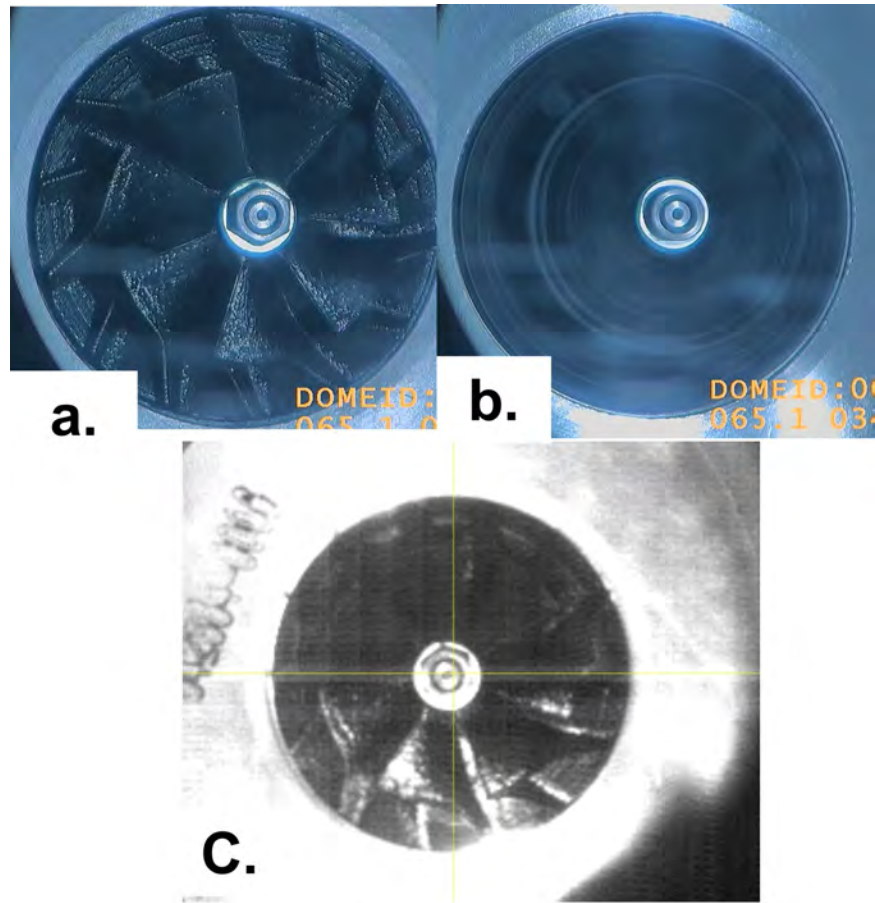
Figure 154. Spin Rig Camera Visual a) Low-Speed Camera, No Spin b) Low-Speed Camera, Spin c) High-Speed Camera, Spin
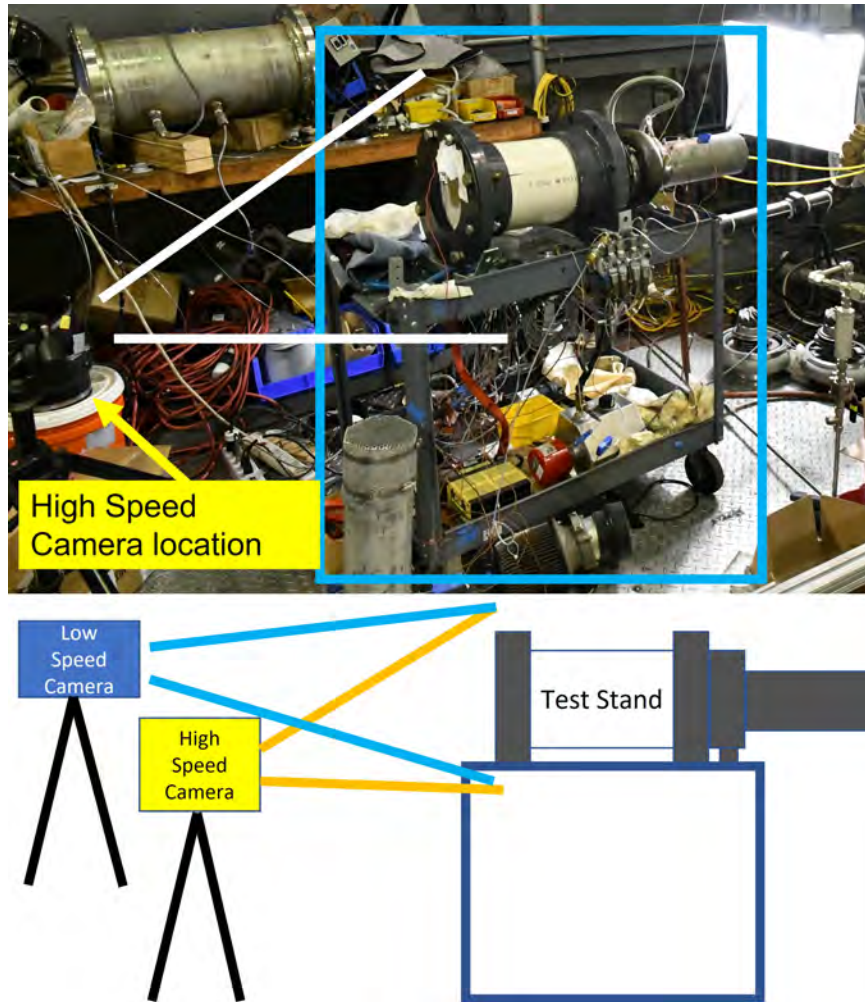
Figure 155. Camera Position with respect to Rig

The amount of kinetic energy involved in compressor rotation can turn one failure into a chain of additional failures. This could happen if, for example, one of the compressor blades fails, which causes a full assembly imbalance and lead to failure at the hub. Figure 156 displays the printed ULTEM 9085 P400 Compressors post-test. Among the three tested ULTEM 9085 compressors, the first survived up to 14,545 RPM at the 1466 second mark of the test as shown in Figure 157. The second compressor recorded several different peaks due to several pauses in testing for system checks or adjustments (i.e. readjusting the camera light). While the four peaks are

shown in Figure 158, but the relevant peak is the one at the highest speed of 13,103 RPM at the 11,818 second mark. The third compressor also had a brief pause for a system check and had two peaks, the initial peak being the higher of the two reaching up to 51,528 RPM at 4,574 seconds into the test while the second peak at 50,054 RPM at 6834 seconds into the test lead to failure. The results of the third spin test are shown in Figure 159.
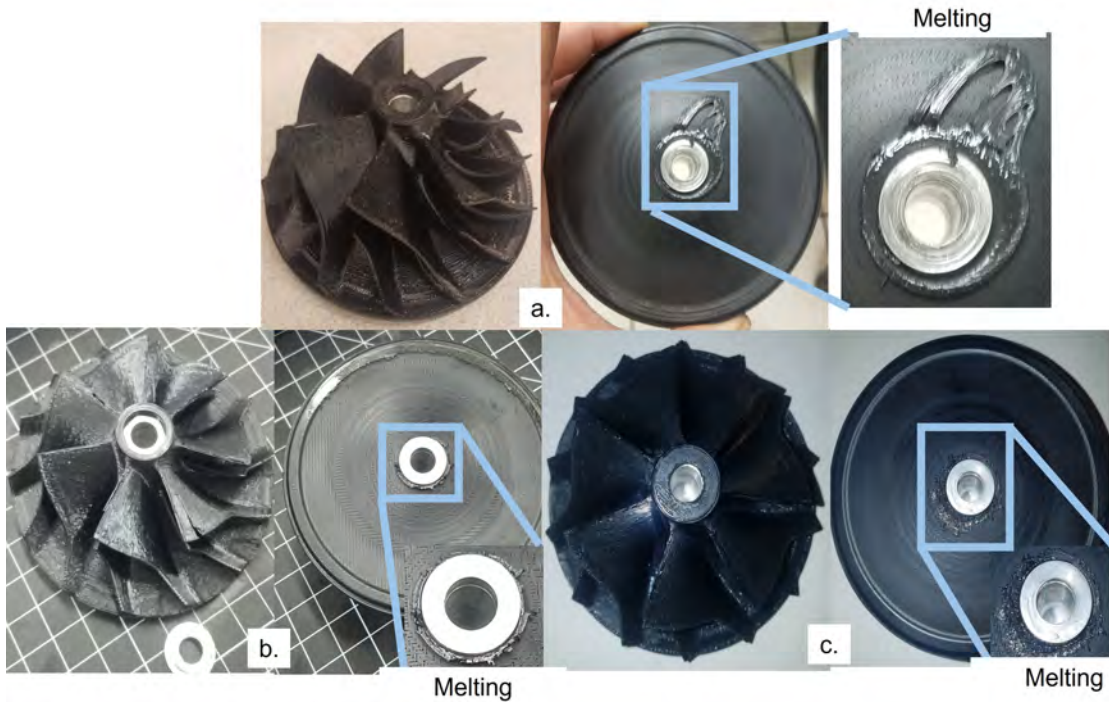

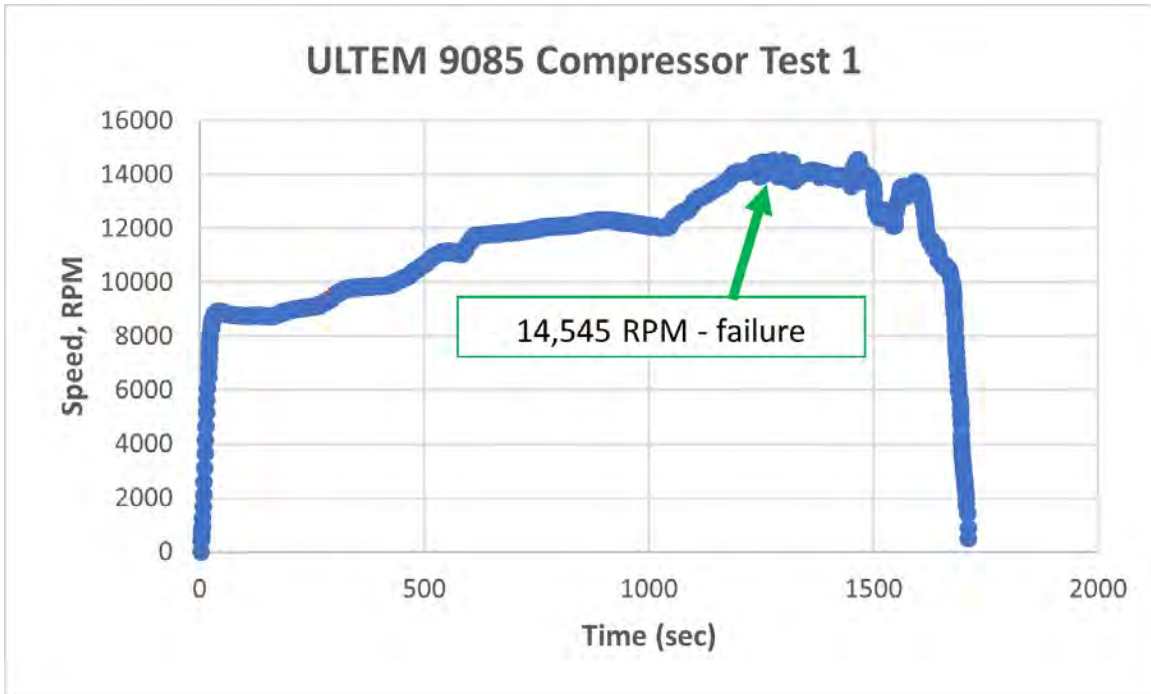
Figure 156. ULTEM 9085 Physical Compressors Post Spin Test
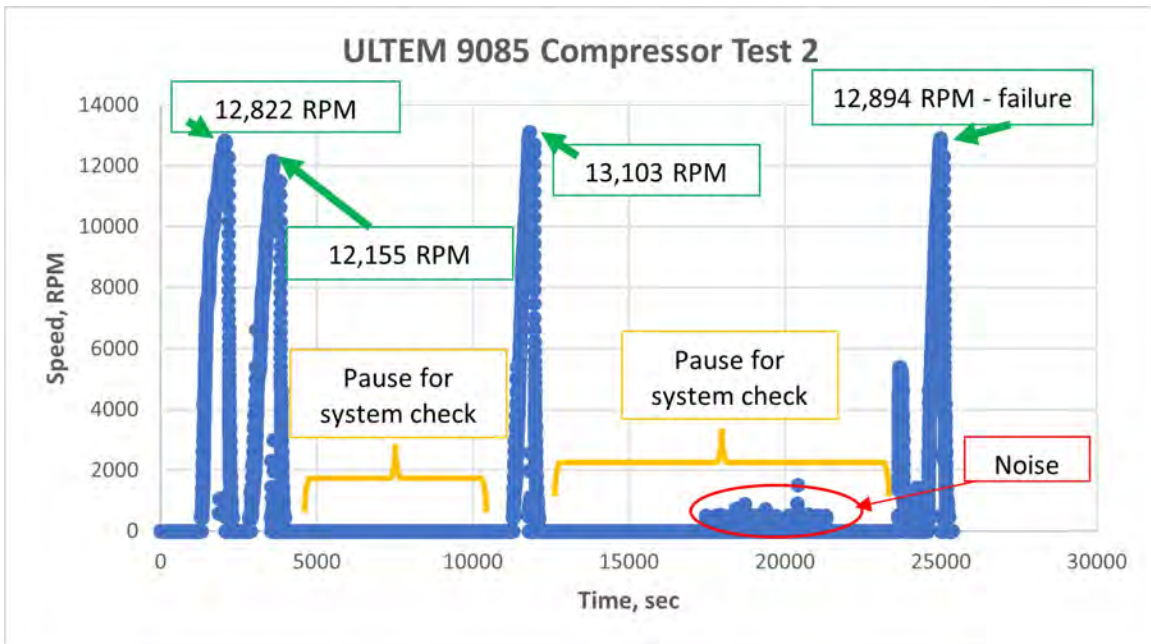
Figure 157. ULTEM 9085 Compressor Test 1

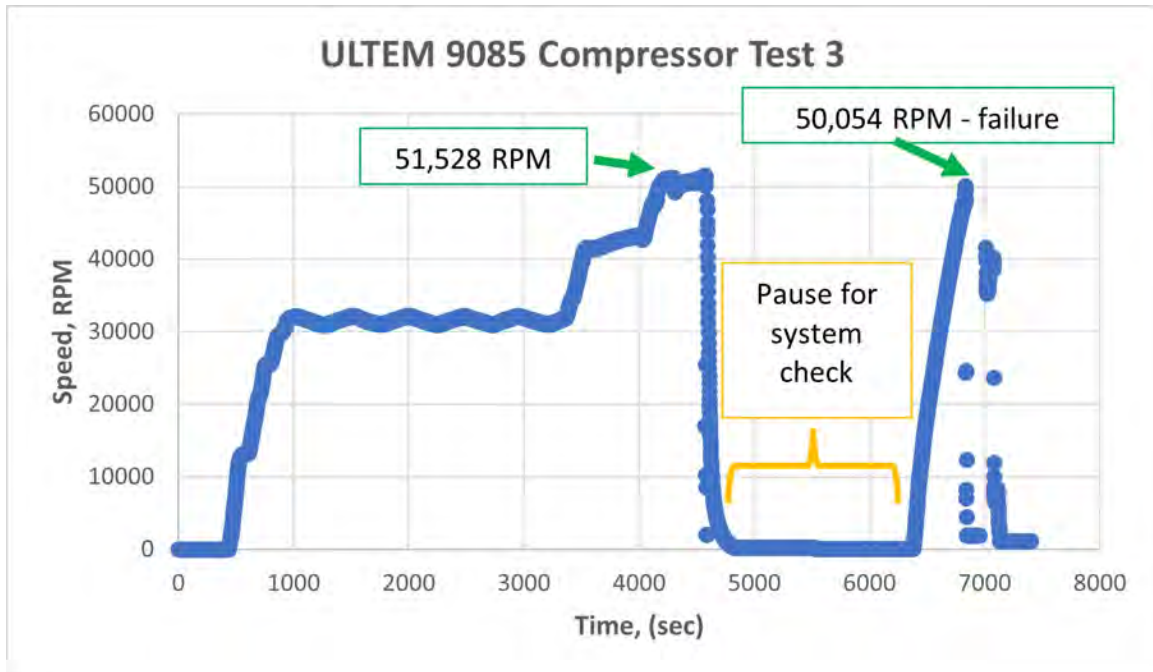**Figure 158. ULTEM 9085 Compressor Test 2**

Figure 159. ULTEM 9085 Compressor Test 3

4.4.2 Repetitive Turbocharger Failures.

One of the recurring issues that this study encountered during spin testing was turbocharger failure. Previous work noted a catastrophic turbocharger failure that required the safety features currently used on the rig. These failures including those in the present study seem to consistently be due to excessive heat due to friction. Three turbochargers have failed due to such issues. The first turbocharger experienced a compressor nut release that caused the compressor to slip on the shaft and generate friction in addition to other potential sources of friction. The friction generated heat melted internal components of the turbocharger, deeming it unusable thereafter. Evidence of the slipping can be seen in the spin-marked damage on the back of the aluminum hex sleeve of the compressor in Figure 156a and shown more closely in Figure 160. The friction generated enough heat to cause melting at the hex sleeve interface of the aluminum to the ULTEM 9085, also shown in Figure 160. The second
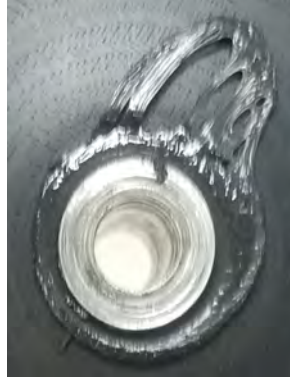
219

Figure 160. ULTEM 9085 Physical Compressors Post Spin Test Zoomed in - 1st Compressor

turbocharger attempted to solve the nut-release problem by applying Loctite to the nut. When that compressor was tested, the Loctite helped the nut remain in position, but the compressor also ended up slipping along the shaft and causing the same heat problem as the first turbocharger. This was because the nut was not tightened further in order to avoid excessive stress on the polymer lip of the inlet side of the compressor. The internal damage that occurred in this turbocharger was significant enough that some pieces inside may have melted into one another and welded the turbocharger assembly together. The second compressor, as shown in Figure 156b, showed signs of slippage with slightly more subtle spin-damage marks on the back of the hex sleeve and similar melting at the hex sleeve interface as the first failure. While the nut did not get loose, the second compressor seemed to have generated friction at the retainer plate side of the compressor, which caused some melting at the balance ring section of the second compressor, as shown in Figure 156b. After disassembling the second turbocharger, there was also visible damage to the retainer plate of the turbocharger, which indicated some amount of axial load that pressed the turbocharger onto the retainer plate. This would explain the significant cracks and slight mushrooming at the oil seal interface on the retainer plate in Figure 161.

Figure 161. Damage from 2nd Turbocharger

The third turbocharger assembly included the custom washer that diverted stress from tightening the nut to the aluminum hex sleeve. This assured that the nut could be tightened to factory specification and not scaled down because of the polymer lip. This turbocharger survived up to 50,000 RPM before it also failed. The compressor did not slip due to the tightness of the nut on the shaft. The failure seemed to be due to internal heating to the turbocharger. Large chunks of aluminum shavings were found in the internal components of the assembly after this third failure, which indicates potential issues with the oil source or bearing damage. It is possible that aluminum contaminated the oil source from previous tests or that the optimum amount of oil needed to cool the turbocharger was not being passed through the oil hoses. The oil seal also has even worse damage than the second turbocharger with the o-rings wrapped around the oil seal interface and ruining that entire region of the retainer plate as shown in Figure 162.
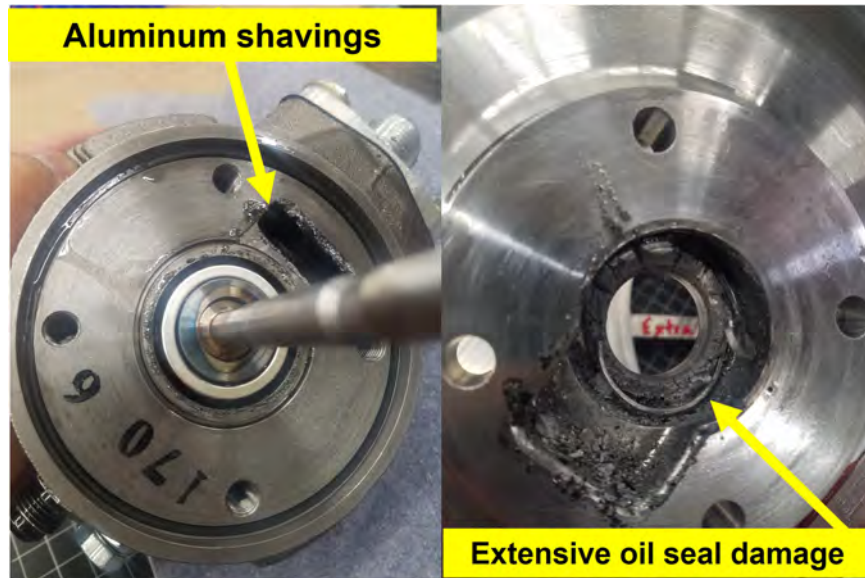
Figure 162. Damage from 3rd Turbocharger

The failure for each compressor was due to melting of the polymer by heating the bore section instead of centrifugal loading. Structural damage at the blade tips or fracture at the bore (as opposed to melting), would be indicators of structural failure due to centrifugal loading. Further, the speeds measured in the test data (between 13,000 and 50,000 RPM) were not a high enough speed to develop useful pressure (which would require at least 70,000 to 80,000 RPM as a minimum) for measuring performance with the shroud. Because of this, the spin test data in this study are inconclusive about the actual failure of the compressor.

After the third failure, it is believed that the cause of the friction failure at the bore is due to change in the direction of the forces on the turbocharger shaft. Since the compressor is not developing pressure, it is not loaded the same way as originally designed. This means that there is likely a reversal of the load direction on the turbocharger shaft. Thrust bearings or angular contact bearings require preloads and additional additive loads to be applied in a specific direction. If these bearings are spun at high speed without a preload or loaded in a direction that was not intended

the result would be excessive frictional forces in the bearing, leading to bearing failure and heating of the turbocharger shaft. The failure of the bearing and melting of the compressor due to the heated shaft is what likely led to the premature failure of the composite compressors during all three tests. The new rig design about lined in Chapter III would provide the ability to control the direction of the loads on angular contact bearings and be able to replace the bearings and regular intervals during testing.

4.4.3   New Test Stand.

Because of problems with the test stand that occurred during experimentation, a new test stand, depicted in Figure 163, is proposed for future testing.
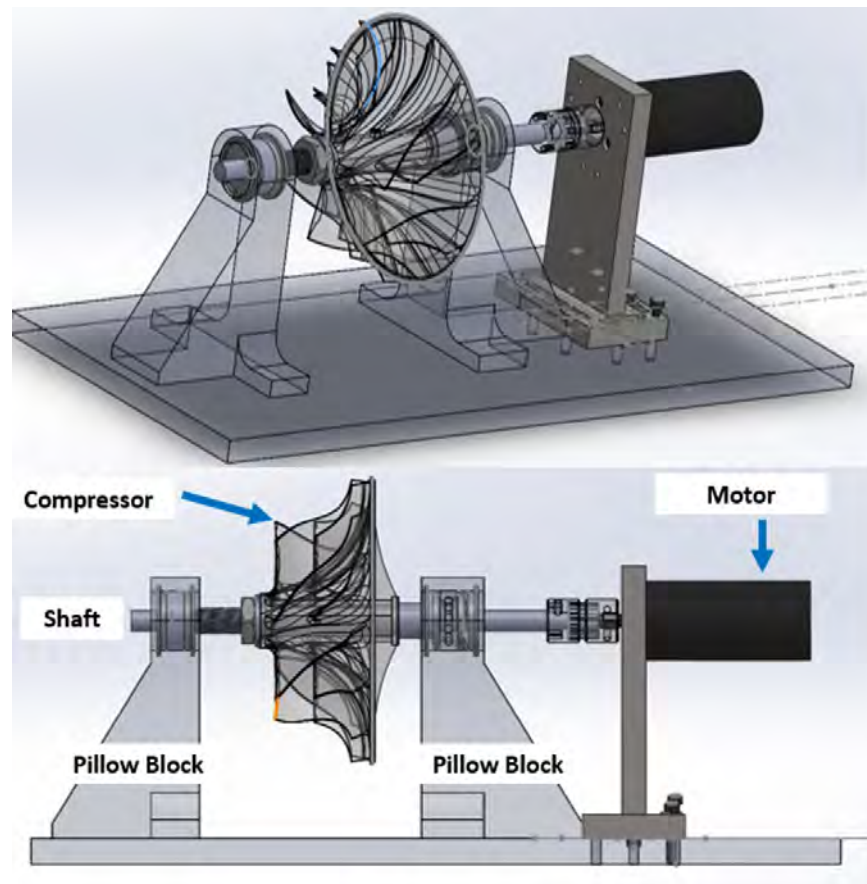

Figure 163. New Test Stand

This new test stand aims to bypass issues with previous setups by reducing the complexity of the system and reducing the potential mechanisms of unintended failure such as friction along the shift or lubrication issues. This rig is comprised of a removable shaft, the compressor, two pillow blocks, and a motor. There are a few particular parts recommended for use. The custom made pillow blocks would be fit with two angular contact bearings (8 x 22 x 7 mm). The bearings recommended for this application are the Angular Contact Stainless Ceramic Bearings (Part Number: D608/602/839 [129]) manufactured by BocaBearings. Four retainer rings (ID=24 mm, OD=25.9 mm) (Part Number:98455A124 [130]) which can be found on Mc-MasterCarr hold the grease seal washers in. Five stainless steel over-sized precision washers, (ID=7.4 mm, OD=22.0 mm) (Part Number:91116A250 [131]) are needed to hold grease around the bearings, and one wave washer (ID=16.5 mm, OD=22.0 mm) (Part Number:1775N33 [132]) to produce a preload on the bearings.
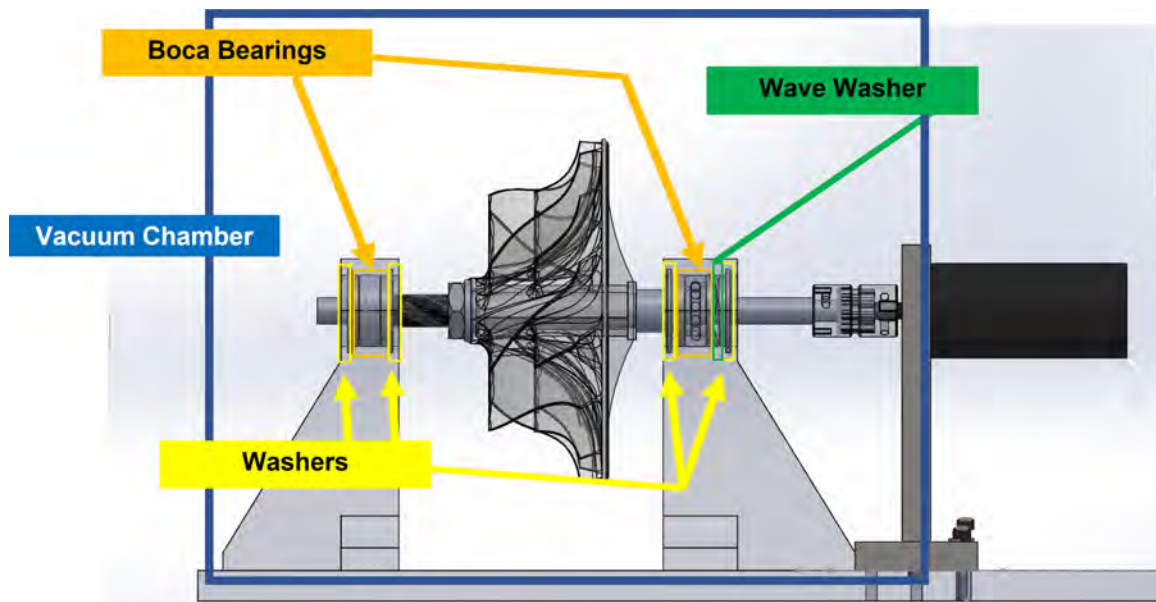

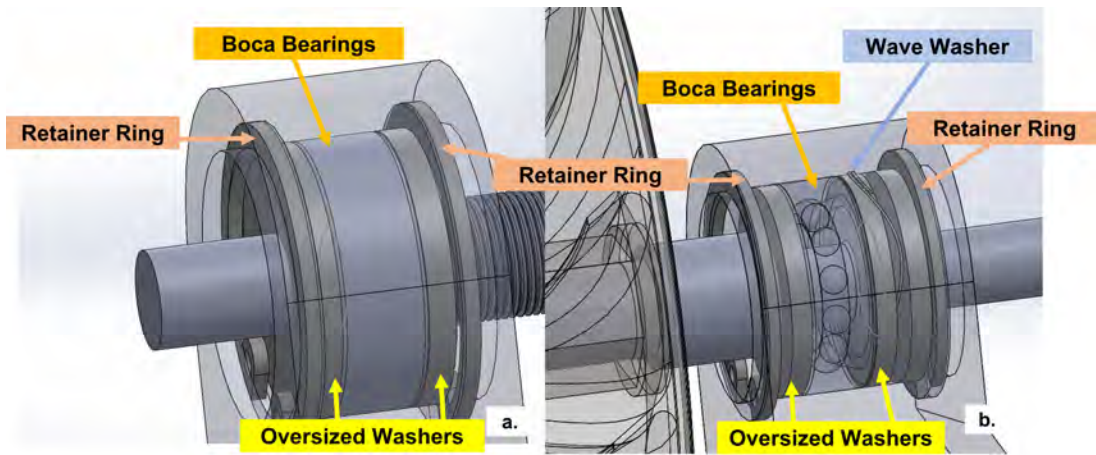**Figure 164. New Test Stand Components labeled**

Figure 165. New Test Stand Components Pillow Blocks a) Front b) Rear
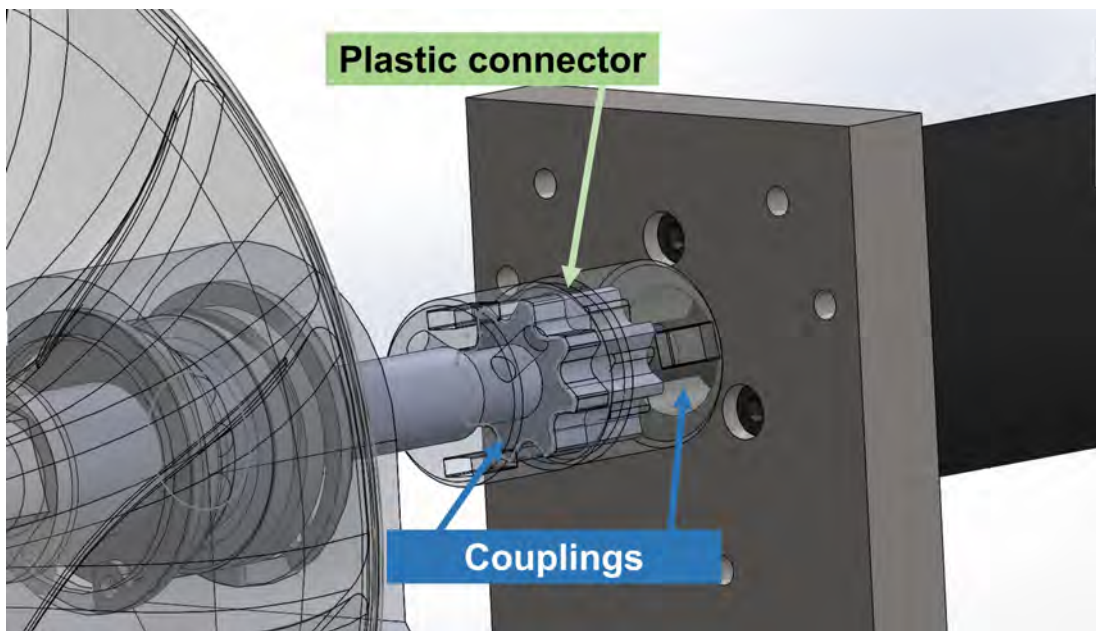
Figure 166. New Test Stand Components Couplers and Plastic Connector

An electric motor could likely not drive at full speed while overcoming aerodynamic loads and temperatures, so a vacuum chamber would maybe needed to enclose the rotor to only test centrifugally loaded forces. Figure 164 displays the proposed test stand identifying the individual components that would require purchase. Figure 165a and b show a zoomed in of the pillow blocks and the internal structure. Figure

225

166 shows the plastic connector and the coupling that connects the electric motor at the rear to the compressor shaft. This coupling assembly is also a component that would require online purchase [133].

Conversations with a bearing expert [134] included additional recommendations for the inclusion of grease for the bearings to lubricate the component without the ability to provide a continuous oil flow. He specifically recommended an aerospace grease meeting the MIL-PRF-81322 grease specifications. Mobilegrease 28 is one option for consideration. The bearing expert also suggested attaching accelerometers over the bearings on the pillow blocks to help determine the cause of any failure. Should both the rotor and bearings fail, the accelerometer will help indicate which was the cause and which was the effect. The bearing expert also recommended reducing the design length of the shaft, particularly in the region between the rear pillow block and the electric motor. The longer the shaft, the more rotordynamic risk. Shortening the shaft (within reason) will reduce risk without undertaking a full rotordynamic analysis. The CAD model of the new test stand also does not have flat surfaces, which would make securing the compressor with a wrench difficult. Because of this, a flattened modification to the shaft is recommended. A left-handed M-10 nut is recommended for securing the compressor on the shaft. Left-handed thread is needed because at the expected operating speeds, the centrifugal loads would loosen the nut if it was right-hand threaded. Part Number: 6343K72 in McMaster-Carr could potentially work for this application [135]. The motor driving the shaft should be capable of reaching the target speed of 100,000 RPM.

V. Conclusion

The three objectives at the start of this study were achieved in different degrees of success. The first objective was to characterize the materials of interest including UL-TEM 9085, Epoxy-Carbon fiber, ULTEM 1000-Carbon fiber, and Onyx-Carbon fiber. ULTEM 9085, Onyx-Carbon fiber, and Epoxy-Carbon fiber were successfully characterized with tensile specimens using MTS load machines. ULTEM 1000 could not be characterized because the samples made in the 3-piece press mold were destroyed trying to remove them from the mold.

The second objective was to conduct FEA to predict failure points on a Jet-Cat P400 compressor geometry based on the material property inputs from the first objective. FEA was conducted for all three tested materials. Each material FEA included a test point with the operating P400 engine speed and the temperature expected to experience the initial onset of yield. The third objective was to conduct spin tests to validate the accuracy of the FEA model predictions. This objective was attempted, but each ULTEM 9085 compressor failed prematurely due to failure of the turbocharger. Due to time constraints, the proposed new test stand could not be manufactured in time to enact further testing.

Tensile tests were conducted for all three of the specimens of interest that were successfully manufactured. The three specimens were tested at room temperature and temperatures up to P400 operating temperature. Each specimen above room temperature was heated in a furnace, and the strain was measured using the built-in LVDT. ULTEM 9085 and Onyx were both printed on their own respective 3D printer. ULTEM 9085 was printed on the Fortus 450cc 3D printer and was printed on the Markforged Mark II printer. The Epoxy-Carbon fiber was molded in a custom mold.

Among the three tested materials, Onyx-Carbon fiber in room temperature con-

227

ditions was found to hold the best strength by far and exhibited an ultimate strength competitive with that of Aluminum. However, Onyx-Carbon fiber proved to have unfavorable qualities when epoxed to elevated temperatures. Its low glassification and melting temperature could not withstand the high temperatures required for P400 compressor operation. ULTEM 9085 exhibited an ultimate strength that was about a third to that of Onyx-Carbon fiber which was enough for further investigation. However, it proved to be incapable of supporting load at P400 operating temperatures because it would glassify close to P400 operating temperature. Epoxy-Carbon fiber was the one material out of the three that still exhibited resistance to tension even at P400 operating conditions, which indicates the ability to remain structurally intact even at high-temperatures. The room temperature experimental ultimate strength and the RoM calculation using published data proved to be significantly different. The differences between the room temperature outputs and the RoM calculations are attributed to the published data indicating bulk properties and not accounting for non-bulk manufactured layers for AM and molding. The experimental dogbones also have internal voids that likely degrade ultimate stresses for the overall material.

Epoxy-Carbon fiber was uniquely explored in this study in the fact that it required custom molds and a hand-mixing process for fiber incorporation. Two molds were designed for use with the Epoxy-Carbon fiber: a one-piece negative mold and a 3-piece mold containing one negative and two positive components. Epoxy-Carbon fiber proved to have an ultimate strength of similar magnitude to that of ULTEM 9085 and proved to have the best resistance to thermal effects between all three of the materials of interest. ULTEM 1000 was also explored in this study, but proved to have manufacturing issues using the 3-piece mold. ULTEM 1000 was investigated in its powder form and produced parts that would not survive the compression molding process. This material is likely better suited for injection molding.

FEA was conducted for all three materials using the material properties extracted from the specimen tests. The FEA models contained underlying assumptions which were no surface forces, steady-state operation, and isotropic material properties. Onyx proved to survive the highest speed, but is known to have an inability to survive high temperatures (not accounted for in the model). Epoxy proved to deform the least among the three materials and the room temperature compressor scenario deformed within the deformation limit (based on the aluminum compressor deformation at maximum speed) to avoid rubbing with the shroud.

Spin tests were attempted to determine how close the FEA model was to a real compressor, but was met with several issues. The turbocharger used to spin the sample compressors built up heat through the shaft and generated friction heating along the shaft that prematurely failed the compressor under test. The first test failed early because of a loose nut that caused the compressor to slip on the shaft and generate additional friction heating. Although the nut remained on the shaft with Loctite applied in the second and third test, shaft heating caused melting at the bore section and premature failure of the compressor. Future work could investigate the repeated issues with turbochargers or, as this study recommends, construct a new rig that aims to avoid the problems experienced in the past altogether.

Future investigations should include a correlation measurement between the LVDT and an available strain gauge to assure accurate strain measurements from the tensile tests. Other materials could also be investigated in the future. Namely, injected molded ULTEM 1000 or ULTEM 1010 molded or printed with reinforcement. Further research with Onyx-Carbon fiber, even with reinforcement, is not recommended due to its low temperature threshold. Reach to further explore Epoxy-Carbon fiber with high reinforcement is recommended. A question that remains at the end of this study is the amount of reinforcement that could be added to an Epoxy before

229

high-temperature compression-molding would fail to adhere epoxy and carbon fiber together. One method yet to be investigated is the application of additional embedded metallic reinforcements or metal blades cast directly into the Epoxy to simplify the manufacturing process. Other high-temperature polymers available in the future could also be investigated with carbon fiber or newer forms of reinforcement that may contain strength properties that could be competitive with those of conventional turbomachinery metals.

Appendix A. FEA Supplemental Results

The following sections display the FEA results for the compressors and the hubs with temperature effects only and centrifugal loads only. This also contains the axial and radial deformation results.

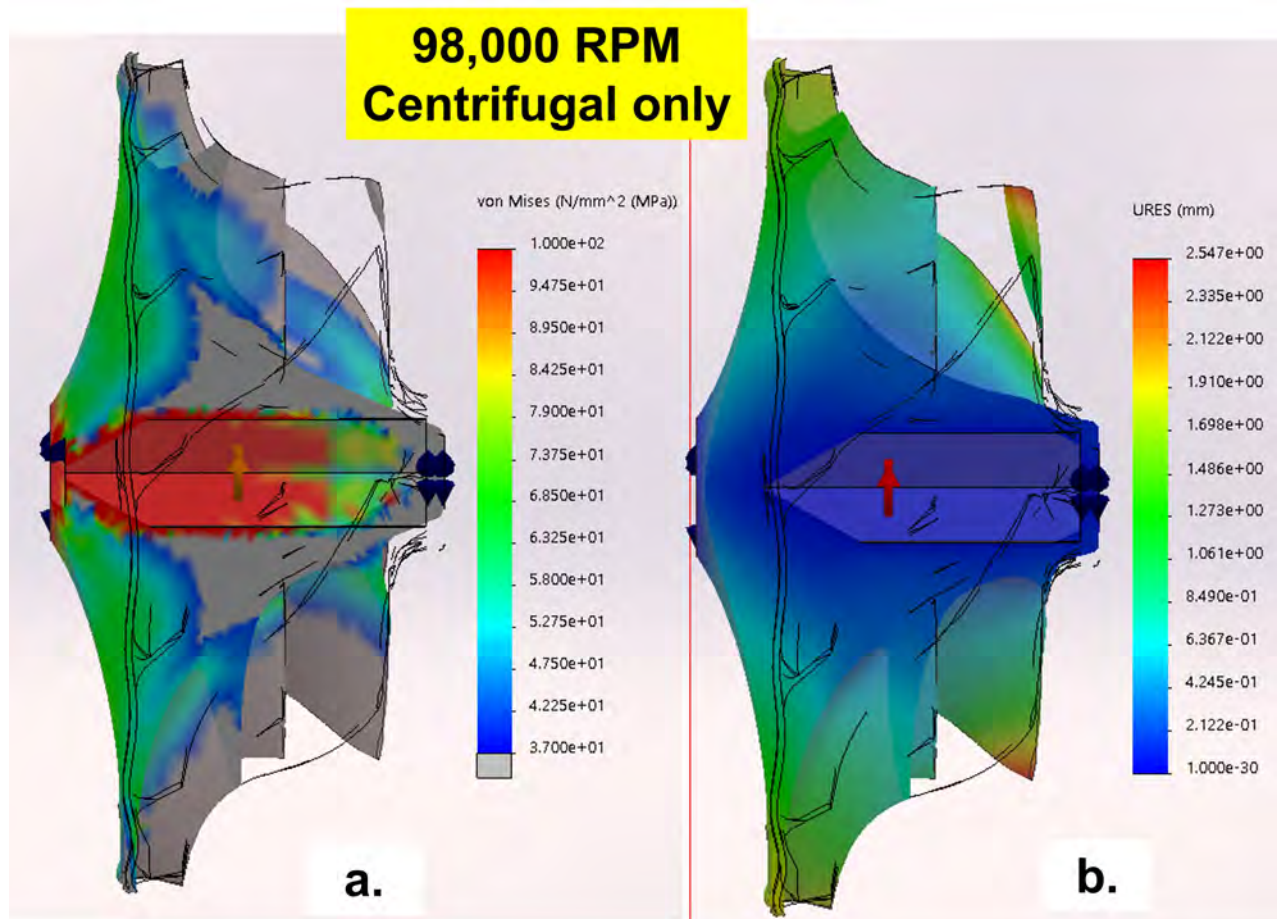## A.1   ULTEM 9085 FEA-Temperature Variant Model

Figure 168. ULTEM 9085 Compressor Centrifugal Only a) Stress Profile b) Deformation Profile
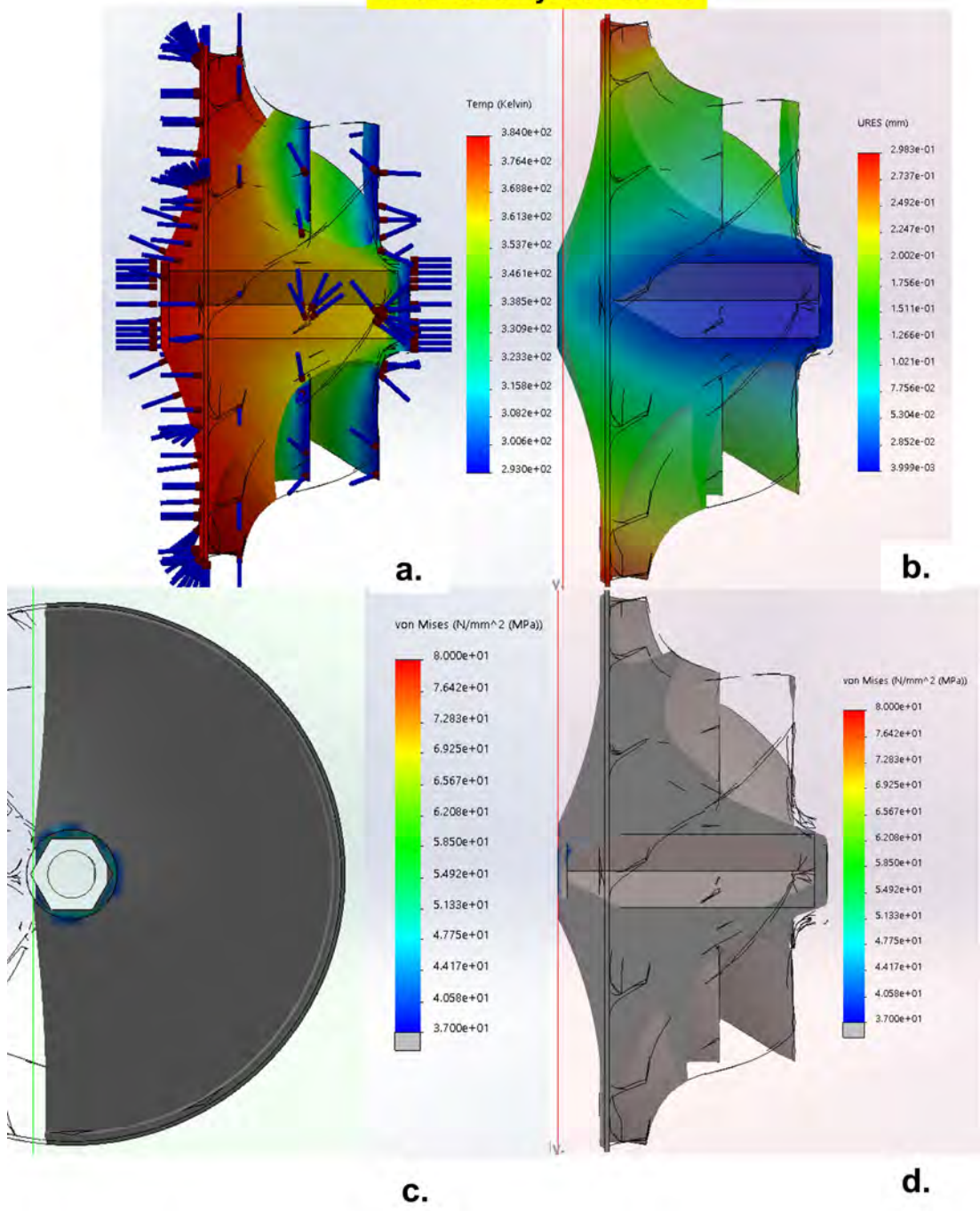
Figure 167. ULTEM 9085 Compressor Temp Only a) Temp Profile b) Deformation c) Stress Profile (1) d) c) Stress Profile (2)

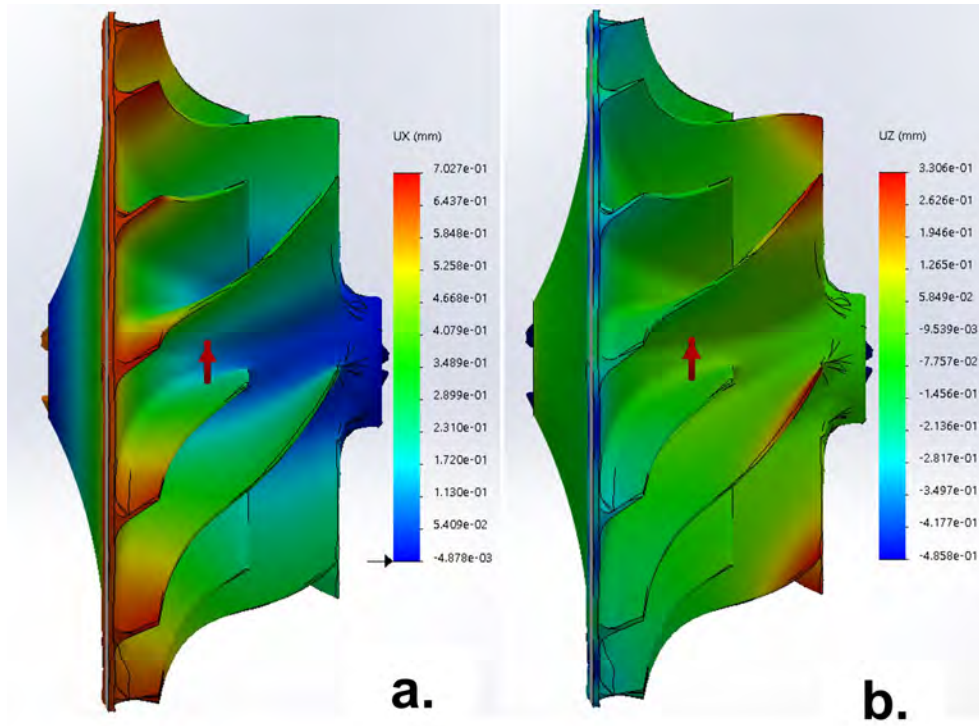**Figure 169.** **ULTEM 9085 Compressor Deformation components a) Radial b) Axial**
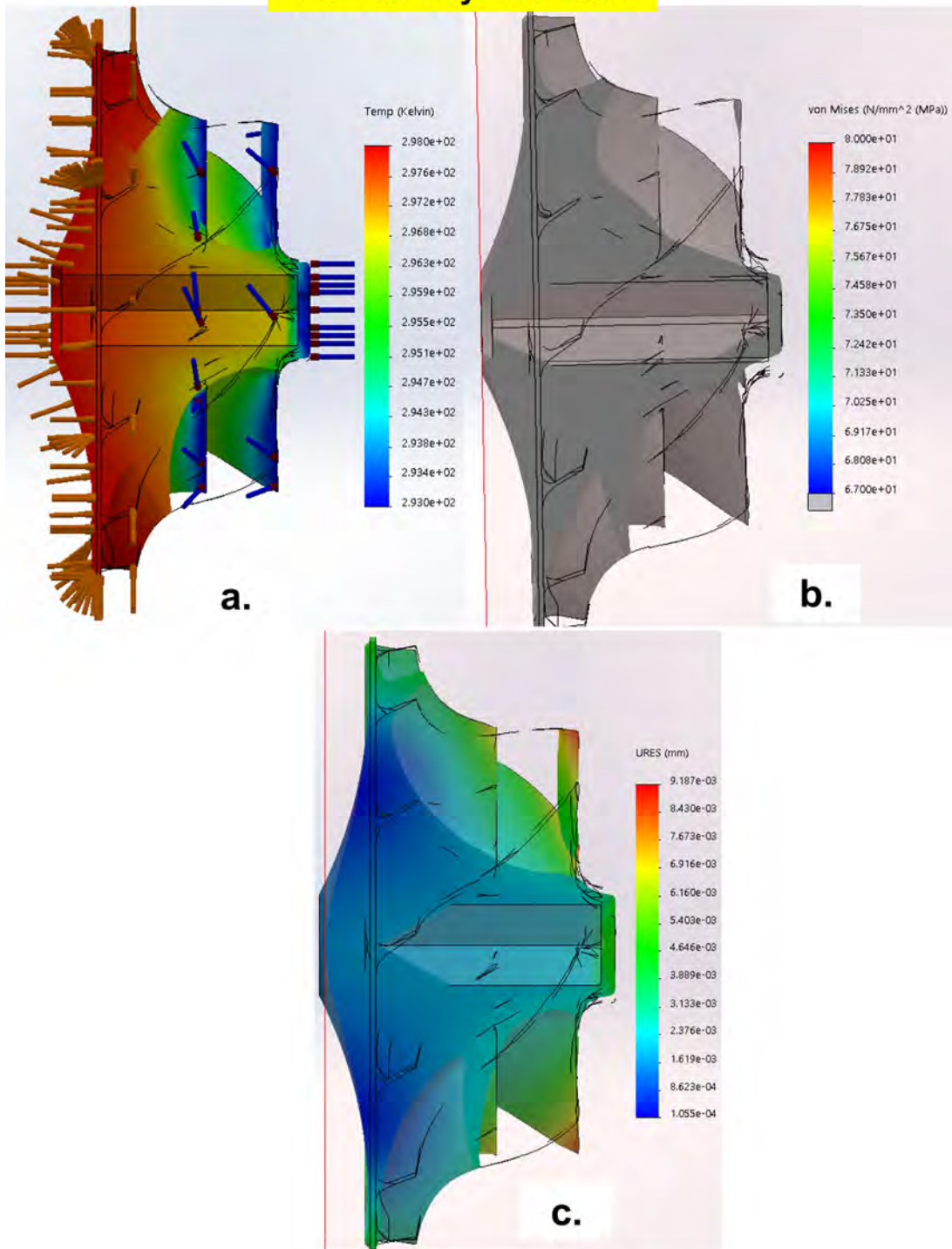
Figure 170. ULTEM 9085 Compressor Room Temperature Temp Only a) Temp Profile b) Deformation c) Stress Profile (1) d) c) Stress Profile (2)

A.2   ULTEM 9085 FEA-Room Temperature Model
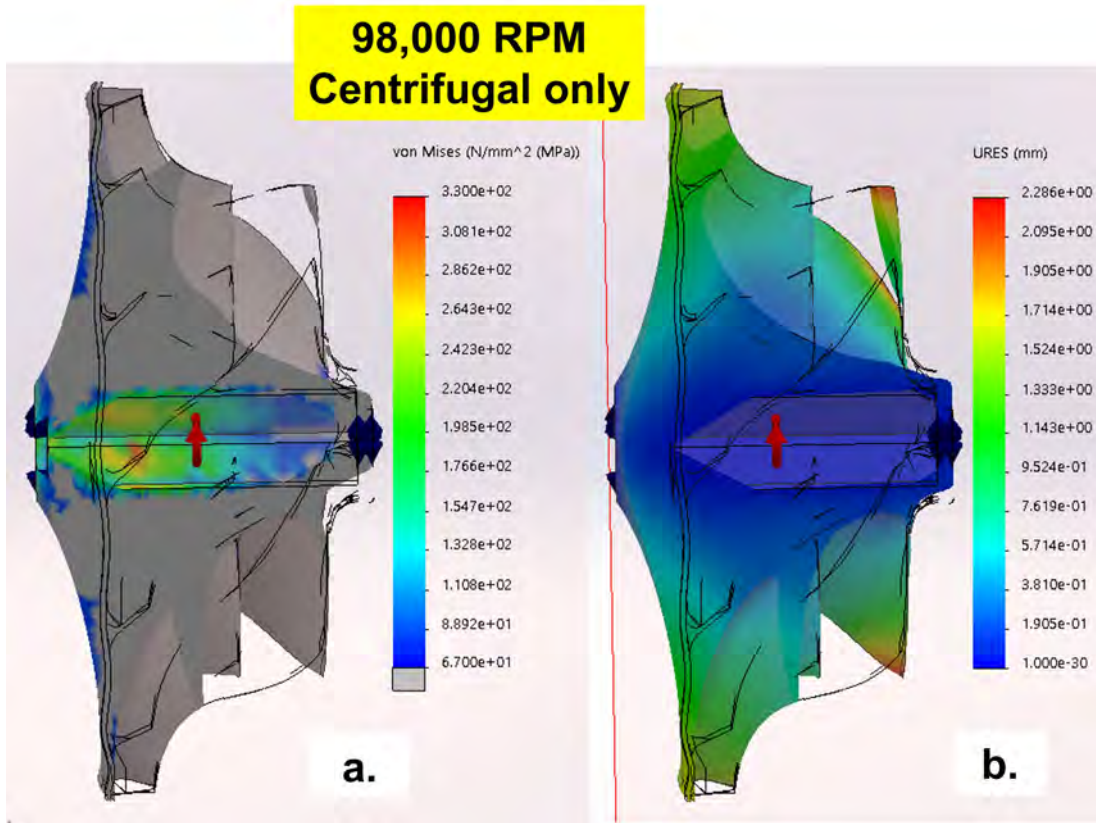

Figure 171. ULTEM 9085 Compressor RMT Centrifugal Only a) Stress Profile b) Deformation Profile
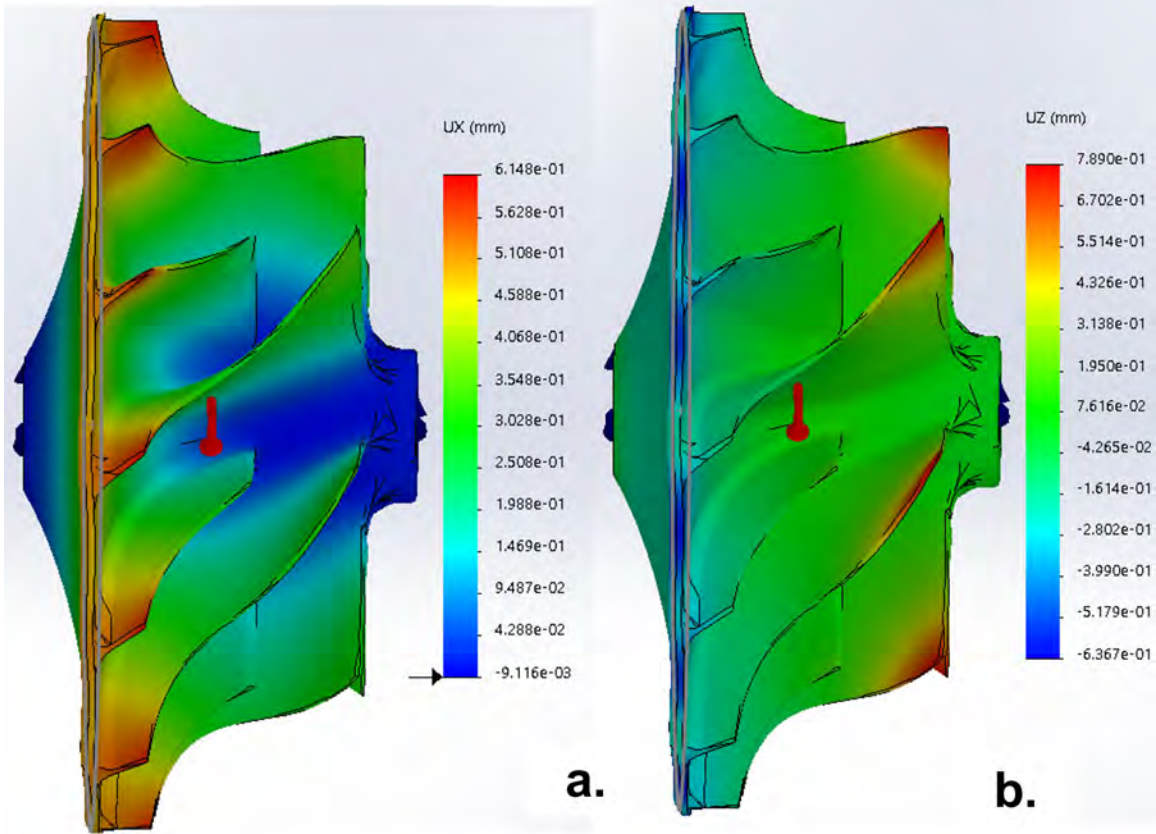
Figure 172. ULTEM 9085 Compressor Room Temperature Deformation components a) Radial b) Axial

A.3 Onyx-Carbon fiber FEA-Temperature Variant Model

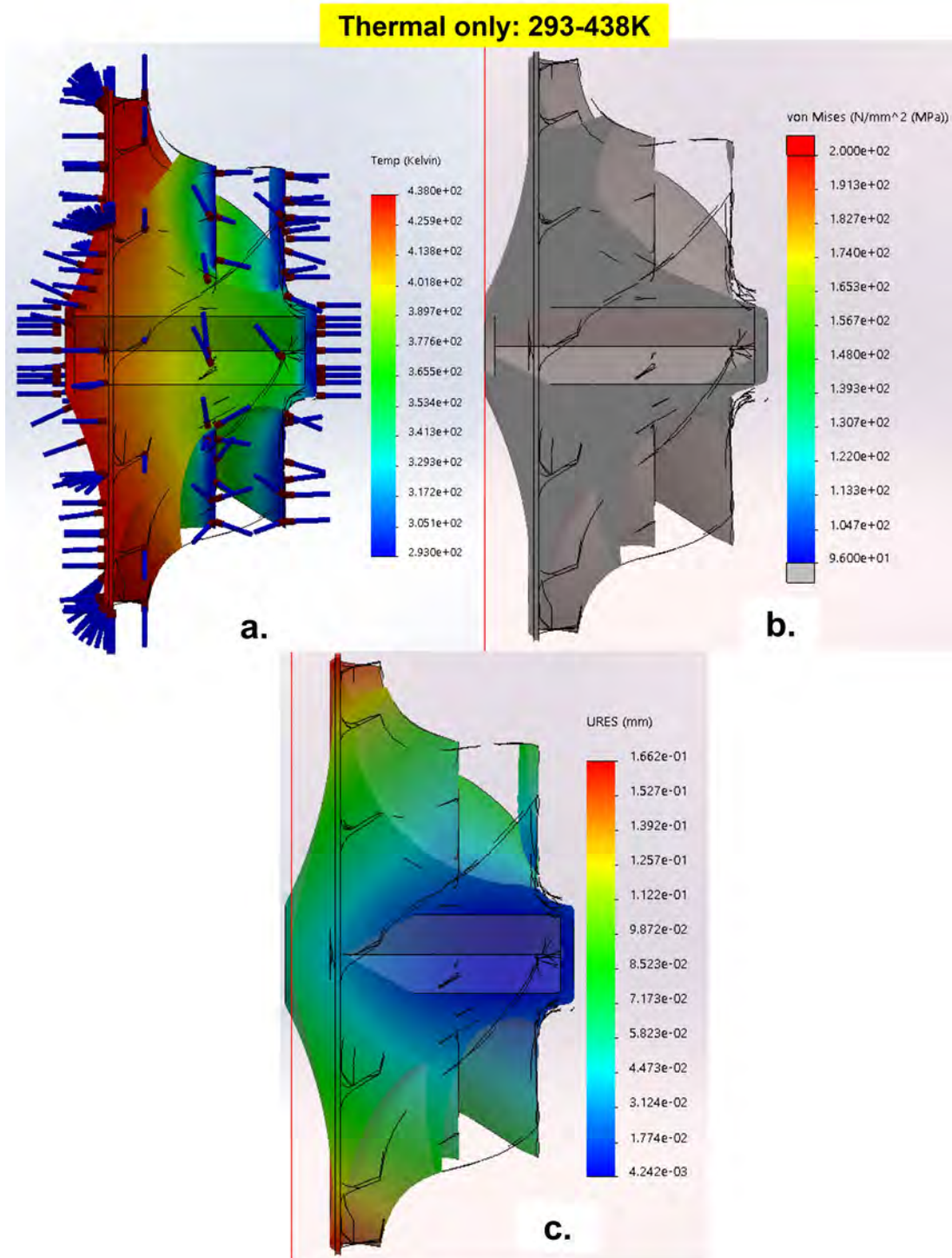**Figure 173.** Onyx-CF Compressor Temp Only a) Temp Profile b) Deformation c) Stress Profile
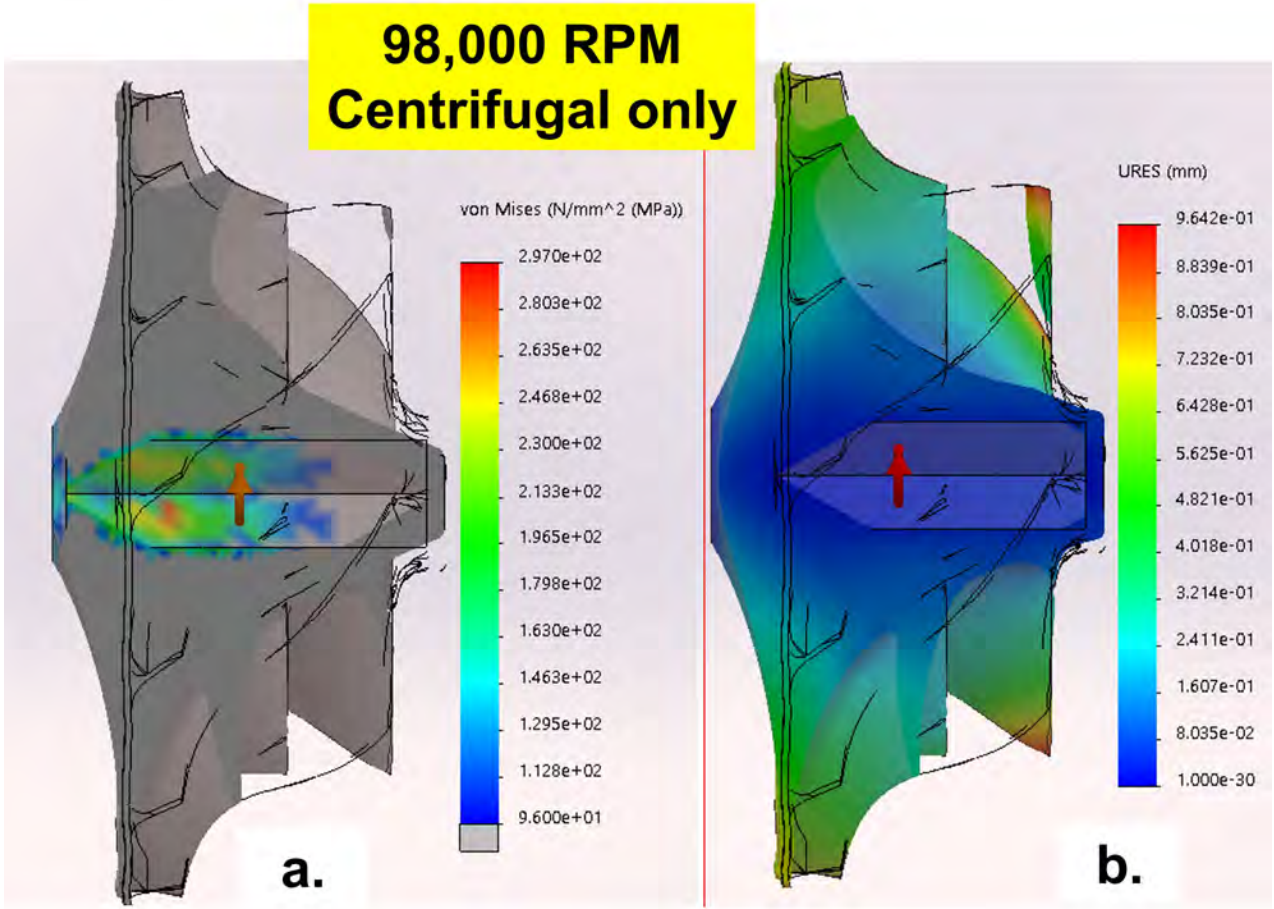
Figure 174. Onyx-CF Compressor Centrifugal Only a) Stress Profile b) Deformation Profile

Figure 175. Onyx-Carbon fiber Deformation components a) Radial b) Axial

A.4 Onyx-Carbon fiber FEA-Room Temperature Model
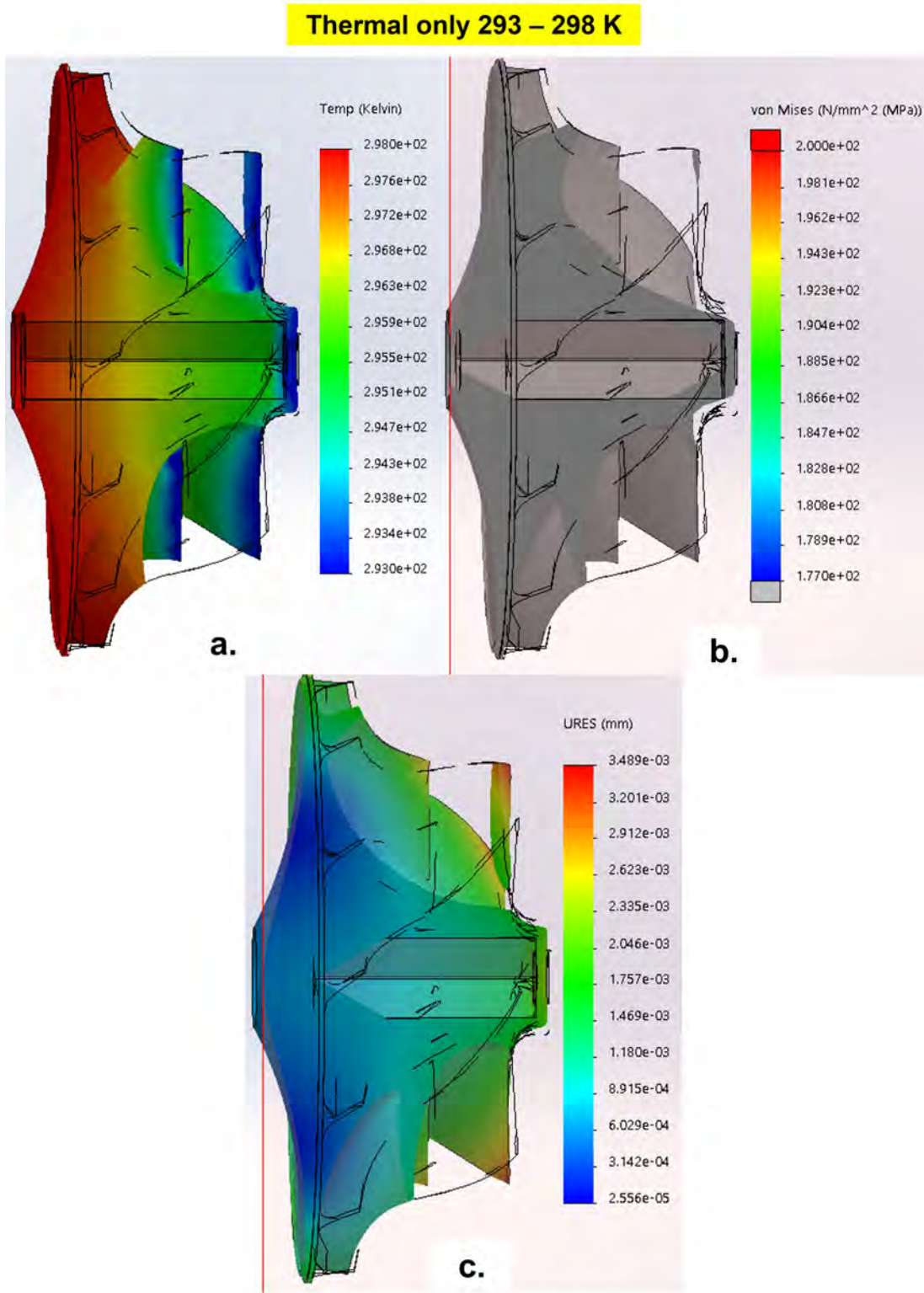
Figure 176. Onyx-CF Compressor Temp Only Room Temperature a) Temp Profile b) Deformation c) Stress Profile

Figure 177. Onyx-CF Compressor Centrifugal Only Room Temperature a) Stress Profile b) Deformation Profile
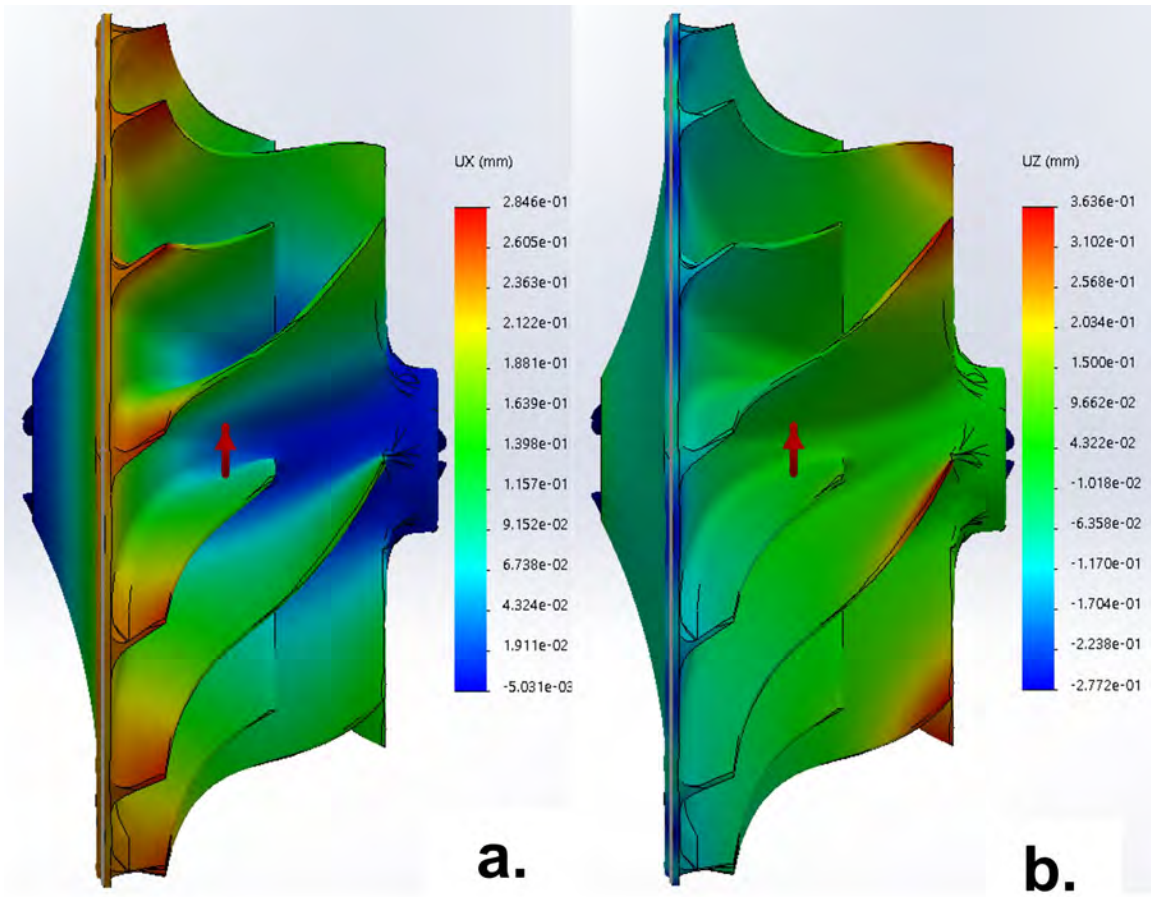
Figure 178. Onyx-Carbon fiber Room Temperature Deformation components a) Radial b) Axial

A.5 Epoxy-Carbon fiber FEA-Temperature Variant Model Hub and Full-bladed Compressor
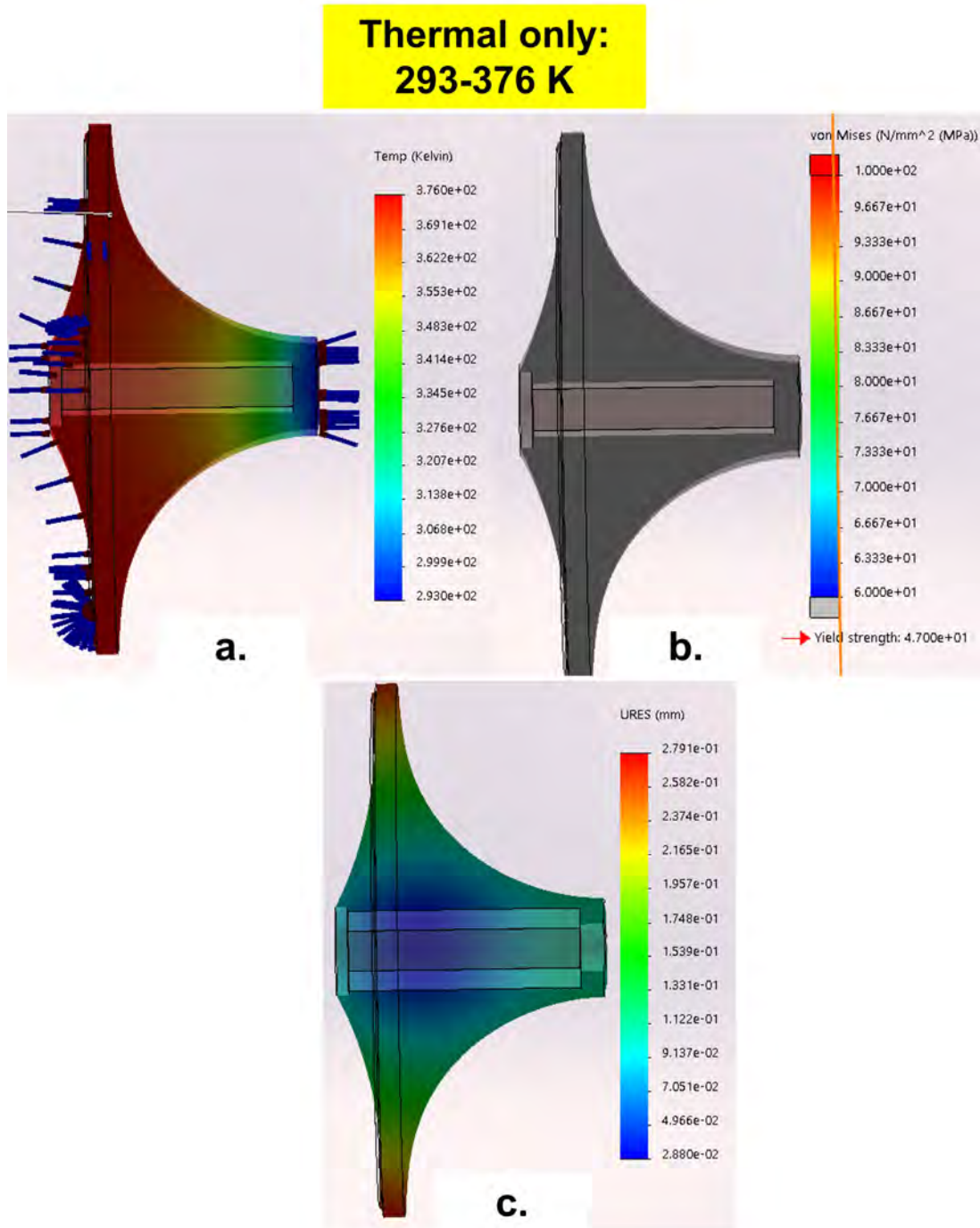
Figure 179. Epoxy-CF Hub Temp Only a) Temp Profile b) Deformation c) Stress Profile
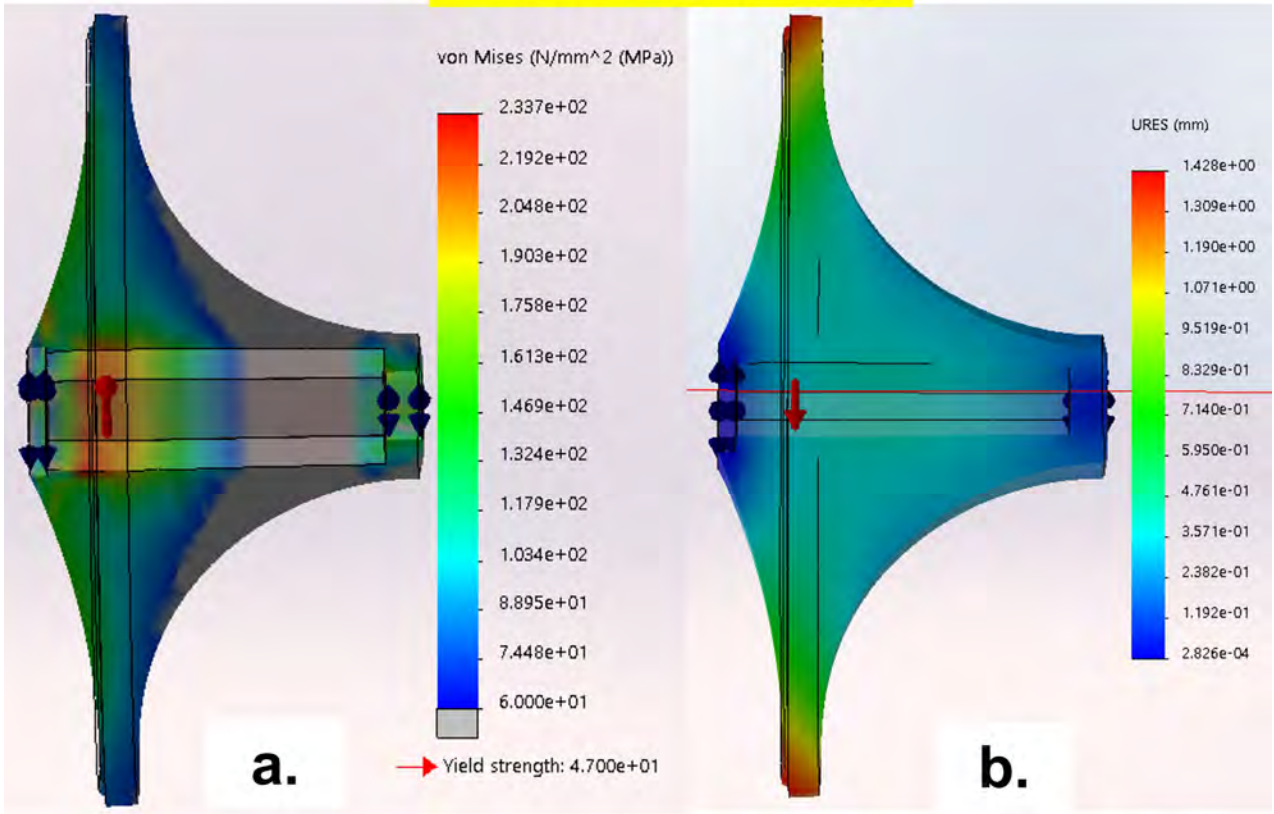
Figure 180. Epoxy-CF Hub Centrifugal Only a) Stress Profile b) Deformation Profile
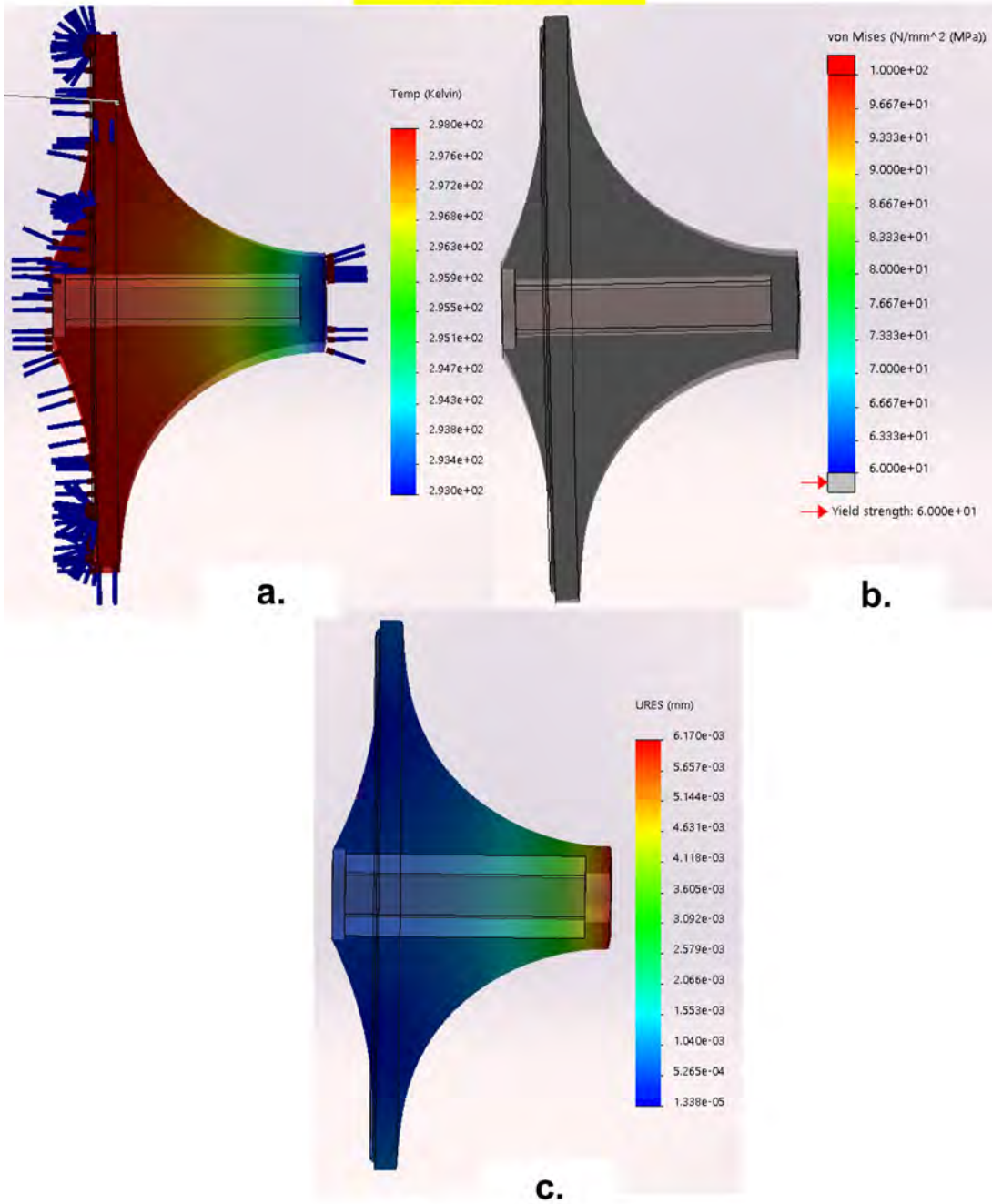
Figure 181. Epoxy-CF Hub Temp Only Room Temp a) Temp Profile b) Deformation c) Stress Profile

245
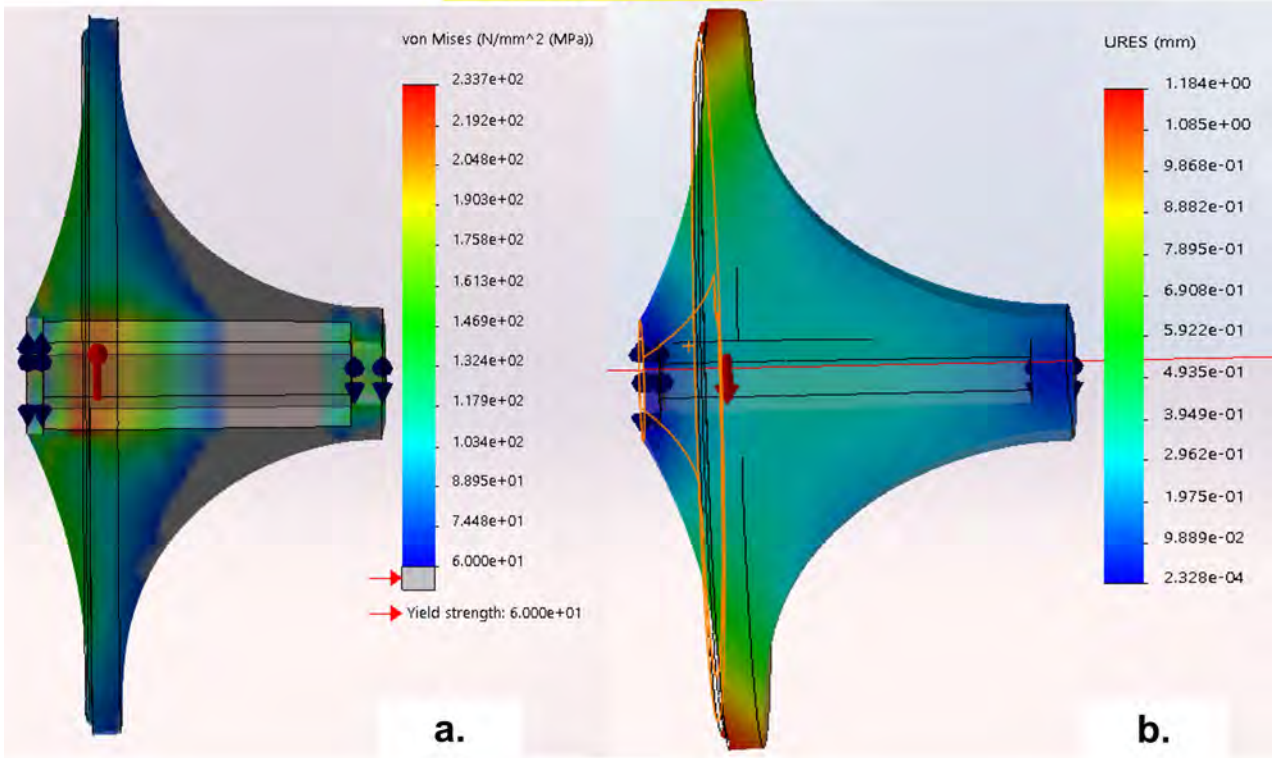
Figure 182. Epoxy-CF Hub Centrifugal Only Room Temp a) Stress Profile b) Deformation Profile

Figure 183. **Epoxy-CF Compressor Temp Only a) Temp Profile b) Deformation c) Stress Profile**

Figure 184. Epoxy-CF Compressor Centrifugal Only a) Stress Profile b) Deformation Profile
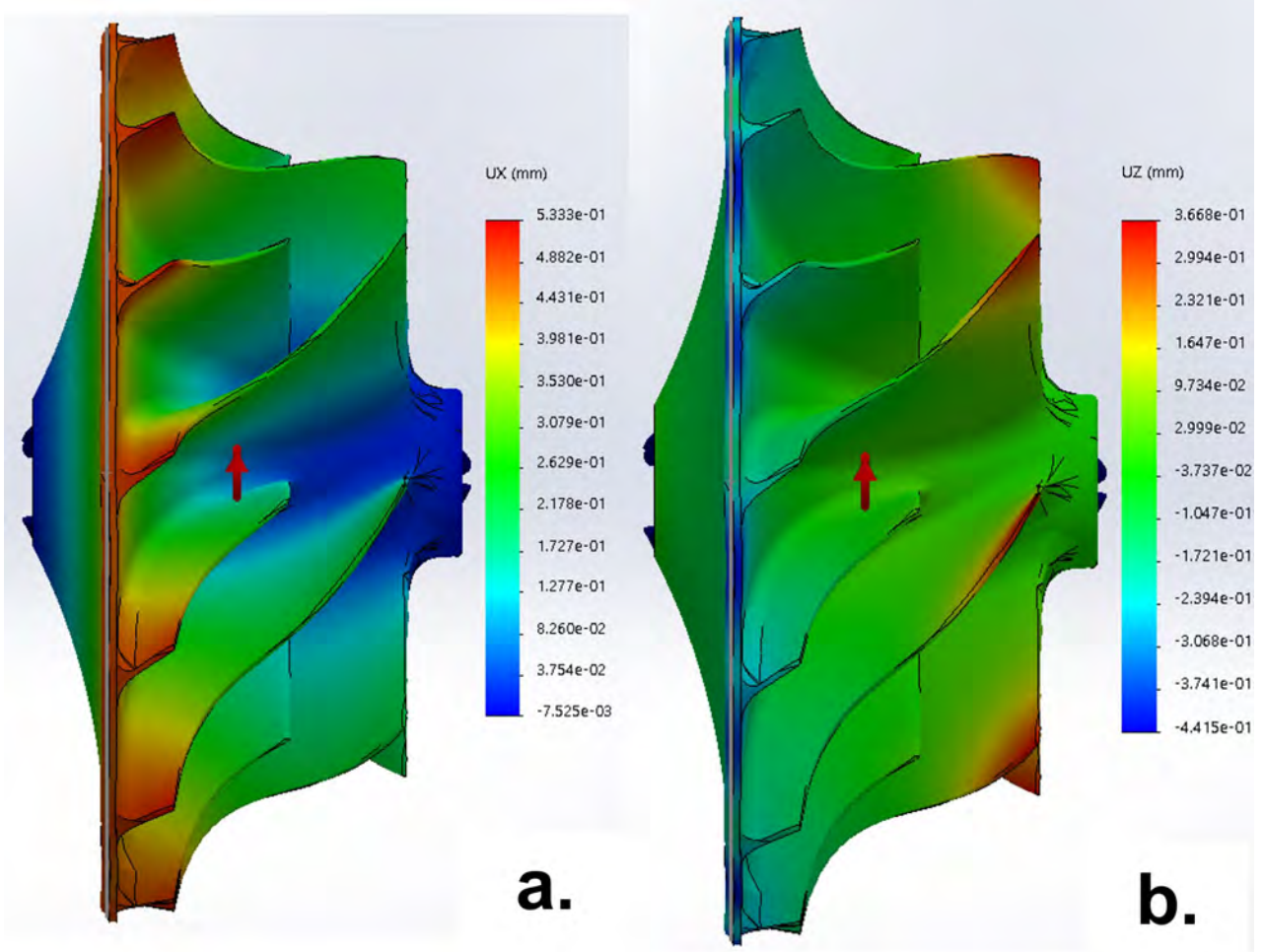
Figure 185. Epoxy-Carbon fiber Deformation components a) Radial b) Axial

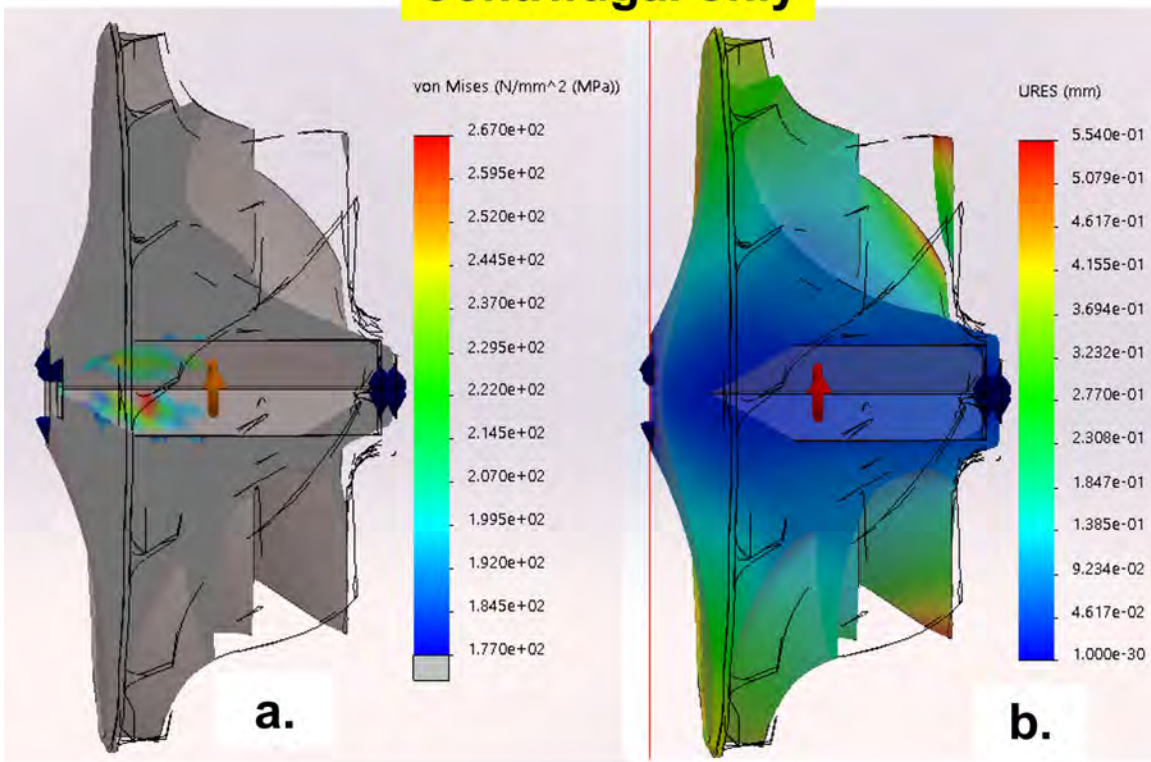**Figure 186. Epoxy-CF Compressor Temp Only Room Temp a) Temp Profile b) Deformation c) Stress Profile**
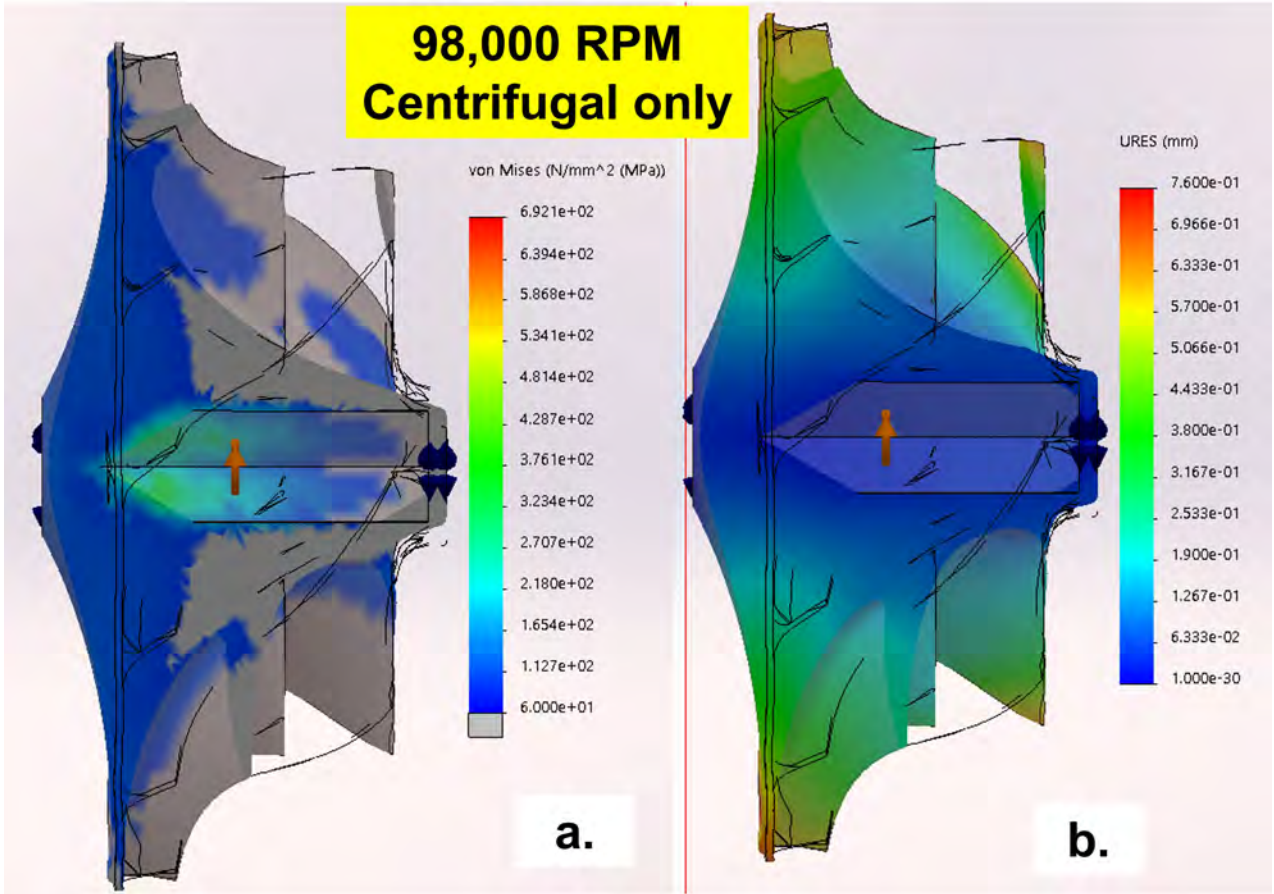
Figure 187. Epoxy-CF Compressor Centrifugal Only Room Temp a) Stress Profile b) Deformation Profile

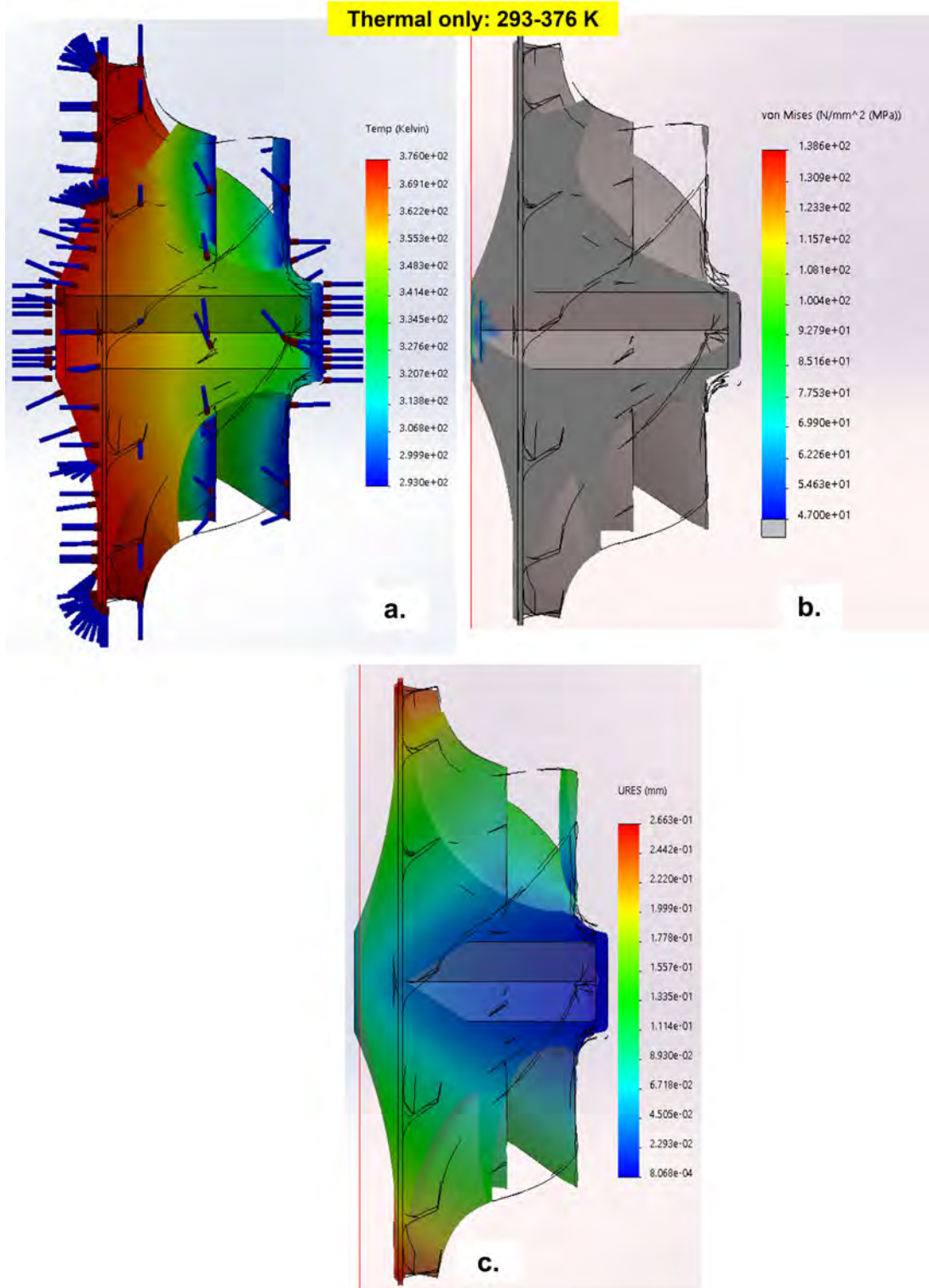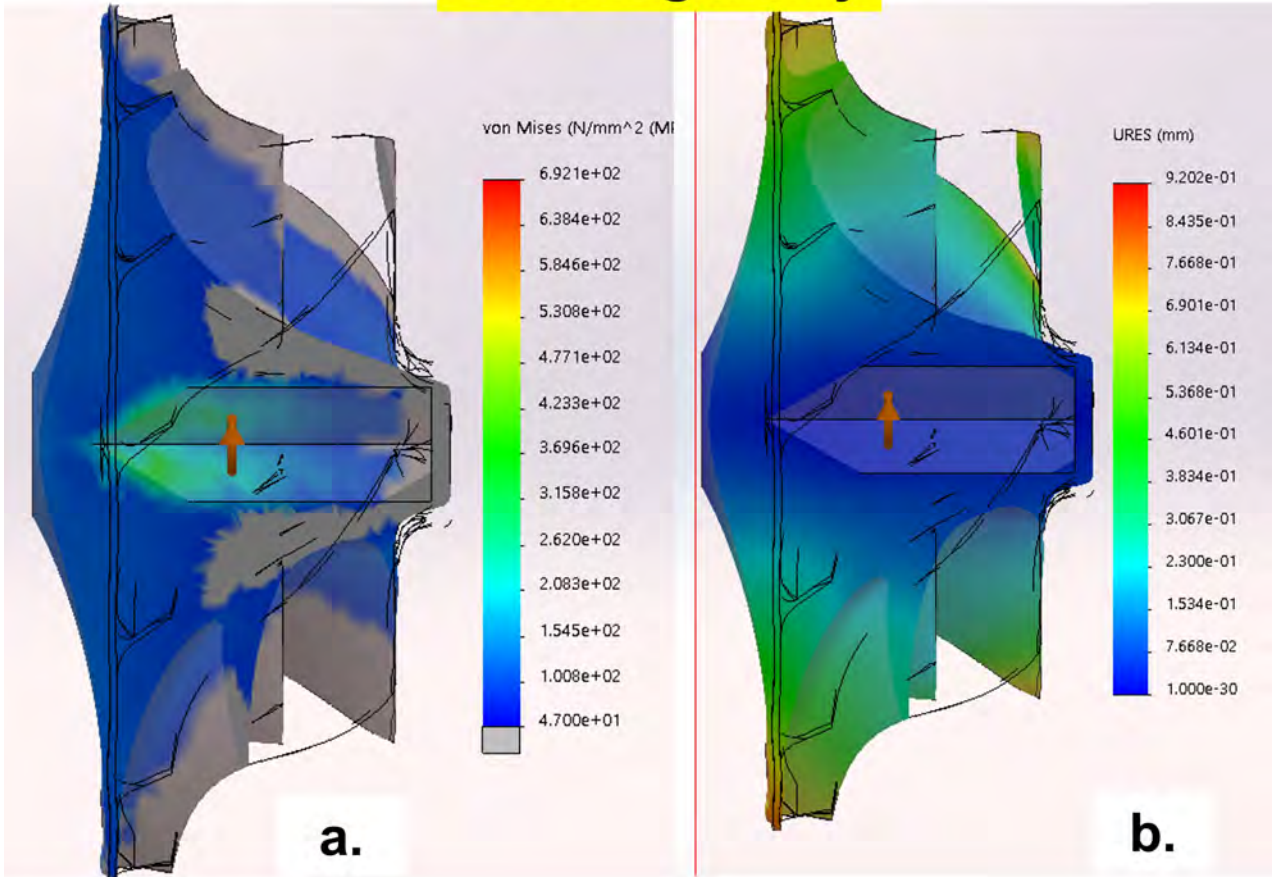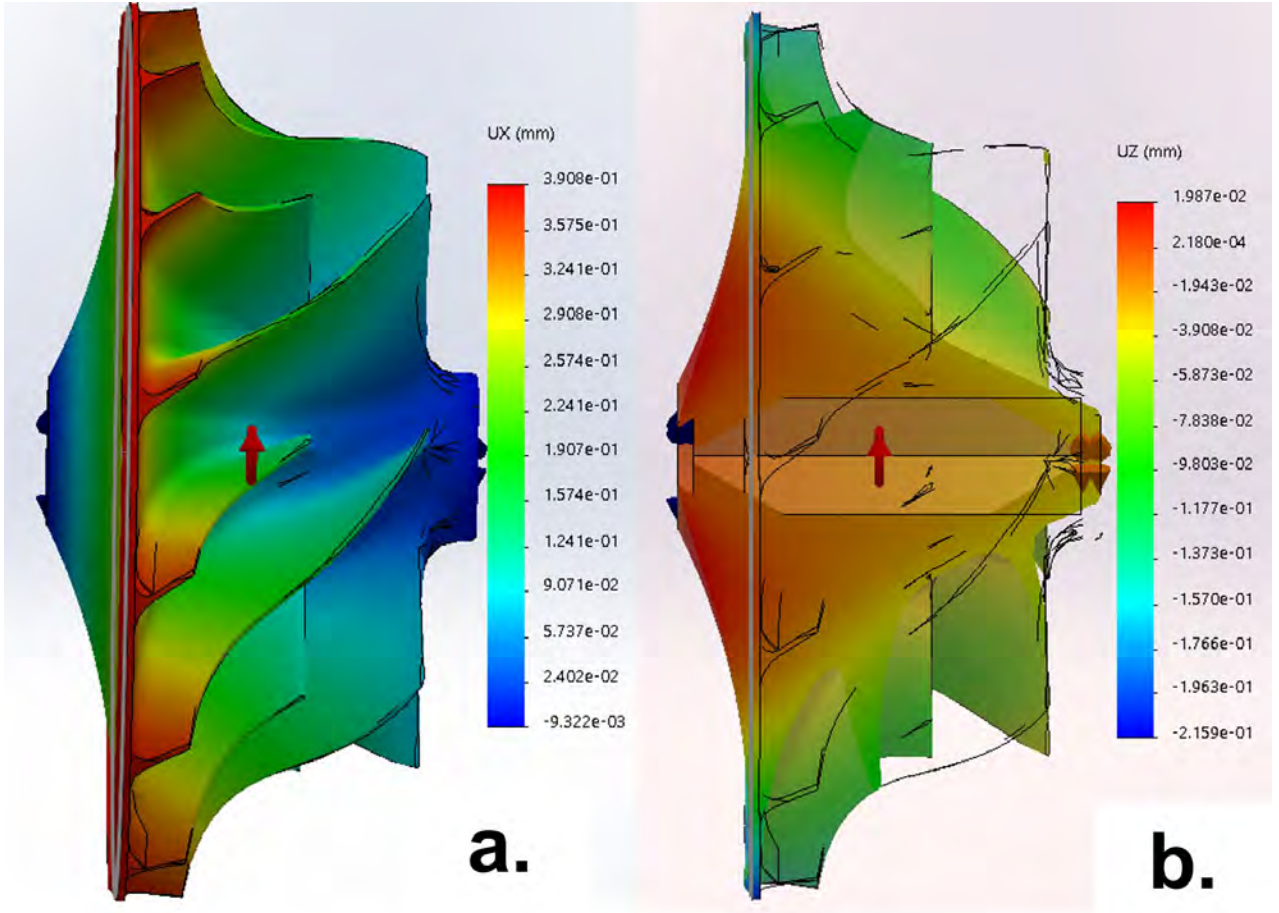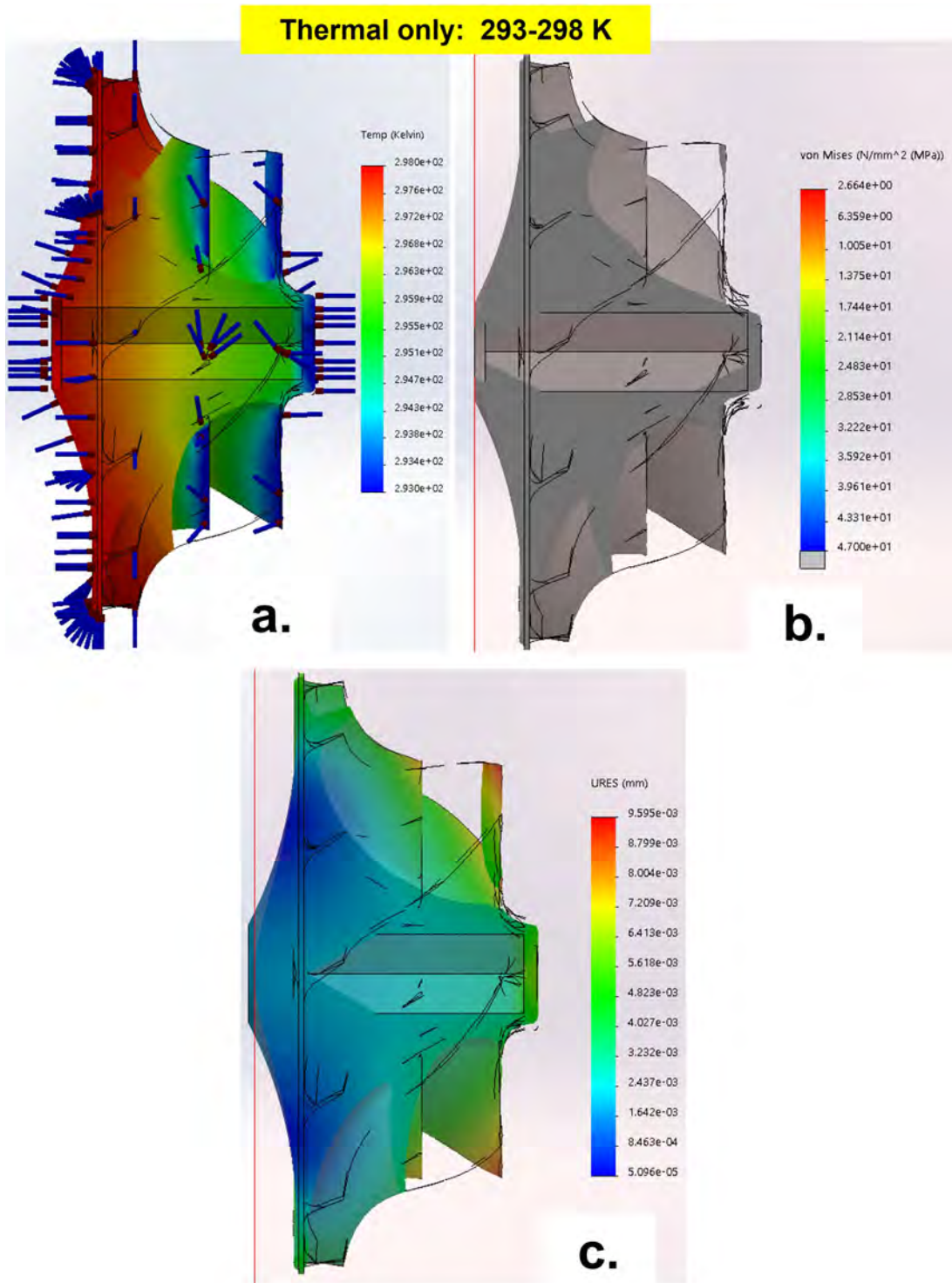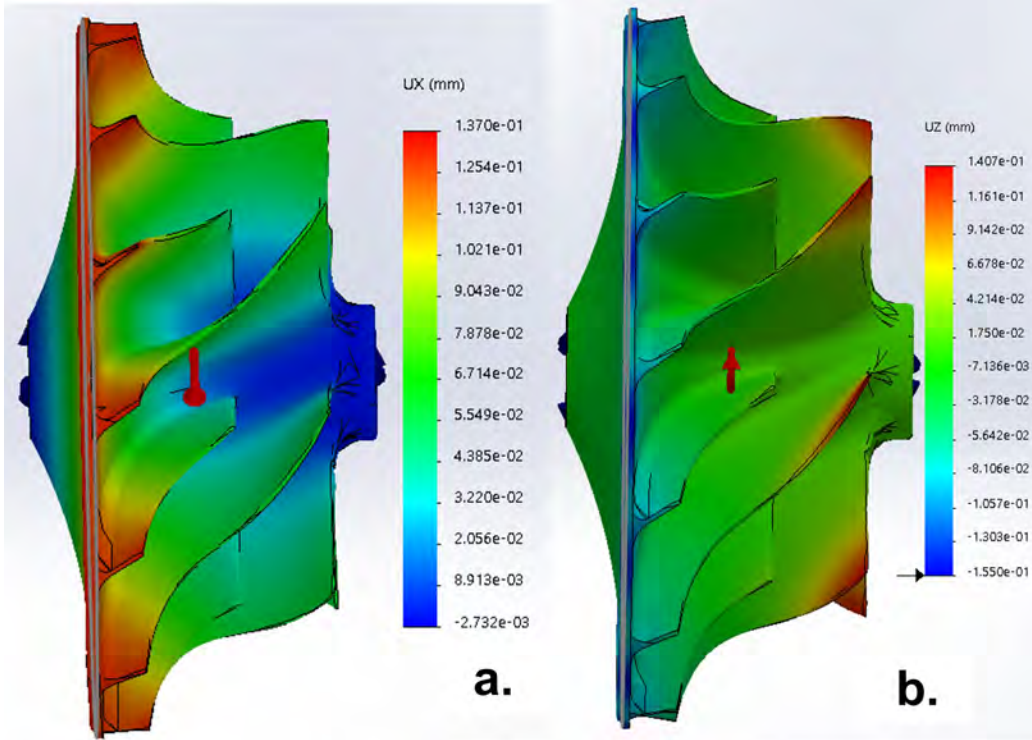**Figure 188. Epoxy-Carbon fiber Room Temperature Deformation components a) Radial b) Axial**

[?]

Bibliography

1. Bauer, A. P., "Design, Development, and Testing of a Low Cost, Additively-Manufactured, Centrifugal Compressor," Tech. rep., AIR FORCE INSTITUTE OF TECHNOLOGY WRIGHT-PATTERSON AFB OH WRIGHT-PATTERSON, 2020.

2. Gibson, I., Rosen, D. W., Stucker, B., Khorasani, M., Rosen, D., Stucker, B., and Khorasani, M., *Additive manufacturing technologies*, Vol. 17, Springer, 2021.

3. Japikse, D. and Baines, N., *Introduction to Turbomachinery*, Concepts ETI, Inc.; Oxford University Press, Norwich, VT; Oxford, England, 1st ed., 1994.

4. Rodgers, C., "Specific Speed and Efficiency of Centrifugal Impellers," *proc. ASME 25th Gas Turbine Conference, No. A80-36101 14-34, March 1980, pp. 191–200.*, March 1980.

5. Logan, E., *Turbomachinery: Basic Theory and Applications*, Marcel Dekker, Inc., New York City, NY, 2nd ed., 1993.

6. Otto, K. and Wood, K., *Product Design: Techniques in Reverse Engineering and New Product Development*, Pearson Education, Inc., Bloomington, MN, 12th ed., 2013.

7. Mattingly, J. D., Boyer, K. M., and von Ohain, H., *Elements of propulsion: gas turbines and rockets*, American Institute of Aeronautics and Astronautics Reston, VA, 2006.

8. Walker, G., Turner, M., Holley, A., and Hoke, J., "Experimental Test Rig for 3D Printed, Axial Compressor Utilizing a COTS Turbocharger," *AIAA SciTech 2020 Forum 6-10 January 2020*, January 2020.

9. Meier, M. A., J.Gooding, W., Fabian, J., and Key, N., "Considerations for Using Additive Manufacturing Technology in Centrifugal Compressor Research," *Engineering for Gas Turbines and Power, Vol 142, Issue 3, March 2020, https://doi.org/10.1115/1.4044937*, March 2020.

10. Jia, D., Li, F., and Zhang, Y., "3D-printing process design of lattice compressor impeller based on residual stress and deformation," *Scientific Reports, Vol. 10, No. 1, December 2020, pp. 600*, December 2020.

11. Daniel, I. M. and Ishai, O., *Engineering mechanics of composite materials*, Vol. 1994, Oxford university press New York, 2006.

12. "Turbine Engine Compressor Sections: Basic theory and operation," AviationPros Website, Available at https://www.aviationpros.com/engines-components/article/10387158/turbine-engine-compressor-sections-basic-theory-and-operation.

13. "Turbine Engines - Engineering," Code 7700 Website, Available at https://code7700.com/turbine_engine.html.

14. "Centrifugal Air Compressors - C.H. Reed Capabilities," C.H. Reed Website, Available at https://www.chreed.com/compressed-air-systems-equipment/centrifugal-air-compressors/.

15. der Merwe, V. and Botha, B., "Design of a centrifugal compressor impeller for micro gas turbine application," 2012.

16. de Villiers, D. and Barend, L. C., "Design of a centrifugal compressor for application in micro gas turbines," 2014.

17. "Gas Turbine Schematic and Station Numbers," NASA Webpage, Available at https://www.grc.nasa.gov/www/k-12/airplane/turbdraw.html.

18. "What is a spool and why does it matter?" GE Aviation, Available at https://www.geaviation.com/military/engines/t901-turboshaft-engine.

19. "JetMan' Yves Rossy Soars Like a Superhero: The Future of Human Flight in Dubai," Forbes.com, Available at https://www.forbes.com/sites/jimdobson/2015/05/11/jetman-yves-rossy-soars-like-a-superhero-the-future-of-human-flight-in-dubai/?sh=4896363d7347.

20. "JetCat P400 Pro Product Information and Specifications," Jet-Cat, Ballrechten-Dottingen, Germany, 2020, Accessed via website https://www.jetcat.de/en/productdetails/produkte/jetcat/produkte/Professionell/p400%20pro, Aug-2021.

21. Fathy, T. S., Elzahaby, A. M., and Khalil, M. K., "Micro TJE centrifugal compressor performance prediction Tamer S." *Journal of Engineering Science and Military Technologies*, Vol. 2, No. 4, 2018, pp. 185–203.

22. "JetCat P400 Pro Product Information and Specifications," ChiefAircraft.com, Available at https://www.chiefaircraft.com/jc-p400-pro.html.

23. "How Turbochargers Work," Auto.howstuffworks.com, Available at https://auto.howstuffworks.com/turbo.htm.

24. "GARRETT GTX5008R Turbocharger Images and Specifications," Motion G. A., AMS Performance.com, Available at https://www.amsperformance.con/product/garrett-gtx500r-turbocharger/.

25. Mattingly, J. D. and Boyer, K. M., *Elements of propulsion*, American Institute of Aeronautics and Astronautics Reston, VA, 2nd ed., 2016.

26. Buckingham, E., *One Physically Similar Systems; Illustrations of the Use of Dimensional Equations*, Physics Revised, Vol. 4, No. 4, pp. 345–376, 1999.

27. Balje, O., "A Study of Reynolds Number Effects in Turbomachinery," *Journal of Engineering for Power*, Vol. 86, No. 3, 1964, pp. 227–235.

28. Harman, R., *Gas Turbine Engines*, John Wiley and Sons, Inc., New York City, NY, 1st ed., 1981.

29. Wilson, D. G. and Korakianitis, T., *The Design of High-Efficiency Turbomachinery and Gas Turbines, with a new preface*, MIT press, 2014.

30. Pfleiderer, C., *Die Kreiselpumpen (The Centrifugal Pumps)*, Springer-Verlag, Berlin, Germany, 1st ed., 1949.

31. Boyce, M., *Gas Turbine Engineering Handbook*, Gulf Publishing Co., Houston, TX, 1st ed., 1981.

32. Zheng, X., Jin, L., Du, T., Gan, B., Liu, F., and Qian, H., "Effect of temperature on the strength of a centrifugal compressor impeller for a turbocharger," *Proceedings of the Institution of Mechanical Engineers, Part C: Journal of Mechanical Engineering Science*, Vol. 227, No. 5, 2013, pp. 896–904.

33. Roark, R. J. Young, W. C. and R., P., *Formulas for Stress and Strain*, Vol. 43, McGraw-Hill, 7th ed., 2002.

34. Callister, W. and Rethwisch, D., *Fundamentals of Materials Sceince and Engineering: an Integrated Approach*, John Wiley and Sons, Inc., Hoboken, NJ, 4th ed., 2012.

35. "MatWeb Material Property Data,," MatWeb, Available at http://www.matweb.com/ Accessed Feb 2020.

36. Fernández, S., Jiménez, M., Porras, J., Romero, L., Espinosa, M., and Dominguez, M., "Additive manufacturing and performance of functional hydraulic pump impellers in fused deposition modeling technology," *Journal of Mechanical Design*, Vol. 138, No. 2, 2016, pp. 024501.

37. Turunen-Saaresti T., J. A., "Influence of the Different Design Parameters to the Centrifugal Compressor Tip Clearance Loss," *Journal of Turbomachinery, Vol. 135, No. 1, 2012, pp. 011017*, October 2012.

38. Jaatinen-Värri, A., Turunen-Saaresti, T., Grönman, A., Röyttä, P., and Backman, J., "The tip clearance effects on the centrifugal compressor vaneless diffuser flow fields at off-design conditions," *10 th European Conference on Turbomachinery Fluid dynamics & Thermodynamics*, European Turbomachinery Society, 2013.

39. Pampreen, R., *Small Turbomachinery Compressor and Fan Aerodynamics*, Journal of Engineering for Power , Vol. 95, 07 1973, pp. 251, 1973.

40. Panton, R., *Incompressible Flow*, John Wiley and Sons, Inc., Hoboken, NJ, 3rd ed., 2005.

41. Kays W., Crawford M., W. B., *Convective Heat and Mass Transfer*, McGraw-Hill, New York City, NY, 4th ed., 2005.

42. Tang, Y., Xi, G., Wang, Z., and Tian, Y., "Quantitative Study on Equivalent Roughness Conversion Coefficient and Roughness Effect of Centrifugal Compressor," *Journal of Fluids Engineering*, Vol. 142, No. 2, 2020, pp. 021208.

43. Adams T., Grant C., W. H., "A Simple Algorithm to Relate Measured Surface Roughness to Equivalent Sand-grain Roughness," *International Journal of Mechanical Engineering and Mechatronics, Vol. 1, January 2012*, January 2012.

44. "Micro Gas Turbines – A Short Survey of Design Problems," Van den Braembussche, R.A., von K´arm´an Institute for Fluid Dynamics, Rhode-St-Genese, Belgium, 2005.

45. Grannan, N. D., McClearn, M. J., Litke, P. J., Hoke, J., and Schauer, F., "Trends in jetCAT microturbojet-compressor efficiency," *55th AIAA Aerospace Sciences Meeting*, 2017, p. 0552.

46. Beckwith, T. G., Buck, N. L., and Marangoni, R. D., *Mechanical Measurements, 3rd edition*, Addison-Wesley, p. 503, 1982.

47. "Drilling Machine - Definition, Types, Parts, Operation, Application & Tools," MechanicalNotes.com, Available at https://mechanicalnotes.com/drilling-machine-definition-types-parts-operation-tools/.

48. "Crash Course in Machining – Milling," CNC Proto.eu, Available at https://cnc-proto.eu/cnc-articles/milling/.

49. "Operation On Lathe Machine," Mechanical Technology website - ranamechanical.blogspot.com, Available at https://ranamechanical.blogspot.com/2019/03/operation-on-lathe.html/.

50. "Collection of Material Property Datasheets,," Stratasys, Strasys, 2019, Accessed via website https://www.stratasys.com/materials, Feb-2020.

51. "The 7 Categories of Additive Manufactuing," Additive Manufacturing Research Group, Loughborough University, 2020, Accessed via website https://www.lboro.ac.uk/research/amrg/about/the7categoriesofadditive manufacturing/, Feb-2020.

52. Molitch-Hou, M., *Additive Manufacturing: Materials, Processes, Quantifications and Applications*, Butterworth-Heinemann, Mississauga, Canada, 1st ed., 2018.

53. "Introduction to Binder Jetting 3D printing," Varotsis, A.B., Accessed via website https://www.hubs.com/knowledge-base/introduction-binder-jetting-3d-printing/, Feb-2020.

54. "Introduction to Material Jetting 3D printing," Varotsis, A.B., Accessed via website https://www.hubs.com/knowledge-base/introduction-material-jetting-3d-printing/, Feb-2020.

55. "The Complete Guide to Directed Energy Deposition (DED) in 3D Printing," Carlota, V., 3D Natives, 2019, Accessed via website https://www.3dnatives.com/en/directed-energy-deposition-ded-3d-printing-guide-100920194/#!, Feb-2020.

56. ASTM-Standard, "Standard terminology for additive manufacturing technologies," *ASTM International F2792-12a*, 2012.

57. Ngo, T. D., Kashani, A., Imbalzano, G., Nguyen, K. T., and Hui, D., "Additive manufacturing (3D printing): A review of materials, methods, applications and challenges," *Composites Part B: Engineering*, Vol. 143, 2018, pp. 172–196.

58. Byberg, K. I., Gebisa, A. W., and Lemu, H. G., "Mechanical properties of UL-TEM 9085 material processed by fused deposition modeling," *Polymer Testing*, Vol. 72, 2018, pp. 335–347.

59. "Types of Molding Processes," CE Wheels Inc., Available at https://www.cewheelsinc.com/types-molding-processes/ Accessed 13 Oct 2021.

60. "What is Casting?" Plastics Intl., Written by Chris Kelly, Accessed via website https://www.plasticsintl.com/blog/what-is-casting/, Jan-2022.

61. "Resin Families," Polysource.net, Accessed via website https://polysource.net/plastic-resin-families-and-applications/, Jan-2022.

62. "Plastic Casting Process Explanation," MechanicalBase.com, Accessed via website https://mechanicalbase.com/plastic-casting-process-explanation/, Jan-2022.

63. "The Basic Plastic Injection Molding Process," Aire Plastics.com, Accessed via website https://www.aireplastics.com/basic-injection-molding-process/, Jan-2022.

64. "What Are Plastic Injection Moulding Advantages And Disadvantages?" ToolcraftPlastic.co, Accessed via website https://www.toolcraft.co.uk/plastic-injection-moulding/advice/advice-plastic-injection-moulding-advantages-disadvantages.htm, Jan-2022.

65. "Injection Molding Machines," Machinery Center, Inc, Accessed via website http://www.machinerycenter.com/news/injection-molding-machines-guide/, Jan-2022.

66. "Guide to Compression Molding From Prototyping to Mass Production," formlabs.com, Accessed via website https://formlabs.com/blog/compression-molding/, Jan-2022.

67. "What is the Difference between Low & High Cycle Fatigue?" Fatec Engineering, Available at https://www.fatec-engineering.com/2018/08/23/what-is-the-difference-between-low-high-cycle-fatigue/.

68. Luca, D. D., "Understanding Fatigue," *Global Gas Turbine News*, 2001.

69. Feraboli, P., Peitso, E., Cleveland, T., and Stickler, P., "Characterization of Discontinuous Carbon Fiber/Epoxy Systems for Aerospace Applications: PART II," *49th AIAA/ASME/ASCE/AHS/ASC Structures, Structural Dynamics, and Materials Conference, 16th AIAA/ASME/AHS Adaptive Structures Conference, 10th AIAA Non-Deterministic Approaches Conference, 9th AIAA Gossamer Spacecraft Forum, 4th AIAA Multidisciplinary Design Optimization Specialists Conference*, 2008, p. 1939.

70. Guzman de Villoria, R., Ydrefors, L., Hallander, P., Ishiguro, K., Nordin, P., and Wardle, B., "Aligned carbon nanotube reinforcement of aerospace carbon fiber composites: substructural strength evaluation for aerostructure applications," *53rd AIAA/ASME/ASCE/AHS/ASC Structures, Structural Dynamics and Materials Conference 20th AIAA/ASME/AHS Adaptive Structures Conference 14th AIAA*, 2012, p. 1566.

71. Ekvall, J. and Griffin, C., "Design allowables for T300/5208 graphite/epoxy composite materials," *Journal of Aircraft*, Vol. 19, No. 8, 1982, pp. 661–667.

72. "Carbon Fiber: The More You Know, The More You Can Do," The O and P Edge.com, Available at https://opedge.com/Articles/ViewArticle/2013-07-10.

73. "Prepreg Uni-Directional Tape," TCR Composites, Available at https://tcrcomposites.com/product/product-tape.php.

74. "What is non-destructive testing (NDT)? - Methods and definition," TWI-Global Website, Available at https://www.twi-global.com/technical-knowledge/faqs/what-is-non-destructive-testing#MethodsofNonDestructiveTesting.

75. "Individual Conversations with a FEA Professional, May-December 2019," Gillaugh, D, AFRL-RQT, Dayton, OH, 2019.

76. "MatWeb Material Property Data," MatWeb, Accessed via website http://www.matweb.com, Feb-2020.

77. "Collection of Material Property Datasheets," 3D Systems, Accessed via website https://www.materialise.com/en/academy-manufacturing/resources/datasheets, Feb-2020.

78. "Collection of Material Property Datasheets,," Markforged, Accessed via website https://markforged.com/materials/plastics/onyx, Feb-2020.

79. "Standard Test Method for Tensile Properties of Plastics," ASTM D638-14, ASTM International, 2014.

80. Miller, A., Brown, C., and Warner, G., "Guidance on the use of existing ASTM polymer testing standards for ABS parts fabricated using FFF," *Smart and Sustainable Manufacturing Systems*, Vol. 3, No. 1, 2019.

81. "Poisson Ratio of Polymeric Materials," A Polymer Properties Database, 2015, Accessed via website https://polymerdatabase.com/polymer%20physics/Poisson.html, Feb-2020.

82. Muthu S.E., Dileep S., M. R., "Optimization of a Centrifugal Impeller for a Small Gas Turbine Engine: A Finite Element Approach," *Proceedings of the ASME 2012 Gas Turbine India Conference, December 2012.*, December 2012.

83. Przemieniecki, J. S., *Finite element structural analysis: new concepts*, American Institute of Aeronautics and Astronautics, 2009.

84. Koutromanos, I., *Fundamentals of Finite Element Analysis: Linear Finite Element Analysis*, John Wiley and Sons, Inc., Hoboken, NJ, 1st ed., 2018.

85. Pletcher R.H., Tannehill J.C., A. D., *Computational Fluid Mechanics and Heat Transfer*, Taylor and Francis Group, LLC., Boca Raton, FL, 3rd ed., 2013, 2013.

86. Mohamed, M., Hashim, F., Amini, M., Janvekar, A., Razab, M., Yusuf, N., and Rizman, Z., "Finite element analysis of car hood for impact test by using Solidworks software in automotive application," *Journal of Fundamental and Applied Sciences*, Vol. 10, No. 1S, 2018, pp. 936–955.

87. "Composite Materials for Future Aeroengines," Kirk, E.G., International Gas Turbine and Aeroengine Congress and Exposition, June 1989.

88. Vo, H. and Trepanier, J., "Undergraduate Project in Compressor Rig Design, Fabrication, and Testing for Complete Engineering Training," *Journal of Engineering for Gas Turbines and Power , Vol. 138, No. 5, May 2016*, May 2016.

89. "Individual Conversations with AFRL/RQ Intern, May-December 2021," Murphy, Z., AFRL-RQ, Dayton, OH, 2021.

90. "ASTM D638 TypeIV," datapointlabs.com, Accessed via https://www.datapointlabs.com/specimens/tensilebars.htm.

91. "Supreme 121AO Technical Data Sheet," Masterbond.com, Document requested from manufacturer via Masterbond website https://www.masterbond.com/tds/supreme-121ao, Jan-2022.

92. "Standard Test Method for Deflection Temperature of Plastics Under Flexural Load in Edgewise Position," ASTM D648-01, ASTM International, 2001.

93. "Calibration Report, 3 Kip Displacement," Scholl, D., MTS Systems Corporation, Eden Prairie, MN, 2021, Calibration performed for AFIT.

94. "Calibration Report, 22 Kip Displacement," Scholl, D., MTS Systems Corporation, Eden Prairie, MN, 2021, Calibration performed for AFIT.

95. "Linear Variable Differential Transformer and Strain Gauge Transducer," UKEssays, Accessed via website https://www.ukessays.com/essays/engineering/linear-variable-differential-transformer-and-strain-gauge-transducer-engineering-essay.php?vref=1.

96. "Meshing," SolidWorks Web Help, Accessed via website https://help.solidworks.com/2020/english/SolidWorks/cworks/c_Background _on_Meshing.htm, Jan-2022.

97. "Collection of Product Specifications for T-type Thermocouple," McMaster-Carr, Available at https://www.mcmaster.com/type-t-thermocouples/response-time 0-6-sec-/.

98. "Collection of Product Specifications," Omega, A Spectric Company, Available at Omega Website, 2019, Accessed via website https://www.omega.com/en-us/pressure-measurement/pressure-transducers/px409-series/p/PX409-250AI-EH, Feb-2020.

99. "Collection of Product Specifications," Omega, A Spectric Company, Available at Omega Website, 2019, Accessed https://www.omega.com/en-us/search/?text=kiel+probe, Nov-2021.

100. "ROLS-W Product Specification Sheet, 2019," Monarch Instruments, Accessed via website https://www.grainger.com/product/36J802?ef_id=Cj0KCQiA15yNBhDTARI sAGnwe0Uw01i2UIJEsic3CizKQa_RMtSiYSpk0KT-PECOMdkZn4Kbv1OLIksaAgFZEALw_wcB:G:s&s_kwcid=AL!2966!3!335677 392229!p!!g!!monarch%20rols-w&gucid=N:N:PS:Paid:GGL:CSM-2296:AB578S:20500731&gclid=Cj0KCQiA15yNBhDTARIsAGnwe0Uw01i2UI JEsic3CizKQa_RMtSiYSpk0KT-PECOMdkZn4Kbv1OLIksaAgFZEALw_wc B&gclsrc=aw.ds, Nov-2021.

101. "Collection of Product Specifications," BiTorq, Bitorq Valve Automation, A Divi sion of Strahman Valves, Inc., 2019, Accessed via website https://www.strahmanvalves.com/es-es/products-389c4d198b47e63a178829273bfa30b5/bi-torq-valve-automation/, Nov-2021.

102. "Balance Quality Requirements of Rigid Rotors, The Practical Application of ISO 1940/1," IRD Balancing, March 2009.

103. "ULTEM™ 9085 Resin," stratasys.com, Accessed via https://www.stratasys.com/materials/search/ultem9085, Jan-2022.

104. "Understanding Confidence Intervals — Easy Examples & Formulas," Scribbr.com, Accessed via website https://www.scribbr.com/statistics/confidence-interval/.

105. "ULTEM™ 9085 Production -Grade Thermoplastic for Fortus 3D Production Systems," Statasys.com, Accessed via website https://www.stratasysdirect.com/-/media/files/direct/material-datasheets/fused-deposition-modeling/fdm_ultem_9085_material_specifications.pdf.

106. "ULTEM 9085," Materialise.com, Accessed via website https://www.materialise.com/en/manufacturing/materials/ultem-9085.

107. "ULTEM ™ 9085 Resin FDM ® Thermoplastic Filament Fit for High-Performance Applications," Statasys.com, Accessed via website https://info.stratasysdirect.com/rs/626-SBR-192/images/Data%20Sheet%20-%20ULTEM%209085%20EN.pdf.

108. Volkov, Y. M., Vorob'ev, E., Drozdov, A., Zemtsov, M., Novogrudskii, L., Kanivets, I., and Kharchenko, V., "Effect of a Temperature on the Mechanical Characteristics of ULTEM 9085 Thermoplastic Produced by Additive Technology," *Strength of Materials*, Vol. 52, No. 3, 2020, pp. 414–418.

109. "Certified ULTEM™ 9085 Resin," stratasys.com, Accessed via https://www.stratasys.com/-/media/files/material-spec-sheets/mds_fdm_ultem9085cert_0618b.pdf, Jan-2022.

110. Pascual-González, C., Iragi, M., Fernández, A., Fernández-Blázquez, J., Aretxabaleta, L., and Lopes, C., "An approach to analyse the factors behind the micromechanical response of 3D-printed composites," .

111. Zhang, Y., Purssell, C., Mao, K., and Leigh, S., "A physical investigation of wear and thermal characteristics of 3D printed nylon spur gears," *Tribology International*, Vol. 141, 2020, pp. 105953.

112. Fernandes, R. R., Tamijani, A. Y., and Al-Haik, M., "Mechanical characterization of additively manufactured fiber-reinforced composites," *Aerospace Science and Technology*, Vol. 113, 2021, pp. 106653.

113. Seifans, A., Ayyagari, S., and Al-Haik, M., "Elastic/viscoplastic characterization of additively manufactured composite based on continuous carbon fibers," *Aerospace Science and Technology*, Vol. 111, 2021, pp. 106562.

114. Spina, R., "Performance analysis of colored PLA products with a fused filament fabrication process," *Polymers*, Vol. 11, No. 12, 2019, pp. 1984.

115. Chawla, K., *Composite Materials: Science and Engineering*, Springer, New York City, NY, 3rd ed., 2013.

116. You, Y.-J., Kim, J.-H. J., Park, K.-T., Seo, D.-W., and Lee, T.-H., "Modification of rule of mixtures for tensile strength estimation of circular GFRP rebars," *Polymers*, Vol. 9, No. 12, 2017, pp. 682.

117. "3D printing of CF/nylon composite mold for CF/epoxy parabolic antenna," journals.sagepub.com, Accessed via website https://journals.sagepub.com/doi/full/10.1177/1558925020969484.

118. "Onyx: General Information," support.markforged.com, Accessed via website https://support.markforged.com/portal/s/article/Onyx.

119. Mulholland, T., Felber, R., and Rudolph, N., "Design and Additive Manufacturing of a Composite Crossflow Heat Exchanger," *2017 International Solid Freeform Fabrication Symposium*, University of Texas at Austin, 2017.

120. "Mechanical Testing And Finite Element Analysis Of 3D Printed Continuous Carbon Fiber Reinforced Onyx Thermoplastic," University of Stavanger, Ghebretinsae Fithawi, Accessed via website https://support.markforged.com/portal/s/article/Onyx.

121. "571 1/4" Chopped Carbon Fibers Safety Sheet," Fiberglast.com, Document requested from manufacturer via Fiberglast website https://www.fibreglast.com/, Jan-2022.

122. Spina, R., "Performance analysis of colored PLA products with a fused filament fabrication process," *Polymers*, Vol. 11, No. 12, 2019, pp. 1984.

123. "MakerBot Tough Model Material / Onyx Black," store.javelin-tech.com, Accessed via website https://store.javelin-tech.com/Store-Catalog/MakerBot-METHOD/MakerBot-Tough-Model-Material-Onyx-Black, Jan-2022.

124. "MakerBot Tough Precision Print Pack Onyx Black," matterhackers.com, Accessed via website https://www.matterhackers.com/store/l/makerbot-tough-precision-print-pack/sk/MW1U23HW, Jan-2022.

125. Pan, N., "The elastic constants of randomly oriented fiber composites: A new approach to prediction," *Science and Engineering of composite materials*, Vol. 5, No. 2, 1996, pp. 63–72.

126. "Overview of materials for Epoxy Cure Resin," MatWeb Material Property Data, Accessed via website http://www.matweb.com/search/DataSheet.aspx?MatGUID=956da5edc80f4c62 a72c15ca2b923494&ckck=1.

127. "Free Flowing Encapsulant meets NASA Low Outgassing Specifications," MasterBond Website, Accessed via website https://www.masterbond-de.com/infographic/free-flowing-encapsulant-meets-nasa-low-outgassing-specifications.

128. "Modulus, Poisson's Ratio and Elongation," MasterBond Website, Accessed via website https://www.masterbond.com/techtips/modulus-poisson%E2%80%99s-ratio-and-elongation.

129. "D608/602C GRW/HQW," BocaBearings.com, Accessed via website https://www.bocabearings.com/products/d608-602c-grw-hqw-1889.

130. "Internal Retaining Ring for 24 mm ID, Black-Phosphate 1060-1090 Spring Steel," McMaster-Carr, Accessed via website https://www.mcmaster.com/98455A124/.

131. "18-8 Stainless Steel Oversized Washer for M7 Screw Size, 7.4 mm ID, 22 mm OD," McMaster-Carr, Accessed via website https://www.mcmaster.com/91116A250/.

132. "Split Wave Disc Spring 16.460 mm ID, 22 mm OD," McMaster-Carr, Accessed via website https://www.mcmaster.com/1775N33/.

133. "MSF-16-4-8 Flexible Couplings - Serration - Type," NBK1560, Accessed via website https://www.nbk1560.com/en-US/products/coupling/couplicon/serration_type/MSF/MSF-16/MSF-16-4-8/.

134. "Individual Conversations with a Turbomachinery Professional, January-2022," Boehle, Matthew, AFRL-RQTM, Dayton, OH, 2019.

135. "Bearing Locknut 303 Stainless Steel, 0.469"-32 Thread Size," McMaster-Carr, Accessed via website https://www.mcmaster.com/6343K72/.

REPORT DOCUMENTATION PAGE

Form Approved
OMB No. 0704–0188

1. REPORT DATE *(DD–MM–YYYY)*	2. REPORT TYPE	3. DATES COVERED *(From — To)*
24-03-2022	Master's Thesis	Sept 2021 — Mar 2022

4. TITLE AND SUBTITLE

DESIGN AND TESTING OF A COMPOSITE COMPRESSOR ROTOR

5a. CONTRACT NUMBER

5b. GRANT NUMBER

5c. PROGRAM ELEMENT NUMBER

6. AUTHOR(S)

Mauro Noel V. de Leon

5d. PROJECT NUMBER

5e. TASK NUMBER

5f. WORK UNIT NUMBER

7. PERFORMING ORGANIZATION NAME(S) AND ADDRESS(ES)

Air Force Institute of Technology
Department of Aeronautics and Astronautics (AFIT/EN)
2950 Hobson Way
WPAFB OH 45433-7765

8. PERFORMING ORGANIZATION REPORT NUMBER

AFIT-ENY-MS-22-M-286

9. SPONSORING / MONITORING AGENCY NAME(S) AND ADDRESS(ES)

Air Force Research Laboratory
8th St. Building 71B
WPAFB OH 45433-7765
COMM 937-713-0047
Email: mark.fernelius.2@us.af.mil

10. SPONSOR/MONITOR'S ACRONYM(S)

AFRL/RQTC

11. SPONSOR/MONITOR'S REPORT NUMBER(S)

12. DISTRIBUTION / AVAILABILITY STATEMENT

DISTRIBUTION STATEMENT A:
APPROVED FOR PUBLIC RELEASE; DISTRIBUTION UNLIMITED.

13. SUPPLEMENTARY NOTES

14. ABSTRACT

Additive manufacturing (AM) and molding are manufacturing methods known for building representations or replicas of conceptualized engine components, but was considered impractical for manufacturing operating engine components. More recent technology has rendered composite materials (combining high-temperature polymers and fiber reinforcement) capable of withstanding the temperature and structural requirements to compete with conventional turbomachinery metals. This study explores the application of several high-temperature polymers (ULTEM 9085, Onyx-Carbon fiber, and Epoxy-Carbon fiber) and their survivability in the operating conditions of a P400 Engine compressor. The tests conducted for this study determined their viability as compressor materials. This study required conducting tensile specimen testing, FEA modeling, and physical compressor spin testing. The results of each will be discussed.

15. SUBJECT TERMS

Additive Manufacturing, Thesis, small scale engine, composite compressor rotor

16. SECURITY CLASSIFICATION OF:			17. LIMITATION OF ABSTRACT	18. NUMBER OF PAGES	19a. NAME OF RESPONSIBLE PERSON
a. REPORT	b. ABSTRACT	c. THIS PAGE			Lt Col Brian Bohan, AFIT/ENY
U	U	U	U	291	**19b. TELEPHONE NUMBER** *(include area code)* (937) 255-3636, x4772; Brian.Bohan@afit.edu

Standard Form 298 (Rev. 8–98)
Prescribed by ANSI Std. Z39.18